

University of Groningen

## Spin transport and relaxation in graphene, functionalized-graphene & graphene-TMD heterostructures

Omar, Siddharta

**IMPORTANT NOTE: You are advised to consult the publisher's version (publisher's PDF) if you wish to cite from it. Please check the document version below.**

*Document Version*

Publisher's PDF, also known as Version of record

*Publication date:*

2018

[Link to publication in University of Groningen/UMCG research database](#)

*Citation for published version (APA):*

Omar, S. (2018). Spin transport and relaxation in graphene, functionalized-graphene & graphene-TMD heterostructures [Groningen]: University of Groningen

### Copyright

Other than for strictly personal use, it is not permitted to download or to forward/distribute the text or part of it without the consent of the author(s) and/or copyright holder(s), unless the work is under an open content license (like Creative Commons).

### Take-down policy

If you believe that this document breaches copyright please contact us providing details, and we will remove access to the work immediately and investigate your claim.

Downloaded from the University of Groningen/UMCG research database (Pure): <http://www.rug.nl/research/portal>. For technical reasons the number of authors shown on this cover page is limited to 10 maximum.

Spin Transport and Relaxation in Graphene,  
Functionalized-Graphene  
&  
Graphene-TMD Heterostructures

Siddhartha Omar



**GRAPHENE FLAGSHIP**



**university of  
 groningen**

**faculty of science  
 and engineering**

Zernike Institute PhD thesis series 2018-11

ISSN: 1570-1530

ISBN:978-94-034-0501-8

ISBN:978-94-034-0502-5 (electronic version)

The work described in this thesis was performed in the research group Physics of Nanodevices of the Zernike Institute for Advanced Materials at the University of Groningen, the Netherlands. This work is part of the European Graphene Flagship Program (190637100).

Cover design: Abhishek Niranjana

Cover image: The thesis cover contains various optical, and scanning electron microscope images of the devices, used in this thesis. Some images are the artistic impression of the electrical circuits, I used for the measurements.

Printed by: Gildeprint, Enschede



**university of  
 groningen**

**Spin Transport and Relaxation in Graphene,  
 Functionalized-Graphene  
 &  
 Graphene-TMD Heterostructures**

**PhD Thesis**

to obtain the degree of PhD at the  
 University of Groningen  
 on the authority of the  
 Rector Magnificus Prof. E. Sterken  
 and in accordance with  
 the decision by the College of Deans.

This thesis will be defended in public on

Friday 9 March 2018 at 16.15 hours

by

**Siddhartha Omar**

born on 1 June 1987  
 in Hamirpur, India

**Supervisor**

Prof. B.J. van Wees

**Co-supervisor**

Dr. I. Vera Marun

**Assessment committee**

Prof. A. Kis

Prof. G.E.W. Bauer

Prof. J. Ye

*Dedicated to Papa*



---

# Contents

<b>1</b>	<b>Introduction</b>	<b>1</b>
1.1	Spintronics . . . . .	3
1.2	Graphene . . . . .	4
1.3	Graphene Spintronics . . . . .	4
1.4	Spintronics with Graphene-hBN and Graphene-TMD heterostructures	5
1.5	This Thesis . . . . .	5
	References . . . . .	8
<b>2</b>	<b>2D-Materials</b>	<b>11</b>
2.1	Graphene . . . . .	12
2.2	Hexagonal Boron Nitride (hBN) . . . . .	13
2.3	Transition Metal Dichalcogenides . . . . .	13
2.4	hBN-Graphene and WS <sub>2</sub> -Graphene Heterostructures . . . . .	15
	References . . . . .	17
<b>3</b>	<b>Principles of Graphene Spintronics</b>	<b>19</b>
3.1	Electrical Spin Injection . . . . .	20
3.2	Spin-valve Measurements . . . . .	20
3.3	Hanle Spin Precession Measurements . . . . .	22
3.4	Spin Relaxation in Graphene . . . . .	23
3.4.1	Spin-Orbit Coupling in Graphene . . . . .	23
3.4.2	Spin Relaxation . . . . .	24
3.4.3	A Summary on Role of Impurities in spin-relaxation in Graphene	26
3.4.4	Effect of Substrate on Spin-transport . . . . .	27
3.4.5	Electric Field induced Spin orbit Coupling . . . . .	30
	References . . . . .	31



---

<b>4</b>	<b>Theory of Noise</b>	<b>35</b>
4.1	White noise . . . . .	36
4.1.1	Thermal Noise . . . . .	36
4.1.2	Shot Noise . . . . .	37
4.2	Colored noise . . . . .	38
4.2.1	Flicker Noise . . . . .	38
4.3	Spin-dependent Noise . . . . .	40
4.3.1	Magnetic Noise . . . . .	40
4.3.2	Noise associated with Spin-accumulation . . . . .	41
	References . . . . .	42
<b>5</b>	<b>Experimental Methods</b>	<b>45</b>
5.1	Sample Preparation . . . . .	46
5.1.1	2D Material Exfoliation . . . . .	46
5.1.2	Dry Pick-up Transfer Method . . . . .	48
5.1.3	Electron Beam Lithography . . . . .	51
5.1.4	Contact Fabrication . . . . .	51
5.2	Electrical Measurements . . . . .	51
5.2.1	Charge Transport . . . . .	53
5.2.2	Spin Transport . . . . .	53
	References . . . . .	55
<b>6</b>	<b>Spin Relaxation in Graphene with self-assembled Cobalt Porphyrin Molecules</b>	<b>57</b>
6.1	Introduction . . . . .	58
6.2	Device Fabrication . . . . .	59
6.3	Results and Discussion . . . . .	59
6.3.1	Charge Transport . . . . .	60
6.3.2	Spin Transport . . . . .	60
6.4	Conclusions . . . . .	67
6.5	Acknowledgements . . . . .	68
	References . . . . .	69
<b>7</b>	<b>Spin Relaxation 1/f Noise</b>	<b>71</b>
7.1	Introduction . . . . .	72
7.2	Sample Preparation . . . . .	72
7.3	Setup . . . . .	73
7.4	Results . . . . .	78
7.4.1	Charge 1/f Noise . . . . .	78
7.4.2	Spin-dependent 1/f Noise . . . . .	80
7.5	Discussion . . . . .	83

## Contents

---

7.5.1	Estimation of Contact Polarization Noise . . . . .	85
7.5.2	Spatial Cross-correlation Measurements for Extracting Spin-transport Parameters . . . . .	86
7.5.3	Spin-dependent Noise: Analytical Expression . . . . .	87
7.6	Conclusions . . . . .	88
7.7	Acknowledgements . . . . .	89
	References . . . . .	90
<b>8</b>	<b>A Two-channel Model for Spin-relaxation Noise Analysis</b>	<b>93</b>
8.1	Introduction . . . . .	94
8.2	Developing a Two-channel Resistor Model . . . . .	94
8.3	Derivation for Spin Relaxation Resistance . . . . .	102
8.4	Scaling of Noise Current in a Two Channel Model . . . . .	103
8.5	Acknowledgments . . . . .	103
	References . . . . .	105
<b>9</b>	<b>Spin Transport &amp; Spin-relaxation in Graphene hBN Heterostructures</b>	<b>107</b>
9.1	Introduction . . . . .	108
9.2	Spin Transport in 1L hBN/Gr/hBN Heterostructure . . . . .	109
9.3	Spin Transport in Bilayer hBN/Gr/hBN Heterostructure . . . . .	110
9.4	Spin-relaxation in all Exfoliated hBN/graphene/hBN Heterostructures	112
9.5	Spin-relaxation in 2L-CVD hBN/Graphene/thick hBN Heterostructures	113
9.6	Conclusions . . . . .	114
9.7	Acknowledgements . . . . .	115
	References . . . . .	116
<b>10</b>	<b>Graphene-WS<sub>2</sub> Heterostructures for Tunable Spin Injection and Spin Transport</b>	<b>117</b>
10.1	Introduction . . . . .	118
10.2	Sample Preparation . . . . .	119
10.3	Measurement . . . . .	121
10.4	Conclusions . . . . .	128
10.5	Acknowledgement . . . . .	129
	References . . . . .	130
<b>11</b>	<b>Spin transport in High-mobility Graphene on WS<sub>2</sub> Substrate with Electric-field Tunable Proximity Spin-orbit Interaction</b>	<b>133</b>
11.1	Introduction . . . . .	134
11.2	Sample preparation . . . . .	136
11.3	Sample Characterization . . . . .	136
11.3.1	Charge Transport Measurements . . . . .	136
11.3.2	Spin Transport Measurements . . . . .	139

11.4 Results and Discussion . . . . .	140
11.5 Low Temperature Quantum Magnetotransport Measurements . . . . .	146
11.6 Conclusions . . . . .	148
11.7 Acknowledgements . . . . .	148
References . . . . .	149
<b>summary</b>	<b>151</b>
<b>Samenvatting</b>	<b>155</b>
<b>Hindi Summary</b>	<b>159</b>
<b>Acknowledgements</b>	<b>163</b>
<b>Publications</b>	<b>169</b>
<b>Curriculum Vitae</b>	<b>171</b>

## Abstract

*Since last decade, graphene has been the favorite 'spintronic' research material, due to its low intrinsic spin-orbit coupling. This very fact is responsible for theoretically expected long spin-relaxation length and spin-relaxation time in graphene but it also hinders the application of graphene as 'Datta-Das' spin-transistor with a tunable spin-orbit coupling. Even, the 'expected' spin transport properties have not been realized yet, leading to various theoretical and experimental attempts in order to understand the root cause of the low spin-relaxation time in graphene.*

*In this thesis, in **chapters one-five** I present a brief overview of graphene-spintronics followed by a brief description of the 2-D materials, theoretical and experimental tools, used in this thesis. On the experimental side, I explore the spin-relaxation in graphene in two different ways. A first set of experiments explores the effect of external factors such as impurities, on the spin-relaxation processes in graphene. I demonstrate in **chapter six** that the magnetic impurities enhance the spin-relaxation via spin-flip processes. In **chapter seven**, I devise a novel way to study the spin-relaxation via 1/f spin-noise studies, which also suggests that the impurity-spin interaction is detrimental for spin-transport in graphene. Equally important, I also demonstrate that the spin-noise can be used as a probe for detecting the spin-accumulation as well as it can 'read-out' the fingerprints of the underlying spin-relaxation, which establishes noise as an alternative tool to study spin-transport and impurity-spin interaction. Same conclusions were obtained in **chapter eight** where I use a two-channel resistor model to simulate the spin-dependent noise.*

*A second set of experiments exploits the potential of the proximity-induced effects in graphene, via which some 'foreign' properties such as an enhanced spin-orbit coupling and a band-gap can be imparted onto graphene, and make it more useful for practical applications. In **chapter ten and eleven** I study the possibility of enhancing the spin-orbit coupling by putting graphene in the neighborhood of WS<sub>2</sub>, a transition metal dichalcogenide (TMD), with a high intrinsic spin-orbit coupling. Here, I also use WS<sub>2</sub> as an intermediate layer which can tune the spin-injection into graphene and acts as a 'dimmer' switch for spin-injection. This can have future applications. This thesis also demonstrates the use of WS<sub>2</sub> as a potential substrate for improving charge transport in graphene with a modified spin-transport due to WS<sub>2</sub>-induced spin-orbit coupling. In **chapter nine**, I also briefly discuss the potential of insulating 2D-hBN thin flakes for efficient spin-injection/detection efficiencies, reaching even up to 100 %, accompanied by a brief analysis of the spin-relaxation process in these structures.*

*In conclusion, graphene-2D material heterostructures, discussed in this thesis, demonstrate enhanced as well as controlled spin-transport in graphene, depending on the choice of the 2D-material. These results promise to pave a way for graphene-based practical spintronic devices.*

## 1.1 Spintronics

Low power electronics with extra functionalities is the driving force for the next generation electronics which necessitates the development of alternative energy efficient routes as well as exploit the extra degree of freedom of the information carriers.

Spin-based electronics or 'Spintronics' relies on the spin degree of freedom of electron instead of its charge degree of freedom in electronics for information manipulation, transport and storage. Electron spins having spin-up ( $\uparrow$ ) and -down ( $\downarrow$ ) states are used as '1' and '0' for logic applications. The present technology, still in its development phase promises low power consumption with fast access to the stored information in magnetic bits [1, 2]. The discovery of the giant magnetoresistance (GMR) effect by the group of Albert Fert and Peter Grünberg in 90s [3, 4] led to realization of the first spintronic devices. In the GMR effect, two magnetic metal layers (FM1 and FM2) are separated by a nonmagnet (NM), and the resistance of the system changes from low to high or vice versa on the application of a magnetic field. The high and low resistance state of the FM1/NM/FM2 system is treated as '0' and '1' states for data storage. Similarly, the tunnel magneto resistance (TMR) effect was realized while replacing the NM with a thin tunnel barrier which are nowadays being used in computer hard disks and nonvolatile magnetic random access memory (MRAM) for data storage applications.

The current development phase of the novel spintronic devices is quite promising. The unique ability of spin-current, which also carries spin-angular momentum, to switch the magnetization state of a FM layer via the spin-transfer-torque (STT) phenomenon has drawn a lot of attention for the development of the STT MRAM devices for memory applications [5]. This technology is attractive for low power applications [6]. A very recent demonstration of this phenomenon in 2D transition metal dichalcogenide (TMD) materials, e.g.,  $\text{MoS}_2, \text{WS}_2$  is very promising [7], not only for memory applications but also for providing the possibility of exploring the additional 'valley' degree of freedom as information carriers in these materials. Among the fast emerging phenomena in spintronics, is the realization of racetrack memory [8], which is based on the current induced domain wall motion in a ferromagnetic material. Recent improvement this technology in terms of durability and read/write speed of the data bits is a positive signature for the racetrack memory based applications [9].

The last decade, after a successful isolation of graphene[10] and other 2D materials [11] with the use of a scotch tape, has provided access to novel spin dependent phenomena in these materials and their heterostructures. Due to the reasons described below in Sec.1.3, graphene is an excellent material for spintronic applications at room temperature (RT). Also, the ability of graphene to induce intrinsic electronic and magnetic properties of the neighboring material such as inducing ferromagnetism in graphene when put on top of ferromagnetic insulators, and an en-

hanced spin-orbit coupling in a contact with transition metal dichalcogenides makes graphene an ideal platform for studying foreign properties, and manipulating the spins via external means. This very ability is a precursor for the 'Datta-Das' transistor [12], a building block for spin-logic applications, where one can control the spin-current via an electrical gate, similar to that in electronic transistors. Graphene with broken space inversion symmetry, provides access to the spin coupled 'valley' degree of freedom which can be realized by combining graphene with different host-materials [13–16] or with the application of an external electric field [17]. This opens a new avenue for the field of 'spin-valleytronics' where one can use two degrees of freedom of electron for information storage and transport and control one degree via another. This could lead to a more complex and advanced generation of spin(valley)tronics devices.

1

## 1.2 Graphene

Graphene is a 2-dimensional network of  $sp^2$  hybridized carbon atoms arranged in hexagonal rings, forming a honeycomb lattice structure. Graphite is a stack of several single layer graphene (SLG) sheets put together via weak van der Waals (vW) forces between the layers. In 2004, it was isolated successfully from graphite via an ingeniously simple scotch-tape method [10] and identified optically due to its unique contrast on substrates such as  $SiO_2/Si$ .

Graphene has shown a lot of outstanding characteristics, for example, high mechanical strength [18], high thermal conductivity [19] and optical sensitivity [20]. It also has remarkable electronic properties [21] due to linear band dispersion and massless nature of electrons at low excitation energies, such as chiral nature of charge carriers and high mobility because of low backscattering and weak electron-phonon coupling.

## 1.3 Graphene Spintronics

Graphene is considered as an ideal material for spintronics due to weak intrinsic spin orbit coupling and hyperfine interactions because of the low atomic mass of the constituent carbon atoms. In pristine graphene, theoretically predicted values reach very high such as spin relaxation time  $\tau_s \sim 100$  ns and the spin relaxation length  $\lambda_s \sim 100 \mu\text{m}$  [22, 23] which is several orders of magnitudes higher than in typical semiconductors and metals. However, external factors such as impurities, substrate roughness, charge inhomogeneities are expected to drastically affect its spintronic properties. Therefore the best experimental values of  $\tau_s \sim 12$  nanoseconds and spin relaxation length  $\lambda_s \sim 30 \mu\text{m}$  [24] are still an order of magnitude less than the theoretical prediction.

## 1.4 Spintronics with Graphene-hBN and Graphene-TMD heterostructures

As mentioned in Sec.1.3, graphene is an excellent material to realize spin transport due to weak spin-orbit coupling. However, the same property hinders the realization as a working spin-transistor due to lack of control of the spin-degree of freedom [12, 25]. On the other hand, TMDs with low mobility, have huge intrinsic SOC up to  $\simeq 0.5$  eV in the valence band and  $\simeq 10$  meV in the conduction band, which is almost three orders larger than in graphene [26]. A combination of graphene and TMD appears to be a promising platform to circumvent the aforementioned shortcomings of both materials [27]. An enhanced SOC can be induced in graphene by proximity to a TMD because of two reasons: i) the spatial inversion symmetry is broken at the graphene-TMD interface which is the precursor for the Rashba SOC [28] and ii) the d-orbitals of the TMD hybridize with graphene and enhance the intrinsic SOC in graphene. In this way, the proximitized graphene maintains its excellent charge transport properties [29]. While the spin transport properties due to induced SOC are expected to be affected significantly [30–35]. This is evident in recent quantum magneto-transport [36–38], spin-Hall [35] and non-local spin transport measurements [39–41]. In these systems, one can tune the Rashba SOC by applying an electric field perpendicular to the device plane and thus electrically control the spins, thus realizing a spin transistor with a gate control.

Apart from introducing an enhanced SOC in graphene via the proximity interactions, TMDs are also expected to induce valley-dependent effects in graphene due to sublattice symmetry breaking. A graphene-TMD system offers a unique platform to study other novel effects such as spin-valley coupling by an in-plane electric field and spin and valley Zeeman effects in the presence of an out-of-plane magnetic field [42]. In summary, spin-valley coupling can provide extra functionalities and new features to the conventional graphene spintronic devices with rich underlying physics that has yet to be fully explored.

## 1.5 This Thesis

This thesis experimentally explores two important avenues of spintronics: first, studying the effect of impurities on spin relaxation in graphene, and second, experimentally exploring the possibility of enhancing the spin-orbit coupling in graphene for spin manipulation. I also briefly discuss the potential of hBN tunnel barriers for efficient spin current injection/detection in graphene. In this way, this work is not only a significant attempt to understand the nature of spin-relaxation in graphene but also provides other necessary tools such as control over spin-current by modifying the spin-injection and transport process which are an important step for future



spintronic devices.

This **introduction** chapter provides a brief history over the developments of the field of spintronics, followed by the recent developments. I have also included a concept summary of spin transport study in graphene and some recent developments of combining graphene with other 2D materials such as semiconductors ( $WS_2$ ) and insulators (hBN) and the potential of these hybrid devices for novel spintronic applications.

**Chapter two** explains the electronic band structure of 2D materials: graphene,  $WS_2$  and hBN. I also summarize the basic concepts of electronic transport in these materials, which are used in the later chapters.

**Chapter three** covers the basic concepts of spin transport which I use to analyze my experiments data. Here, I explain the electrical spin-injection into a nonmagnetic material and discuss the spin-detection and manipulation methods, i.e., spin-valve and Hanle spin-precession in the nonlocal spin-transport channel. In the second half, I give a brief overview of different spin-relaxation mechanisms in graphene, followed by a note on the effect of external factors such as impurities on the spin-transport with a summary of the previously reported experiments. Concepts needed in the later chapters such as proximity-induced spin-orbit coupling, spin-valley coupling, electric field controlled Rashba spin-orbit coupling, are also explained.

In **chapter four**, I explain the basic concepts of electronic and spin-dependent noise. In this thesis, instead of directly measuring the DC spin signal, we measure the fluctuations in the spin-signal and demonstrate for the first time, that spins can transport noise. Basic concepts to understand these measurements are explained in this chapter.

**Chapter five** provides a description of the steps for preparing the samples discussed in this thesis, viz a detailed step-by-step protocol for the stack preparation, which is the heart of the sample preparation nowadays. Then a brief description of the lithographic steps such as polymer spin-coating, electron-beam lithography, and the lift-off process is also provided.

After introducing the basic concepts and experimental tools, I present my first experimental findings in **chapter six**. Here, I try to address the long standing puzzle that external, specifically magnetic impurities affect the spin transport and are the dominating factor in reducing the spin-relaxation time in graphene. We study this effect in a four probe nonlocal geometry with ferromagnetic contacts.

In **chapter seven**, I introduce a new tool to explore the interaction of impurities with the spins in graphene. Here I measure the noise in the spin-signal using a low frequency spectrum analyzer. We also show that the measured spin-dependent noise is dominated by spin relaxation processes and propose the noise measurement as a tool for further exploring its nature. In this chapter, I also describe in detail the setup calibration for the noise measurements, which are useful for understanding the noise in normal dc transport measurements.

**Chapter eight** is a re-interpretation of the results obtained in **chapter seven** by circuit simulations. Here, I develop a two channel resistor model to calculate the spin signal and simulate the charge and spin-dependent  $1/f$  noise, and estimate the noise from different resistors in the circuits, representing different physical phenomena.

In **chapter nine**, I present a short summary of the results obtained for spin-injection using single and bi layer hBN tunnel barriers. I also present the analysis of spin-relaxation processes, present during spin-transport in graphene-hBN heterostructures.

In **chapter ten**, I present my experimental findings of spin transport in graphene- $WS_2$  heterostructures in detail. Here, a thick  $WS_2$  crystal is placed on top of a graphene flake. I demonstrate that a spin current can be injected into graphene using a thick  $WS_2$  crystal as an intermediate layer that controls the interface resistance. I also demonstrate a suppressed spin transport in graphene in the proximity of  $WS_2$  which is an indicative of a proximity-induced SOC in graphene.

In **chapter eleven**, I use  $WS_2$  as a substrate for graphene and explore the possibility of inducing spin-orbit coupling in graphene, which is essential to realize the Datta-Das spin-transistor. In this device architecture, I observe improved charge transport properties with significantly reduced spin-transport parameters, confirming the presence of an enhanced SOC in graphene, and opens up a new route to study the novel spintronic phenomena in graphene, in the proximity of a TMD. Further, I also demonstrate that the induced Rashba SOC in graphene can be modified by applying an external electric field perpendicular to the device plane, resulting in a gate control over the spin-relaxation time.

## References

- [1] H. Dery, P. Dalal, L. Cywiński, and L. J. Sham, "Spin-based logic in semiconductors for reconfigurable large-scale circuits," *Nature* **447**, pp. 573–576, May 2007.
- [2] H. Dery, H. Wu, B. Ciftcioglu, M. Huang, Y. Song, R. Kawakami, J. Shi, I. Krivorotov, I. Zutic, and L. J. Sham, "Nanospintronics Based on Magnetologic Gates," *IEEE Trans. Electron Dev.* **59**, pp. 259–262, Jan. 2012.
- [3] M. N. Baibich, J. M. Broto, A. Fert, F. N. Van Dau, F. Petroff, P. Etienne, G. Creuzet, A. Friederich, and J. Chazelas, "Giant Magnetoresistance of (001)Fe/(001)Cr Magnetic Superlattices," *Phys. Rev. Lett.* **61**, pp. 2472–2475, Nov. 1988.
- [4] G. Binasch, P. Grnberg, F. Saurenbach, and W. Zinn, "Enhanced magnetoresistance in layered magnetic structures with antiferromagnetic interlayer exchange," *Phys. Rev. B* **39**, pp. 4828–4830, Mar. 1989.
- [5] H.-S. P. Wong and S. Salahuddin, "Memory leads the way to better computing," *Nat. Nanotechnol.* **10**, pp. 191–194, Mar. 2015.
- [6] "Memory with a spin," *Nat. Nanotechnol.* **10**, pp. 185–185, Mar. 2015.
- [7] D. MacNeill, G. M. Stiehl, M. H. D. Guimaraes, R. A. Buhrman, J. Park, and D. C. Ralph, "Control of spin-orbit torques through crystal symmetry in WTe<sub>2</sub>/ferromagnet bilayers," *Nat. Phys.* **13**, pp. 300–305, Mar. 2017.
- [8] S. S. P. Parkin, M. Hayashi, and L. Thomas, "Magnetic Domain-Wall Racetrack Memory," *Science* **320**, pp. 190–194, Apr. 2008.
- [9] S. Parkin and S.-H. Yang, "Memory on the racetrack," *Nat. Nanotechnol.* **10**, pp. 195–198, Mar. 2015.
- [10] K. S. Novoselov, A. K. Geim, S. V. Morozov, D. Jiang, Y. Zhang, S. V. Dubonos, I. V. Grigorieva, and A. A. Firsov, "Electric Field Effect in Atomically Thin Carbon Films," *Science* **306**, pp. 666–669, Oct. 2004.
- [11] K. S. Novoselov, D. Jiang, F. Schedin, T. J. Booth, V. V. Khotkevich, S. V. Morozov, and A. K. Geim, "Two-dimensional atomic crystals," *PNAS* **102**, pp. 10451–10453, July 2005.
- [12] S. Datta and B. Das, "Electronic analog of the electrooptic modulator," *Appl. Phys. Lett.* **56**, pp. 665–667, Feb. 1990.
- [13] A. Manchon, H. C. Koo, J. Nitta, S. M. Frolov, and R. A. Duine, "New perspectives for Rashba spin-orbit coupling," *Nat. Mater.* **14**, pp. 871–882, Sept. 2015.
- [14] X. Xu, W. Yao, D. Xiao, and T. F. Heinz, "Spin and pseudospins in layered transition metal dichalcogenides," *Nat. Phys.* **10**, pp. 343–350, May 2014.
- [15] D. Pesin and A. H. MacDonald, "Spintronics and pseudospintronics in graphene and topological insulators," *Nat. Mater.* **11**, pp. 409–416, May 2012.
- [16] W. Han, "Perspectives for spintronics in 2d materials," *APL Mater.* **4**, p. 032401, Feb. 2016.
- [17] A. Rycerz, J. Tworzydo, and C. W. J. Beenakker, "Valley filter and valley valve in graphene," *Nat. Phys.* **3**, pp. 172–175, Mar. 2007.
- [18] C. Lee, X. Wei, J. W. Kysar, and J. Hone, "Measurement of the Elastic Properties and Intrinsic Strength of Monolayer Graphene," *Science* **321**, pp. 385–388, July 2008.
- [19] A. A. Balandin, S. Ghosh, W. Bao, I. Calizo, D. Teweldebrhan, F. Miao, and C. N. Lau, "Superior Thermal Conductivity of Single-Layer Graphene," *Nano Lett.* **8**, pp. 902–907, Mar. 2008.
- [20] K. F. Mak, M. Y. Sfeir, Y. Wu, C. H. Lui, J. A. Misewich, and T. F. Heinz, "Measurement of the Optical Conductivity of Graphene," *Phys. Rev. Lett.* **101**, p. 196405, Nov. 2008.
- [21] A. H. Castro Neto, F. Guinea, N. M. R. Peres, K. S. Novoselov, and A. K. Geim, "The electronic properties of graphene," *Rev. Mod. Phys.* **81**, pp. 109–162, Jan. 2009.
- [22] V. K. Dugaev, E. Y. Sherman, and J. Barnaś, "Spin dephasing and pumping in graphene due to random spin-orbit interaction," *Phys. Rev. B* **83**, p. 085306, Feb. 2011.
- [23] H. Min, J. E. Hill, N. A. Sinitsyn, B. R. Sahu, L. Kleinman, and A. H. MacDonald, "Intrinsic and

- Rashba spin-orbit interactions in graphene sheets," *Phys. Rev. B* **74**, p. 165310, Oct. 2006.
- [24] M. Drögel, C. Franzen, F. Volmer, T. Pohlmann, L. Banszerus, M. Wolter, K. Watanabe, T. Taniguchi, C. Stampfer, and B. Beschoten, "Spin Lifetimes Exceeding 12 ns in Graphene Nonlocal Spin Valve Devices," *Nano Lett.* **16**, pp. 3533–3539, June 2016.
- [25] J. C. Egues, G. Burkard, and D. Loss, "DattaDas transistor with enhanced spin control," *Appl. Phys. Lett.* **82**, pp. 2658–2660, Apr. 2003.
- [26] D. Huertas-Hernando, F. Guinea, and A. Brataas, "Spin-Orbit-Mediated Spin Relaxation in Graphene," *Phys. Rev. Lett.* **103**, p. 146801, Sept. 2009.
- [27] A. K. Geim and I. V. Grigorieva, "Van der Waals heterostructures," *Nature* **499**, pp. 419–425, July 2013.
- [28] A. Dyrdał, J. Barnaś, and V. K. Dugaev, "Current-induced spin polarization in graphene due to Rashba spin-orbit interaction," *Phys. Rev. B* **89**, p. 075422, Feb. 2014.
- [29] A. V. Kretinin, Y. Cao, J. S. Tu, G. L. Yu, R. Jalil, K. S. Novoselov, S. J. Haigh, A. Gholinia, A. Mishchenko, M. Lozada, T. Georgiou, C. R. Woods, F. Withers, P. Blake, G. Eda, A. Wirsig, C. Huch, K. Watanabe, T. Taniguchi, A. K. Geim, and R. V. Gorbachev, "Electronic Properties of Graphene Encapsulated with Different Two-Dimensional Atomic Crystals," *Nano Lett.* **14**, pp. 3270–3276, June 2014.
- [30] P. Goswami, "Spin-orbit coupling and exchange field induced band inversion in graphene on a two dimensional transition metal dichalcogenide substrate," *arXiv:1606.02413 [cond-mat]*, June 2016. arXiv: 1606.02413.
- [31] M. Gmitra, D. Kochan, P. Högl, and J. Fabian, "Trivial and inverted Dirac bands and the emergence of quantum spin Hall states in graphene on transition-metal dichalcogenides," *Phys. Rev. B* **93**, p. 155104, Apr. 2016.
- [32] M. Gmitra and J. Fabian, "Graphene on transition-metal dichalcogenides: A platform for proximity spin-orbit physics and optospintronics," *Phys. Rev. B* **92**, p. 155403, Oct. 2015.
- [33] A. W. Cummings, J. H. García, J. Fabian, and S. Roche, "Giant Spin Lifetime Anisotropy in Graphene Induced by Proximity Effects," *arXiv:1705.10972 [cond-mat]*, May 2017. arXiv: 1705.10972.
- [34] D. Kochan, S. Irmer, and J. Fabian, "Model spin-orbit coupling Hamiltonians for graphene systems," *Phys. Rev. B* **95**, p. 165415, Apr. 2017.
- [35] A. Avsar, J. Y. Tan, T. Taychatanapat, J. Balakrishnan, G. K. W. Koon, Y. Yeo, J. Lahiri, A. Carvalho, A. S. Rodin, E. C. T. O'Farrell, G. Eda, A. H. Castro Neto, and B. Zyilmaz, "Spinorbit proximity effect in graphene," *Nat. Commun.* **5**, p. 4875, Sept. 2014.
- [36] Z. Wang, D.-K. Ki, J. Y. Khoo, D. Mauro, H. Berger, L. S. Levitov, and A. F. Morpurgo, "Origin and Magnitude of 'Designer' Spin-Orbit Interaction in Graphene on Semiconducting Transition Metal Dichalcogenides," *Phys. Rev. X* **6**, p. 041020, Oct. 2016.
- [37] B. Yang, M.-F. Tu, J. Kim, Y. Wu, H. Wang, J. Alicea, R. Wu, M. Bockrath, and J. Shi, "Tunable spinorbit coupling and symmetry-protected edge states in graphene/WS<sub>2</sub>," *2D Mater.* **3**(3), p. 031012, 2016.
- [38] Z. Wang, D.-K. Ki, H. Chen, H. Berger, A. H. MacDonald, and A. F. Morpurgo, "Strong interface-induced spin-orbit interaction in graphene on WS<sub>2</sub>," *Nat. Commun.* **6**, p. 8339, Sept. 2015.
- [39] W. Yan, O. Txoperena, R. Llopis, H. Dery, L. E. Hueso, and F. Casanova, "A two-dimensional spin field-effect transistor," *arXiv:1605.09159 [cond-mat]*, May 2016. arXiv: 1605.09159.
- [40] A. Dankert and S. P. Dash, "Electrical gate control of spin current in van der Waals heterostructures at room temperature," *Nat. Commun.* **8**, p. ncomms16093, July 2017.
- [41] S. Omar and B. J. van Wees, "Graphene-WS<sub>2</sub> heterostructures for tunable spin injection and spin transport," *Phys. Rev. B* **95**, p. 081404, Feb. 2017.
- [42] D. Xiao, W. Yao, and Q. Niu, "Valley-Contrasting Physics in Graphene: Magnetic Moment and Topological Transport," *Phys. Rev. Lett.* **99**, p. 236809, Dec. 2007.



### Abstract

*Thin 2D materials with distinguished properties are at the heart of modern day research, dedicated to the development of next- generation electronic, optoelectronic and spintronic devices. A unique ability of these materials of borrowing the electronic and magnetic properties from the neighboring materials, when stacked together, makes them an interesting platform for tuning their intrinsic properties as well as a playground to realize a rich physics such as spin-valley coupling, spin-charge conversion, spin-Hall effects and many more. This chapter provides a summary of basic electronic properties of three different 2D materials: graphene, hBN and WS<sub>2</sub>, discussed in the later chapters of this thesis.*

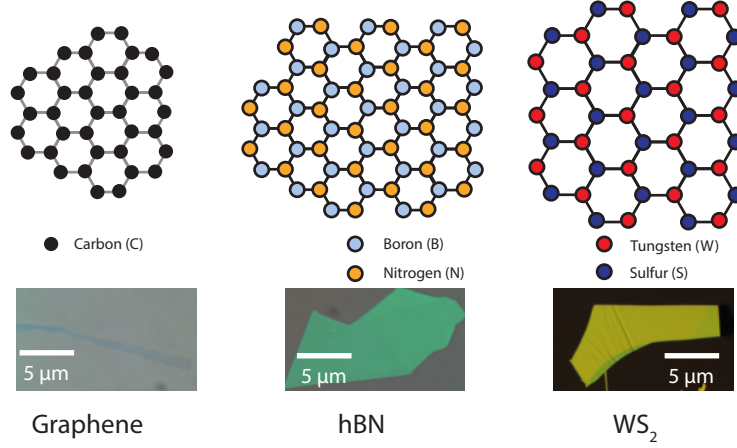


**Figure 2.1:** Lattice structures of a monolayer graphene, hBN and WS<sub>2</sub>. Optical images of the exfoliated flakes are shown in the lower panels. Graphene has been exfoliated on a SiO<sub>2</sub>/Si substrate with 300 nm oxide thickness ( $t_{SiO_2}$ ), and hBN has been exfoliated on a  $t_{SiO_2}=90$  nm substrate. WS<sub>2</sub> has been exfoliated on a poly dimethyl siloxane (PDMS) substrate.

## 2.1 Graphene

As predicted by Wallace in 1946 [1], graphene is a zero band gap semiconductor, i.e., a semi-metal with a linear band dispersion (Fig. 2.2) of the low energy excitations close to the Fermi energy [2]:

$$E(k) = \hbar v_F |k|. \quad (2.1)$$

Here,  $E$  is the energy difference with the Fermi level of the neutral state,  $v_F$  is the Fermi velocity  $\simeq 10^6$  ms<sup>-1</sup>, and  $k$  is the wave vector relative to the symmetry points K and K' in the Brillouin zone (BZ). There are no electronic states where the valence and conduction bands meet, also known as Dirac points. The conical shape band structures around K and K' are the same, though they are nonequivalent and represent the two valley degrees of freedom. The linear dispersion relation for both electrons and holes has two implications: i) they have a constant velocity independent of the applied electric field and ii) do not have any mass at low energies.

Unlike other conventional two-dimensional systems such as transition metal dichalcogenides and 2D-electron gas, the density of states (DOS) in graphene has a linear dependence in energy:

$$\nu(E) = \frac{g_s g_v |E|}{2\pi \hbar^2 v_F^2} \quad (2.2)$$

Here,  $g_s=2$  and  $g_v=2$  represent the spin and valley degrees of freedom, respec-

tively. The Fermi level  $E_F$  can be modulated in graphene by electrostatic gating. The total number of induced charge carriers due to a change in the Fermi energy can be calculated by integrating  $\nu(E)$  over this range, i.e.,  $n(E_F) = \int_0^{E_F} \nu(E)dE$ . In the metallic regime, the conductivity ( $\sigma = \frac{1}{R_{sq}}$ ) of graphene, where  $R_{sq}$  is the graphene sheet-resistance, can be written as:

$$\sigma = ne\mu \quad (2.3)$$

implying that the sheet resistance of graphene decreases with increasing carrier density.

2

## 2.2 Hexagonal Boron Nitride (hBN)

Boron nitride is a member of the 2D-family arranged in a stack of layers like graphene and can be exfoliated using the same scotch-tape method. It is an insulator with a band gap of  $\simeq 6$  eV [3] and is atomically flat [4]. Being an insulator, it can be used as a substrate. A complete encapsulation of a graphene flake between two hBN flakes [5] improves the carrier mobility and spin transport properties of graphene on a  $\text{SiO}_2/\text{Si}$  substrate [6]. Graphene's charge and the spin transport properties are significantly affected by the roughness [7], presence of dangling bonds and electron-phonon coupling [8] of the underlying substrate. These shortcomings are suppressed in graphene on a hBN substrate, resulting in an improved mobility and higher spin relaxation length [9]. These parameters can be improved further, if one completely encapsulates graphene by fabricating a sandwich of a hBN/Gr/hBN heterostructure [10]. In this way one can protect graphene from the chemical impurities which are introduced during various lithographic steps and can further improve the charge and spin transport properties of graphene.

Recently, there has been a lot of attention on exploring hBN as a tunnel barrier for spin-injection/detection in graphene as a replacement for the conventional oxide tunnel barriers which suffer from inhomogeneities and pinholes and hinder an efficient spin-injection and spin transport [6, 11]. Thin hBN layers down to monolayers have been used for this purpose and due to their crystalline and pinhole free nature, have proved to be superior to oxide tunnel barriers.

## 2.3 Transition Metal Dichalcogenides

Transition metal Dichalcogenides (TMDs) are represented as  $\text{MX}_2$ , where  $\text{M}(=\text{Mo},\text{W})$  is a transition metal and  $\text{X}(\text{S},\text{Se},\text{Te})$  is an element from the chalcogen family. In a TMD monolayer (ML) M atoms are sandwiched between two X atoms and M and X are connected via the covalent bonds. A bulk  $\text{MX}_2$  crystal consists of several  $\text{MX}_2$



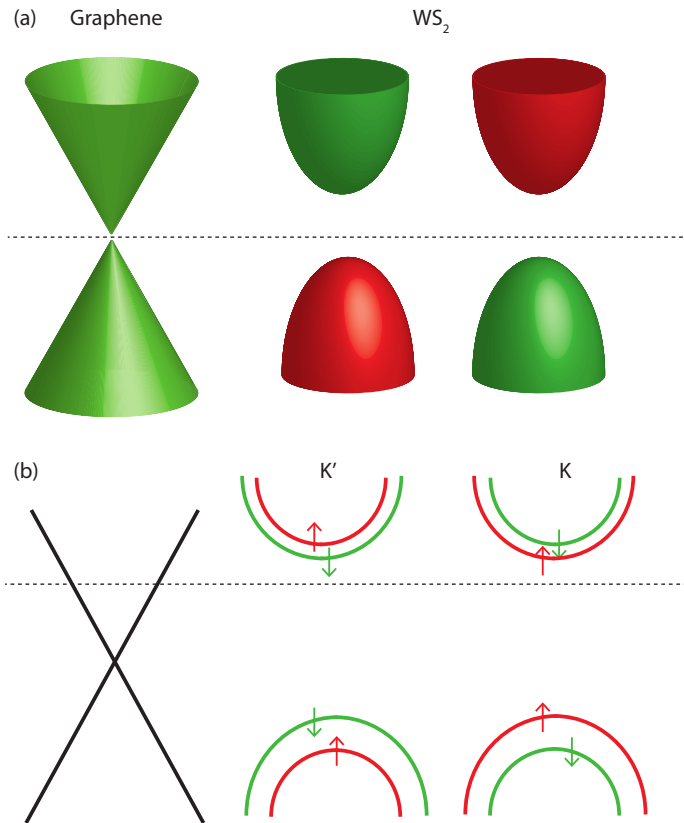


**Figure 2.2:** (a) Band structure of graphene near the K(K') point shows a linear energy-momentum dispersion. A parabolic band structure of a monolayer WS<sub>2</sub> has spin-split conduction (shown below in Fig. 2.2(b)) and valence bands near K and K' symmetry points. The dashed line denotes the Fermi energy  $E_F$  of the electrons. (b) Line-representation of the band structures with n-type doping, i.e.  $E_F$  is close to the conduction band.

MLs stacked on each other via the van der Waals interactions, similar to graphene, and they can be cleaved into thinner layers up to single layer by the same scotch-tape method. The electronic and optical properties of a TMD can be tuned depending on the number of electrons in d-orbital of the constituent transition-metal. Also, because of different crystal symmetries, these properties can be tuned with respect to the number of layers. For example, a bulk WS<sub>2</sub> exhibits indirect band gap around 1.3 eV which is enhanced up to  $\simeq 2$  eV, while reducing the number of layers down to a monolayer WS<sub>2</sub> [12, 13]. Because of the presence of a sizable band gap, it is suitable for the electronic and optoelectronic applications [14]. However, for electronic

applications, low mobility and the presence of a Schottky barrier at the contact-TMD interface [15] hinders the efficient charge injection and high current on/off ratio [16]. The Schottky barrier height can be reduced by choosing a low work function material [17] and by introducing an insulating tunnel barrier such as Al<sub>2</sub>O<sub>3</sub> or hBN between the metal and TMD. The mobility of the transport channel can also be enhanced by more than an order of magnitude by the encapsulation of MX<sub>2</sub> with insulating hBN crystals [18–20]. For a bi-layer WS<sub>2</sub>, the carrier mobility  $\simeq 300 \text{ cm}^2\text{V}^{-1}\text{s}^{-1}$  (at T=83 K) has been reported [15], which can be even enhanced further, and is comparable to the mobility of low quality CVD graphene [21].

TMDs not only have a desirable band gap but also offer rich properties that are either missing or difficult to realize in graphene. Due to lack of inversion center in odd number layer TMDs, they have inequivalent K and K' valleys in the BZ, as shown in the band diagram of a single layer TMD in Fig. 2.2. These valleys acquire a finite Berry curvature and orbital angular momentum due to a contribution from the d-orbitals of the transition metal 'M' that are opposite in sign for both valleys. When circular polarized light is shone on a TMD, it excites the electrons from the valence band to the conduction band only in one valley due to optical selection rules. In presence of a nonzero Berry curvature which acquires opposite signs for each valley, the electrons moving in a finite electric field acquire a nonzero anomalous velocity perpendicular to the applied electric field. The electrons in K and K' valleys therefore move in opposite direction [22]. This effect, analogous to the Spin-Hall Effect (SHE), is known as Valley Hall Effect (VHE). Due to the spin-orbit coupling, both effects can be observed together in odd-layer TMDs. For even-layer TMDs, no valley effect is expected. Since each valley acquires a finite magnetic moment at K and K', which is oriented perpendicular to the plane of the 2D crystal, on applying an out of plane magnetic field, electrons in different valleys move in opposite directions with respect to the Fermi energy. This phenomenon is referred to as the Valley-Zeeman effect [23, 24]. TMDs also exhibit Rashba spin-orbit coupling which can generate efficient spin-to-charge conversion compared to bulk materials. This effect is known as 'Inverse Rashba-Edelstein Effect', and is analogous to the inverse spin-Hall-effect [25, 26].

The lattice structure and the optical images of the 2D-materials discussed above are shown in Fig. 2.1

## 2.4 hBN-Graphene and WS<sub>2</sub>-Graphene Heterostructures

Graphene, via its  $\pi/ (p_z)$  orbitals can interact with the neighboring material. However, this interaction being weak, graphene can preserve its band structure and still can adopt the foreign properties such as opening of a band-gap at K(K') point, and an enhanced spin-orbit coupling (SOC) [27–29], Zeeman interaction [30] and exchange splitting [31] from the host material, which are missing in pristine graphene. This

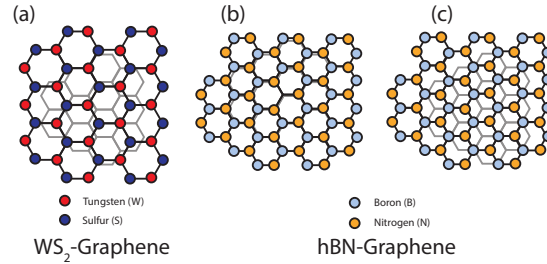


**Figure 2.3:** (a) Top view of a WS<sub>2</sub>-graphene heterostructure. Due to a mismatch in the lattice constants of graphene ( $a=2.46 \text{ \AA}$ ) and WS<sub>2</sub> ( $a=3.18 \text{ \AA}$ ), these structures do not align and. On the other hand, due to almost matched lattice constants of graphene and hBN ( $a=2.5 \text{ \AA}$ ), (a) graphene (gray lattice) and hBN and almost aligned, with a position of one carbon atom on B and another on N, or (b) one carbon atom in the center and the other on B or N.

unique ability of graphene makes it an attractive platform for studying proximity induced effects.

The induced properties depend both on the lattice constant and constituent atoms of the stacked material. For example, graphene and hBN have similar lattice constants, as schematically demonstrated in Fig. 2.3(b)-(c). As a result, a carbon atom on-top of a boron atom and the neighboring carbon atom on-top of a nitrogen atom, experience different periodic crystal potentials, which allows to open up a finite sized band-gap in graphene [32]. The commensurability of the structure, i.e. the relative alignment angle between the hBN and graphene crystallographic axes is important to observe moiré patterns [33]. Since hBN consists of light atoms, i.e., boron and nitrogen, it can not induce any SOC in graphene. On the other hand, TMDs, having larger lattice constants than graphene, as shown in Fig. 2.3(a), are relatively insensitive to the commensurability. However, having intrinsic SOC due to the presence of  $d$ -orbitals in transition metals, they can interact with the  $\pi$  orbitals of graphene, and have shown to induce almost 100-1000 times larger SOC in graphene [28, 34], compared to its pristine state [7].

In addition to the induced SOC, the sublattice symmetry is also broken at the graphene-host material interface, which allows the possibility of inequivalent valleys in graphene and valley-related effects [35] and also the Rashba SOC at the interface [29, 34]. These effects are discussed in detail in ch. 11 of this thesis.

In summary, a coupled spin-valley physics with spin-orbit coupling in TMDs and graphene-TMD heterostructures offers an exciting platform to explore a variety of physical phenomena that can add novel functionalities to the future electronic devices.

## References

- [1] P. R. Wallace, "The Band Theory of Graphite," *Phys. Rev.* **71**, pp. 622–634, May 1947.
- [2] A. H. Castro Neto, F. Guinea, N. M. R. Peres, K. S. Novoselov, and A. K. Geim, "The electronic properties of graphene," *Rev. Mod. Phys.* **81**, pp. 109–162, Jan. 2009.
- [3] G. Cassabois, P. Valvin, and B. Gil, "Hexagonal boron nitride is an indirect bandgap semiconductor," *Nat. Photonics* **10**, pp. 262–266, Apr. 2016.
- [4] J. D. Thomsen, T. Gunst, S. S. Gregersen, L. Gammelgaard, B. S. Jessen, D. M. A. Mackenzie, K. Watanabe, T. Taniguchi, P. Bøggild, and T. J. Booth, "Suppression of intrinsic roughness in encapsulated graphene," *Phys. Rev. B* **96**, p. 014101, July 2017.
- [5] C. R. Dean, A. F. Young, I. Meric, C. Lee, L. Wang, S. Sorgenfrei, K. Watanabe, T. Taniguchi, P. Kim, K. L. Shepard, and J. Hone, "Boron nitride substrates for high-quality graphene electronics," *Nat. Nanotechnol.* **5**, pp. 722–726, Oct. 2010.
- [6] N. Tombros, C. Jozsa, M. Popinciuc, H. T. Jonkman, and B. J. van Wees, "Electronic spin transport and spin precession in single graphene layers at room temperature," *Nature* **448**, pp. 571–574, Aug. 2007.
- [7] C. Ertler, S. Konschuh, M. Gmitra, and J. Fabian, "Electron spin relaxation in graphene: The role of the substrate," *Phys. Rev. B* **80**, p. 041405, July 2009.
- [8] I. M. Vicent, H. Ochoa, and F. Guinea, "Spin relaxation in corrugated graphene," *Phys. Rev. B* **95**, p. 195402, May 2017.
- [9] P. J. Zomer, M. H. D. Guimarães, N. Tombros, and B. J. van Wees, "Long-distance spin transport in high-mobility graphene on hexagonal boron nitride," *Phys. Rev. B* **86**, p. 161416, Oct. 2012.
- [10] M. Gurram, S. Omar, S. Zihlmann, P. Makk, C. Schönenberger, and B. J. van Wees, "Spin transport in fully hexagonal boron nitride encapsulated graphene," *Phys. Rev. B* **93**, p. 115441, Mar. 2016.
- [11] W. Han, K. Pi, K. M. McCreary, Y. Li, J. J. I. Wong, A. G. Swartz, and R. K. Kawakami, "Tunneling Spin Injection into Single Layer Graphene," *Phys. Rev. Lett.* **105**, p. 167202, Oct. 2010.
- [12] T. Georgiou, H. Yang, R. Jalil, J. Chapman, K. S. Novoselov, and A. Mishchenko, "Electrical and optical characterization of atomically thin WS<sub>2</sub>," *Dalton Trans.* **43**, pp. 10388–10391, June 2014.
- [13] H.-C. Kim, H. Kim, J.-U. Lee, H.-B. Lee, D.-H. Choi, J.-H. Lee, W. H. Lee, S. H. Jhang, B. H. Park, H. Cheong, S.-W. Lee, and H.-J. Chung, "Engineering Optical and Electronic Properties of WS<sub>2</sub> by Varying the Number of Layers," *ACS Nano* **9**, pp. 6854–6860, July 2015.
- [14] Q. H. Wang, K. Kalantar-Zadeh, A. Kis, J. N. Coleman, and M. S. Strano, "Electronics and optoelectronics of two-dimensional transition metal dichalcogenides," *Nat. Nanotechnol.* **7**, pp. 699–712, Nov. 2012.
- [15] A. Allain, J. Kang, K. Banerjee, and A. Kis, "Electrical contacts to two-dimensional semiconductors," *Nat. Mater.* **14**, pp. 1195–1205, Dec. 2015.
- [16] D. Ovchinnikov, A. Allain, Y.-S. Huang, D. Dumcenco, and A. Kis, "Electrical Transport Properties of Single-Layer WS<sub>2</sub>," *ACS Nano* **8**, pp. 8174–8181, Aug. 2014.
- [17] S. Das, H.-Y. Chen, A. V. Penumatcha, and J. Appenzeller, "High Performance Multilayer MoS<sub>2</sub> Transistors with Scandium Contacts," *Nano Lett.* **13**, pp. 100–105, Jan. 2013.
- [18] F. Withers, T. H. Bointon, D. C. Hudson, M. F. Craciun, and S. Russo, "Electron transport of WS<sub>2</sub> transistors in a hexagonal boron nitride dielectric environment," *Sci. Rep.* **4**, p. srep04967, May 2014.
- [19] G.-H. Lee, X. Cui, Y. D. Kim, G. Arefe, X. Zhang, C.-H. Lee, F. Ye, K. Watanabe, T. Taniguchi, P. Kim, and J. Hone, "Highly Stable, Dual-Gated MoS<sub>2</sub> Transistors Encapsulated by Hexagonal Boron Nitride with Gate-Controllable Contact, Resistance, and Threshold Voltage," *ACS Nano* **9**, pp. 7019–7026, July 2015.
- [20] J. I.-J. Wang, Y. Yang, Y.-A. Chen, K. Watanabe, T. Taniguchi, H. O. H. Churchill, and P. Jarillo-Herrero, "Electronic Transport of Encapsulated Graphene and WSe<sub>2</sub> Devices Fabricated by Pick-up of Prepatterned hBN," *Nano Lett.* **15**, pp. 1898–1903, Mar. 2015.

- [21] H. S. Song, S. L. Li, H. Miyazaki, S. Sato, K. Hayashi, A. Yamada, N. Yokoyama, and K. Tsukagoshi, "Origin of the relatively low transport mobility of graphene grown through chemical vapor deposition," *Scientific Reports* **2**, p. 337, Mar. 2012.
- [22] X. Xu, W. Yao, D. Xiao, and T. F. Heinz, "Spin and pseudospins in layered transition metal dichalcogenides," *Nat. Phys.* **10**, pp. 343–350, May 2014.
- [23] G. Aivazian, Z. Gong, A. M. Jones, R.-L. Chu, J. Yan, D. G. Mandrus, C. Zhang, D. Cobden, W. Yao, and X. Xu, "Magnetic control of valley pseudospin in monolayer WSe<sub>2</sub>," *Nat. Phys.* **11**, pp. 148–152, Feb. 2015.
- [24] Y. Li, J. Ludwig, T. Low, A. Chernikov, X. Cui, G. Arefe, Y. D. Kim, A. M. van der Zande, A. Rigosi, H. M. Hill, S. H. Kim, J. Hone, Z. Li, D. Smirnov, and T. F. Heinz, "Valley Splitting and Polarization by the Zeeman Effect in Monolayer MoSe<sub>2</sub>," *Phys. Rev. Lett.* **113**, p. 266804, Dec. 2014.
- [25] W. Zhang, J. Sklenar, B. Hsu, W. Jiang, M. B. Jungfleisch, J. Xiao, F. Y. Fradin, Y. Liu, J. E. Pearson, J. B. Ketterson, Z. Yang, and A. Hoffmann, "Research Update: Spin transfer torques in permalloy on monolayer MoS<sub>2</sub>," *APL Materials* **4**, p. 032302, Mar. 2016.
- [26] C. Cheng, M. Collet, J.-C. R. Sánchez, V. Ivanovskaya, B. Dlubak, P. Seneor, A. Fert, H. Kim, G. H. Han, Y. H. Lee, H. Yang, and A. Anane, "Spin to charge conversion in MoS<sub>2</sub> monolayer with spin pumping," *arXiv:1510.03451 [cond-mat]*, Oct. 2015. arXiv: 1510.03451.
- [27] A. Avsar, J. Y. Tan, T. Taychatanapat, J. Balakrishnan, G. K. W. Koon, Y. Yeo, J. Lahiri, A. Carvalho, A. S. Rodin, E. C. T. O'Farrell, G. Eda, A. H. C. Neto, and B. zylmaz, "Spinorbit proximity effect in graphene," *Nature Communications* **5**, p. 4875, Sept. 2014.
- [28] Z. Wang, D.-K. Ki, J. Y. Khoo, D. Mauro, H. Berger, L. S. Levitov, and A. F. Morpurgo, "Origin and Magnitude of 'Designer' Spin-Orbit Interaction in Graphene on Semiconducting Transition Metal Dichalcogenides," *Phys. Rev. X* **6**, p. 041020, Oct. 2016.
- [29] M. Gmitra and J. Fabian, "Graphene on transition-metal dichalcogenides: A platform for proximity spin-orbit physics and optospintronics," *Phys. Rev. B* **92**, p. 155403, Oct. 2015.
- [30] P. Wei, S. Lee, F. Lemaitre, L. Pinel, D. Cutaia, W. Cha, F. Katmis, Y. Zhu, D. Heiman, J. Hone, J. S. Moodera, and C.-T. Chen, "Strong interfacial exchange field in the graphene/EuS heterostructure," *Nat. Mater.* **15**, pp. 711–716, Mar. 2016.
- [31] J. C. Leutenantsmeyer, A. A. Kaverzin, M. Wojtaszek, and B. J. v. Wees, "Proximity induced room temperature ferromagnetism in graphene probed with spin currents," *2D Mater.* **4**(1), p. 014001, 2017.
- [32] G. Giovannetti, P. A. Khomyakov, G. Brocks, P. J. Kelly, and J. van den Brink, "Substrate-induced band gap in graphene on hexagonal boron nitride: Ab initio density functional calculations," *Phys. Rev. B* **76**, p. 073103, Aug. 2007.
- [33] C. R. Woods, L. Britnell, A. Eckmann, R. S. Ma, J. C. Lu, H. M. Guo, X. Lin, G. L. Yu, Y. Cao, R. V. Gorbachev, A. V. Kretinin, J. Park, L. A. Ponomarenko, M. I. Katsnelson, Y. N. Gornostyrev, K. Watanabe, T. Taniguchi, C. Casiraghi, H.-J. Gao, A. K. Geim, and K. S. Novoselov, "Commensurate-incommensurate transition in graphene on hexagonal boron nitride," *Nat. Phys.* **10**, pp. 451–456, June 2014.
- [34] B. Yang, M. Lohmann, D. Barroso, I. Liao, Z. Lin, Y. Liu, L. Bartels, K. Watanabe, T. Taniguchi, and J. Shi, "Strong electron-hole symmetric Rashba spin-orbit coupling in graphene/monolayer transition metal dichalcogenide heterostructures," *Phys. Rev. B* **96**, p. 041409, July 2017.
- [35] D. Xiao, W. Yao, and Q. Niu, "Valley-Contrasting Physics in Graphene: Magnetic Moment and Topological Transport," *Phys. Rev. Lett.* **99**, p. 236809, Dec. 2007.

# Principles of Graphene Spintronics

### Abstract

*Spintronics studies spin-related effects in mainly transport properties of materials and devices, often at nanoscale. In this chapter, I present basic concepts of spintronics which are extensively used to analyze the experiments in this thesis. I first explain the concept of electrical spin injection into a nonmagnet by a ferromagnet. Then, I discuss the nonlocal spin-valve measurements for detecting spin-signals, followed by Hanle spin-precession measurements that help to extract the spin-transport properties of the nonmagnetic spin-transport channel. In the second half of the chapter, I summarize the dominant spin-relaxation mechanisms in graphene, followed by a brief review of the effect of impurities on the spin-relaxation process. A recently developed pickup-transfer method has made it possible to realized graphene-2D material heterostructures and study the effect of the substrate on spin-relaxation processes with a possibility of coupling the electron spin with other, such as 'valley' degrees of freedom. I also review the basic concepts of substrate (transition metal dichalcogenide)-induced and electric-field induced SOCs in graphene, which can be used to artificially enhance the intrinsic SOC of graphene and can lay a foundation for the graphene based spin-valleytronic devices.*

### 3.1 Electrical Spin Injection

The charge conductivity ( $\sigma$ ) of a FM in a two-channel model [1] is defined as:

$$\sigma = \sigma_{\uparrow} + \sigma_{\downarrow} \quad (3.1)$$

and

$$\sigma_{\uparrow,\downarrow} = De^2v_{\uparrow,\downarrow}(E_F) \quad (3.2)$$

where  $\sigma_{\uparrow,\downarrow}$  is the conductivity for the spin up (down) electrons with respect to the magnetization axis of the ferromagnet, ' $D$ ' is the diffusion coefficient of the material, ' $e$ ' is electronic charge and  $v(E_F)$  is the density of states (DOS) at the Fermi energy  $E_F$ . For a ferromagnet,  $v_{\uparrow}(E_F) \neq v_{\downarrow}(E_F)$ , therefore, a current flowing through the FM is spin polarized.

For a nonmagnetic (NM) material:  $v_{\uparrow}(E)=v_{\downarrow}(E)$ . A charge current flowing through a FM-NM system, generates a non-equilibrium spin accumulation close to the FM-NM interface, which decays in the bulk of both magnetic and nonmagnetic material at a distance away from the interface. The spin accumulation  $\mu_s$  is defined as  $\mu_s = (\mu_{\uparrow} - \mu_{\downarrow})/2$  [2]. In case of spin injection, spin accumulation  $\mu_{S0}$  at the injection point is given by the formula [3]:

$$\mu_{S0} = P_i I R_{\lambda} \quad (3.3)$$

where  $P_i$  is the spin-injection efficiency of the injection electrode,  $R_{\lambda} = R_{sq}\lambda_s/W$  is the channel spin resistance, in the characteristic spin relaxation length  $\lambda_s$ ,  $W$  is the channel width, and  $I$  is the DC injection current. The spin-accumulation  $\mu_s(x)$ ,  $x$  distance from the injector electrode is:

$$\mu_s(x) = \mu_{S0} \exp(-x/\lambda_s) \quad (3.4)$$

and the detected non-local voltage  $V_{nl}$  at  $x = L$  is given by:

$$V_{nl}(x = L) = \mu_s(L) \times P_d = \frac{P_d P_i I R_{sq} \lambda_s \exp(-L/\lambda_s)}{2W} \quad (3.5)$$

where  $P_d$  is the spin-detection efficiency of the detector electrode [4].

### 3.2 Spin-valve Measurements

Figure 3.1(a) shows the measurement scheme for spin injection and detection in a lateral spin valve geometry. For the spin-valve measurements, we pre-magnetize all the electrodes along their easy axis of magnetization, here the -y axis. When all ferromagnets are magnetized in the same direction as shown in Figure 3.1(b) (-y direction), FM1 injects a positive spin-accumulation with the electron spins having

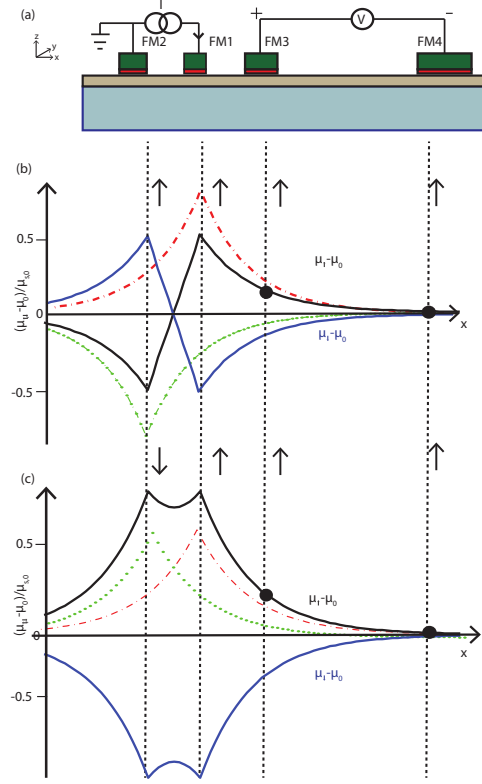


**Figure 3.1:** (a). A four probe nonlocal connection scheme for lateral spin-valve measurements. A charge current is injected between electrodes FM2 and FM1 while a non-local voltage is detected between electrodes FM3 and FM4. An oxide tunnel barrier such as  $\text{TiO}_2$  or  $\text{Al}_2\text{O}_3$  is deposited between the ferromagnet and graphene. (b) A sketch of the spin accumulation profile when both the injectors are aligned in the same direction (+y direction). The dotted red (green) curves denote the individual contribution of FM1 (FM2), and the black (blue) curve represents the net spin -up (-down) chemical potential along the channel. A positive non-local voltage is detected as  $V_{\text{NL}} = V_{\text{FM3}} - V_{\text{FM4}}$  corresponding to black dots in the curve. (c) An anti-parallel configuration leads to a larger spin accumulation and an enhanced  $V_{nl}$  is detected.

their quantization axes in +y direction and FM2 will extract the spins along this direction. The spin accumulations, created by each of these electrodes decay according to Eq.3.4. For simplicity, FM4 is taken far from the injection circuit where  $\mu_s = 0$ , and serves as a reference electrode. Since all electrodes have the same magnetization direction, FM3 detects a positive nonlocal voltage with respect to the background, corresponding to a positive spin up chemical potential underneath the detector. Now, a magnetic field along +y axis, reverses the magnetization direction of FM2 at  $\vec{B} = +B_0\hat{y}$ , aligning it along +y-axis. It, then extracts a negative spin-



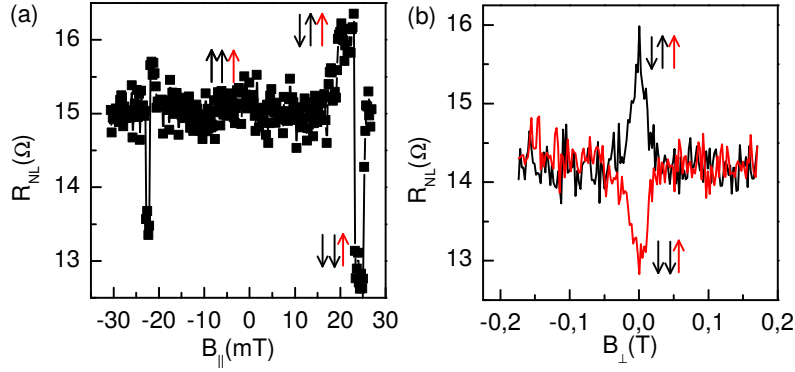


**Figure 3.2:** (a) Spin-valve signal for a graphene flake on  $\text{SiO}_2$  as a function of in-plane magnetic field  $B_{\parallel}$ . Three switches are observed because of the contribution of the outer injector. Black (red) arrow denotes the magnetization direction of the injector (detector) (b) Hanle spin-precession measurements as a function of an out-of-plane magnetic field  $B_{\perp}$  with the FMs premagnetized in config.  $\downarrow\uparrow\uparrow$  (black curve) and config.  $\downarrow\downarrow\uparrow$  (red curve).

accumulation or in other words, injects a positive spin-accumulation, resulting in an enhanced positive spin accumulation in the channel. On increasing  $\vec{B}$  further, the magnetization of FM1 is reversed along the  $+y$  direction as well. Now, both injectors are aligned opposite to the detector. This situation is similar to the first case when all the electrodes are aligned along- $y$ -axis, except the detector magnetization direction. FM3 detects the same magnitude of the spin-accumulation with respect to the background, but with a negative sign. The ferromagnets are defined to be in a parallel (P) configuration when the inner injector and detector electrodes have their magnetization axis in the same direction, in an anti-parallel (AP) configuration for the opposite case. Finally, by increasing  $\vec{B}$  further, FM3 is also aligned along the  $+y$ -axis. This situation is same as the first case when all electrodes had their magnetization axes in the same direction, leading to the same nonlocal voltage. A spin valve measurement for a graphene device with three switches are is shown in Fig. 3.2(a).

### 3.3 Hanle Spin Precession Measurements

Spin valve measurements can only provide the information about the switching field of the electrodes and the magnitude of the non-local signal. To extract the information about the spin transport properties ( $\lambda_s, \tau_s$ ), we perform Hanle measurements. For this, a magnetic field  $B_{\perp}$  is applied perpendicular to the plane of the device. The ferromagnetic electrodes are magnetized in a specific configuration (parallel or anti-parallel) in advance by applying an in-plane magnetic field. Their magnetization

state does not change while applying an out-of-plane magnetic field unless a high out of plane field is applied. On applying  $B_{\perp}$ , the spins in graphene precess around  $B_{\perp}$  with a frequency  $\vec{\omega}_L$  and the spin transport is modified in two ways: 1)- On increasing the magnetic field  $B_{\perp}$ , it increases the dephasing of the spins in the channel and reduces the net spin accumulation at the detector. 2)- the magnetic field also provides an averaged precession to the spin-accumulation and results in an oscillatory change in the sign of the spin voltage on increasing the magnetic field. Both changes are reflected in the non-local spin signal on increasing the  $B_{\perp}$  magnitude [4, 5].

The dynamics of  $\mu_s$  in the presence of a magnetic field is given by the Bloch equation:

$$\frac{d\vec{\mu}_s}{dt} = D_s \nabla^2 \vec{\mu}_s - \frac{\vec{\mu}_s}{\tau_s} + \vec{\omega}_L \times \vec{\mu}_s \quad (3.6)$$

with spin diffusion constant  $D_s$ , spin relaxation time  $\tau_s$  and the Larmor frequency  $\vec{\omega}_L = g\mu_B/\hbar \vec{B}$ . For  $\vec{B} = 0$  and at the stationary state  $d\mu_s/dt = 0$ , the solution to Eq.3.6 has  $\mu_s \propto \exp(-x/\lambda_s)$ . Here  $\lambda_s = \sqrt{D_s \tau_s}$  is the spin diffusion length.

Fig. 3.2 (b) shows a typical Hanle measurement for the parallel ( $\uparrow\uparrow$ ) (black curve) and the anti-parallel ( $\uparrow\downarrow$ ) (red curve) configuration. Here,  $\uparrow\uparrow$  ( $\downarrow\uparrow$ ) denote the relative magnetization directions of the inner injector and detector electrodes. In order to remove the background contribution, the Hanle signal for the anti-parallel configuration is subtracted from the signal in parallel configuration. The resultant signal, i.e.,  $(R_{nl}^P - R_{nl}^{AP})/2$ , is fitted with the solutions to the steady state Bloch equation (Eq. 3.6). From the fitting, we extract the spin diffusion coefficient ( $D_s$ ) and the spin relaxation time ( $\tau_s$ ). When the extracted  $D_s$  and  $\tau_s$  are put into eq. 3.5, one can also estimate the contact polarization  $P = \sqrt{P_i P_d}$ .

## 3.4 Spin Relaxation in Graphene

### 3.4.1 Spin-Orbit Coupling in Graphene

Graphene is considered to be an ideal spintronic material due to low intrinsic spin orbit coupling (SOC) of about  $\sim 1\mu\text{eV}$  [6]. However, according to first-principle calculations, the contribution of  $d$  orbitals to the band-gap opening due to  $\sigma - \pi$  bond mixing caused by the ripples and substrate roughness, enhances this value up to  $\sim 25\text{-}50\mu\text{eV}$  [7, 8].

In the absence of SOC, the electronic band structure around  $K(K')$  point is described by the Hamiltonian  $H_o = \hbar v_F \times (\tau k_x \sigma_x + k_y \sigma_y)$  where  $k_x$  and  $k_y$  are the Cartesian coordinates of the wave vector  $k$  around  $K(K')$  point,  $v_F$  is the Fermi velocity of the Dirac electrons,  $\sigma_x, \sigma_y$  are the Pauli matrices operating on the pseudospin space formed by triangular A and B sublattices of graphene, and  $\tau$  is the valley index = 1(-1) for K ( $K'$ ) valley.

Intrinsic SOC in graphene is described by the effective Hamiltonian  $H_{SO} = \tau \lambda_I \sigma_z s_z$ , where  $\lambda_I$  is the SOC strength and  $s_z$  is the spin Pauli matrix. This is the Hamiltonian proposed by Kane and Mele [9], where a very small spin orbit gap is present. The space and time reversal symmetries, and therefore the spin degeneracy of the bands are also preserved in this system. In the presence of a transverse electric field or due to a substrate potential, the space inversion symmetry is broken which gives rise to the splitting of the valence and conduction bands at each momentum, similar to the Bychkov-Rashba type spin-orbit coupling, as shown in Fig. 3.3. The Hamiltonian for the Rashba SOC is written as  $H_R = \lambda_R (\tau \sigma_x s_y + \sigma_y s_x)$  where  $\lambda_{BR}$  is the Bychkov-Rashba SOC strength, and  $s_x, s_y$  are the spin Pauli matrices. However due to constant velocity of Dirac electrons in graphene, the splitting is momentum independent.

3

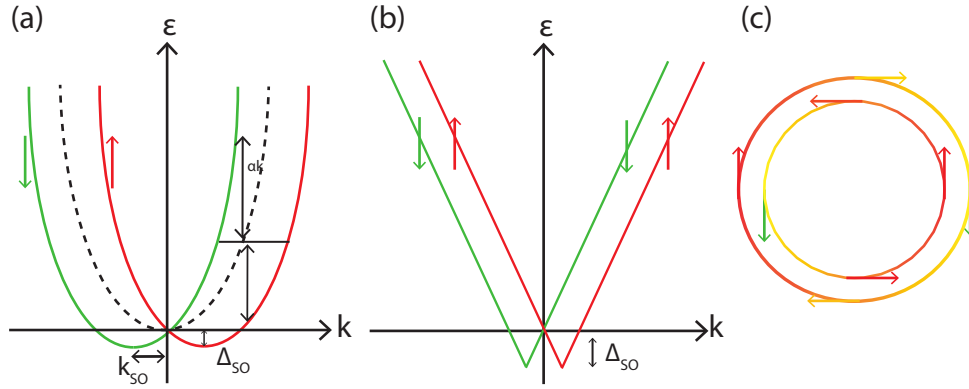


**Figure 3.3:** (a) Band splitting in a monolayer TMD and (b) ML graphene, due to the presence of a surface Rashba SOC. Red and Green sub-bands denote the opposite spin-split sub-bands. Here, spin-up (red) and -down (green) arrows only represent the opposite orientation of the spins in  $k_x - k_y$  plane. (c) top view of the in-plane spin components in the  $k_x - k_y$  plane.

### 3.4.2 Spin Relaxation

In order to explain the low spin relaxation time ( $\tau_s$ ) in contrast with the theoretical expectations, following mechanisms have been considered to be responsible for a high spin relaxation rate in graphene:

#### Elliot-Yafet (EY) Mechanism

This mechanism explains the spin relaxation by spin-flip during a scattering event. In the presence of weak spin-orbit coupling  $\lambda_I$ , a spin is an admixture of spin 'up'

and spin 'down' states. When a spin 'up (down)' electron is scattered by a spin conserving way by an impurity or a phonon, it has a finite probability of ending up in spin 'down (up)' state [10]. For EY type spin relaxation, an enhancement in the scattering events gives rise to more spin-flips and an enhanced spin-relaxation, i.e.,

$$\frac{1}{\tau_s} = \frac{\lambda_I^2}{\varepsilon_F^2} \frac{1}{\tau_P} \quad (3.7)$$

Here  $\varepsilon_F$  is the Fermi energy of the charge carriers in graphene and  $\tau_P$  is their momentum scattering time.

3

#### Dykonov-Perel (DP) Mechanism

The DP mechanism explains the spin-relaxation in the presence of SOC due to broken structural inversion symmetry. A Rashba-type spin orbit coupling is induced in graphene when the spatial-inversion symmetry is broken. Between the two scattering events, the spins precess in an effective spin-orbit field governed by  $\lambda_{BR}$ . Since the Rashba SOC couples the electron spin with its direction of motion around the field, the sense of precession is reversed during the scattering event, which is known as 'motion narrowing' of the spin. With more scattering events, there is an enhanced motion narrowing and the spins dephase less in the spin-orbit field. Therefore,  $\tau_s$  is enhanced by more scattering, i.e.,

$$\frac{1}{\tau_s} = \frac{\lambda_{BR}^2}{\hbar^2} \tau_P \quad (3.8)$$

#### Resonant Scattering Mechanism

According to recent studies of spin transport [11] and weak localization measurements [12], magnetic impurities with randomly oriented magnetic moments in graphene, even when present only at small concentrations ( $\sim 1$  ppm), are responsible for the enhanced spin-flip events and a reduced  $\tau_s$  in graphene. This highlights the role of magnetic impurities as powerful scatterers. When the electron spins are near these scattering centers, they precess around the impurities in their exchange fields. When trapped by (quasi) resonant states, their proximity dwell time strongly increases. When the spin escapes the impurity, it has equal chances of coming out as a spin-up and spin-down, i.e.  $\tau_s$  equals the spin-flip rate and with the broadening of the resonant energies due to different effects, it can lead to the experimentally observed  $\tau_s$  of  $\sim 100$  ps.

### 3.4.3 A Summary on Role of Impurities in spin-relaxation in Graphene

Impurities present in graphene are expected to affect the intrinsic spin relaxation time ( $\tau_s$ ) significantly and reduce it to the experimentally observed values of 100 ps-1 ns. In presence of the impurities,  $\tau_s$  is reduced via three possible mechanisms:

- Via the EY mechanism: an impurity can increase the SOC locally by forming a  $sp^3$  bond with the carbon atom in graphene [13]. Due to distortion of the graphene lattice, a local magnetic moment is formed at the carbon site which gives rise to enhanced spin-flip scattering [14]. The spin relaxation rate is then enhanced with the defect density, giving rise to the EY type spin-relaxation [10].
- Via the DP mechanism: the impurities present in the substrate or in graphene can give rise to spatially fluctuating Rashba spin orbit field, resulting in a motion narrowing and the possibility of the DP spin-relaxation [15].
- Via the resonant scattering mechanism [16]: when the impurity has a magnetic moment such as in the case of hydrogenated graphene or magnetic impurities, it can dephase the spins drastically, even present in a small concentration (1ppm).

Many experiments have explored the role of impurities on the spin-relaxation processes in graphene, either by introducing the impurities externally [11, 17–19], by hydrogenation [20, 21] or by studying the effect of impurities, intrinsically present in graphene by weak localization [12] or spin-noise measurements [22]. However, all these studies ending up in providing different explanations, probably depend on the source of the impurity and the sample preparation method [14, 20, 23].

The effect of charge impurity scattering was studied in ref. [18, 19] and no significant effect on  $\tau_s$  was observed when changing  $\tau_p$  and the mobility, which rules out significant contributions from charge scattering on the spin relaxation in graphene. The effect of heavy metal such as Au, was explored to study the effect of enhanced SOC in graphene [17]. A modest increase in  $\tau_s$  was observed with increasing gold concentration and reduced  $\tau_p$ , indicating that the DP mechanism causes spin relaxation.

Introducing magnetic moments by hydrogenating graphene [20] and formation of defects [24] cause enhanced spin-precession with the enhanced spin-flip scattering in the latter case, which is a signature of EY type spin relaxation.

In ch.6 of this thesis, I study the effect of magnetic impurities on spin transport in graphene using cobalt-porphyrin molecules and show that the presence of magnetic centers enhances the spin-flip scattering, suggesting the EY type spin relaxation in the presence of magnetic impurities [11].

Lundenberg *et al.* [12] studied the effect of the impurities in graphene by weak localization experiments [12] and concluded that the magnetic impurities, even when present in only small concentration can drastically enhance the spin flip processes. In ch. 7 of the thesis, I study the effect of the impurities on spin transport by spin-dependent  $1/f$  noise measurements and come to the same conclusion, viz that (magnetic) impurities in graphene affect the spin relaxation process drastically, which might result in a very short spin relaxation time in graphene.

In summary, most experimental efforts point towards impurities with magnetic moments as the main culprit degrading the spin transport in graphene, which should be studied more carefully in the future in order to improve the figure of merit of spintronic devices.

#### 3.4.4 Effect of Substrate on Spin-transport

Graphene tends to conform to the substrate topography, therefore acquires extrinsic properties that depend on the substrate lattice constant and its constituent atoms. Graphene interacts with the substrate atoms by weak van der Waals interactions which do not significantly affect its charge transport but it can acquire some properties of the host substrate such as a sizable band gap at the Dirac point, an enhanced intrinsic spin-orbit coupling, Rashba SOC due to breaking of inversion symmetry, and spin-valley coupling, all are either lacking or have a very small magnitude in pristine graphene.

Graphene on an insulating hBN ( $E_g \sim 6$  eV) substrate, due to their almost matched lattice constants, the hBN-Gr heterostructure is nearly commensurate. The carbon atoms in the A and B sublattices lie on top of Boron (B) and Nitrogen (N) atoms, respectively and experience a different crystal potential, referred as ‘staggered’ potential. For a commensurate graphene-hBN heterostructure, a finite band gap of about 50 meV is expected to open up at the Dirac points K (K') [25]. However, in experiments, such values are not realized due to incommensurability of graphene on the substrate [26], which averages out the effect. Due to breaking of the sublattice symmetry at the interface, a Rashba SOC should also exist. However, it is not observed in the absence of interacting d-orbitals from the hBN substrate [27]. Unlike the Si/SiO<sub>2</sub> substrate, the hBN substrate is atomically flat and does not have dangling bonds at the interface to the graphene. This helps in mitigating the effect of substrate induced ripples and charge inhomogeneities in graphene and enhances the mobility by more than an order of magnitude [28–30]. For a high mobility graphene, the coexistence of EY and DP mechanisms was reported by Zomer *et al.* [29], similar to graphene on SiO<sub>2</sub>, indicating that external impurities and contacts might play an important role rather than the substrate in limiting  $\tau_s$  in graphene. For low quality samples ( $\mu < 1000$  cm<sup>2</sup>V<sup>-1</sup>s<sup>-1</sup>), the spin relaxation is dominated by the EY mechanism [31].

Graphene on a TMD substrate (WS<sub>2</sub> in this thesis) is particularly interesting for

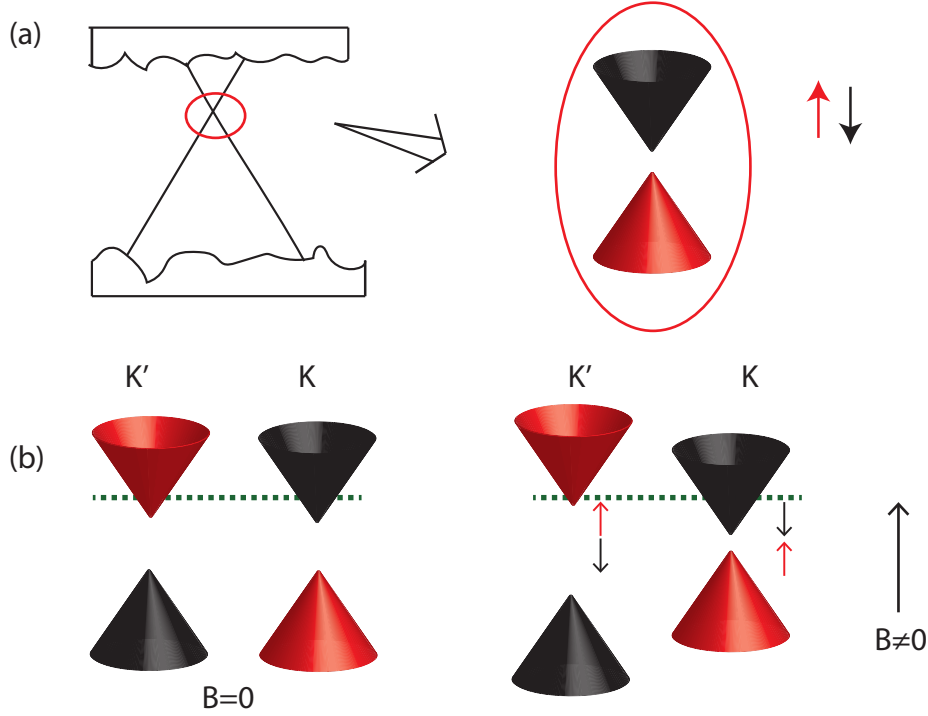


**Figure 3.4:** (a) Graphene on  $\text{WS}_2$  substrate. A finite band gap in the order of meV [32, 33] is expected by the sublattice symmetry breaking, as well as spin-split valence and conduction bands in graphene. (b) A schematic for Valley-Zeeman effect in graphene on  $\text{WS}_2$  at  $B_{\perp} = 0$  and  $B_{\perp} \neq 0$ . Due to orbital magnetic moments, perpendicular to the graphene plane with opposite in signs for K and  $K'$  valleys, a  $B_{\perp}$  induces different numbers of spin-up (red) and -down (black) states at the Fermi energy (green dashed lines) in the valleys, which constitutes the valley Zeeman effect.

several reasons. The effective Hamiltonian for a graphene-TMD heterostructure is represented by:

$$H = H_0 + H_{\lambda} + H_I + H_R \quad (3.9)$$

Here  $H_0$  is the Hamiltonian for pristine graphene without SOC,  $H_I$  is the intrinsic SOC in graphene,  $H_{\lambda}$  and  $H_R$  are the spin-orbit Hamiltonians for the valley-Zeeman and Rashba SOC. Similar to hBN, a TMD substrate also induces a staggered potential in graphene by sublattice symmetry breaking which may induce a band gap and different magnitudes of intrinsic SOC in A and B sublattices, along with the Rashba SOC.

However, the incommensurability between graphene and TMD crystals reduces

the induced band gap to the order of a meV [32]. The host TMD has a large intrinsic orbit coupling due to the contribution of d-orbitals of the transition metal (Mo,W). Because, the TMD d-orbitals can couple with the graphene  $\pi$  band, it induces a large SOC in graphene as well as a Rashba SOC at the TMD-graphene interface, both of in the order of  $\sim 10$  meV [34, 35]. The induced SOC is 1000 times higher than in pristine graphene, which opens up a possibility to realize the Quantum Spin Hall Effect (QSHE) and Anomalous Quantum Hall Effect (AQHE) in graphene. The SOC splits the valence and conduction bands in graphene and lifts the spin degeneracy by the intrinsic valley-Zeeman SOC and the Rashba SOC at the interface [33]. This can also cause an anti-crossing of the spin-split bands for a large induced SOC which can lead to a topologically conducting state in the graphene band gap [36]. Because the valley  $K(K')$  acquires spin selectivity in the presence of a staggered potential and SOC, i.e., spin  $\uparrow$  ( $\downarrow$ ) has a preference towards valley  $K(K')$ , graphene-TMD heterostructures offer a unique platform to study the spin-valley Hall and valley-Zeeman effects in graphene [37](Fig. 3.4(b)). Recent magneto-conductivity experiments demonstrate clear signature of proximity induced SOC by weak anti-localization [33–35, 38], which leads to an estimation of the SOC in the range of 5-15 meV, along with a meV size valley-Zeeman splitting.

The interplay between the valley-Zeeman SOC ( $\lambda_V$ ) and Rashba SOC ( $\lambda_R$ ) can also be detected in the anisotropy of the out-of-plane  $\tau_s^\perp$  and in-plane  $\tau_s^\parallel$  spin-relaxation times [39]. A large  $\tau_s^\perp / \tau_s^\parallel \sim 5-10$  is an indication for a high intervalley scattering rate of the electrons. In this case, the in-plane spins experience a motion-narrowing, i.e., their sense of precession is reversed while being scattered from one valley to another valley due to the reversal of the SOC field direction in each valley, analogous to the DP type scattering, i.e.,  $\frac{1}{\tau_s^\parallel} = \frac{\lambda_V^2}{\hbar^2} \tau_{iv}$ , where  $\tau_{iv}$  is the intervalley scattering time. The out-of-plane spins, on the other hand are dephased by the in-plane Rashba field  $\lambda_R$  with motional narrowing during momentum scattering, resulting in a DP type spin-relaxation:  $\frac{1}{\tau_s^\perp} = \frac{\lambda_R^2}{\hbar^2} \tau_p$ , where  $\tau_p$  is the momentum relaxation time. Usually  $\lambda_V > \lambda_R$  and  $\tau_V > \tau_p$ , which results in a higher  $\tau_s^\perp$  than  $\tau_s^\parallel$ , as was found by Ghiasi *et al.* [40].

When the intervalley scattering is weak, the in-plane spins experience a constant  $\lambda_V$  and get dephased only by time fluctuations, not the out-of plane SOC. The out of plane spins get dephased by  $\lambda_R$  in the same way with  $\tau_s^\perp / \tau_s^\parallel \sim 0.5$ , which is typical for the Rashba systems. In this case,  $B_\perp$  can modify the spin-orbit coupling in each valley. Since electrons in  $K$  and  $K'$  valleys have opposite and equal orbital magnetic moments  $\mu_B$ , the effective valley-dependent SOC at  $K(K')$  is  $\approx +(-)g\mu_B B_\perp + 2\lambda_V$ . This can create an imbalance in the spin-accumulation of each valley via different spin-relaxation rates, that would increase with the magnetic field  $B_\perp$ .



### 3.4.5 Electric Field induced Spin orbit Coupling

The in-plane Rashba SOC can be induced in graphene by applying an out of plane electric field generated by top and bottom gates. The induced SOC strength is also controlled by the external electric field [30] via electrical gating and provides a platform for the realization of a Datta-Das spin-transistor [41].

## References

- [1] A. Fert, J.-L. Duvail, and T. Valet, "Spin relaxation effects in the perpendicular magnetoresistance of magnetic multilayers," *Phys. Rev. B* **52**, pp. 6513–6521, Sept. 1995.
- [2] I. Žutić, J. Fabian, and S. Das Sarma, "Spintronics: Fundamentals and applications," *Rev. Mod. Phys.* **76**, pp. 323–410, Apr. 2004.
- [3] F. J. Jedema, H. B. Heersche, A. T. Filip, J. J. A. Baselmans, and B. J. van Wees, "Electrical detection of spin precession in a metallic mesoscopic spin valve," *Nature* **416**, pp. 713–716, Apr. 2002.
- [4] N. Tombros, C. Jozsa, M. Popinciuc, H. T. Jonkman, and B. J. van Wees, "Electronic spin transport and spin precession in single graphene layers at room temperature," *Nature* **448**, pp. 571–574, Aug. 2007.
- [5] T. Maassen, *Electron spin transport in graphene-based devices*, s.n., 2013.
- [6] H. Min, J. E. Hill, N. A. Sinitsyn, B. R. Sahu, L. Kleinman, and A. H. MacDonald, "Intrinsic and Rashba spin-orbit interactions in graphene sheets," *Phys. Rev. B* **74**, p. 165310, Oct. 2006.
- [7] M. Gmitra, S. Konschuh, C. Ertler, C. Ambrosch-Draxl, and J. Fabian, "Band-structure topologies of graphene: Spin-orbit coupling effects from first principles," *Phys. Rev. B* **80**, p. 235431, Dec. 2009.
- [8] S. Konschuh, M. Gmitra, and J. Fabian, "Tight-binding theory of the spin-orbit coupling in graphene," *Phys. Rev. B* **82**, p. 245412, Dec. 2010.
- [9] C. L. Kane and E. J. Mele, "Quantum Spin Hall Effect in Graphene," *Phys. Rev. Lett.* **95**, p. 226801, Nov. 2005.
- [10] H. Ochoa, A. H. Castro Neto, and F. Guinea, "Elliot-Yafet Mechanism in Graphene," *Phys. Rev. Lett.* **108**, p. 206808, May 2012.
- [11] S. Omar, M. Gurram, I. J. Vera-Marun, X. Zhang, E. H. Huisman, A. Kaverzin, B. L. Feringa, and B. J. van Wees, "Spin relaxation in graphene with self-assembled cobalt porphyrin molecules," *Phys. Rev. B* **92**, p. 115442, Sept. 2015.
- [12] M. B. Lundeberg, R. Yang, J. Renard, and J. A. Folk, "Defect-Mediated Spin Relaxation and Dephasing in Graphene," *Phys. Rev. Lett.* **110**, p. 156601, Apr. 2013.
- [13] A. H. Castro Neto and F. Guinea, "Impurity-Induced Spin-Orbit Coupling in Graphene," *Phys. Rev. Lett.* **103**, p. 026804, July 2009.
- [14] D. Soriano, D. V. Tuan, S. M.-M. Dubois, M. Gmitra, A. W. Cummings, D. Kochan, Frank Ortmann, J.-C. Charlier, J. Fabian, and S. Roche, "Spin transport in hydrogenated graphene," *2D Mater.* **2**(2), p. 022002, 2015.
- [15] C. Ertler, S. Konschuh, M. Gmitra, and J. Fabian, "Electron spin relaxation in graphene: The role of the substrate," *Phys. Rev. B* **80**, p. 041405, July 2009.
- [16] D. Kochan, M. Gmitra, and J. Fabian, "Spin Relaxation Mechanism in Graphene: Resonant Scattering by Magnetic Impurities," *Phys. Rev. Lett.* **112**, p. 116602, Mar. 2014.
- [17] K. Pi, W. Han, K. M. McCreary, A. G. Swartz, Y. Li, and R. K. Kawakami, "Manipulation of Spin Transport in Graphene by Surface Chemical Doping," *Phys. Rev. Lett.* **104**, p. 187201, May 2010.
- [18] A. G. Swartz, J.-R. Chen, K. M. McCreary, P. M. Odenthal, W. Han, and R. K. Kawakami, "Effect of in situ deposition of Mg adatoms on spin relaxation in graphene," *Phys. Rev. B* **87**, p. 075455, Feb. 2013.
- [19] W. Han, J.-R. Chen, D. Wang, K. M. McCreary, H. Wen, A. G. Swartz, J. Shi, and R. K. Kawakami, "Spin Relaxation in Single-Layer Graphene with Tunable Mobility," *Nano Lett.* **12**, pp. 3443–3447, July 2012.
- [20] K. M. McCreary, A. G. Swartz, W. Han, J. Fabian, and R. K. Kawakami, "Magnetic Moment Formation in Graphene Detected by Scattering of Pure Spin Currents," *Phys. Rev. Lett.* **109**, p. 186604, Nov. 2012.
- [21] A. A. Kaverzin and B. J. van Wees, "Electron transport nonlocality in monolayer graphene modified with hydrogen silsesquioxane polymerization," *Phys. Rev. B* **91**, p. 165412, Apr. 2015.
- [22] S. Omar, M. H. D. Guimarães, A. Kaverzin, B. J. van Wees, and I. J. Vera-Marun, "Spin relaxation 1/f

- noise in graphene," *Phys. Rev. B* **95**, p. 081403, Feb. 2017.
- [23] M. Wojtaszek, I. J. Vera-Marun, T. Maassen, and B. J. van Wees, "Enhancement of spin relaxation time in hydrogenated graphene spin-valve devices," *Phys. Rev. B* **87**, p. 081402, Feb. 2013.
- [24] B. Birkner, D. Pachniewski, A. Sandner, M. Ostler, T. Seyller, J. Fabian, M. Ciorga, D. Weiss, and J. Eroms, "Annealing-induced magnetic moments detected by spin precession measurements in epitaxial graphene on SiC," *Phys. Rev. B* **87**, p. 081405, Feb. 2013.
- [25] G. Giovannetti, P. A. Khomyakov, G. Brocks, P. J. Kelly, and J. van den Brink, "Substrate-induced band gap in graphene on hexagonal boron nitride: Ab initio density functional calculations," *Phys. Rev. B* **76**, p. 073103, Aug. 2007.
- [26] C. R. Woods, L. Britnell, A. Eckmann, R. S. Ma, J. C. Lu, H. M. Guo, X. Lin, G. L. Yu, Y. Cao, R. V. Gorbachev, A. V. Kretinin, J. Park, L. A. Ponomarenko, M. I. Katsnelson, Y. N. Gornostyrev, K. Watanabe, T. Taniguchi, C. Casiraghi, H.-J. Gao, A. K. Geim, and K. S. Novoselov, "Commensurate-incommensurate transition in graphene on hexagonal boron nitride," *Nat. Phys.* **10**, pp. 451–456, June 2014.
- [27] W. Han, R. K. Kawakami, M. Gmitra, and J. Fabian, "Graphene spintronics," *Nat. Nanotechnol.* **9**, pp. 794–807, Oct. 2014.
- [28] C. R. Dean, A. F. Young, I. Meric, C. Lee, L. Wang, S. Sorgenfrei, K. Watanabe, T. Taniguchi, P. Kim, K. L. Shepard, and J. Hone, "Boron nitride substrates for high-quality graphene electronics," *Nat. Nanotechnol.* **5**, pp. 722–726, Oct. 2010.
- [29] P. J. Zomer, M. H. D. Guimarães, N. Tombros, and B. J. van Wees, "Long-distance spin transport in high-mobility graphene on hexagonal boron nitride," *Phys. Rev. B* **86**, p. 161416, Oct. 2012.
- [30] M. Guimarães, P. Zomer, J. Ingla-Aynés, J. Brant, N. Tombros, and B. van Wees, "Controlling Spin Relaxation in Hexagonal BN-Encapsulated Graphene with a Transverse Electric Field," *Phys. Rev. Lett.* **113**, p. 086602, Aug. 2014.
- [31] C. Józsa, T. Maassen, M. Popinciuc, P. J. Zomer, A. Veligura, H. T. Jonkman, and B. J. van Wees, "Linear scaling between momentum and spin scattering in graphene," *Phys. Rev. B* **80**, p. 241403, Dec. 2009.
- [32] M. Gmitra and J. Fabian, "Graphene on transition-metal dichalcogenides: A platform for proximity spin-orbit physics and optospintronics," *Phys. Rev. B* **92**, p. 155403, Oct. 2015.
- [33] B. Yang, M.-F. Tu, J. Kim, Y. Wu, H. Wang, J. Alicea, R. Wu, M. Bockrath, and J. Shi, "Tunable spinorbit coupling and symmetry-protected edge states in graphene/WS<sub>2</sub>," *2D Mater.* **3**(3), p. 031012, 2016.
- [34] Z. Wang, D.-K. Ki, H. Chen, H. Berger, A. H. MacDonald, and A. F. Morpurgo, "Strong interface-induced spinorbit interaction in graphene on WS<sub>2</sub>," *Nat. Commun.* **6**, p. ncomms9339, Sept. 2015.
- [35] Z. Wang, D.-K. Ki, J. Y. Khoo, D. Mauro, H. Berger, L. S. Levitov, and A. F. Morpurgo, "Origin and Magnitude of 'Designer' Spin-Orbit Interaction in Graphene on Semiconducting Transition Metal Dichalcogenides," *Phys. Rev. X* **6**, p. 041020, Oct. 2016.
- [36] M. Gmitra, D. Kochan, P. Högl, and J. Fabian, "Trivial and inverted Dirac bands and the emergence of quantum spin Hall states in graphene on transition-metal dichalcogenides," *Phys. Rev. B* **93**, p. 155104, Apr. 2016.
- [37] D. Xiao, W. Yao, and Q. Niu, "Valley-Contrasting Physics in Graphene: Magnetic Moment and Topological Transport," *Phys. Rev. Lett.* **99**, p. 236809, Dec. 2007.
- [38] B. Yang, M. Lohmann, D. Barroso, I. Liao, Z. Lin, Y. Liu, L. Bartels, K. Watanabe, T. Taniguchi, and J. Shi, "Strong electron-hole symmetric Rashba spin-orbit coupling in graphene/monolayer transition metal dichalcogenide heterostructures," *Phys. Rev. B* **96**, p. 041409, July 2017.
- [39] A. W. Cummings, J. H. García, J. Fabian, and S. Roche, "Giant Spin Lifetime Anisotropy in Graphene Induced by Proximity Effects," *arXiv:1705.10972 [cond-mat]*, May 2017. arXiv: 1705.10972.
- [40] T. S. Ghiasi, J. Ingla-Aynés, A. A. Kaverzin, and B. J. van Wees, "Large Proximity-Induced Spin Lifetime Anisotropy in Transition Metal Dichalcogenide/Graphene Heterostructures," *arXiv:1708.04067 [cond-mat]*, Aug. 2017. arXiv: 1708.04067.

- [41] S. Datta and B. Das, "Electronic analog of the electrooptic modulator," *Appl. Phys. Lett.* **56**, pp. 665–667, Feb. 1990.



### Abstract

*In experiments, noise is often considered as an unwanted random signal that limits the measurement accuracy of the signal of interest. The statistical accuracy of a measurement can be quantified by the signal to noise ratio (SNR). However, noise can also provide fundamental information on the system dynamics. Some of the sources of electrical noise are carrier traps, energy barriers, current redistribution in inhomogeneous materials, defect motion and thermal fluctuations. In the first half of this chapter, I describe the basic concepts such as definition and types of electrical noise and its potential sources producing such fluctuations. In the second half, I briefly discuss about the noise that depends on the external magnetic field, such as 'magnetic noise' in ferromagnets, and the noise caused by a spin-accumulation present in non-magnetic materials, termed as 'spin-relaxation noise'.*

Noise is a statistical signal. Signal fluctuations in time domain, when transformed to frequency domain, can be characterized in form of a power spectrum. From Parseval's law [1], a correlation function  $R(\tau)$ , which represents the fluctuations in time domain, is equivalent to its power spectrum  $S(\omega)$  i.e. power per unit frequency in the frequency domain:

$$R_v(\tau) = \frac{1}{2\pi} \int S_v(\omega) e^{i\omega\tau} d\omega \quad (4.1)$$

where  $R_v(\tau)$  (units  $V^2/s$ ) is the correlation function of voltage over time  $\tau$ . Physically speaking, the correlation function tells us about the characteristic time scale  $\tau$  on which the fluctuations are related. For example, random fluctuations are represented by the delta function, which implies that the fluctuations are not correlated at all.

Based on its frequency dependence, noise can be classified into two main categories:

- White noise
- Coloured noise

The average root mean square (rms) value of the white noise is frequency independent. On the other hand, colored noise is frequency dependent. There are two important types of white noise : Thermal noise and Shot noise.

## 4.1 White noise

### 4.1.1 Thermal Noise

Thermal noise was first measured by J.B. Johnson. He measured voltage fluctuations in various types of resistors without applying any current/voltage [2]. Johnson, along with his colleague H. Nyquist, found a universal relation between the voltage fluctuations and the resistance of the sample, which is given by:

$$S_v^{\text{Thermal}} = 4k_B T R \quad (4.2)$$

or

$$V_{\text{Thermal}} = \sqrt{4k_B T R \Delta f} \quad (4.3)$$

Here  $S_v^{\text{Thermal}}$  is the thermal noise power spectral density in  $V^2 \text{ Hz}^{-1}$ .  $V_{\text{Thermal}}$  is the measured rms noise voltage.  $k_B = 1.38 \times 10^{-23} \text{ J/K}$  is the Boltzmann constant,  $T$  is the temperature of the sample and  $\Delta f$  is the noise measurement bandwidth in Hz. Thermal noise is also known as Johnson- Nyquist noise. It originates due to temperature assisted fluctuations in the number of charge carriers and is observed

as voltage fluctuations at equilibrium in the transport channel [3]. Since the source of these fluctuations is Gaussian (due to the Brownian motion of the carriers), the nature of fluctuation amplitude has a Gaussian distribution.

### 4.1.2 Shot Noise

Shot noise, also like thermal noise, is 'white' in nature. Shot noise was first observed by Walter Schottky while measuring the emission current in vacuum tubes. At the cathode surface, there are trap states which make the emission of the electrons random. This randomness is observed as fluctuations in the emission current. Randomness of the fluctuations follows the Poissonian statistics which gives the fluctuation magnitude:

$$S_I^{\text{shot}} = 2I_{\text{DC}}e\mathcal{F} \quad (4.4)$$

or in terms of voltage power spectrum:

$$S_v^{\text{shot}} = 2I_{\text{DC}}e\mathcal{F}R^2 \quad (4.5)$$

$$V_{\text{shot}} = \sqrt{2I_{\text{DC}}e\mathcal{F}R^2\Delta f} \quad (4.6)$$

here  $S_v^{\text{shot}}$  is the shot noise power spectral density in  $\text{V}^2 \text{Hz}^{-1}$  and  $S_I^{\text{shot}}$  is the shot noise power spectral density in  $\text{A}^2 \text{Hz}^{-1}$ .  $V_{\text{shot}}$  is the shot noise rms voltage,  $I_{\text{DC}}$  is the DC current flowing through the channel,  $e=1.602 \times 10^{-19}$  C is the electronic charge, R is the sample resistance,  $\mathcal{F}$  stands for the 'Fano' factor. The Fano factor varies in following ways, depending on the transport type [4]:

- $\mathcal{F}=0$ , if there is no shot noise generated in the channel. That is the case for absolute transmission, for example in quantum point contacts.
- $\mathcal{F}=1$ , if there is transmission only due to burst or random emission of the charge carriers, as in the case of vacuum tubes and tunnel barriers .
- and  $0 \leq \mathcal{F} \leq 1$  for the diffusive transport ( $\approx 1/3$ ) [5].

The origin of the shot noise is due to the quantized nature of charge carriers. Shot noise is observed only when the flow of charge carriers is unidirectional, i.e.,  $\langle I_{\text{DC}} \rangle \neq 0$ , and every charge carrier is independent. This is the reason why we observe shot noise in p-n junctions [6] while normal metal resistors do not exhibit any shot noise.



## 4.2 Colored noise

### 4.2.1 Flicker Noise

Flicker noise, also known as pink noise, is a frequency dependent noise and can be quantified by the following equation:

$$S_{1/f}^V = \frac{\gamma_H V^2}{N f^\alpha} \quad (4.7)$$

or

$$S_{1/f}^V = \frac{\gamma_H I_{DC}^2 R_{sample}^2}{N f^\alpha} \quad (4.8)$$

where  $S_{1/f}^V$  is the noise power spectral density of the fluctuations in  $V^2\text{Hz}^{-1}$ ,  $N$  is the total number of charge carriers in the transport channel,  $f$  is the frequency in Hz,  $\alpha$  is a real number exponent and  $\gamma_H$  is called the 'Hooge Parameter' which is a characteristic quantity of the material and quantifies the materials' noisiness.  $\gamma_H$  is dimensionless when  $\alpha = 1$ . In this case, the flicker noise is known as 1/f noise. In most of the cases  $\alpha \approx 1$  but it can also range between 0.8 and 1.4 [7]. An average rms voltage  $V$  measured across the sample, can also be rewritten as a product of  $I_{DC}$  flowing in the sample and the sample's resistance  $R_{sample}$ , (Eq.4.8). Although 1/f noise is intrinsically present in the sample, there has to be a net nonzero current flow in order to measure the 1/f noise [8].

Flicker noise is one of the most studied and still unsolvable phenomena in science. The mathematical aspect which makes it interesting is that the variance of the process which can also be written as  $\int S_{1/f}^V df$ , should diverge at any positive exponent value. However, in reality we never observe an infinite variance. Therefore, there must be a cut-off frequency below which the behavior of the spectrum changes and the integral  $\int S_{1/f}^V df$  converges. A lot of models have been proposed to explain this behavior. A nice summary of those models is provided in reference [9].

An activated random process with a single characteristic time  $\tau$  has a Debye-Lorentzian spectrum:

$$S(\omega) \propto \frac{\tau}{1 + \omega^2 \tau^2}. \quad (4.9)$$

If  $\tau$  is uniformly distributed between  $\tau_1$  and  $\tau_2$ , Eq.4.9 follows a  $S(\omega) \propto \omega^{-1}$  form. To explain the 1/f noise in semiconductor field-effect transistors, McWhorter [10] proposed that the 1/f noise in this system arises due to fluctuations in the number as well as mobility of the charge carriers. Both types of fluctuations may be due to trapping-detraping of the carriers by impurities present in the transport channel. It is the same idea of the activated random processes described by Eq.4.9, just with a distribution of  $\tau$ . Another model proposed by Voss and Clarke [11], also known as 'Thermal fluctuation model' tries to couple the fluctuations in the resistance with the

temperature fluctuations:

$$\frac{\langle \Delta V^2 \rangle}{V_{DC}^2} = \frac{\langle \Delta R^2 \rangle}{R^2} \quad (4.10)$$

with

$$\langle \Delta R^2 \rangle = (dR/dT)^2 C_v^{-1} k_B T^2 \quad (4.11)$$

Here  $C_v$  is the specific heat of the material. As  $C_v \propto N$ , Eq.4.10 has the same form as presented by the Hooge equation (Eq.4.7). However, this model fails to explain the large macroscopic noise in semiconductor devices. For metals which have large  $dR/dT$ , Eq.4.10 quantifies the fluctuation magnitude successfully. Until today no formal explanation exists for the origin of  $1/f$  noise.

For graphene, several noise measurements have been reported over the years [5, 12–14]. Since graphene is a 2-dimensional sheet, it offers a unique platform to probe the physics behind the surface versus volume dependence of the  $1/f$  noise [15]. For the flicker noise measurements in graphene, typical values of the Hooge parameter  $\gamma_H$  are in the order of  $10^{-4}$  to  $10^{-3}$ .  $\gamma_H$  magnitude goes down as the number of graphene layers increases. The reason for the lower noise in multilayer layer graphene is explained by the screening of the charge fluctuations by the outer layers [7]. Flicker noise has also been studied as a function of charge carrier density in graphene field effect transistors. The Hooge parameter as a function of back-gate voltage (carrier density) shows different behaviors for single, bi and few layer graphene, described in detail in references [7, 14].

Graphene also exhibits the shot noise. Typical values for the Fano Factor ( $\mathcal{F}$ ), reported in graphene are in the range of 0.29-0.40 [5, 12]. Graphene exhibits a very high  $1/f$  noise due to its surface sensitivity towards impurities, therefore, the shot noise measurements have to be performed at very high frequencies ( $f > 1\text{MHz}$ ) and low temperatures where the thermal and  $1/f$  noise contributions are negligible.

We can estimate the total noise in graphene by adding the individual contribution from the thermal, shot and  $1/f$  noise given by Eqs. 4.2, 4.5 and 4.7, respectively.

We obtain the spectra shown in Fig. 4.1, using typical values for  $\gamma_H \approx 10^{-3}$ , graphene resistance  $R_{\text{sample}} \approx 1k\Omega$ ,  $n \approx 10^{12} \text{ cm}^{-2}$ , sample area  $A \approx 1 \mu\text{m}^2$ ,  $\alpha = 1$  and  $\mathcal{F} = 0.33$ . At room temperature (300 K) the thermal noise is much higher than the shot noise level (Figure 4.1(a)) and we only see a crossover between the thermal and the  $1/f$  noise. While reducing the temperature to liquid helium temperature (4K), the thermal noise is below the shot noise level for reasonable currents ( $\approx \mu\text{A}$ ) and we can now see the crossover from  $1/f$  noise to the shot noise level. It can be understood from Figure 4.1(b) why shot noise is measured at very high frequencies ( $\approx \text{MHz}$ ) and low temperatures.

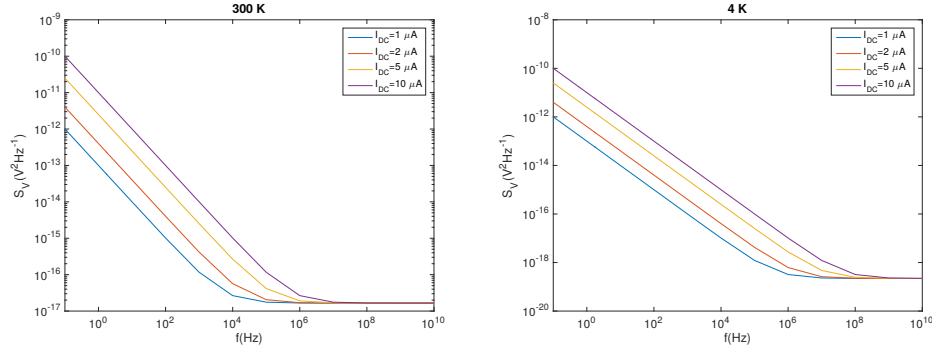


**Figure 4.1:** Estimation of the total noise spectrum for a graphene device at (a)  $T=300\text{K}$  and (b)  $T=4\text{K}$  for different values of DC currents

4

### 4.3 Spin-dependent Noise

There exists a special class of noise in ferromagnetic materials, which unlike the charge noise is sensitive to the external magnetic field and spin-dependent density of states in the ferromagnets. In literature, this noise is termed as ‘magnetic noise’.

In non-magnetic/paramagnetic materials, a finite non-equilibrium spin-accumulation can be created using a ferromagnetic injector or via optical means. The spin accumulation diffuses away and is brought into equilibrium via the spin-relaxation processes due to the non-conserved nature of the spin-current. These ‘spin-relaxation’ processes are believed to produce noise in the spin-current. The non-conserved nature of the spin-current is reflected in a higher Fano-factor for spin-current than in charge current for the shot-noise measurements [16, 17]. There is no standard term for this noise. For further discussion, we call this noise ‘spin-relaxation noise’.

#### 4.3.1 Magnetic Noise

The ferromagnetic transport channel exhibits the noise due to magnetization fluctuations along with the background electronic noise. Noise related to magnetization fluctuations in the ferromagnet which also depend on the applied magnetic field, has been studied in the GMR (Giant Magneto Resistance) and TMR (Tunnel Magneto Resistance) geometry over the previous years and is a well understood phenomenon. In a TMR structure, a low frequency flicker ( $1/f$ ) noise is observed which has its origin both from the magnetization fluctuations and nonmagnetic electronic fluctuations. The first contribution is caused by the thermally activated domain wall hopping and domain wall rotation [18, 19] and the later contribution comes from the impurity states near the tunnel barrier or due to the non-ideal growth of the tunnel

barrier [20]. There is also an alternative explanation that the spin-current exerts a torque on the ferromagnetic electrodes, causing magnetization fluctuations [21–23].

### 4.3.2 Noise associated with Spin-accumulation

Since last decade, several theoretical proposals have surfaced, predicting the existence of noise in the spin-accumulation and in spin-current [16, 24, 25]. In fact, one can measure the spin-accumulation via noise measurements which leads to the field of spin-noise spectroscopy and establishes noise measurements as a probe for spin-accumulation without the need of the ferromagnetic contacts [26]. One can also study other fundamental aspects related to the spin-current and its behavior during the transport, e.g., interaction of the spin-current with the underlying impurities during spin-transport can be studied by measuring the noise in the low frequency ( $1/f$ ) regime. One can also probe the non-conserved nature of spin-current via shot noise measurements for the spin-transport. In a recent experiment, Arakawa *et al.* [27] have measured the shot-noise related to spin-accumulation and found the same Fano factor for charge and spin-transport. They show that the non-equilibrium spin-accumulation generates the spin-dependent shot noise, which depends on the relative alignments of the ferromagnetic electrodes and there is negligible spin-flip scattering during the spin-injection, confirming the fact that the spin-current is conserved during the spin-injection process and the spin-up and spin-down channel behave independently.

In case of graphene, the literature reported so far aims to study the noise associated with the electron transport in single, bi and few layer graphene [7, 13, 15, 28]. But there has been no experiments performed to measure the noise associated with the spin transport.

In this thesis (refer to ch. 7 for details), we for the first time, measure the spin-dependent  $1/f$  noise in graphene in presence of the spin-accumulation via the cross-correlation methods and also use the noise signal to estimate the spin-transport parameters in graphene. The extracted spin-transport parameters comply with those obtained independently from the spin-transport measurements, and establish the noise measurements as an alternative probe for measuring the underlying spin-accumulation. For the  $1/f$  regime, we quantify the charge and spin-dependent  $1/f$  noise with their respective noise magnitudes, and find that the noise magnitude for the spin-dependent  $1/f$  noise is three-to four orders higher than that for the charge  $1/f$  noise and is modified with the spin-relaxation rate in graphene. The observations clearly support the hypothesis, that the finger prints of spin-relaxation can be detected by measuring the noise in the spin-current and can be used as a tool to further study the spin-relaxation processes.

## References

- [1] A. V. . S. Oppenheim, Ronald W., *Discrete-time Signal Processing, 2nd, Second Edition*, Prentice Hall, 2nd, second edition edition ed., 1999.
- [2] J. B. Johnson, "Thermal Agitation of Electricity in Conductors," *Phys. Rev.* **32**, pp. 97–109, July 1928.
- [3] H. Nyquist, "Thermal Agitation of Electric Charge in Conductors," *Phys. Rev.* **32**, pp. 110–113, July 1928.
- [4] Y. M. Blanter and M. Büttiker, "Shot noise in mesoscopic conductors," *Phys. Rep.* **336**, pp. 1–166, Sept. 2000.
- [5] L. DiCarlo, J. R. Williams, Y. Zhang, D. T. McClure, and C. M. Marcus, "Shot Noise in Graphene," *Phys. Rev. Lett.* **100**, p. 156801, Apr. 2008.
- [6] N. Kumada, F. D. Parmentier, H. Hibino, D. C. Glattli, and P. Roulleau, "Shot noise generated by graphene  $pn$  junctions in the quantum Hall effect regime," *Nat. Commun.* **6**, p. ncomms9068, Sept. 2015.
- [7] A. N. Pal, S. Ghatak, V. Kochat, E. S. Sneha, A. Sampathkumar, S. Raghavan, and A. Ghosh, "Microscopic Mechanism of  $1/f$  Noise in Graphene: Role of Energy Band Dispersion," *ACS Nano* **5**, pp. 2075–2081, Mar. 2011.
- [8] F. N. Hooge, " $1/f$  noise sources," *IEEE Trans. Electron Dev.* **41**, pp. 1926–1935, Nov. 1994.
- [9] P. Dutta and P. M. Horn, "Low-frequency fluctuations in solids:  $\frac{1}{f}$  noise," *Rev. Mod. Phys.* **53**, pp. 497–516, July 1981.
- [10] A. L. A. L. McWhorter and L. Laboratory, " $1/f$  noise and related surface effects in germanium," 1955.
- [11] R. F. Voss and J. Clarke, "Flicker ( $\frac{1}{f}$ ) noise: Equilibrium temperature and resistance fluctuations," *Phys. Rev. B* **13**, pp. 556–573, Jan. 1976.
- [12] R. Danneau, F. Wu, M. F. Craciun, S. Russo, M. Y. Tomi, J. Salmilehto, A. F. Morpurgo, and P. J. Hakonen, "Shot Noise in Ballistic Graphene," *Phys. Rev. Lett.* **100**, p. 196802, May 2008.
- [13] A. A. Kaverzin, A. S. Mayorov, A. Shytov, and D. W. Horsell, "Impurities as a source of  $1/f$  noise in graphene," *Phys. Rev. B* **85**, p. 075435, Feb. 2012.
- [14] Q. Shao, G. Liu, D. Teweldebrhan, A. A. Balandin, S. Romyantsev, M. S. Shur, and D. Yan, "Flicker Noise in Bilayer Graphene Transistors," *IEEE Electron Dev. Lett.* **30**, pp. 288–290, Mar. 2009.
- [15] G. Liu, S. Romyantsev, M. S. Shur, and A. A. Balandin, "Origin of  $1/f$  noise in graphene multilayers: Surface vs. volume," *Appl. Phys. Lett.* **102**, p. 093111, Mar. 2013.
- [16] E. G. Mishchenko, "Shot noise in a diffusive ferromagnetic-paramagnetic-ferromagnetic spin valve," *Phys. Rev. B* **68**, p. 100409, Sept. 2003.
- [17] A. Lamacraft, "Shot noise of spin-polarized electrons," *Phys. Rev. B* **69**, p. 081301, Feb. 2004.
- [18] L. Jiang, E. R. Nowak, P. E. Scott, J. Johnson, J. M. Slaughter, J. J. Sun, and R. W. Dave, "Low-frequency magnetic and resistance noise in magnetic tunnel junctions," *Phys. Rev. B* **69**, p. 054407, Feb. 2004.
- [19] S. Ingvarsson, G. Xiao, R. A. Wanner, P. Trouilloud, Y. Lu, W. J. Gallagher, A. Marley, K. P. Roche, and S. S. P. Parkin, "Electronic noise in magnetic tunnel junctions," *J. Appl. Phys.* **85**, pp. 5270–5272, Apr. 1999.
- [20] E. R. Nowak, R. D. Merithew, M. B. Weissman, I. Bloom, and S. S. P. Parkin, "Noise properties of ferromagnetic tunnel junctions," *J. Appl. Phys.* **84**, pp. 6195–6201, Nov. 1998.
- [21] J. Foros, A. Brataas, Y. Tserkovnyak, and G. E. W. Bauer, "Magnetization Noise in Magneto-electronic Nanostructures," *Phys. Rev. Lett.* **95**, p. 016601, June 2005.
- [22] J. Foros, A. Brataas, G. E. W. Bauer, and Y. Tserkovnyak, "Resistance noise in spin valves," *Phys. Rev. B* **75**, p. 092405, Mar. 2007.
- [23] J. Foros, A. Brataas, G. E. W. Bauer, and Y. Tserkovnyak, "Noise and dissipation in magneto-electronic nanostructures," *Phys. Rev. B* **79**, p. 214407, June 2009.
- [24] J. Meair, P. Stano, and P. Jacquod, "Measuring spin accumulations with current noise," *Phys. Rev.*

- B* **84**, p. 073302, Aug. 2011.
- [25] W. Belzig and M. Zareyan, "Spin-flip noise in a multiterminal spin valve," *Phys. Rev. B* **69**, p. 140407, Apr. 2004.
- [26] O. Sauret and D. Feinberg, "Spin-Current Shot Noise as a Probe of Interactions in Mesoscopic Systems," *Phys. Rev. Lett.* **92**, p. 106601, Mar. 2004.
- [27] T. Arakawa, J. Shiogai, M. Ciorga, M. Utz, D. Schuh, M. Kohda, J. Nitta, D. Bougeard, D. Weiss, T. Ono, and K. Kobayashi, "Shot Noise Induced by Nonequilibrium Spin Accumulation," *Phys. Rev. Lett.* **114**, p. 016601, Jan. 2015.
- [28] A. A. Balandin, "Low-frequency  $1/f$  noise in graphene devices," *Nat. Nanotechnol.* **8**, pp. 549–555, Aug. 2013.



### Abstract

*In this chapter, I describe the experimental techniques involved for fabricating the devices in this thesis. The chapter starts with describing the methods for exfoliating different 2D-materials such as graphene, WS<sub>2</sub> and hBN. Following this, I explain the dry-pick up transfer method in detail which is used for fabricating the graphene-2D material heterostructures. In the second half of the chapter, I briefly mention the lithographic steps for contact preparation and deposition. In the last part, I explain the electrical connection scheme for charge and spin transport measurements.*



## 5.1 Sample Preparation

### Substrate Preparation

We use a heavily n-doped silicon (Si) substrate with a 300 nm SiO<sub>2</sub> insulating layer which can be used as a capacitor with a capacitance  $\approx 7.1 \times 10^{10} \text{ cm}^{-2} \text{ V}^{-1}$  ( $\sim 110 \mu\text{F m}^{-2}$  is SI units). The n<sup>++</sup> doped region is used as a back gate electrode. For cleaning of the substrate surface we ultrasonicate it in acetone and then in isopropylalcohol (IPA) solution for 2 minutes in each step. Further we bake the substrate in oven at 170°C to get rid of the water molecules from the surface. We use these pre-cleaned substrates for the exfoliation of graphene and hBN flakes.

#### 5.1.1 2D Material Exfoliation

##### Graphene

Graphene source material comes in several forms and grades, which quantify the impurity level present in the material. We use a Highly Oriented Pyrolytic Graphite (HOPG) crystal as a source material for this because the HOPG has a bigger surface area with a very low amount of impurities. The scotch-tape method [1] is used to cleave the HOPG crystal and transfer it onto a pre-cleaned SiO<sub>2</sub>/Si substrate. We use an optical microscope to find the graphene flakes on the substrate. A contrast in optical reflectivity helps to distinguish different numbers of graphene layers. The optical contrast also depends on the oxide thickness and the wavelength of the light source we use. Therefore, for each exfoliation we calibrate the contrast for a structure with respect to the increasing number of layers, one by one (Fig. 5.1). The difference in the optical reflectivity of the layers gives us the optical contrast of a single layer graphene, which usually turns out to be around 4-6%.

##### Tungsten Disulfide (WS<sub>2</sub>)

Thin WS<sub>2</sub> flakes down to few nanometers can be easily exfoliated on a polydimethylsiloxane (PDMS) substrate and similar to graphene, are identified by their optical contrast. Exfoliation of WS<sub>2</sub> on a PDMS stamp helps a direct polymer free transfer of the desired flake onto a target substrate with the help of a transfer stage arrangement ( Fig. 5.2).

After the transfer onto a desired substrate, the WS<sub>2</sub> flake is annealed in an Ar-H<sub>2</sub> environment for two hours at 200-250°C in order to remove the polymer residues on the flake coming from the PDMS stamp. Though, this procedure has not shown a significant improvement in the surface morphology. In an attempt to anneal at higher temperatures ( 350°C), the WS<sub>2</sub> flakes were seen to crumble.

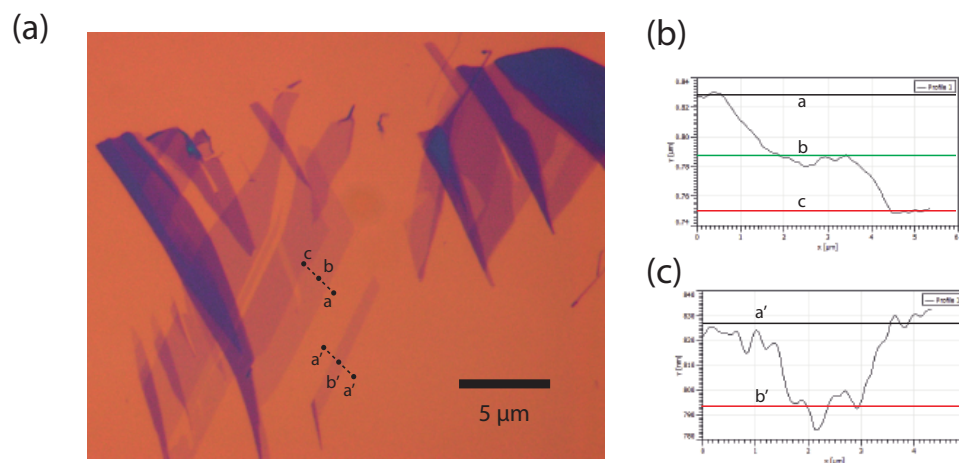


**Figure 5.1:** (a) A few-layer-graphene flake after exfoliation on a  $\text{SiO}_2/\text{Si}$  substrate. The optical contrast varies with the flake thickness due to change in the optical reflectivity. The lightest region (with line profile  $a'-b'-a'$ ) represents a single layer. The optical contrast (OC) of the single layer is determined by measuring the difference in the OCs of the structures with increasing no. of layers, as denoted by the line profile  $a-b-c$ . The difference in the OC between point  $b$  and  $c$  is the contrast of a single layer. It can be seen in the optical profile in (b) with increasing the no. of layers one by one, the optical contrast increases almost by the same amount. (c) The optical profile of a single layer along the line  $a'-b'-a'$ .

5

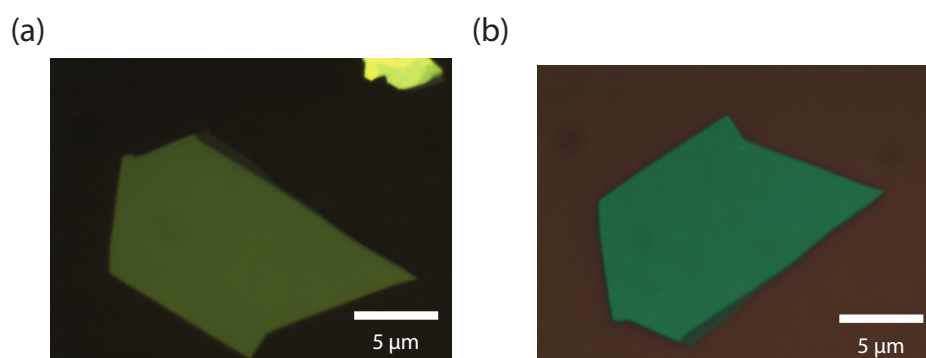


**Figure 5.2:** (a)  $\text{WS}_2$  flake on a PDMS substrate and (b) on a  $\text{SiO}_2/\text{Si}$  substrate after the transfer.

### Boron Nitride

Boron Nitride (hBN) flakes are exfoliated in a similar way onto a pre-cleaned  $\text{Si}/\text{SiO}_2$  substrate. Boron nitride powder is bought from the external sources (HQ graphene)

and few nm thick hBN flakes are obtained by the exfoliation in multiple steps via the standard scotch tape method.

### 5.1.2 Dry Pick-up Transfer Method

The dry pick-up transfer recipe for making graphene heterostructures in the group was developed and optimized by Zomer *et al.* [2] and Guimarães *et al.* [3]. I follow the similar recipe with some modifications. In this method, a 3mm x 3mm x 1mm PDMS stamp on a glass slide with a polycarbonate film covering the stamp is used. The glass slide is mounted on a transfer stage equipped with a heater and an optical microscope. The whole procedure is schematically demonstrated in Fig. 5.3. I prepared four types of stacks with different combinations of 2D materials (hBN or WS<sub>2</sub>) with graphene:

- stack I- top-hBN/graphene(Gr)/bottom-hBN
- stack II- top-WS<sub>2</sub>/Gr
- stack III- Gr/bottom-WS<sub>2</sub>
- stack IV- top hBN/Gr/bottom WS<sub>2</sub>

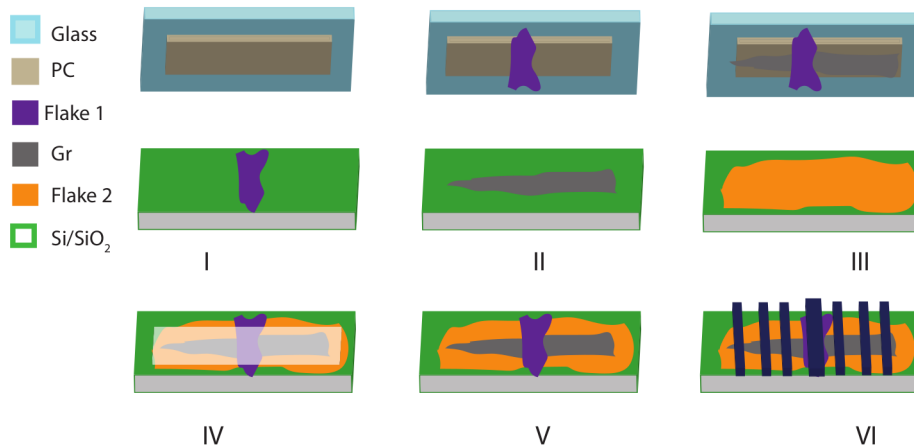


**Figure 5.3:** A step-by step schematic of the pick-up transfer method. Here, flake 1 and flake 2 are either WS<sub>2</sub> or hBN.

Below, I summarize the full procedure for making a three layer flake 1/Gr/flake 2 stack where flake 1 is hBN and flake 2 can be either of the hBN or WS<sub>2</sub> flakes:

- First, a mask with a polycarbonate (PC) film, which is in contact with a PDMS stamp on a glass slide, is mounted on the slide holder of a micro-manipulator. A slide holder is an aluminum plate in which we can create vacuum to hold the glass slide with the mask. There also may be other arrangements to hold the glass slide, depending on the design of the system. After fixing the polymer mask, we adjust the focus of the optical microscope onto the polycarbonate film and move the microscope optics to find out a wrinkle free region of the polymer.
- A substrate containing the top boron nitride flake (flake 1) is put on an aluminum chuck, situated below the optical microscope, both attached to the transfer stage system. The chuck can be moved in x-y plane in the range of 5 cm. Now we adjust the focus of the microscope on the hBN flake and try to align it along y-axis. After we have aligned the substrate under the desired polymer region, we slide the chuck outwards in the x-y plane outside the microscope arrangement and fix the sample with a glue tape in the same position, so that it does not move during the flake transfer process. The aligned hBN flake and mask are shown schematically in step I of Fig. 5.3.
- After the sample is fixed on the chuck, it is moved back underneath the polymer mask and the sample is moved towards the mask along the z-axis with the help of a lever.
- As the sample is beneath the mask, the focus of the microscope is set in between the sample and the mask. When the sample is pushed towards the mask along z-axis, it gets in focus and we keep repeating to put focus in between the sample and the mask unless both are in the same focal plane and can be seen in the same focus of the microscope.
- Now the sample is pressed more towards the mask to make a physical contact and we see the fringes appearing in the outer region of the polymer. The stamp has to be kept pressed until the fringes reach close to the stack. One should be careful at this moment that the fringes do not cross the stack.
- After the fringes are very close to the sample, we start heating the substrate around 60-90°C approximately for 1-4 minutes. The heating time varies from sample to sample and depends on the compound thermal conductivity of the substrate+polymer. The substrate-polymer contact increases due to thermal expansion of the substrate. As a consequence of heating, the polymer gets more sticky, and now, it is possible to pick up the hBN flake (flake 1). At this point, the fringes move due to heating. We stabilize the fringes while adjusting the force from the lever.

- After the pick up, for retracting the substrate on the stage from the polymer, we first switch off the heating so that the substrate cools down and is not in a contact with the polymer anymore. In this duration, the fringes moving away from the flake can be seen. Now we can retract it back mechanically with the help of the lever. The transferred hBN flake is shown schematically in step II of Fig. 5.3.

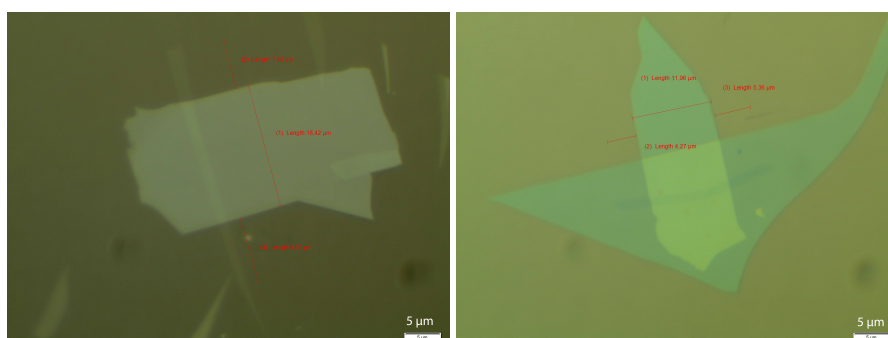


**Figure 5.4:** graphene-top hBN stack and top hBN-graphene-bottom hBN stack

- We use the same process again to pick up the graphene flake via the top hBN flake (flake 1). A graphene flake is placed in a perpendicular orientation (along x-axis) with respect to the picked up hBN flake and following the earlier step, it is picked up. While heating up the substrate, when the polymer with the top hBN comes in contact with graphene, it can easily pick up the flake even outside the top hBN region due to increased adhesion of the graphene to the polymer (step III of Fig. 5.3). The graphene flake underneath the hBN is picked up due to the van der Waals force between the flakes.
- In order to transfer the graphene-hBN stack on the flake 2 (hBN or  $WS_2$ ) which also acts as a target substrate, we repeat the same transfer process. In the last step of heating, we overheat the substrate up to  $150^\circ\text{C}$ , approximately for 30 seconds so that instead of picking up the flake, the polymer with the top hBN and the graphene flake, breaks on top of flake 2, and now we have a bottom flake 2/graphene/top hBN stack covered with the polycarbonate film (step IV of Fig. 5.3).

An optical image of a hBN/graphene/hBN stack, prepared via the dry pick-up transfer method is shown in Fig. 5.4. Procedure for preparing stack II, i.e. top  $WS_2$ /graphene is much easier. Since  $WS_2$  is directly exfoliated on the PDMS stamp, it can be transferred onto the graphene flake on  $SiO_2/Si$  substrate by just pressing the  $WS_2$  covered PDMS stamp onto the graphene flake, using the same transfer stage arrangement.

### Removal of Polycarbonate

The PC film on top of the stack is dissolved in a chloroform solution. The stack is put in the chloroform solution for at least 6 hours so that the polycarbonate is removed from the top of the stack. Afterwards the stack is rinsed gently in a IPA bath 2-3 times so that the chloroform residues are washed by the IPA solution (step V of Fig. 5.3). After the PC removal, the stack is annealed in an Ar-H<sub>2</sub> environment at 250-350°C for 3-6 hours, in order to remove the remaining PC residues from the stack. This completes the stack preparation process.

### 5.1.3 Electron Beam Lithography

In order to define the sub-micron size contacts, we use the electron beam lithography (EBL) technique. These techniques provide a good control over the dimensions down to tens of nanometers. We first spin-coat a polymer on top of the substrate. We use a polymethylmethacrylate (PMMA) polymer with molecular weight of 950K. A selective exposure of the polymer to the electron beam breaks the polymer chains. After the EBL, we develop the pattern by rinsing the EBL exposed sample in Methyl Isobutyl Ketone(MIBK)+Iso Propyl Alcohol(IPA) (1:3) solution for 1 minute and then in IPA solution for 30 seconds. The parts of the polymer exposed to the electron beam, get dissolved and the remaining part stays on the substrate.

### 5.1.4 Contact Fabrication

As a first step to define the tunnel barriers, we deposit 0.4 nm of titanium (Ti) or Aluminum (Al) at  $\approx 10^{-6}$  Torr with a deposition rate of 0.7 Å/s, then we introduce an oxygen gas flow to the chamber at  $\approx 10^{-1}$  Torr for 15 minutes to fully oxidize the Ti(Al) layer. This process is repeated to obtain approximately 1 nm thick tunnel barrier. After this step, we deposit a desired thickness of the ferromagnetic cobalt (Co) layer. As cobalt may get oxidized easily, we encapsulate it by depositing a 3 nm thick layer of aluminum (Al), which forms a thin protective layer of Al<sub>2</sub>O<sub>3</sub> on top of it. After the deposition, the remaining PMMA is removed by putting the sample in hot acetone ( $\approx 50^\circ\text{C}$ ), leaving the desired pattern on the sample (step VI of Fig. 5.3).

## 5.2 Electrical Measurements

In order to characterize the charge and spin transport properties of graphene, we use a low-frequency lock-in detection method to apply an AC current and measure the voltage response in our samples. A schematic of the measurement setup is shown in Fig. 5.5.

It consists of following components:

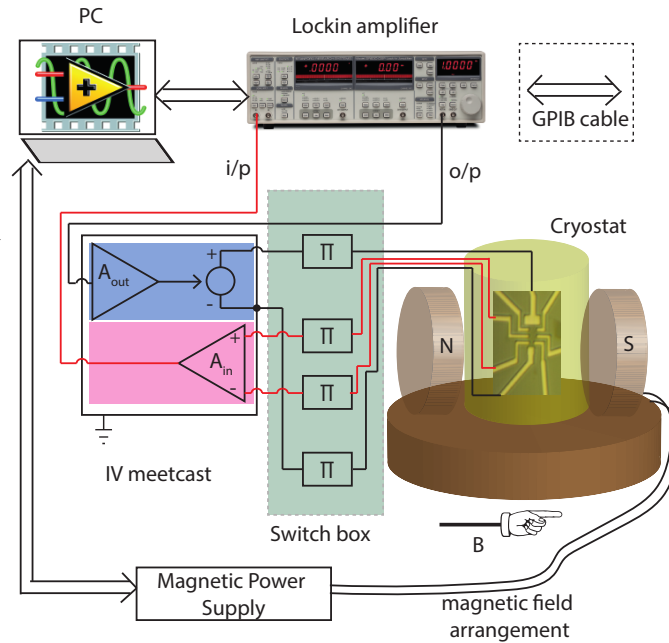


**Figure 5.5:** A schematic of the measurement setup. An IV meetcast (IVM) is a home made current source, which also has an input amplifier with its gain in  $1-10^5$  range. An AC voltage at frequency  $f_{ref}$  is applied from the lock-in to the voltage controlled current source in the IVM which flows a constant current in the sample via a switch box (black wires). The voltage drop across the sample (red wires) is connected to the input amplifier of the IVM via the switch box and is amplified with  $A_{in}$ . The amplified signal is fed back to the lock-in input. The lock-in measures the signal at  $f_{ref}$ , filtering out the other frequency components.

- A SR 830 lock-in amplifier which can generate a sinusoidal voltage with an oscillation frequency in the range of 1 mHz-102 kHz.
- Keithly 2410 DC source meters for applying/reading a DC voltage/current. Mostly a DC voltage is used for a back-gate voltage application or characterizing the high resistance devices which have resistance  $> 100 \text{ k}\Omega$ , because the lock-in has an input impedance of about  $10 \text{ M}\Omega$ .
- A home-made voltage controlled current source which can generate a current from  $10 \text{ nA/V}$ - $10 \text{ mA/V}$ .
- A connection switch box with  $\pi$  filters consisting of a resistance  $R_{filter}=1 \text{ k}\Omega$  and a capacitance  $C_{filter}= 10 \text{ nF}$ .
- A cryostat for keeping the sample in vacuum.

- A computer system with a LabView program to control the equipments and store the measured data.

In this arrangement, an alternating voltage, oscillating with frequency  $f_{\text{ref}}$  is applied via the lock-in voltage source to the voltage-controlled current source and an AC current  $i_{\text{ac}}$  of the same frequency, proportional to the applied voltage flows into the sample via the switch box. The lock-in detection method works on a feedback loop, which only measures the input signal at  $f_{\text{ref}}$  and discards the signals at other frequencies. This very ability of the lock-in-detection method helps to filter out the noise present at other frequencies and measure the small signal buried in noise. The filters at the connection box help to filter out the noise at higher frequencies and also protect the sample from sudden electrical discharge and disturbances in the power supply. For the signal averaging, the lock-in measurement unit performs the digital averaging over a certain time constant  $\tau$ . The thumb rule for selecting  $f_{\text{ref}}$  is  $\tau > 3 \times \frac{1}{f_{\text{ref}}}$ . The lock-in detection also provides other advanced functions for filtering out the noise such as using the 'high reserve', and/or 'roll-off' option of the low pass filter around  $f_{\text{ref}}$ . All these options apparently require more averaging of the measured signal, and therefore require more measurement time. So, there is a clear trade-off between clean signal and the required waiting time.

### 5.2.1 Charge Transport

In order to measure contact+flake resistance, contact resistance and flake resistance, we use the 2 probe, 3 probe and 4 probe connection scheme, respectively. In Fig. 5.6, C1, C2, C3 and C4 represent the contact resistances, which is the sum of the interface resistance, resistance of the contact path and the resistance of the filter, depending on the connection box used. G1, G2 and G3 represent the resistances of the flake segments. By applying a current between pins C1 and C4 and measuring the voltage between the same pins (two probe measurement), the total resistance measured is  $R^{2\text{p}} = R_{C1} + R_{G1} + R_{G2} + R_{G3} + R_{C4}$ . Applying a current between pins C1 and C2 and probing the voltage between C3 and C2 (three probe measurement) gives  $R^{3\text{p}} = R_{C2}$ , the contact resistance. Applying a current between pins C1 and C4 and measuring the voltage between C2 and C3 (four probe measurement) gives  $R^{4\text{p}} = R_{G2}$ , the flake resistance of the central region.

### 5.2.2 Spin Transport

For spin-transport measurements, we use an AC four probe non-local detection scheme. A fixed charge current  $I$  is applied using a current source between C1 and C2, and a voltage difference is measured non-locally between C3-C4. This method reduces the effect of the local charge contribution and we are able to observe the effects purely



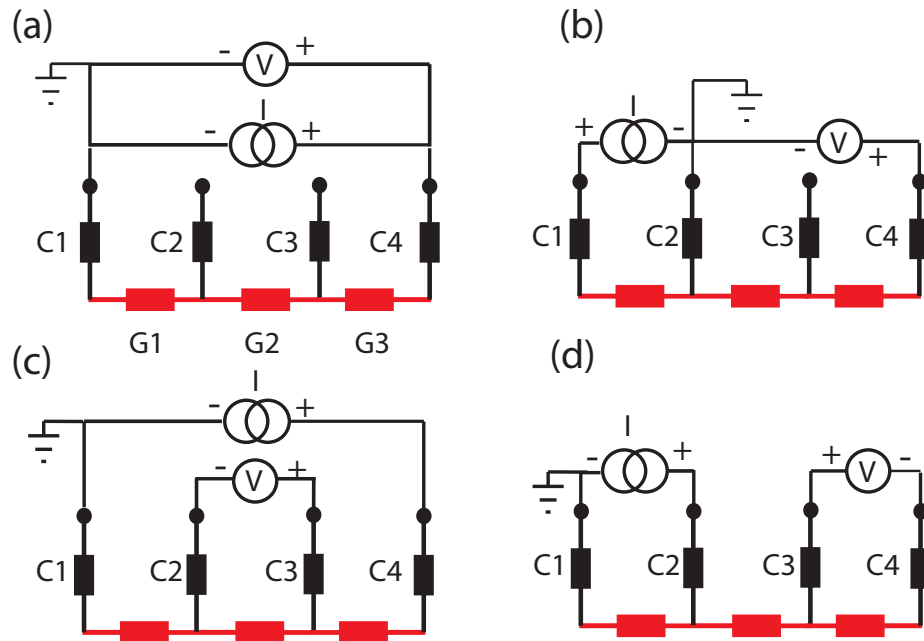


**Figure 5.6: Electrical measurement scheme:** the panel shows different resistors corresponding to three graphene segments G1, G2 and G3 (in red) and four contacts C1, C2, C3 and C4 (in black). Each contact represents the resistances contribution from the ferromagnet, tunnel barrier, connection path and the resistance from the filter box. (a) The two probe (2p), (b) three probe (3p) and (c) four probe (4p) connection schemes for measuring the contact+flake resistance, contact resistance and flake resistance, respectively. (d) the four-probe non-local spin-injection and detection scheme. Here, no charge current flows in the non-local path and ideally a zero charge voltage is measured between C3 and C4

related to spin transport [4]. A detailed description of the spin-valve and the Hanle spin-precession measurement method is provided in chapter. 3.

## References

- [1] K. S. Novoselov, A. K. Geim, S. V. Morozov, D. Jiang, Y. Zhang, S. V. Dubonos, I. V. Grigorieva, and A. A. Firsov, "Electric Field Effect in Atomically Thin Carbon Films," *Science* **306**, pp. 666–669, Oct. 2004.
- [2] P. J. Zomer, M. H. D. Guimarães, J. C. Brant, N. Tombros, and B. J. v. Wees, "Fast pick up technique for high quality heterostructures of bilayer graphene and hexagonal boron nitride," *Appl. Phys. Lett.* **105**, p. 013101, July 2014.
- [3] M. Guimarães, P. Zomer, J. Ingla-Aynés, J. Brant, N. Tombros, and B. van Wees, "Controlling Spin Relaxation in Hexagonal BN-Encapsulated Graphene with a Transverse Electric Field," *Phys. Rev. Lett.* **113**, p. 086602, Aug. 2014.
- [4] N. Tombros, C. Jozsa, M. Popinciuc, H. T. Jonkman, and B. J. van Wees, "Electronic spin transport and spin precession in single graphene layers at room temperature," *Nature* **448**, pp. 571–574, Aug. 2007.



## Chapter 6

---

# Spin Relaxation in Graphene with self-assembled Cobalt Porphyrin Molecules

### Abstract

*In graphene spintronics, interaction of localized magnetic moments with the electron spins paves a new way to explore the underlying spin relaxation mechanism. A self-assembled layer of organic cobalt-porphyrin (CoPP) molecules on graphene provides a desired platform for such studies via the magnetic moments of porphyrin-bound cobalt atoms. In this work a study of spin transport properties of graphene spin-valve devices functionalized with such CoPP molecules as a function of temperature via non-local spin-valve and Hanle spin precession measurements is reported. For the functionalized (molecular) devices, we observe a decrease in the spin relaxation time ( $\tau_s$ ) even up to 50 %, which could be an indication of enhanced spin-flip scattering of the electron spins in graphene in the presence of the molecular magnetic moments. The effect of the molecular layer is masked for low quality samples (low mobility), possibly due to dominance of Elliot-Yafet (EY) type spin relaxation mechanisms.*

published as:  
S. Omar, M. Gurram, I.J. Vera-Marun, X. Zhang,  
E.H. Huisman, A. Kaverzin, B.L. Feringa, and B.J. van Wees  
*Phys. Rev. B* **92**, 115442 (2015).

## 6.1 Introduction

Graphene, one atom thick layer of  $sp^2$  carbon atoms, has potential for spintronic applications due to theoretically predicted high spin relaxation time ( $\tau_s \approx 100$  ns) and long spin diffusion length ( $\lambda_s \approx 100 \mu\text{m}$ ) [1, 2]. These exceptional properties are attributed to negligible spin orbit coupling and weak hyperfine interaction due to the low atomic mass of carbon [3]. However, the maximum reported experimental values demonstrate  $\lambda_s$  of about  $12 \mu\text{m}$  [4] for encapsulated graphene and  $\tau_s$  about 2.7 ns for the hydrogenated graphene [5], which although remarkable when compared with other metals and semiconductors, are still lower by more than an order in magnitude than the theoretically predicted values. A mismatch between theory and experiments suggests towards external factors such as impurities/defects present near the graphene lattice, which dominate the spin relaxation process and result in a lower value for  $\lambda_s$ .

In order to probe the role of impurities on spin transport, one can systematically introduce them to graphene. In recent years, different research groups have demonstrated several ways of introducing impurities (magnetic and non-magnetic) in graphene such as doping with adatoms (Au, Mg), introducing defects and chemical-functionalization [6–10], each method introducing a different spin relaxation source. For example heavy metal atoms such as Au can change the spin transport properties in graphene via spin orbit coupling [11]. On the other hand, light metal (Mg) ions can introduce charge impurity scattering of spins in graphene [12], although the experimental study rules out the role of this mechanism [13]. A significant change in the spin transport properties of graphene was reported in the presence of magnetic moments [14], which can be introduced via hydrogenation or by introducing vacancies in the graphene lattice. Remarkably, recent weak localization measurements on graphene [15] also show that magnetic impurities could play the key role in limiting the spin relaxation time in graphene. As it has been shown theoretically that [16, 17]

If the localized moments are present at adatoms, they can act as spin hot spots and enhance the spin relaxation process via resonant scattering. Therefore, the recent findings serve as an imperative to introduce magnetic impurities in graphene and investigate their effect on the spin transport.

Introducing the impurities via the methods described above may damage the graphene lattice and modify its electronic band structure [18]. Alternatively, the self-assembly of molecular layers on graphene is a non-destructive way to functionalize the graphene surface and one can still tune the electronic properties of this two dimensional material [19]. Recently, Zhang *et al.* have reported the self-assembly of porphyrin ligand bound cobalt atoms (CoPP) on top of a graphene surface [20]. Porphyrins are attached to graphene via weak Van der Waals interactions, while the cobalt atoms do not form any chemical bond with graphene in contrast to the direct deposition of metal atoms or ions as discussed above [21]. Therefore, the self-

assembly is not supposed to change the electronic properties of graphene significantly. On the other hand, cobalt atoms have an unpaired spin ( $S=1/2$ ), which can act as a localized magnetic moment.

In this work, we study spin transport properties of a CoPP-graphene system as a function of temperature, using non-local spin-valve and Hanle spin precession measurements. After the self assembly of magnetic molecules, a reduced  $\tau_s$  up to 50% with a lowered spin diffusion coefficient  $D_s$  is obtained compared to the values for the sample without functionalization (pristine sample). A pronounced effect of the molecular layer was observed for samples with high mobility and high diffusion coefficient, alluding to the sample quality playing an important role in determining the spin transport properties in graphene in contrast to previous studies [22].

## 6.2 Device Fabrication

Graphene spin-valve devices are prepared using highly oriented pyrolytic graphite (HOPG), which has very small amount of impurities (ZYA grade, supplier: SPI). Graphene is mechanically exfoliated onto a pre-cleaned  $\text{SiO}_2/\text{Si}$  substrate (300 nm thick  $\text{SiO}_2$ ), where  $n^{++}$  doped Si is used as a back gate electrode. Ferromagnetic (FM) contacts are patterned via electron beam lithography on the PMMA coated graphene flake. Then 0.4 nm of titanium (Ti) is deposited in two steps, each step followed by oxidation to define a tunnel barrier, which is to overcome the conductivity mismatch problem[23]. The deposited Ti oxide is only present under the contacts, the rest of the graphene surface is uncovered. On top of the oxide barrier we deposit 35 nm of cobalt for the spin selective contacts. To prevent oxidation of the ferromagnetic electrodes, the contacts are covered with 3 nm thick aluminum layer followed by the lift-off process.

In order to equip graphene with magnetic molecules, a cobalt-porphyrin solution (conc. 0.56 mg/ml in tetradecane) is drop cast on top of the device and left to dry for 10 minutes. The residual porphyrin layers on top are removed by rinsing the device with hexane (Fig. 6.1(b)). Since the exfoliated samples on the insulating  $\text{SiO}_2$  substrate are not big enough to perform scanning tunneling microscopy (STM), in order to confirm the self-assembly of porphyrins on graphene we perform STM on the large area CVD graphene-CoPP system. An STM image (Fig. 6.1(d)) of a CVD graphene sample ( $\text{Si}/\text{SiO}_2$  substrate) with the CoPP molecules on top confirms the self-assembly of cobalt-porphyrin molecules on graphene.

## 6.3 Results and Discussion

A lock-in amplifier detection technique is used to measure the charge and the spin transport properties of our samples. All the measurements are carried out using

a cryostat in vacuum ( $\sim 1 \times 10^{-7}$  mbar) at different temperatures between 4K and 300K. First, the sample is characterized in its pristine state. Afterwards, the magnetic impurities are added to the sample and the change in the charge and spin transport properties is measured. We report the measurements for three samples, prepared under identical conditions. For discussion, they are labeled as sample A, B and C. A scanning electron microscope (SEM) image of sample A is shown in Figure. 6.1(c).

### 6.3.1 Charge Transport

For the charge transport measurements, an alternating current (ac) is applied between contacts 1 and 4 and the voltage is measured between contacts 2 and 3 (Fig. 6.1(c)). In order to measure the carrier density dependence of the graphene resistivity (Dirac curve), we sweep the back-gate voltage. After the self-assembly of the CoPP molecules on the sample, the gate dependence is found to have a positive hysteresis at room temperature (inset Fig. 6.2), which alludes to a charge transfer process between graphene and the CoPP molecules [24, 25]. At low temperatures charge states are frozen in the molecules and no hysteresis is observed. The field effect electron mobility  $\mu_e$  for the pristine device is  $7100 \text{ cm}^2\text{V}^{-1}\text{s}^{-1}$ , and for the CoPP device  $\mu_e \sim 5000 \text{ cm}^2\text{V}^{-1}\text{s}^{-1}$ , both mobilities calculated at room temperature (RT) for a carrier density  $\sim 10^{12} \text{ cm}^{-2}$ . Contact resistances ( $R_c$ ) for all the samples were high enough ( $\geq 1.5 \text{ k}\Omega$ ) to be in the non-invasive regime as described in ref. [23].

### 6.3.2 Spin Transport

For the spin transport measurements, a four probe non-local detection scheme is used (Fig. 6.1(b)). This method allows us to decouple the charge and spin current paths and thus minimize the charge contribution to the detected spin signal ( $R_{NL} = V_{NL}/I$ ) [26]. The spin-valve measurement is performed by first setting a high magnetic field  $\vec{B}$  along the -y direction (Fig. 6.1(b)), so all the FM electrodes are magnetized along the field (parallel configuration). Then sweeping the field in the opposite direction, the electrodes reverse their magnetization at different fields depending on their coercivity, leading to an anti-parallel configuration between the inner injector and the detector electrodes, which appears as a switch in the non-local signal. At high magnetic field, all the electrodes are again magnetized in the same direction in the parallel configuration. The difference between the parallel and the anti-parallel signals is the spin-valve signal  $\Delta R_{NL}$ . The outer contacts are chosen far away from the inner electrodes. In this way their influence on the measured spin signal is eliminated and we see only two distinct switches that correspond to the magnetization reversal of the inner injector and the inner detector.

Spin-valve measurements for sample A before and after the functionalization are shown in Fig. 6.3 at different temperatures. For both pristine and functionalized

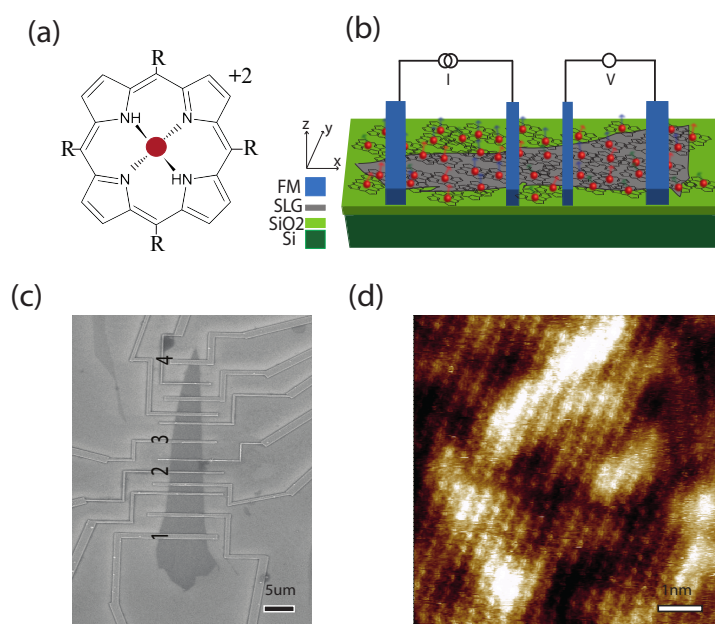


**Figure 6.1:** (a) Molecular structure of a cobalt bound porphyrin (CoPP) complex. Co<sup>++</sup> (in red circle) is the central atom in the complex, surrounded by the Porphyrin ligand. In the porphyrin ring ‘-R’ represents a long chain alkyl group (-C<sub>10</sub>H<sub>21</sub>), which is responsible for making weak Van der Waals interaction with graphene during the self-assembly. (b) Non-local measurement scheme for a graphene spin-valve. Graphene (in gray) with a self-assembly of cobalt-porphyrin molecules on top (cobalt magnetic moments in red), is probed with ferromagnetic tunnel contacts (in blue). (c) Scanning electron micro-graph (SEM) of sample A. The distance between contacts 2-3 (transport channel) is 5 μm. Outer contacts are chosen far enough from the inner ones, in order to make sure that they do not affect the spin transport. (d) A scanning tunneling microscopy (STM) image of CVD graphene functionalized with cobalt-porphyrin molecules on top (scan area 39 nm<sup>2</sup>) on Si/SiO<sub>2</sub> substrate, which demonstrates an ordered self-assembly of the CoPP molecules on graphene. A bright spot in the image corresponds to the core of the porphyrin molecule.

states of the sample, the spin-valve signal shows the switches corresponding to the contacts magnetization. However, after the functionalization, the signal magnitude is significantly reduced. At low temperature, the signal magnitude is increased for both the pristine and the CoPP devices (Fig. 6.3).

In order to understand the effect of localized magnetic moments on spin trans-



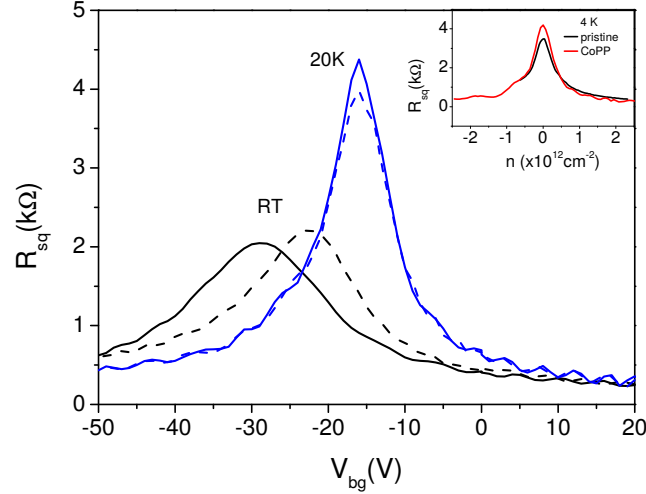


**Figure 6.2:** Resistivity as a function of gate voltage for the CoPP device (sample A) at different temperatures. Solid (dashed) lines in the plot correspond to forward (backward) sweeping direction of the back-gate voltage. The CoPP device shows hysteresis at room temperature (black curve), which disappears at low temperatures (blue curve). Hysteresis at RT indicates towards a charge transfer process between the CoPP molecules and graphene, which disappears at low temperatures due to freezing of the charged states in the molecules [24]. A comparison between the Dirac measurement for the pristine and the CoPP state of the sample A is shown in the inset (at 4 K) (see inset of Fig. 6.2 (b)). After functionalization, the sheet resistance increases near the charge neutrality point, which is not significant at high carrier densities.

6

port in graphene, we refer to the exchange field model, explained by McCreary *et al.* [14]. In this model, an electron spin in graphene can interact with the magnetic moments via an exchange field  $\bar{B}_{ex}$ , which is the average exchange field produced by the localized moments.  $B_{ex}$  varies spatially and in time in a random fashion and influences locally the Larmor precession of the diffusing spins. The effect of varying precession frequencies at different locations resembles the D'yakonov-Perel mechanism of spin relaxation [27] and is responsible for an additional spin dephasing. In a spin-valve measurement, an enhanced relaxation (a reduced signal) is expected when the moments are randomized. As one starts applying an in-plane magnetic field, the magnetic moments try to align themselves along the field and their dephasing effect gets suppressed. This feature would appear as a dip in the spin-valve signal. Within this picture, the spin relaxation rate by the fluctuating exchange field

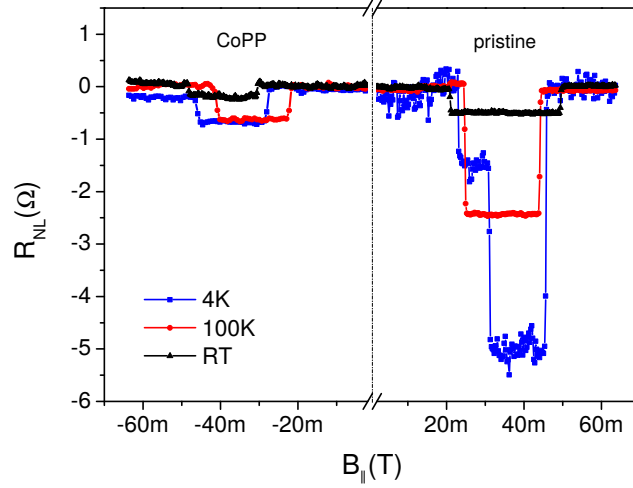


**Figure 6.3:** Spin-valve measurements for sample A (all the measurements in the electron doped regime at  $n \sim 10^{12} \text{ cm}^{-2}$ ) are shown in the positive x-axis for the pristine state and for the device after the functionalization are shown in the negative x-axis. A strongly reduced spin-valve signal is observed after the functionalization.

causing the dip is given by the following equation:

$$\frac{1}{\tau_{ex}} = \frac{\Delta B^2}{\tau_c} \frac{1}{(B_{app,y} + \bar{B}_{ex,y})^2 + \left(\frac{\hbar}{g_e \mu_B \tau_c}\right)^2}, \quad (6.1)$$

where  $\Delta B$  is the exchange field fluctuation magnitude,  $g_e=2$  is the gyromagnetic factor of the free electrons,  $\mu_B$  is the Bohr magneton,  $\hbar$  is the reduced Plank constant and  $\tau_c$  is the fluctuation correlation time [14]. According to the formula above, the maximum relaxation (dip) in the spin-valve measurement should appear when  $B_{app} = -\bar{B}_{ex}$ . Therefore the magnetic ordering of the localized moments affects the observation of the dip. For paramagnetic ordering one would observe the dip around  $B_{app}=0$ . On the other hand, for ferromagnetic ordering, there is a non-zero exchange field  $B_{ex}$  present ( $\bar{B}_{ex} \neq 0$ ) even when no external field is applied ( $B_{app}=0$ ). Now the dip would occur at finite external applied field and would exhibit hysteresis.

For the measured spin-valve signal for the CoPP device, we do not observe any dip, either around zero or non-zero applied field. The only clear effect of introducing the CoPP molecules is the reduced magnitude of the spin-valve signal. The observed behavior can be explained by considering the magnetic moments playing the role of spin-flip scatterers in the transport channel, which enhance the spin relaxation process but do not produce a measurable effective exchange field. In order to confirm

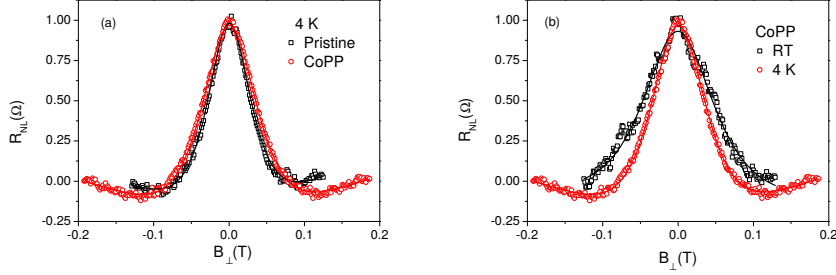


**Figure 6.4:** a) Hanle measurements  $((R_P - R_{AP})/2)$  for the pristine (black squares) and the CoPP state (red circles) at 4K (sample B). The corresponding fittings are plotted in line. The curves are normalized with respect to the signal at  $B=0$ . After the functionalization Hanle line shape is broadened, indicating a reduced spin relaxation time ( $\tau_s$ ). (b) Hanle measurements for sample B after self-assembly at RT and 4K. The curves are normalized. Broadening of the black curve (with square symbol) (RT) is dominated by the enhanced  $D_s$ . The spin relaxation time ( $\tau_s$ ) only changes from 100 ps (RT) to 112 ps (4K). All the measurements were done at fixed carrier density ( $n \sim 10^{12} \text{ cm}^{-2}$ ).

## 6

if the source of the reduced spin signal is due to an enhanced spin relaxation rate, we now need to measure the spin transport parameters via Hanle spin precession measurements.

Hanle precession measurement is a reliable tool to study the spin transport properties. Here, a magnetic field is applied perpendicular to the direction of the injected spins, which precess around this field  $\vec{B}$  with Larmor frequency  $\vec{\omega}_L = g_e \mu_B \vec{B} / \hbar$ . While sweeping the magnetic field, due to the precession, spins can be reoriented to a direction opposite to the injected one, leading to a sign reversal in the spin signal. Simultaneously, they also dephase and result in a lower spin accumulation at higher fields. The Hanle precession can be fitted with the steady state solution to the Bloch equation (Eq. 6.2) with appropriate boundary conditions [26]:

$$D_s \nabla^2 \vec{\mu}_s - \frac{\vec{\mu}_s}{\tau_s} + \vec{\omega}_L \times \vec{\mu}_s = 0 \quad (6.2)$$

where  $D_s$  is the spin diffusion coefficient,  $\tau_s$  the spin relaxation time and  $\omega_L$  is the Larmor frequency.

Referring back to the exchange field model, a Hanle measurement in the presence of an exchange magnetic field  $B_{ex}$  by the magnetic moments would represent a spin precession due to a net field  $B_{app} + B_{ex}$ . The precession can result in a narrower Hanle shape due to an enhanced  $g$  factor [5, 14, 28] for a paramagnetic ordering of the localized moments. Whereas for the case of ferromagnetic ordering, we would expect a shifted Hanle peak.

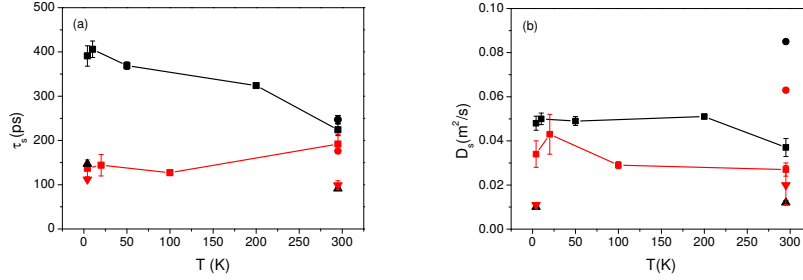


**Figure 6.5:** A summary of (a)  $\tau_s$  and (b)  $D_s$ , extracted from Hanle analysis, for sample A (square+line), B (triangle) and C (circle) before (black) and after (red) the functionalization. Black data corresponds to the pristine and red data is for the CoPP state of the samples. A reduced  $\tau_s$  and  $D_s$  were observed for the samples after the functionalization with a weak temperature dependence, which rules out any exchange coupling between the localized magnetic moments and the electron spins in graphene [28] and indicates towards an enhanced spin-flip process, where the present magnetic moments play only the role of spin-flip scatterers. The effect of the molecular layer is determined by the sample quality ( $\mu_e$ ,  $D$ ) in the pristine state. Since sample A and C have higher mobility and diffusion coefficient,  $\tau_s$  is highly reduced for these samples after the functionalization. Sample B, having lower mobility did not show any significant change in  $\tau_s$ .

Hanle precession curves for both pristine and CoPP devices are shown in Fig. 6.4. Here we show the purely spin dependent signal, obtained by subtracting the anti-parallel signal from the parallel signal and the result is fitted by the steady state solution to Eq. 6.2. The plots have been normalized to the value at  $B_{app}=0$  for clearly demonstrating the change in the Hanle line shape. We observe two general trends for all measured samples. First, the Hanle curve becomes broader after the CoPP self-assembly. This is in contrast to the expected narrowing of the Hanle curve in the presence of a paramagnetic exchange field according to the model described above. The observed broadening indicates a reduction of the spin relaxation time, in accordance with our interpretation of the signal reduction in spin-valve measurements. Second, upon decreasing the temperature from RT down to 4 K we do not observe any significant narrowing of the Hanle line shape which could be interpreted as an enhanced  $g$  factor. On the contrary, the typical line widths and extracted spin lifetimes are not strongly dependent on temperature.

A summary of the extracted spin parameters for all samples studied in this work is presented in Fig. 6.5. For sample A we observed the strongest effect of the molecular layer on the spin parameters. In its pristine state, the extracted spin relaxation time  $\tau_s$  is in the range of 300–400 ps for all the measured temperatures, with a corresponding spin diffusion length  $\lambda_s (= \sqrt{D_s \tau_s})$  3–4.5  $\mu\text{m}$ . On the other hand, after self-assembly sample A exhibited a strongly reduced  $\tau_s$  in the range 100–200 ps and

	4K				RT			
	pristine		CoPP		pristine		CoPP	
	Dc	Ds	Dc	Ds	Dc	Ds	Dc	Ds
A	0.052	0.048	0.039	0.034	0.100	0.037	0.050	0.027
B	0.010	0.010	0.011	0.010	0.014	0.012	0.020	0.020
C	–	–	–	0.12	–	0.085	–	0.063

**Table 6.1:** A summary of  $D_c$  and  $D_s$  (units in  $m^2/s$ ) for sample A, B and C, before (pristine) and after (CoPP) functionalization. For all the samples,  $D_c$  and  $D_s$  are approximately in the similar order. For sample A,  $D_c$  in the pristine state is found around  $0.05 m^2/s$ . We also sometimes observed an asymmetry in the Dirac curve at different temperatures. This asymmetry rises due to contact induced doping at different regions [29], resulting in a different value for  $D_c$  at different temperatures.

	4K		RT	
	pristine	CoPP	pristine	CoPP
sample A	391 ps	137 ps	310 ps	192 ps
sample B	147 ps	112 ps	92 ps	100 ps
sample C	–	189 ps	247 ps	176 ps

**Table 6.2:** A summary of  $\tau_s$  for sample A, B and C for the pristine and the CoPP device.

a correspondingly lower  $\lambda_s \sim 2\text{--}2.5 \mu\text{m}$ . Interestingly, we did not observe any significant temperature dependence for the extracted  $\tau_s$  in the measured temperature range, which would have otherwise been expected due to the presence of an effective exchange field via localized molecular paramagnetic moments [14, 28]. Therefore the added magnetic molecules seem to only increase the spin relaxation rate via the introduction of more spin-flip scattering events.

Furthermore, we also observed a minor reduction of the extracted spin diffusion coefficient  $D_s$  after self-assembly, consistent with the observed reduction in mobility as discussed in Fig. 6.2. Note that the reliability of a Hanle fit is typically established by comparing the agreement between the extracted spin diffusion coefficient  $D_s$  with the charge diffusion coefficient  $D_c$  [5, 14, 23]. The latter can be independently calculated via the resistivity of the sample at a known density of states  $\nu$  using the Einstein relation  $D_c = 1/R_{sq}e^2\nu$ . In the absence of electron-electron interaction  $D_c$  and  $D_s$  should match [30]. As shown in Table. 6.1 both parameters are in a reasonable agreement, confirming the validity of the the Hanle analysis.

It is worth mentioning that the earlier work of molecular doping on graphene [22] did not exhibit any measurable change in the spin transport properties of graphene, while the charge transport properties were modified. However, we find that sample quality, as determined by the magnitude of the diffusion coefficient ( $D_c$ ,  $D_s$ ) or electronic mobility ( $\mu_e$ ), plays an important role on the influence that the cobalt-porphyrin molecular layer exerts on the spin transport parameters. For example, for sample B we do not observe a significant change in  $D_s$  and  $\tau_s$  after self-assembly. This reduced sensitivity can be attributed to its low mobility (and diffusion coefficient) which in the pristine state was  $\sim 2000 \text{ cm}^2 \text{ V}^{-1} \text{ s}^{-1}$ , almost a factor of 3.5 times lower than for sample A. On the other hand, for sample C which had a comparatively better quality ( $D_s \sim 0.1 \text{ m}^2/\text{s}$ ) we again observed a significant reduction of 30 % on the spin relaxation time, confirming our initial observations.

A significant reduction in  $\tau_s$ , with a simultaneous moderate reduction in  $D_s$ , is inconsistent with the picture of localized magnetic moments creating an effective exchange field as discussed above [14, 28], or a model where localized states act as spin reservoirs [31]. Both models imply a significant increase of the extracted  $\tau_s$  and a proportionally reduced  $D_s$ , which can be understood via an enhanced  $g$  factor and the symmetry of the Hanle equation [5, 28]. Even for a reduced  $g$  factor, one would observe a reduced  $\tau_s$  and an enhanced  $D_s$ , which also does not comply with our observation. Furthermore, both models are also expected to show a strong temperature dependence, which is not observed here.

The reduction on the spin transport parameters indicates that the main role of the Co-porphyrin molecular layer is to act as an extra source of spin-flip scattering. This interpretation is consistent with the lack of sensitivity to the molecular layer by low-quality samples, where the initial spin relaxation rate was already large and therefore masks the relaxation process introduced by the molecular layer. In addition, the concomitant reduction in  $D_s$  and  $\tau_s$  observed can be partially understood by the enhanced momentum scattering introduced by the molecular layer, since in single layer graphene the leading spin relaxation mechanism is of the Elliot-Yafet type, which results in the proportionality relation  $\tau_s \propto D$  [32–34]. This observation is interesting, since previous experiments rule out the role of mobility dependence of  $\tau_s$  [22] or seem to observe an opposite relation between  $\tau_s$  and  $\mu_e$  i.e. higher spin lifetime for lower mobility samples [29].

## 6.4 Conclusions

To summarize, we observe a change both in the charge and spin transport properties of graphene in the presence of cobalt-porphyrin molecules. In the charge transport measurements, we observe an increase in the graphene sheet resistance after functionalization due to their interaction with graphene via weak Van der Waals forces.

For the spin transport measurements we observe lower values of  $\tau_s$  and  $\lambda_s$  for the CoPP-graphene system compared to the pristine one. The measurements are not strongly temperature dependent, which are not consistent with the presence of an exchange field and suggesting that the exchange interactions, if present, are random. At present, however, we cannot explicitly identify the origin, either due to exchange interaction or spin-orbit interaction, of the enhanced spin relaxation produced by the magnetic impurities. The changes are also sensitive to the sample quality ( $D, \mu_e$ ) in the pristine state and are masked for a lower value of the mobility or diffusion coefficient, indicating also the presence of Elliot-Yafet type spin relaxation mechanism.

## 6.5 Acknowledgements

We acknowledge J. G. Holstein, H. M. de Roosz and H. Adema for their technical assistance. We would like to thank M.H.D. Guimãraes and J.J. van den Berg for their help in sample preparation. This research work was financed under EU-graphene flagship program (637088) and supported by the Zernike Institute for Advanced Materials, the Ministry of Education Culture and Science (Gravitation program 024.601035,B.L.F.) and the Netherlands Organization for Scientific Research (NWO).

## References

- [1] V. K. Dugaev, E. Y. Sherman, and J. Barnaś, "Spin dephasing and pumping in graphene due to random spin-orbit interaction," *Phys. Rev. B* **83**, p. 085306, Feb. 2011.
- [2] H. Min, J. E. Hill, N. A. Sinitsyn, B. R. Sahu, L. Kleinman, and A. H. MacDonald, "Intrinsic and Rashba spin-orbit interactions in graphene sheets," *Phys. Rev. B* **74**, p. 165310, Oct. 2006.
- [3] M. Wojtaszek, I. J. Vera-Marun, E. Whiteway, M. Hilke, and B. J. van Wees, "Absence of hyperfine effects in 13c-graphene spin-valve devices," *Phys. Rev. B* **89**, p. 035417, Jan. 2014.
- [4] M. Guimarães, P. Zomer, J. Ingla-Aynés, J. Brant, N. Tombros, and B. van Wees, "Controlling spin relaxation in hexagonal BN-encapsulated graphene with a transverse electric field," *Phys. Rev. Lett.* **113**, p. 086602, Aug. 2014.
- [5] M. Wojtaszek, I. J. Vera-Marun, T. Maassen, and B. J. van Wees, "Enhancement of spin relaxation time in hydrogenated graphene spin-valve devices," *Phys. Rev. B* **87**, p. 081402, Feb. 2013.
- [6] R. R. Nair, M. Sepioni, I.-L. Tsai, O. Lehtinen, J. Keinonen, A. V. Krasheninnikov, T. Thomson, A. K. Geim, and I. V. Grigorieva, "Spin-half paramagnetism in graphene induced by point defects," *Nat. Phys.* **8**, pp. 199–202, Mar. 2012.
- [7] L. Xie, X. Wang, J. Lu, Z. Ni, Z. Luo, H. Mao, R. Wang, Y. Wang, H. Huang, D. Qi, R. Liu, T. Yu, Z. Shen, T. Wu, H. Peng, B. Özyilmaz, K. Loh, A. T. S. Wee, Ariando, and W. Chen, "Room temperature ferromagnetism in partially hydrogenated epitaxial graphene," *Appl. Phys. Lett.* **98**, p. 193113, May 2011.
- [8] P. Esquinazi, D. Spemann, R. Höhne, A. Setzer, K.-H. Han, and T. Butz, "Induced magnetic ordering by proton irradiation in graphite," *Phys. Rev. Lett.* **91**, p. 227201, Nov. 2003.
- [9] J. Červenka, M. I. Katsnelson, and C. F. J. Flipse, "Room-temperature ferromagnetism in graphite driven by two-dimensional networks of point defects," *Nat. Phys.* **5**, pp. 840–844, Nov. 2009.
- [10] X. Hong, S.-H. Cheng, C. Herding, and J. Zhu, "Colossal negative magnetoresistance in dilute fluorinated graphene," *Phys. Rev. B* **83**, p. 085410, Feb. 2011.
- [11] K. Pi, W. Han, K. M. McCreary, A. G. Swartz, Y. Li, and R. K. Kawakami, "Manipulation of spin transport in graphene by surface chemical doping," *Phys. Rev. Lett.* **104**(18), p. 187201, 2010.
- [12] C. Ertler, S. Konschuh, M. Gmitra, and J. Fabian, "Electron spin relaxation in graphene: The role of the substrate," *Phys. Rev. B* **80**, p. 041405, July 2009.
- [13] A. G. Swartz, J.-R. Chen, K. M. McCreary, P. M. Odenthal, W. Han, and R. K. Kawakami, "Effect of in situ deposition of Mg adatoms on spin relaxation in graphene," *Phys. Rev. B* **87**, p. 075455, Feb. 2013.
- [14] K. M. McCreary, A. G. Swartz, W. Han, J. Fabian, and R. K. Kawakami, "Magnetic moment formation in graphene detected by scattering of pure spin currents," *Phys. Rev. Lett.* **109**, p. 186604, Nov. 2012.
- [15] M. B. Lundeberg, R. Yang, J. Renard, and J. A. Folk, "Defect-mediated spin relaxation and dephasing in graphene," *Phys. Rev. Lett.* **110**, p. 156601, Apr. 2013.
- [16] D. Kochan, M. Gmitra, and J. Fabian, "Spin relaxation mechanism in graphene: Resonant scattering by magnetic impurities," *Phys. Rev. Lett.* **112**, p. 116602, Mar. 2014.
- [17] D. Soriano, D. V. Tuan, S. M.-M. Dubois, M. Gmitra, A. W. Cummings, D. Kochan, F. Ortman, J.-C. Charlier, J. Fabian, and S. Roche, "Spin transport in hydrogenated graphene," *2D Mater.* **2**, p. 022002, June 2015.
- [18] D. W. Boukhvalov and M. I. Katsnelson, "Destruction of graphene by metal adatoms," *Appl. Phys. Lett.* **95**, p. 023109, July 2009.
- [19] X. Zhang, E. H. Huisman, M. Gurrum, W. R. Browne, B. J. van Wees, and B. L. Feringa, "Supramolecular Chemistry on Graphene Field-Effect Transistors," *Small* **10**(9), pp. 1735–1740, 2014.
- [20] X. Zhang, *Graphene-based functional materials*. PhD thesis, University of Groningen, 2013.
- [21] C. F. Hermanns, K. Tarafder, M. Bernien, A. Krüger, Y.-M. Chang, P. M. Oppeneer, and W. Kuch, "Magnetic coupling of porphyrin molecules through graphene," *Adv. Mater.* **25**, pp. 3473–3477, July 2013.



- [22] W. Han, J.-R. Chen, D. Wang, K. M. McCreary, H. Wen, A. G. Swartz, J. Shi, and R. K. Kawakami, "Spin relaxation in single-layer graphene with tunable mobility," *Nano Lett.* **12**(7), pp. 3443–3447, 2012.
- [23] T. Maassen, I. J. Vera-Marun, M. H. D. Guimarães, and B. J. van Wees, "Contact-induced spin relaxation in hantle spin precession measurements," *Phys. Rev. B* **86**, p. 235408, Dec. 2012.
- [24] D. Wang, X. Liu, L. He, Y. Yin, D. Wu, and J. Shi, "Manipulating graphene mobility and charge neutral point with ligand-bound nanoparticles as charge reservoir," *Nano Lett.* **10**, pp. 4989–4993, Dec. 2010.
- [25] A. Veligura, P. J. Zomer, I. J. Vera-Marun, C. Józsa, P. I. Gordiichuk, and B. J. v. Wees, "Relating hysteresis and electrochemistry in graphene field effect transistors," *J. Appl. Phys.* **110**, p. 113708, Dec. 2011.
- [26] N. Tombros, C. Józsa, M. Popinciuc, H. T. Jonkman, and B. J. van Wees, "Electronic spin transport and spin precession in single graphene layers at room temperature," *Nature* **448**, pp. 571–574, Aug. 2007.
- [27] J. Fabian, A. Matos-Abiague, C. Ertler, P. Stano, and I. Zutic, "Semiconductor spintronics," *Acta Phys. Slov.* **57**, p. 565, 2007.
- [28] B. Birkner, D. Pachniowski, A. Sandner, M. Ostler, T. Seyller, J. Fabian, M. Ciorga, D. Weiss, and J. Eroms, "Annealing-induced magnetic moments detected by spin precession measurements in epitaxial graphene on SiC," *Phys. Rev. B* **87**, p. 081405, Feb. 2013.
- [29] F. Volmer, M. Drögeler, E. Maynicke, N. von den Driesch, M. L. Boschen, G. Güntherodt, C. Stampfer, and B. Beschoten, "Suppression of contact-induced spin dephasing in graphene/MgO/co spin-valve devices by successive oxygen treatments," *Phys. Rev. B* **90**, p. 165403, Oct. 2014.
- [30] C. P. Weber, N. Gedik, J. E. Moore, J. Orenstein, J. Stephens, and D. D. Awschalom, "Observation of spin coulomb drag in a two-dimensional electron gas," *Nature* **437**, pp. 1330–1333, Oct. 2005.
- [31] T. Maassen, J. J. van den Berg, E. H. Huisman, H. Dijkstra, F. Fromm, T. Seyller, and B. J. van Wees, "Localized states influence spin transport in epitaxial graphene," *Phys. Rev. Lett.* **110**, p. 067209, Feb. 2013.
- [32] C. Józsa, T. Maassen, M. Popinciuc, P. J. Zomer, A. Veligura, H. T. Jonkman, and B. J. van Wees, "Linear scaling between momentum and spin scattering in graphene," *Phys. Rev. B* **80**, p. 241403, Dec. 2009.
- [33] W. Han and R. Kawakami, "Spin relaxation in single-layer and bilayer graphene," *Phys. Rev. Lett.* **107**, p. 047207, July 2011.
- [34] T.-Y. Yang, J. Balakrishnan, F. Volmer, A. Avsar, M. Jaiswal, J. Samm, S. Ali, A. Pachoud, M. Zeng, M. Popinciuc, G. Güntherodt, B. Beschoten, and B. Özyilmaz, "Observation of long spin-relaxation times in bilayer graphene at room temperature," *Phys. Rev. Lett.* **107**, p. 047206, July 2011.

# Spin Relaxation 1/f Noise

### Abstract

Noise measurements are a powerful tool to probe the system dynamics. Studying the noise associated with spin accumulation can be helpful in understanding the very nature of the spin relaxation processes. More precisely, the 1/f noise associated with the spin accumulation can be helpful in understanding the electron spin-impurity interaction. In this chapter, I study 1/f type noise associated with electronic spin transport, using single layer graphene as a prototypical material with a large and tunable Hooze parameter. The presence of two contributions is identified to the measured spin-dependent noise: contact polarization noise from the ferromagnetic electrodes, and the noise originated from the spin relaxation processes. The noise magnitude for spin and charge transport differs by three orders of magnitude, implying different scattering mechanisms for the 1/f fluctuations in the charge and spin transport processes. A modulation of the spin-dependent noise magnitude by changing the spin relaxation length and time indicates that the spin-flip processes dominate the spin-dependent noise.

published as:  
S. Omar, M.H.D. Guimarães, A. Kaverzin,  
B.J. van Wees, and I.J. Vera-Marun  
*Phys. Rev. B* **95**, 081403(R) (2017).

## 7.1 Introduction

Noise in electronic transport is often treated as nuisance. However, it can have much more information than the average (mean) of the signal and can probe the system dynamics in greater detail than conventional DC measurements [1]. Low frequency fluctuations with a power spectral density (PSD) that depend inversely on frequency, also known as 1/f noise are commonly observed phenomena in solid state devices. A textbook explanation of the processes generating 1/f noise is given by the McWhorter model where traps are distributed over an energy range, leading to a distribution of characteristic time scales of trapping-detrapping processes of the electrons in the transport channel and causing slow fluctuations in conductivity [2–4].

Graphene is an ideal material for spin transport due to low spin-orbit coupling and small hyperfine interactions [5, 6]. However, the experimentally observed spin relaxation time  $\tau_s \sim 3$  ns and spin relaxation length  $\lambda_s \sim 24$   $\mu$  m are [7] lower than the theoretically predicted  $\tau_s \sim 100$  ns and  $\lambda_s \sim 100$   $\mu$  m [8, 9]. There are a number of experiments and theories suggesting that the charge and magnetic impurities present in graphene might play an important role for the lower value of observed spin relaxation time [10–14]. It is an open question whether these impurities affect the spin transport in a similar way as the charge transport, or if the scattering mechanisms in both processes behave differently. For electronic transport in graphene, the effect of impurities can be studied via 1/f noise measurements. In a similar line, measuring low frequency fluctuations of the spin accumulation can unravel the role of impurities on the spin transport.

7

## 7.2 Sample Preparation

We use graphene as a prototypical material for measuring the spin-dependent noise associated with the spin signal. Graphene is mechanically exfoliated from a highly oriented pyrolytic graphite (HOPG) ZYA grade crystal onto a pre-cleaned Si/SiO<sub>2</sub> substrate (300 nm thick SiO<sub>2</sub>), where n<sup>++</sup> doped Si is used as a back gate electrode. Single layer graphene flakes were identified using optical contrast. Ferromagnetic contacts are patterned via electron beam lithography on the PMMA (poly (methyl methacrylate)) coated graphene flake. Then, 0.8 nm of titanium (Ti) is deposited in two steps, each step of 0.4 nm of Ti deposition followed by in-situ oxidation by pure O<sub>2</sub> to form an oxide tunnel barrier to overcome the conductivity mismatch problem [15]. On top of the oxide barrier we deposit 35 nm of cobalt for the spin selective contacts. To prevent oxidation of the ferromagnetic electrodes, the contacts are covered with 3 nm thick aluminum (Al) layer. Since we use the cross correlation (XC) method in order to eliminate the noise from external electronics, the contact are designed on

both sides of the FM electrodes, as shown in Fig. 7.1.

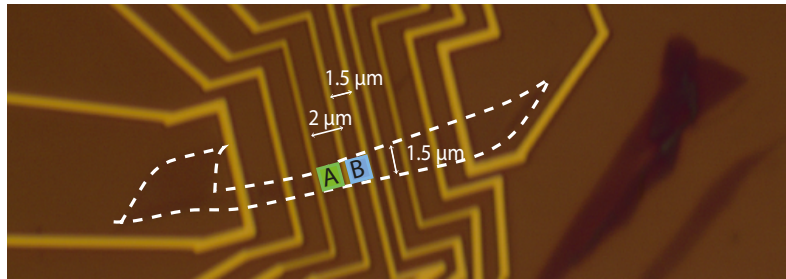


**Figure 7.1:** contacts are designed on both sides of the electrodes. An optical picture of the sample of single layer graphene (white dotted line) connected via FM electrodes. Noise measurements are done in two regions of the sample, labeled A ( $l=2 \mu\text{m}$ ,  $w=1.5 \mu\text{m}$ ) and B ( $l=1.5 \mu\text{m}$ ,  $w \sim 1.5 \mu\text{m}$ )

### 7.3 Setup

In order to measure the electrical noise from the sample, we use a dynamic signal analyzer from Stanford Research System (model SR785) which can acquire and analyze two channel signal measurements (i.e. cross correlation) in time domain and convert it into a frequency domain signal via the Fast Fourier Transform (FFT) algorithm. The input signal is digitized at a high sampling rate (262 kHz). The acquisition time and the frequency resolution is set by the number of samples and the frequency range. Further we also perform root mean square averaging over the recorded FFT spectra. So the total acquisition time is  $N * t_{acq}$ , where N is the no. of averaging performed on the data.

Now, we describe the noise measurement scheme in detail. Since, the signal of interest, i.e., the noise from the sample, can be very small ( $\approx$  nano volts), we need to amplify the signal with the low noise preamplifiers (from NF corporation (Gain-100x) specified noise floor  $\approx 2 \text{ nV}/\sqrt{\text{Hz}}$ ) over the noise level of the spectrum analyzer. Note that there is an additional noise introduced in the measurement during every amplification and input step. To estimate the sample noise correctly, it is necessary to know the noise contribution from each step individually for the single channel measurement.

Noise contribution from the spectrum analyzer (SA) can be estimated by the scheme illustrated in Fig. 7.2(a). If no input voltage/signal is applied to the SA, signal appearing at the output will only be due to the noise at the input.

As can be seen in Figure 7.3, the noise output changes with the gain of the input stage amplifier. The total noise can be factorized in two components: **i)** gain

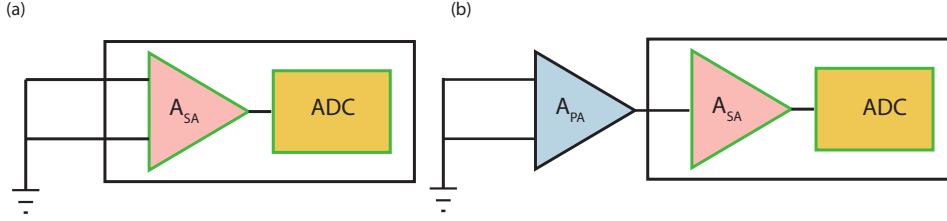


**Figure 7.2:** The schematic inside the rectangle represents the signal flow path for a single channel inside the spectrum analyzer. Input voltage of the differential amplifier at the input stage is set to zero in order to measure the noise in the channel. (b) The schematic represents the noise measurement circuit for the preamplifier, integrated with the spectrum analyzer. In the cartoon,  $A_{PA}$  represents the gain of the preamplifier. Voltage input to the preamplifier is made zero in order to measure the noise from the circuit.

dependent component and **ii)** gain independent component. Estimation of both the components can be done by:

$$V_{SA}^2 = \frac{A_{SA}^2 V_d^2 + V_{id}^2}{A_{SA}^2} \quad (7.1)$$

where  $A_{SA}$  is the SA input stage gain,  $V_d$  is the gain dependent and  $V_{id}$  is the gain independent input noise component ( $V/\sqrt{\text{Hz}}$ ).  $V_d$  and  $V_{id}$  can be estimated by a linear fit which gives  $V_d \approx 8 \text{ nV}/\sqrt{\text{Hz}}$  and  $V_{id} \approx 300 \text{ nV}/\sqrt{\text{Hz}}$ .

After knowing the noise contribution from the SA, we can use the same idea to estimate the noise floor of the preamplifiers. We short the inputs of the preamplifiers using the connection scheme shown in Fig. 7.2(b).

Now the total noise is given by:

$$V_{\text{total}}^2 = \frac{A_{PA}^2 V_{PA}^2 + V_{SA}^2}{A_{PA}^2} \quad (7.2)$$

Here  $A_{PA}$  is the gain of preamplifier (100),  $V_{PA}$  is the noise ( $V/\sqrt{\text{Hz}}$ ) of the preamplifier,  $V_{SA}$  is the noise contribution from the spectrum analyzer (Eq. 7.1) and  $V_{\text{total}}$  is the net measured noise.

We measure the noise of the preamplifier at different input gains ( $A_{SA}$ ) of the spectrum analyzer (Fig. 7.4). At high gain of the SA input stage, we get the correct value for the preamplifier noise floor due to the dominance of the external preamplifier noise. At low input gain, the internal noise of the spectrum analyzer dominates. Estimated noise voltage of the preamplifier was around  $1.5 \text{ nV}/\sqrt{\text{Hz}}$  which is below the value given by the manufacturer ( $2 \text{ nV}/\sqrt{\text{Hz}}$ ).

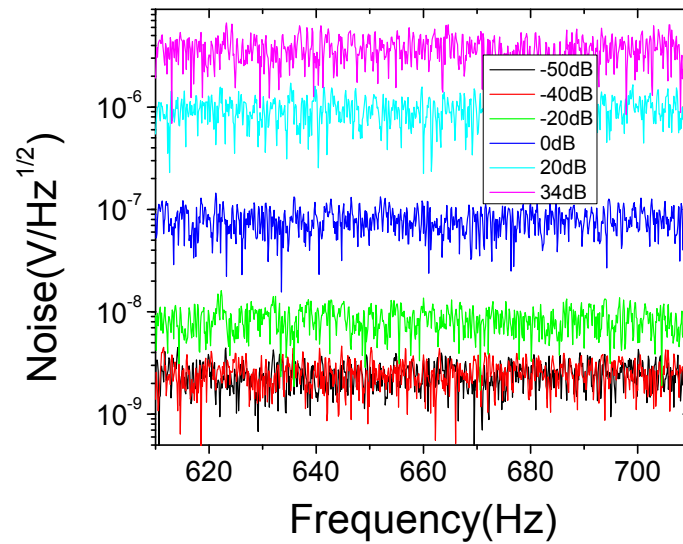


**Figure 7.3:** Noise appearing in a single channel at different gain values of the input stage amplifier for the connection scheme of Fig. 7.2(a)

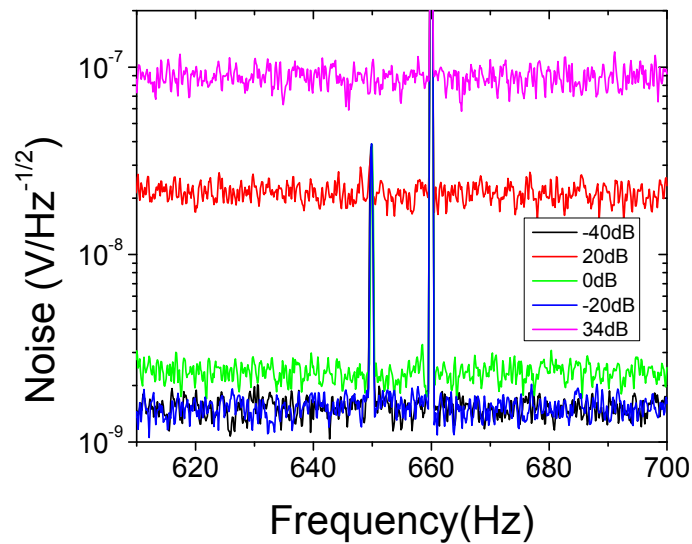


**Figure 7.4:** Total noise (from SA+preamplifiers) of the circuit shown at different gains of the input stage amplifiers for the connection scheme of Fig. 7.2(b).

In order to exclude the noise appearing on the independent paths (ch1 and ch2) at the input stage amplifiers, we can use the XC technique. Here, we short the inputs of

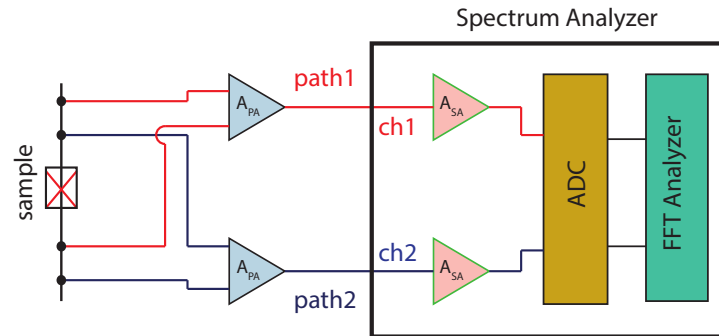


**Figure 7.5:** The XC connection scheme for the sample (shown as a box with red cross) noise measurements. Here, the voltage fluctuations from the sample are recorded independently via two paths : path 1 (red) and path 2 (blue). In each path, the noise from the sample is amplified with a low noise preamplifier with the gain  $A_{PA}$ . The amplified signal is fed to two independent input channels ch1 and ch2 at the SA. The signal is again amplified ( $A_{SA}$ ) with the input stage amplifiers of the SA and then digitized via an Analog-to-digital converter (ADC). The digital signals from ch1 and ch2 are then converted into the frequency domain signals via the Fast Fourier Transform (FFT) algorithm. Later, the mathematical analysis function such as auto-correlation or cross-correlation are performed on these FFT signals to remove the contribution of the independent noise sources in each path.

7

both ch1 and ch2 and perform the cross-correlation analysis on the signals at ch1 and ch2. The XC analysis allows to filter out the independently fluctuating noise sources such as the noise from the preamp and the input stage amplifiers, and we only see the noise which is common to the cross-correlation path. Using the same scheme as described in Fig. 7.2(a), we obtain the noise spectra at different  $A_{SA}$  values with zero input voltage at ch1 and ch2. Using Eq.7.1 again, we get  $V_d \approx 2 \text{ nV}/\sqrt{\text{Hz}}$  and the  $V_{id} \approx 77 \text{ nV}/\sqrt{\text{Hz}}$  which clearly shows the power of this technique to suppress the uncorrelated noise.

Knowing the noise contribution from various parts of our setup, we can estimate the signal of interest buried in the total signal by subtracting the setup noise contribution. In order to calibrate our setup we perform the standard thermal noise measurement of resistors at room temperature (293 K), which is given by Eq.4.2. Using the measurement scheme shown in Fig. 7.5, we can do a single channel or cross-correlation measurement.

In a single channel measurement, we have to subtract the noise contribution from the preamplifier and the spectrum analyzer in the total signal. The total noise is

given by:

$$V_{\text{total}}^2 = (A_{\text{PA}} V_s)^2 + (A_{\text{PA}} V_{\text{PA}})^2 + V_{\text{SA}}^2 \quad (7.3)$$

where  $V_{\text{PA}}$  and  $V_{\text{SA}}$  are obtained by Eq.7.2 and Eq.7.1 respectively.  $V_s$  is the signal, we want to measure, i.e., the thermal noise from the resistance. A single channel measurement of the sample resistance provides a good estimation of the thermal noise down to  $1\text{k}\Omega$  (Figure 7.6), which is of the order of the noise introduced by the preamplifier. Therefore, the total noise in the single channel measurement is limited by the noise of the noisiest source in the measurement path.

In order to exclude the noise from the uncorrelated setup components such as preamplifiers and the SA input stage, we can use the XC technique to extract the signal of interest directly without any estimation. As it can be seen in Fig. 7.6, the thermal noise of the different resistors obtained from the XC analysis are more accurate than the single channel measurement. The XC technique can measure the noise value down to  $0.7\text{ nV}/\sqrt{\text{Hz}}$  which is equivalent to the thermal noise of a resistance of  $\approx 50\ \Omega$ .

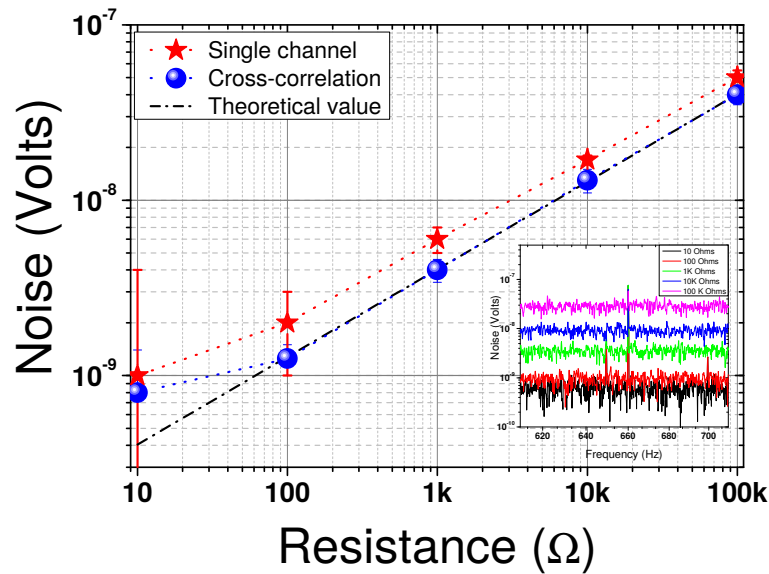


**Figure 7.6:** Thermal noise measured for different resistor values. The noise values extracted from the single channel measurement (red stars) deviate more from the theoretical value (dashed black line) compare to the noise values measured the via cross-correlation method (blue spheres).



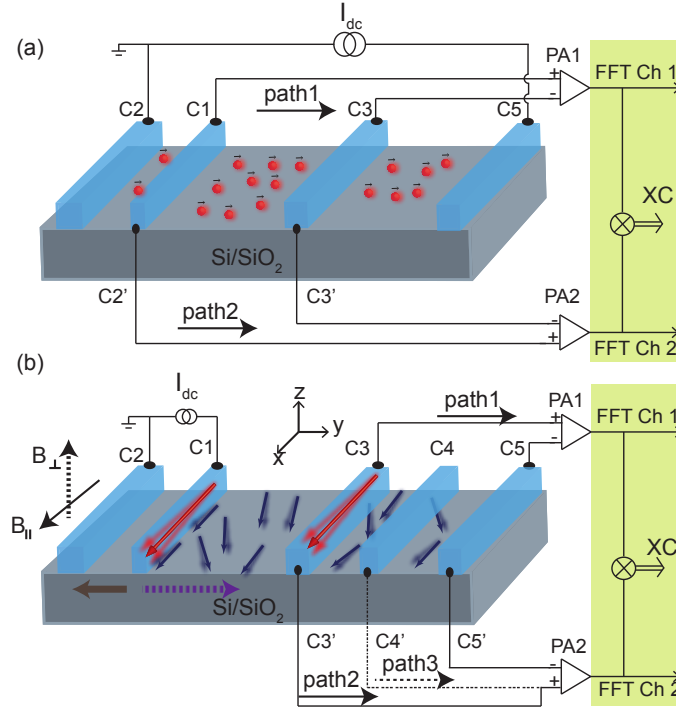


**Figure 7.7:** (a) Cross correlation (XC) connection scheme for local charge noise measurement and (b) non-local spin-dependent noise measurements. A connection scheme for spatial cross correlation (SXC) is also shown where the XC analysis is performed over the voltage measured between contacts C3-C5 ( $V_{NL}^{C3-C5}$ , path1) and contacts C4-C5 ( $V_{NL}^{C4-C5(C4'-C5')}$ , path 3).

## 7.4 Results

For the noise measurements, we record 800 samples in one spectrum at a high sampling frequency (262 kHz) and measure the 1/f noise in the frequency range of 25 Hz with the resolution of 31.2 mHz. The final spectrum is recorded after performing the root mean square averaging over 20 FFT spectra.

### 7.4.1 Charge 1/f Noise

The 1/f noise of the charge transport in graphene is measured in a local four probe scheme, similar to the charge transport measurements (Fig. 7.7(a)). A dc current is applied between the ferromagnetic injectors C2 and C5. Since the contacts are designed lithographically on both sides of the ferromagnetic electrode, the fluctuations in the voltage drop  $V_{local}$  across the flake can be measured via the contact pair C1-C3

(path 1) and C1'-C3' (path 2). The measured signals are cross correlated in order to filter out the noise from external electronics such as preamplifiers and the spectrum analyzer [16]. The electronic  $1/f$  noise  $S_V^{\text{local}}$  is measured at different bias currents ( $I_{\text{dc}}$ ) at a fixed carrier density.

For the local charge noise measurements,  $1/f$  noise in Fig. 7.8 nicely scales with  $I_{\text{dc}}^2$ , implying that we are only sensitive to the  $1/f$  noise fluctuations from the flake and the current source is not introducing the frequency dependent fluctuations from the contact through capacitive coupling.

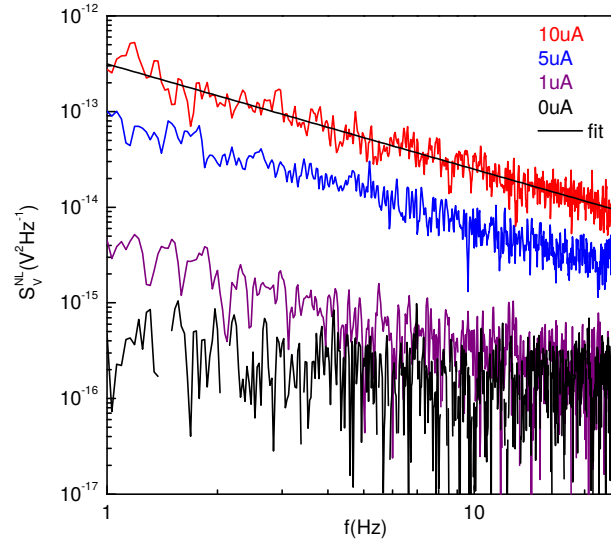


**Figure 7.8:**  $1/f$  noise of the flake is measured in a local four terminal geometry (Fig. 7.7(a))

By fitting the spectrum with the Hooge formula for  $1/f$  noise i.e.  $S_V^{\text{local}} = \frac{\gamma^c V_{\text{local}}^2}{f^a}$ , where  $V_{\text{local}}$  is the average voltage drop across the flake and  $a$  is the exponent  $\sim 1$ , we obtain the noise magnitude for the charge transport  $\gamma^c \sim 10^{-7}$  (device A in Fig. 7.1), similar to the values reported in literature [17–19]. The charge noise magnitude is defined as the Hooge parameter  $\gamma_H^c$  divided by the total number of carriers in the transport channel, i.e.  $\gamma^c = \gamma_H^c / (n * W * L)$ . Here  $n$  is charge carrier density,  $W$  and  $L$  are the width and length of the transport channel.  $\gamma^c$  depends both on the concentration and the type of scatterers e.g. short range and long range scatterers [17–21]. Now, we would like to briefly explain the case when the contact noise dominates over the channel noise. In the case of contact noise as a dominant noise source, the impedance of the current source becomes equivalent to the contact resistance at higher frequencies ( $\sim \geq 10$  MHz) due to capacitive coupling, and, the noise in the

injected spin current can come from the fluctuating contact resistance. In this case, the noise would increase at higher frequencies. On the other hand, we observe the opposite frequency dependence for the measured noise going down at higher frequencies complying with the  $1/f$  noise behavior, and the noise is measured at very low frequencies where the impedance of the current source is almost constant and is much higher than the contact resistance, ruling out the effect of the contact noise on the measured signal.

### 7.4.2 Spin-dependent 1/f Noise

The spin-dependent  $1/f$  noise can be expressed as:

$$\Delta S_V^{\text{NL}} = \frac{\gamma^s \Delta V_{\text{NL}}^2}{f^a} = \frac{\gamma^s (P\mu_s/e)^2}{f^a} \quad (7.4)$$

Here  $\Delta S_V^{\text{NL}}$  is the spin-dependent non-local noise,  $\gamma^s = \gamma_{\text{H}}^s / (n * W * \lambda_s)$  is the noise magnitude for spin transport,  $e$  is the electronic charge and  $\Delta V_{\text{NL}} = P\mu_s/e$  is the measured non-local spin signal due to the average spin accumulation  $\mu_s$  in the channel<sup>1</sup>. Here  $\gamma_{\text{H}}^s$  represents the Hooge parameter for spin transport. In contrast with the charge current, spin current is not a conserved quantity and exists over an effective length scale of  $\lambda_s$ .

Spin transport in a non-local geometry is realized in three fundamental steps: i) spin current injection, ii) spin diffusion through the transport channel and iii) detection of the spin accumulation. All these steps can contribute to the spin-dependent noise. For the first step of spin injection, we use a dc current source to inject spin current, which helps to eliminate the resistance fluctuations in the injector contact, leaving only the polarization fluctuations of the injector electrode as a possible noise source. The polarization fluctuations of the injector can arise due to thermally activated domain wall hopping/rotation in the ferromagnet [22, 23]. The second possible noise source contributing to the fluctuations in the spin accumulation is the transport channel itself, either via the fluctuating channel resistance or via fluctuations in the spin-relaxation process. The third noise source, similar to the first one, can be present at the detector electrode due to fluctuating contact polarization.

The spin-dependent noise in graphene is measured non-locally as shown in the connection diagram of Fig. 7.7(b). A dc current  $I_{\text{dc}}$  is applied between C1 and C2 and a nonlocal noise between C3 and C5 is measured via path 1 and path 2, using XC method. During the noise measurement, we keep the spin injection current  $I_{\text{dc}}$  fixed ( $10\mu\text{ A}$ ) and change the detected spin accumulation in three different ways. At  $B_{\perp} = 0\text{ T}$ , i) by changing the spin accumulation by switching the relative magnetization direction of the injector electrodes, ii) by keeping the spin accumulation constant

<sup>1</sup>variables  $V_{\text{local}}$ ,  $\Delta V_{\text{NL}}$ ,  $\mu_s$ ,  $P$ ,  $\lambda_s$  represent the time average of the quantities

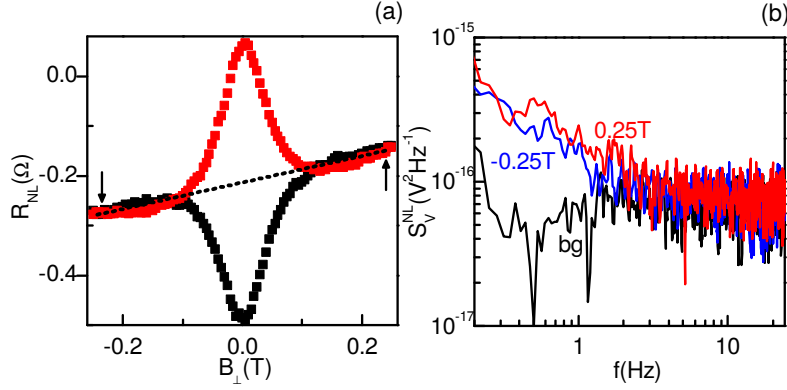


**Figure 7.9:** (a) Hanle precession measurements for parallel [ $\uparrow\uparrow$ ] and the anti-parallel [ $\uparrow\downarrow$ ] magnetization of the inner injector and the detector electrodes. The background signal is denoted by black dash line (b) Non-local noise measurement for  $B_{\perp}$  at -0.25 T and 0.25 T corresponding to the black vertical arrows in the Hanle curve. Here, the signal labeled as 'bg' (black) is the background thermal noise.

and changing the spin detection sensitivity by switching the relative magnetization direction of detector electrodes, and iii) at  $B_{\perp} \neq 0$  T, by dephasing the spins during transport and thus reducing the spin accumulation. We can also measure the noise due to a spin independent background signal at high  $B_{\perp} \sim 0.12$  T, where the spin accumulation is suppressed. In order to confirm that the magnetic field dependence of the measured noise is not originated by the non-local background, we measure the non-local noise at high positive and negative perpendicular magnetic fields ( $B_{\perp} \sim 0.25$  T and -0.25 T) where no spin accumulation is present (Fig. 7.9(a)). the non-local signal is different due to different background MR (dashed line in Fig. 7.9(a)). However, we do not observe any difference in the noise level for high positive and negative  $B_{\perp}$ , confirming that there is no detectable noise contribution from the non-local background MR signal (Fig. 7.9(b)).

The spin-dependent component  $\Delta S_V^{NL}$  can be estimated by subtracting  $S_V^{NL}$  (at  $B_{\perp} \sim 0.12$  T) from the measured  $S_V^{NL}$ . For the non-local noise measurements in spin valve configuration, the noise PSD measured (Fig. 7.10(c)) for the magnetization configuration corresponding to a higher spin accumulation (level II; blue spectrum) is higher in magnitude than for the one corresponding to a lower spin accumulation (level I; red spectrum) of the spin valve in Fig. 7.10(a). In a similar way for the Hanle configuration, we measure the maximum magnitude of the spin-dependent noise for  $B_{\perp} = 0$  T, corresponding to maximum spin accumulation (Fig. 7.10(d)). On increasing  $|B_{\perp}|$ , both the spin accumulation and the associated noise are reduced. In order to study its dependence with the spin accumulation, we fit each measured spectrum

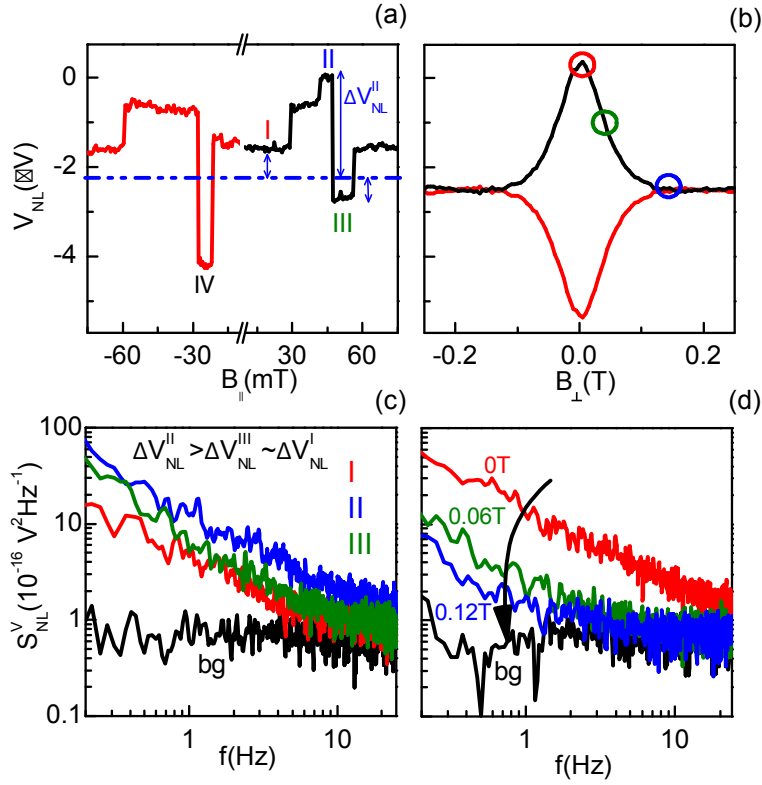


**Figure 7.10:** (a) Non-local spin valve measurement. The dot-dash line represents the background level, which is estimated from the Hanle measurement.  $\Delta V_{NL}$  is defined as the spin accumulation above or below with respect to the background level. (b) Hanle measurement is shown for the level II and level IV of the spin valve. (c) noise PSD measured for the magnetization configurations corresponding to level I, II and III in the spin-valve measurement in Fig. 7.10(a). (d) the PSD plot for the Hanle configuration obtained at different magnetic fields, corresponding to the circles indicated in Fig. 7.10(b). In Fig. 7.10(c) and (d), ‘bg’ represents the zero current background thermal noise.

of  $S_V^{NL}$  versus frequency, obtained at different spin accumulation values ( $\Delta V_{NL}$ ) with Eq. 7.4 in the frequency range of 0.5-5 Hz. We take the value of  $S_V^{NL}$  at  $f = 1$  Hz from the fit as a representative value of the  $1/f$  spectrum. The exponent  $a$  obtained from the fit is  $\sim 1$ . A summary of the data points for the noise PSD at different values of spin accumulation, obtained for device A using Hanle precession is plotted in Fig. 7.11(a). The  $\Delta S_V^{NL} \propto \mu_s^2$  relation is valid in the lowest order approximation. The parabolic fit of the measured non local noise using Eq. 7.4 gives  $\gamma^s \sim 10^{-4}$ .

## 7.5 Discussion

Via charge and spin-dependent  $1/f$  noise measurements for the same transport channel, we achieve  $\gamma^s \sim 10^{-4} \text{ Hz}^{-1}$  which is surprisingly  $10^3$  times higher than  $\gamma^c \sim 10^{-7} \text{ Hz}^{-1}$ . Certainly, the geometrical factors such as length scales cannot be accounted for such a huge difference, as for this sample we obtain  $\lambda_s \sim 1.5 \mu\text{m}$  which is similar to the channel length for charge  $1/f$  noise. The three orders of magnitude enhanced  $\gamma^s$  points towards distinctive scattering processes affecting the spin dependent noise, in contrast to the charge  $1/f$  noise. One possible explanation could be found along the direction of the recently proposed resonant scattering mechanism [12] for spin transport where intrinsically present magnetic impurities strongly scatter the spins without a significant effect on the charge scattering strength. The scattering cross section of these impurities can fluctuate in time and could give rise to a spin dependent  $1/f$  noise.

Now, we qualitatively analyze the possible noise sources, contributing to the spin-dependent noise and their dependence on the spin-transport parameters. An analytical expression for the spin-dependent noise (at  $f = 1 \text{ Hz}$ ) which is derived from the equation for the non-local spin signal  $\Delta V_{\text{NL}}$  (see subsec. 7.5.3 for complete derivation) can be written as:

$$\frac{\Delta S_V^{\text{NL}}}{\Delta V_{\text{NL}}^2} = \gamma^s \simeq \frac{S_P}{P^2} + \frac{S_{\lambda_s}}{\lambda_s^2} \left(1 + \frac{L}{\lambda_s}\right)^2 \quad (7.5)$$

where  $S_P$  is the contact polarization noise which is Fourier transform of the auto correlation function for the time dependent polarization fluctuations i.e.  $\mathcal{F}\langle P(t)P(t + \tau) \rangle$ ,  $S_{\lambda_s}$  is the noise associated with the spin transport i.e. spin relaxation noise ( $\mathcal{F}\langle \lambda_s(t)\lambda_s(t + \tau) \rangle$ ),  $L$  is the separation between the inner injector and detector electrodes. Eq. 7.5 suggests that  $\gamma^s$  is increased for lower values of  $\lambda_s$ . In order to confirm that the spin-dependent noise is affected by the spin transport properties, we measure  $S_V^{\text{NL}}$  as a function of the back-gate voltage (carrier density). In agreement with literature [24, 25], a higher  $\tau_s$  is observed at higher charge carrier densities for single layer graphene (Fig. 7.11(c)). The representative data is shown for device B. It is worth emphasizing here that for similar charge and spin transport parameters ( $R_{\text{sq}}, \lambda_s$ ) for device A ( $350 \Omega, 1.8 \mu\text{m}$ ) and device B ( $400 \Omega, 1.6 \mu\text{m}$ ), we obtain similar values of  $\gamma^s \sim 10^{-4}$ . However, both devices have different values of contact polarization. For device A,  $P \sim 5\%$  and for device B,  $P \sim 10\%$ . This similarity in  $\gamma^s$  values despite the difference in  $P$  indicates that there is insignificant contribution of the contact polarization noise to the extracted  $\gamma^s$ . On the other hand, for the noise measurements at different carrier densities, we get an increase in  $\gamma^s$  at lower values of  $\tau_s$  (Fig. 7.11(d)). The carrier density dependent behavior of the extracted  $\gamma^s$  is in qualitative agreement with the  $\lambda_s$  dependence of  $\gamma^s$  in Eq. 7.5 (red curve in Fig. 7.11(d)), supporting our hypothesis that the measured spin-dependent noise is dominated by

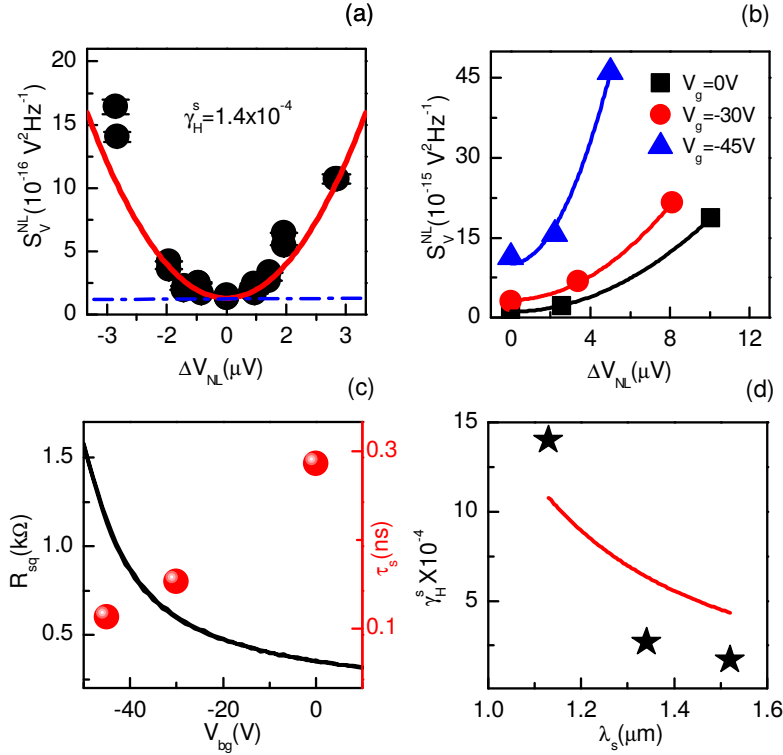


**Figure 7.11:** (a) summary of noise measured for different spin accumulation potentials in Hanle configuration (device A) and the parabolic fit for the data (red line) using Eq. 7.4. Here blue dotted line denotes the spin independent charge noise background i.e.  $S_V^{NL}$  (at  $B_{\perp} \sim 0.12\text{T}$ ) (b) Spin dependent 1/f noise in Hanle configuration, measured as a function of back-gate voltage (device B). The increased background noise at  $\Delta V_{NL}=0 \text{ V}$  can come from the charge noise contribution to the non-local signal ( $S_{1/f}^V \propto I^2 R_{sq}^2$ ). (c) The graphene sheet resistance increases at negative back-gate voltage reflecting the n-type doping in graphene and the spin relaxation time (red circles) decreases at lower carrier density for the single layer graphene, resulting in lower value for  $\lambda_s$ . (d)  $\gamma^s$  is increased for lower value of  $\lambda_s$  ( $\tau_s$ ) (black stars), indicating the influence of the spin-flip processes on the extracted noise magnitude for spin transport. A plot of  $\gamma^s$  versus  $\lambda_s$  with Eq. 7.5 (red curve) shows similar behavior. For the plot, we assume the polarization noise (offset) to be zero, the values for  $L = 1.5 \mu\text{m}$  and  $S_{\lambda_s} \sim 10^{-16} \text{ m}^2 \text{ Hz}^{-1}$

the noise produced by the spin transport (relaxation) process in graphene.

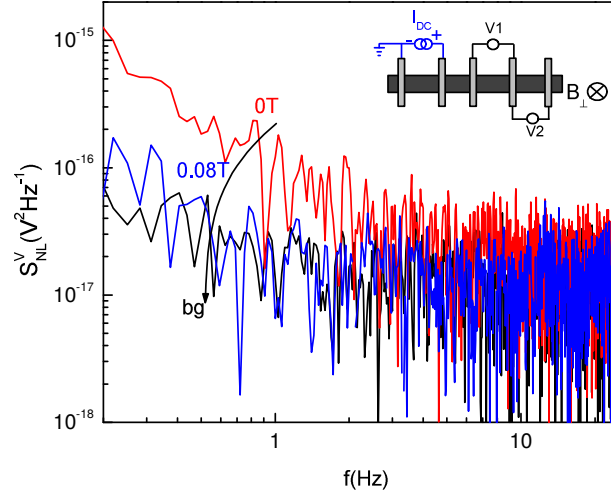


**Figure 7.12:** Contact polarization noise measured for contact C4 at  $B = 0$  T (red) and at  $B = 80$  mT. For the current injection at C1-C2, the spin-dependent noise between contacts C3-C4 and C4-C5 are cross correlated and only the noise at C4 is measured. For  $B_{\perp} \sim 80$  mT, the polarization noise is reduced to the background noise in the absence of the spin accumulation underneath the contact. The connection scheme is shown in the inset.

### 7.5.1 Estimation of Contact Polarization Noise

We check the possibility whether the contact polarization noise is a dominant source of the spin-dependent noise. We measure the contact polarization noise ( $=S_P/P^2 \times \Delta V_{NL}^2 \sim 10^{-16} \text{ V}^2\text{Hz}^{-1}$ ) separately by cross correlating the noise measured from the detector pairs C3-C4 and C4-C5, while C1 and C2 are the current injectors. Here only the noise from contact C4 is measured for different values of  $B_{\perp}$  (spin accumulation) underneath the contact. We clearly see the spin-dependent noise (contact polarization noise in this case) is reduced to the background noise at  $B_{\perp} \sim 80$  mT, where spin accumulation is suppressed (Fig. 7.12). The polarization noise is  $\sim 10^{-16} \text{ V}^2\text{Hz}^{-1}$  (at 1 Hz), which is negligible compared to the measured spin relaxation noise i.e.  $\sim 10^{-14} \text{ V}^2\text{Hz}^{-1}$ . Here, based on the reciprocity argument for the injector and detector in spin-valve configuration, we can assume equal noise contribution from the injector electrode and can safely rule out the effect of the polarization noise.



## 7.5.2 Spatial Cross-correlation Measurements for Extracting Spin-transport Parameters

In order to estimate/filter out the contribution of the contact polarization noise in our measurements, we use the spatial cross-correlation (SXC) method.

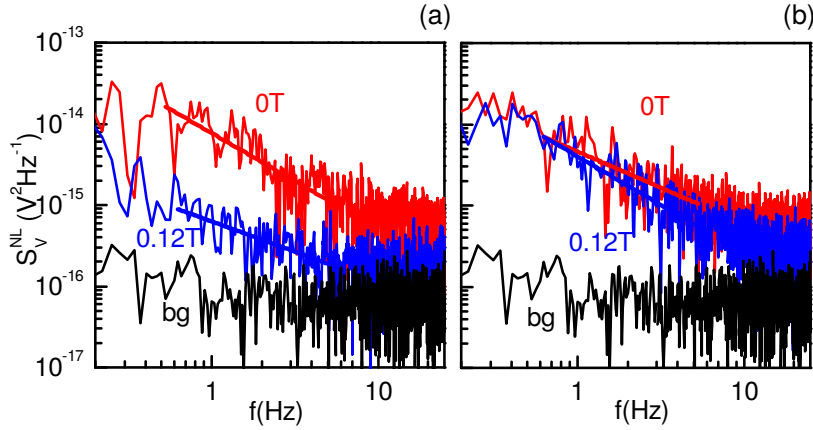


**Figure 7.13:** SXC noise (spin relaxation noise) measured at contact C4 at (a)  $V_g=0V$  and (b)  $V_g=-45V$ , for different magnetic fields. The spin relaxation noise at C4 for  $V_g=-45V$  is lower due to reduced spin transport parameters.

A measured non-local noise at the detector ( $S_{NL}^V$ ) in the presence of spin-accumulation (spin-current) can be represented by Eq. 7.6:

$$S_{NL}^V = S_P^{C1} + S_P^{C2} + S_{\lambda_s}^{C1-C2} + S_{bg} \quad (7.6)$$

Here  $S_P^{C_i}$  is the contact polarization noise,  $S_{\lambda_s}$  is the noise due to spin accumulation (relaxation) between contacts C1-C2 and  $S_{bg}$  is the electronic noise contribution due to residual charge current flowing in the non-local circuit and the thermal noise background.  $S_{bg}$  does not carry any spin-dependent information. On applying a high magnetic field  $B_{\perp} \sim 0.1$  T, perpendicular to the device plane, one can suppress the spin transport and the measured non-local noise contribution at high  $B_{\perp}$  can come from the background charge 1/f noise ( $S_{bg}$ ) due to non-homogeneous charge current distribution in the non-local regime. In this way the spin-dependent noise (polarization and spin accumulation) can be separated from the total noise.

Polarization fluctuations in each contact are independent from each other and one can filter the polarization noise from the spin current noise by using the spatial XC method. We measure the non-local noise via XC scheme as shown in Fig. 7.7(b). Simultaneously we also record the single channel noise for contact pair C3-C5 (path

1) and C4-C5 (path 3). Single channel noise includes the polarization noise contribution of the contact pair on top of the spin relaxation noise between the contacts. These contributions can be summarized in following equations:

$$S_{NL}^{channel1} = S_P^{C3} + S_P^{C5} + S_{\lambda_s}^{C3-C5} \quad (7.7)$$

$$S_{NL}^{channel2} = S_P^{C4} + S_P^{C5} + S_{\lambda_s}^{C4-C5} \quad (7.8)$$

$$S_{XC}^{C3-C5 \otimes C4-C5} = S_{\lambda_s}^{C3-C5} + S_P^{C5} \quad (7.9)$$

Note that we have not included the background noise contribution term here as it can be estimated separately at  $B_{\perp} \sim 0.1$  T via the procedure described above and the final equations can be rewritten without the background contribution. On the other hand, the spatial cross correlation of  $V_{C3-C5}$  and  $V_{C4-C5}$  will have total noise contribution  $S_{XC}^{C3-C5 \otimes C4-C5}$  only from the outer detector C5 ( $S_P^{C5}$ ) and the spin relaxation noise  $S_{\lambda_s}^{C4-C5}$ .

Since the spin accumulation  $\mu_s \propto \exp(-L/\lambda_s)$ , the spin relaxation noise is also expected to decay exponentially in accordance with the relation  $\Delta S_V^{NL} \propto \mu_s^2$ . We extend our analysis to study the distance dependence of the spin relaxation noise. With the spatial cross-correlation we can also measure the spin relaxation noise between the detector contacts C4 and C5 while removing the polarization noise from contact C4. For this, we measure the spin-dependent noise at different detector contacts via path 1 and path 3 in Fig. 7.7(b) independently, and cross correlate the measured signals.

The polarization noise contribution from the reference detector C5 is expected to be negligible due to the lower value of spin accumulation at the contact ( $L_{C1-C5}/\lambda_s \sim 4$ ). We measure  $\Delta S_V^{NL}$  at the detectors C3 and C4 for two back-gate voltages: at  $V_g = 0$  V (metallic regime) and at  $V_g = -45$  V (close to the Dirac point) (Fig. 7.13).

Using the derived Eq. 7.5, we can now calculate  $\lambda_s$  from the noise measurement as:

$$\frac{S_{\lambda_s}^{C3}}{S_{\lambda_s}^{C4}} \simeq \left( \exp \frac{L^{C3-C4}}{\lambda_s} \right)^2 \left( \frac{1 + \frac{L^{C1-C3}}{\lambda_s}}{1 + \frac{L^{C1-C4}}{\lambda_s}} \right)^2 \quad (7.10)$$

Here  $S_{\lambda_s}^{C3}$  and  $S_{\lambda_s}^{C4}$  are the spin relaxation noise at contacts C3 and C4, and  $L^{Ci-Cj}$  is the separation between contacts  $C_i$  and  $C_j$  ( $i, j = 1,3,4$ ). The solution to Eq. 7.10 for the experimentally obtained noise ratios gives a value of  $\lambda_s \sim 1.5 \mu\text{m}$  and  $1.0 \mu\text{m}$  at  $V_g = 0$  and  $-45$  V, respectively. A close agreement with the values obtained independently from the Hanle measurements ( $\lambda_s \sim 1.5 \mu\text{m}$  at  $V_g = 0$  V and  $1.1 \mu\text{m}$  at  $V_g = -45$  V) validates the analytical framework of Eq. 7.5 and Eq. 7.10.

### 7.5.3 Spin-dependent Noise: Analytical Expression

We quantitatively analyze the analytical expression of the non-local spin signal in order to figure out the dominant sources of spin sensitive noise. The measured non-

local voltage  $\Delta V_{NL} = \Delta R_{NL} \times I$  for the spin-valve geometry is expressed by Eq. 7.11:

$$\Delta V_{NL} = \frac{P^2 I R_{sq} \lambda_s \exp(-L/\lambda_s)}{2W} \quad (7.11)$$

Here  $P$  is the contact spin polarization,  $I$  is the current applied at the injector contact,  $R_{sq}$  is the square resistance of graphene,  $\lambda_s$  is the spin diffusion length in graphene,  $L$  is the spacing between the injector and the detector contact and  $W$  is the width of the transport channel.

The fluctuations in  $\Delta V_{NL}$  in time are represented by the correlation function:

$$R_V^{NL}(\tau) = \langle \Delta V_{NL}(t) * \Delta V_{NL}(t + \tau) \rangle \quad (7.12)$$

The noise associated with different parameters ( $P, R_{sq}, I, \lambda_s$ ) can be written in form of a power spectrum  $S_V^{NL}(f)$ , which is the Fourier transform of  $R_V^{NL}(\tau)$ :

$$S_V^{NL}(f) \simeq \frac{\exp(-\frac{L}{\lambda_s})^2}{4W^2} [(P^2 I R_{sq})^2 \left(1 + \frac{L}{\lambda_s}\right)^2 S_{\lambda_s}(f) + (P^2 \lambda_s R_{sq})^2 S_I(f) + (P^2 \lambda_s I)^2 S_{R_{sq}}(f) + (2P I R_{sq} \lambda_s)^2 S_P(f)] \quad (7.13)$$

This equation can be rewritten as

$$S_V^{NL}(f) = A_{\lambda_s} S_{\lambda_s}(f) + A_I S_I(f) + A_{R_{sq}} S_{R_{sq}}(f) + A_P S_P(f) \quad (7.14)$$

where  $S_P$  is the due to the polarization fluctuations at the injector/detector electrode which is the Fourier transform of the auto correlation function for the time dependent polarization fluctuations i.e.  $\mathcal{F}\langle P(t)P(t + \tau) \rangle$ ,  $S_{\lambda_s}$  is the noise associated with the spin transport i.e. spin relaxation noise ( $\mathcal{F}\langle \lambda_s(t)\lambda_s(t + \tau) \rangle$ ),  $S_I(f)$  is the noise from the external current source ( $\mathcal{F}\langle I(t)I(t + \tau) \rangle$ ),  $S_{R_{sq}}$  is the 1/f charge noise and the thermal noise from the channel ( $\mathcal{F}\langle R_{sq}(t)R_{sq}(t + \tau) \rangle$ ). Here we take the assumption that the fluctuations in all four parameters ( $P, R_{sq}, I, \lambda_s$ ) are uncorrelated. We can measure  $S_I$  independently and  $S_{R_{sq}}$  is the local 1/f noise (Fig. 7.8). After removing the contribution of  $S_I$  ( $\sim 10^{-23}$  V<sup>2</sup>/Hz) and  $S_{R_{sq}}$  ( $\sim 10^{-22}$  V<sup>2</sup>/Hz) to  $S_V^{NL}$ , which are negligible compared to the observed noise ( $\sim 10^{-14}$  V<sup>2</sup>/Hz), the only dominant sources of noise in the measured non-local signal are the polarization fluctuations at the injector/detector electrodes and the fluctuations in the spin transport parameters ( $\lambda_s = \sqrt{D_s \tau_s}$ ). However, assuming  $R_{sq}$  and  $\lambda_s$  uncorrelated is not strictly true. These quantities are correlated as  $\lambda_s$  depends on the channel resistance with  $\lambda_s$  going down with the increase in the channel resistance, which would lead to different  $\lambda_s$  dependence of the analytical expression i.e. Eq. 7.14.

## 7.6 Conclusions

By performing the first measurement of 1/f noise associated with spin transport, we demonstrate that the non-local spin-dependent noise in graphene is dominated by

the underlying spin relaxation processes. The obtained noise magnitude for charge and spin transport differ by three orders of magnitude, indicating fundamentally different scattering mechanisms such as resonant scattering of the spins, where the fluctuating scattering cross-section of the intrinsically present impurities could produce the spin dependent  $1/f$  fluctuations [12].

## 7.7 Acknowledgements

We acknowledge J. G. Holstein, H. M. de Roosz and H. Adema for their technical assistance. This research work was financed under EU-graphene flagship program (637088) and supported by the Zernike Institute for Advanced Materials, the Nederlandse Organisatie voor Wetenschappelijk (NWO, Netherlands) and the Future and Emerging Technologies (FET) programme within the Seventh Framework Programme for Research of the European Commission, under FET-open Grant No. 618083 (CN-TQC).

## References

- [1] R. Landauer, "Condensed-matter physics: The noise is the signal," *Nature* **392**, pp. 658–659, Apr. 1998.
- [2] R. Jayaraman and C. Sodini, "A 1/f noise technique to extract the oxide trap density near the conduction band edge of silicon," *IEEE Trans. Electron Dev.* **36**, pp. 1773–1782, Sept. 1989.
- [3] F. N. Hooge, T. G. M. Kleinpenning, and L. K. J. Vandamme, "Experimental studies on 1/f noise," *Rep. Prog. Phys.* **44**(5), p. 479, 1981.
- [4] P. Dutta and P. M. Horn, "Low-frequency fluctuations in solids:  $\frac{1}{f}$  noise," *Rev. Mod. Phys.* **53**, pp. 497–516, July 1981.
- [5] C. Ertler, S. Konschuh, M. Gmitra, and J. Fabian, "Electron spin relaxation in graphene: The role of the substrate," *Phys. Rev. B* **80**, p. 041405, July 2009.
- [6] D. Huertas-Hernando, F. Guinea, and A. Brataas, "Spin-Orbit-Mediated Spin Relaxation in Graphene," *Phys. Rev. Lett.* **103**, p. 146801, Sept. 2009.
- [7] J. Ingla-Aynés, M. H. D. Guimarães, R. J. Meijerink, P. J. Zomer, and B. J. van Wees, "24-um spin relaxation length in boron nitride encapsulated bilayer graphene," *Phys. Rev. B* **92**, p. 201410, Nov. 2015.
- [8] V. K. Dugaev, E. Y. Sherman, and J. Barnaś, "Spin dephasing and pumping in graphene due to random spin-orbit interaction," *Phys. Rev. B* **83**, p. 085306, Feb. 2011.
- [9] H. Min, J. E. Hill, N. A. Sinitsyn, B. R. Sahu, L. Kleinman, and A. H. MacDonald, "Intrinsic and rashba spin-orbit interactions in graphene sheets," *Phys. Rev. B* **74**, p. 165310, Oct. 2006.
- [10] C. Ertler, S. Konschuh, M. Gmitra, and J. Fabian, "Electron spin relaxation in graphene: The role of the substrate," *Phys. Rev. B* **80**, p. 041405, July 2009.
- [11] M. B. Lundberg, R. Yang, J. Renard, and J. A. Folk, "Defect-mediated spin relaxation and dephasing in graphene," *Phys. Rev. Lett.* **110**, p. 156601, Apr. 2013.
- [12] D. Kochan, M. Gmitra, and J. Fabian, "Spin relaxation mechanism in graphene: Resonant scattering by magnetic impurities," *Phys. Rev. Lett.* **112**, p. 116602, Mar. 2014.
- [13] D. Soriano, D. V. Tuan, S. M.-M. Dubois, M. Gmitra, A. W. Cummings, D. Kochan, F. Ortman, J.-C. Charlier, J. Fabian, and S. Roche, "Spin transport in hydrogenated graphene," *2D Mater.* **2**, p. 022002, June 2015.
- [14] S. Omar, M. Gurram, I. J. Vera-Marun, X. Zhang, E. H. Huisman, A. Kaverzin, B. L. Feringa, and B. J. van Wees, "Spin relaxation in graphene with self-assembled cobalt porphyrin molecules," *Phys. Rev. B* **92**, p. 115442, Sept. 2015.
- [15] T. Maassen, I. J. Vera-Marun, M. H. D. Guimarães, and B. J. van Wees, "Contact-induced spin relaxation in hBN spin precession measurements," *Phys. Rev. B* **86**, p. 235408, Dec. 2012.
- [16] H. E. van den Brom and J. M. van Ruitenbeek, "Quantum Suppression of Shot Noise in Atom-Size Metallic Contacts," *Phys. Rev. Lett.* **82**, pp. 1526–1529, Feb. 1999.
- [17] A. A. Balandin, "Low-frequency 1/f noise in graphene devices," *Nat. Nanotechnol.* **8**, pp. 549–555, Aug. 2013.
- [18] A. N. Pal, S. Ghatak, V. Kochat, E. S. Sneha, A. Sampathkumar, S. Raghavan, and A. Ghosh, "Microscopic Mechanism of 1/f Noise in Graphene: Role of Energy Band Dispersion," *ACS Nano* **5**, pp. 2075–2081, Mar. 2011.
- [19] G. Liu, S. Rumyantsev, M. S. Shur, and A. A. Balandin, "Origin of 1/f noise in graphene multilayers: Surface vs. volume," *Appl. Phys. Lett.* **102**, p. 093111, Mar. 2013.
- [20] A. A. Kaverzin, A. S. Mayorov, A. Shytov, and D. W. Horsell, "Impurities as a source of 1/f noise in graphene," *Phys. Rev. B* **85**, p. 075435, Feb. 2012.
- [21] M. A. Stolyarov, G. Liu, S. L. Rumyantsev, M. Shur, and A. A. Balandin, "Suppression of 1/f noise in near-ballistic h-BN-graphene-h-BN heterostructure field-effect transistors," *Appl. Phys. Lett.* **107**, p. 023106, July 2015.

- [22] L. Jiang, E. R. Nowak, P. E. Scott, J. Johnson, J. M. Slaughter, J. J. Sun, and R. W. Dave, "Low-frequency magnetic and resistance noise in magnetic tunnel junctions," *Phys. Rev. B* **69**, p. 054407, Feb. 2004.
- [23] S. Ingvarsson, G. Xiao, R. A. Wanner, P. Trouilloud, Y. Lu, W. J. Gallagher, A. Marley, K. P. Roche, and S. S. P. Parkin, "Electronic noise in magnetic tunnel junctions," *J. Appl. Phys.* **85**, pp. 5270–5272, Apr. 1999.
- [24] P. J. Zomer, M. H. D. Guimarães, N. Tombros, and B. J. van Wees, "Long-distance spin transport in high-mobility graphene on hexagonal boron nitride," *Phys. Rev. B* **86**, p. 161416, Oct. 2012.
- [25] C. Józsa, T. Maassen, M. Popinciuc, P. J. Zomer, A. Veligura, H. T. Jonkman, and B. J. van Wees, "Linear scaling between momentum and spin scattering in graphene," *Phys. Rev. B* **80**, p. 241403, Dec. 2009.



## Chapter 8

---

# A Two-channel Model for Spin-relaxation Noise Analysis

### Abstract

*We develop a two-channel resistor model for simulating spin transport with general applicability. Using this model, for the case of graphene as a prototypical material, we calculate the spin signal consistent with experimental values. More importantly, using the same model we also simulate the charge and spin-dependent  $1/f$  noise in the four-probe local and nonlocal measurement schemes, respectively and identify the noise from the spin-relaxation resistances, i.e. noise from the spin-relaxation processes as the major source of spin-dependent  $1/f$  noise.*



## 8.1 Introduction

The ubiquitous nature of  $1/f$  noise in a variety of systems is quite surprising [1]. The origin of the signal fluctuations with  $1/f$  power spectral density is believed to be a broad distribution of time scales related with the measured quantity [2, 3], which for electronic transport is associated to the trapping-detrapping times of charge carriers via impurities [2, 4]. A two dimensional sheet of graphene, owing to its surface sensitivity [5–9] and superior spin transport properties [10, 11], offers a unique platform to study the interaction of impurities with the electron spin via the universally observed phenomenon of  $1/f$  noise. Such an approach leads to the expectation of a *spin-dependent*  $1/f$  noise in the average spin accumulation ( $\mu_s$ ) studied in spintronic devices [12], and to the fundamental question of how this noise is related to spin transport. In our recent experiment, we measured for the first time the spin-dependent  $1/f$  noise [13]. For this, we used graphene as a prototypical spin channel, leading to two major observations. First, we extracted a noise magnitude  $\gamma$  for spin transport, i.e.,  $\gamma^s$  three to four orders of magnitude higher than for charge transport ( $\gamma^c$ ), which was attributed to a drastically enhanced spin scattering as compared to charge scattering, along the lines of the recently proposed resonant scattering mechanism [7]. Second, we identified that the spin-dependent noise was dominated by the noise from the spin-relaxation processes.

In this work, we develop a two-channel resistor model in a four-probe measurement geometry, where different resistors represent charge and spin transport, and spin-relaxation processes. Using this model, we can simulate the charge  $1/f$  noise of similar magnitude as that experimentally measured in ref., employing  $\gamma = \gamma^c \sim 5 \times 10^{-8}$  [13]. More importantly, we use the same model to simulate the spin signal and the spin-dependent  $1/f$  noise in the *nonlocal* geometry. The simulated spin signal is in agreement with the experimental results. Nevertheless, we find that the simulated spin-dependent noise is significantly lower than the experimental counterpart, using the noise magnitude  $\gamma \sim \gamma^c$  for each process. Via further analysis, we show that an agreement with the measured  $1/f$  spin-dependent noise [13] is obtained by considering  $\gamma$  three to four orders of magnitude higher than  $\gamma^c$ , i.e.  $\gamma \sim \gamma^s$ , only for the spin-relaxation processes. This result lead to a quantitative demonstration of a spin-dependent noise dominated by the spin-relaxation processes, with a large  $\gamma$ .

## 8.2 Developing a Two-channel Resistor Model

In order to measure spin transport unambiguously, we use a four-probe nonlocal scheme [12], as shown in Fig. 8.1(b). Here, we develop an elementary two-channel resistor model for the nonlocal geometry, as an extension to ref. [14]. In this model,

a region of length  $l$  in the device is modeled as  $n$  basic units connected in series, with each unit corresponding to the spin transport within a length  $\Delta x = l/n$ . For our simulations, we consider  $\Delta x = \lambda_s/3$ , with  $\lambda_s$  the spin relaxation length in the channel, measured in ref. [13], as shown in Fig. 8.1(c). One channel unit is represented by a spin-up and a spin-down channel resistances,  $R_{\text{ch}}^\uparrow$  and  $R_{\text{ch}}^\downarrow$ , connected via a spin relaxation resistance  $R_{\uparrow\downarrow}$ . The resistance to an unpolarized charge current, for a channel length  $\Delta x$  and width  $w$ , is  $R_{\text{ch}} = R_{\text{sq}}\Delta x/w$ , with  $R_{\text{sq}}$  the square resistance. For a two-channel model, this can be represented as a parallel configuration of  $R_{\text{ch}}^\uparrow$  and  $R_{\text{ch}}^\downarrow$ , both expressed as,

$$R_{\text{ch}}^\uparrow = R_{\text{ch}}^\downarrow = 2 \times R_{\text{ch}} = \frac{2R_{\text{sq}}\Delta x}{w}, \quad (8.1)$$

which holds true due to the non-magnetic nature of the channel. To complete the model of the channel we introduce the spin relaxation resistance  $R_{\uparrow\downarrow}$  given by,

$$R_{\uparrow\downarrow} = \frac{2R_{\text{sq}}\lambda_s^2}{w\Delta x}, \quad (8.2)$$

which corresponds to the spin relaxation within a channel length of  $\Delta x$ . Within the transport channel there are two current branches,  $I_\uparrow$  (in the upper branch) and  $I_\downarrow$  (in the lower branch), see Fig. 8.1(d). In the nonlocal part of the circuit, where the charge current is zero,  $I_c = I_\uparrow + I_\downarrow = 0$ , there exists only a pure spin current,  $I_s = I_\uparrow - I_\downarrow \neq 0$ . Therefore, the spin accumulation,  $\mu_s$ , or the chemical potential difference between the upper branch,  $\mu_\uparrow$ , and the lower branch,  $\mu_\downarrow$ , is present only due to spin transport in the channel.

With respect to the contacts, each spin-polarized injector (detector) is represented as a combination of two resistors,  $R_C^\uparrow$  and  $R_C^\downarrow$ , corresponding to injection into the spin-up and spin-down channels, as shown in Fig. 8.1(d). These resistors must satisfy the following conditions [15] regarding the measured contact polarization,  $P$ , and the measured contact resistance,  $R_C$ , namely,

$$P = \frac{R_C^\downarrow - R_C^\uparrow}{R_C^\downarrow + R_C^\uparrow}, \text{ and } R_C = \frac{R_C^\downarrow R_C^\uparrow}{R_C^\downarrow + R_C^\uparrow}, \quad (8.3)$$

in order to achieve consistency between the experimental results and the model calculations. For the case of non-invasive contacts [15, 16], the nonlocal spin signal  $\Delta V_{\text{NL}}$  due to an injection current  $I$ , can be estimated using,

$$\Delta V_{\text{NL}} = \frac{P^2 I R_{\text{sq}} \lambda_s e^{-L/\lambda_s}}{2w}, \quad (8.4)$$

where  $L$  is the separation between the injector and detector contacts. For the device used in ref. [13],  $L \sim \lambda_s$ .

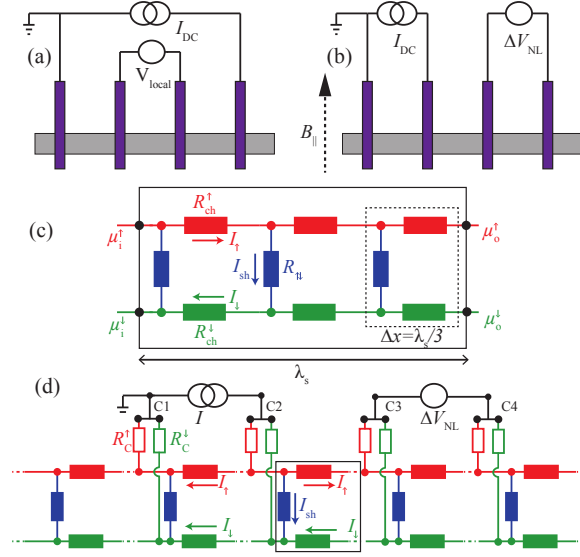


**Figure 8.1:** Schematic diagram of nonmagnetic channel (gray) with spin-polarized contacts (purple) for a four probe (a) charge transport and (b) spin transport measurement scheme. A region of length  $l \approx \lambda_s$  is modeled as  $n=3$  basic units connected in series (c), each formed by an equivalent circuit of a spin-up resistance  $R_{\text{ch}}^{\uparrow}$  (red) and a spin-down resistance  $R_{\text{ch}}^{\downarrow}$  (green), connected via a spin-relaxation resistance  $R_{\uparrow\downarrow}$  (blue). (d) A two-channel model for spin transport is constructed by replacing the spin channel with a series connection of basic units from (c), and by modelling the spin-polarized contacts with two resistors  $R_{\text{C}}^{\uparrow}$  and  $R_{\text{C}}^{\downarrow}$ .

All values for the parameters in Eq. 8.4 are experimentally obtained and consequently used to construct the two-channel model shown in Fig. 8.1(d), by using Eqs. 8.1–8.3. In order to check the validity of our model for spin transport, we compare the simulated spin signal with the experimental values [13]. First, we consider the measured spin signal for the graphene spintronic device at different values of  $L$ . Next, we apply our circuit model from Fig. 8.1(d) with the corresponding number of repetitions for our basic unit (Fig. 8.1(c)), therefore replicating the experimental device for the same values of  $L$ , and simulate the spin signal  $\Delta V_{\text{NL}}$ . The agreement between the experiment and the calculations is remarkable, as shown in Fig. 8.2, confirming its validity for further analysis.

Let us now consider electronic noise in our circuit model. At equilibrium, in the absence of any charge current, there is always a finite thermal noise present in a transport channel, which is represented as a resistor. However, in a non-equilibrium situation due to a net charge current  $I$ , a frequency dependent  $1/f$  noise is present and it can dominate at low frequencies. This noise is generated due to the trapping-

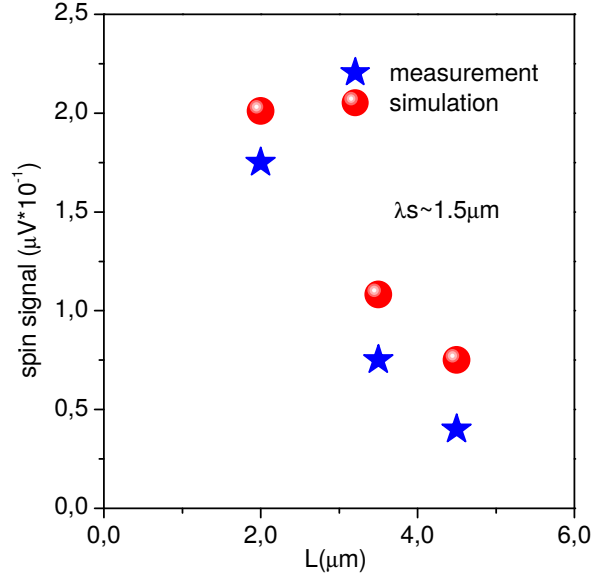


**Figure 8.2:** Spin signal as a function of injector-detector separation  $L$ . Data obtained from measurements in a graphene spintronic device (blue stars) and simulations for the corresponding two-channel models (red circles). For the circuit models, we use the experimentally obtained  $P \sim 5\%$ ,  $\lambda_s \sim 1.5 \mu\text{m}$ ,  $R_{\text{sq}} \sim 400 \Omega$  and  $w = 1.7 \mu\text{m}$ .

detrapping of charge carriers at a finite time scale, via impurities present at the contact-channel interface or at the substrate-transport channel interface [2, 4]. For the case of spin transport, a spin-dependent  $1/f$  noise can be generated either by fluctuations in contact polarization during spin current injection/detection [17, 18], or by a fluctuating channel or spin relaxation resistors, during spin transport. The origin of the recently observed  $1/f$  spin-dependent noise is believed to come from the noise present in the spin relaxation processes [13].

In the present work, we simulate the charge and the spin-dependent noise originating from the contacts, the channel, and the spin-relaxation resistances, and analyze their individual contributions to find out the dominant source of spin-dependent noise. Noise associated with each of these resistor elements is represented as a root mean squared (*rms*) current noise source,  $i$ , in parallel with the noiseless resistor  $R$ , as shown in Fig. 8.3(a). For a noise spectral density  $S$  [ $\text{A}^2\text{Hz}^{-1}$ ] at the element  $R$ , the magnitude of the equivalent noise current is  $i \equiv S^{1/2}$  [ $\text{A Hz}^{-1/2}$ ]. For each noise source  $i_n$  applied across a resistor  $R_n$ , we must evaluate the corresponding noise voltage appearing between the detector contacts,  $v_n = \eta_n i_n$ . Here,  $\eta_n$  is a coefficient that depends on the circuit topology, relating the element to the measurement contacts, and therefore depends on the measurement geometry. The total noise,  $V$ , due

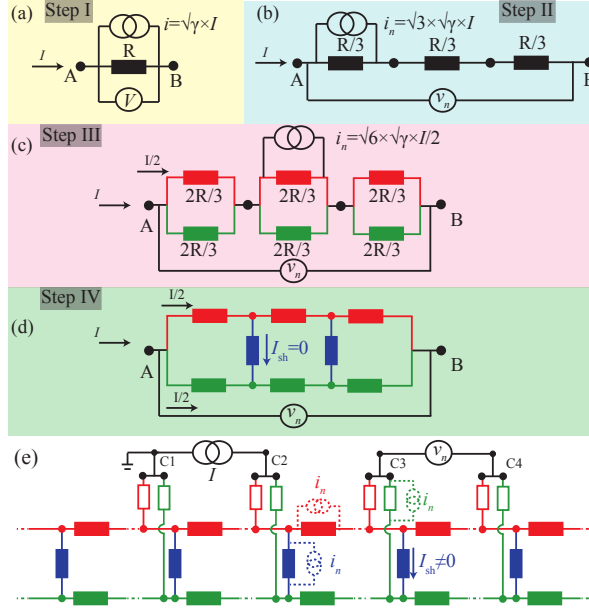


**Figure 8.3:** Circuit model for  $1/f$  noise (at 1 Hz) for (a) a single-channel region of resistance  $R$ , under an applied current  $I$ , with a current noise source  $i = \sqrt{\gamma}I$ . (b) Same region as in (a), represented as a series of three resistors, each with a scaled  $i_n = \sqrt{3\gamma}I$ , which keeps consistent the total noise,  $V$  [19]. (c) Transition to a two-channel model in the limit of fast spin relaxation, where the channel resistors,  $R_{\text{ch}}^{\uparrow(\downarrow)} = 2R/3$ , each have an equivalent noise current source  $i_n = \sqrt{6\gamma} \times I/2$ . (d) Introduction of the spin relaxation resistance,  $R_{\uparrow\downarrow}$ . For an unpolarized current  $I$ , there is no current present at these resistors, so they do not contribute to  $1/f$  noise. To keep a consistent  $V$  for cases (a)–(d), we must consider  $i_n$  in the spin channel resistors as independent noise sources. (e) Full two-channel model, as in Fig. 8.1(d), including also noise sources for the contact resistances and for the spin relaxation resistances. The latter contribute to the total noise, as in a spin injection geometry there is now a spin current present in the channel. A noise voltage  $v_n$  appears between C3–C4 due to noise current  $i_n$  in the circuit

to all circuit elements will be,

$$V = \sqrt{v_1^2 + v_2^2 + v_3^2 + \dots + v_{n-1}^2 + v_n^2}, \quad (8.5)$$

where we assume that all noise sources are independent. This condition is necessary to achieve a consistent description of the total noise,  $V$ , as shown in Fig. 8.3(a)–(e).

We start by calculating thermal noise between C3–C4, using the circuit model of Fig. 8.3(e) with  $I = 0$ , as a test case for our model. This contribution acts as a white noise background at C3–C4, which we simulate for each element  $R_n$ , by considering a current noise spectral density  $S_n = 4k_B T \Delta f / R_n$ . The resulting equivalent noise current source  $i_n$  across each element, is then used to calculate the total noise voltage

at  $\Delta f = 1$  Hz for the nonlocal measurement geometry, according to Eq. 8.5. In this way, we can estimate the contribution from the spin-relaxation resistors, channel resistors, and contacts, separately (1<sup>st</sup> column of Table. 8.1). The simulation result for the nonlocal thermal background,  $\sim 6 \times 10^{-17} \text{ V}^2 \text{ Hz}^{-1}$  (see Table 8.1), is in good agreement with the measured thermal noise,  $\sim 10^{-16} \text{ V}^2 \text{ Hz}^{-1}$ , as shown in Fig. 8.4, supporting the validity of the model also for the noise simulations.

Next we proceed to consider  $1/f$  noise, first in the local measurement configuration. For a local measurement as in Fig. 8.1(a), the (charge)  $1/f$  noise spectral density  $S_I^{\text{local}}$  has a frequency and current dependent power spectral density, described by the Hooge formula,

$$S_I^{\text{local}} = \frac{\gamma^c I^2}{f^\alpha}, \quad (8.6)$$

where  $\alpha \sim 1$  and  $\gamma^c$  is the charge noise magnitude. The latter is defined as the Hooge parameter,  $\gamma_{\text{H}}^c$ , divided by the total number of carriers in the transport channel, i.e.  $\gamma^c = \gamma_{\text{H}}^c / (nwL)$ , where  $n$  is the (2D) charge carrier density. From our measurements of a graphene device we obtained  $\gamma^c \sim 5 \times 10^{-8}$  at  $f = 1$  Hz [13], of a similar magnitude as in Refs. [3] and [4].

For our calculations of  $1/f$  noise we consider this value of  $\gamma^c$ . We first proceed to scale the experimental noise magnitude  $\gamma^c$  with respect to the length of the basic unit element in our two-channel model, ( $\Delta x = \lambda_s/3 \sim L/3$ ), as shown in Fig. 8.3(a)–(c). This results in  $\gamma_{\text{scaled}} = 6\gamma^c$  for the spin channel resistors. Each resistor element has an equivalent current noise source  $i_n = \sqrt{S_I} = \sqrt{\gamma_{\text{scaled}}} I_n = \sqrt{6\gamma^c} I_n$  for  $f = 1$  Hz. For the contacts,  $\gamma = \gamma_{\text{contact}}^c \sim 2 \times 10^{-8}$  is used for the calculation, as obtained experimentally by measuring the  $1/f$  noise across the contacts [13]. Furthermore, we must calculate the current  $I_n$  through each resistor element, for the specific measurement geometry under consideration. For the local configuration we consider an applied dc current  $I = 10 \mu\text{A}$  between contacts C1–C4, similar to the experiment. In this way we can obtain the equivalent noise current sources,  $i_n$ , for all the elements, and subsequently calculate their contribution to the total noise at the detector contacts C2–C3, using Eq. 8.5. Here it is relevant to clarify the role of the spin-relaxation resistors,  $R_{\uparrow\downarrow}$ . In the local geometry of Fig. 8.1(a), we do not expect to inject any significant spin accumulation within the center of the channel, using the similar circuit of Fig. 8.3(d). Here, we assume that the outer contacts are situated far away, which results in negligible spin-accumulation between the detector electrodes C2–C3. Even if we would like to quantify their contribution in this local measurement, at this point we lack a direct experimental determination of their corresponding noise magnitude. For further discussion we denote it as  $\gamma_{\uparrow\downarrow}$ . As an initial estimation, we assume that the noise from the charge scattering and spin-relaxation have same origin and use  $\gamma_{\uparrow\downarrow} = 3 \times \gamma^c (\Delta x \sim L/3)$ . The simulation results for the local measurement show that the contribution towards  $1/f$  charge noise from the spin-relaxation resistors is  $\sim 10^{-20} \text{ V}^2 \text{ Hz}^{-1}$ , which is seven orders of magnitude

lower than the experimentally obtained noise magnitude of  $\sim 3 \times 10^{-13} \text{ V}^2 \text{ Hz}^{-1}$ . On the contrary, the calculated contribution from the channel spin resistors,  $R_{\text{ch}}^{\uparrow(\downarrow)}$  amounts to a noise of  $\sim 4 \times 10^{-13} \text{ V}^2 \text{ Hz}^{-1}$ , which is in excellent agreement with the measured local (charge) noise, as shown in Fig. 8.4.

Finally, we consider the nonlocal noise. In analogy to Eq. 8.6, the spin-dependent contribution to the  $1/f$  noise,  $\Delta S_V^{\text{NL}}$ , can be expressed as,

$$\Delta S_V^{\text{NL}} = \frac{\gamma^s \Delta V_{\text{NL}}^2}{f^a}, \quad (8.7)$$

where  $\gamma^s = \gamma_{\text{H}}^s / (nw\lambda_s)$  is the noise magnitude for spin transport, and  $\gamma_{\text{H}}^s$  represents the Hooge parameter for spin transport. Here, for the normalization of the Hooge parameter by the total number of carriers in the channel under measurement, we consider the non-conserved nature of the spin current and take the spin relaxation length  $\lambda_s$  as the characteristic length for this normalization.  $\Delta V_{\text{NL}} = P\mu_s/e$  is the measured nonlocal spin signal due to the average spin accumulation  $\mu_s$ .

We use the nonlocal measurement configuration, Fig. 8.3(e) for simulating the spin-dependent  $1/f$  in order to eliminate the contribution of charge noise. We consider a dc current  $I = 10 \mu\text{A}$  between contacts C1–C2 and calculate the noise between C3–C4 due to each circuit element, following the procedure established for the thermal and charge  $1/f$  noise simulations, assuming the same  $\gamma_{\text{scaled}} \sim 6\gamma^c$  for  $R_{\text{ch}}^{\uparrow}, R_{\text{ch}}^{\downarrow}$ ,  $\gamma_{\uparrow\downarrow} \sim 3\gamma^c$  for  $R_{\uparrow\downarrow}$ , and  $\sim 2 \times 10^{-8}$  for the spin-polarized contacts. Here, we assume that the mechanisms, producing the  $1/f$  charge and spin-dependent noise are same. The simulated  $1/f$  noise results in  $\sim 5 \times 10^{-17} \text{ V}^2 \text{ Hz}^{-1}$ , which is lower by an order than the experimental counterpart,  $\sim 5 \times 10^{-16} \text{ V}^2 \text{ Hz}^{-1}$ , i.e. the magnitude denoted by the red arrow in Fig. 8.4. In particular, the noise from the spin-relaxation resistances, which was identified as a dominant noise source in the measurements [13], is only  $\sim 10^{-20} \text{ V}^2 \text{ Hz}^{-1}$ , so lower than the measured spin-dependent noise by almost four orders of magnitude. From the simulation results it is clear that the processes producing the spin-dependent  $1/f$  noise are very distinct from that of charge  $1/f$  noise and cannot be explained by the noise magnitude  $\gamma^c$  associated to the charge  $1/f$  noise. Given that the noise sources of the channel resistances and the contacts are experimentally determined, the only unknown noise sources are those related to the spin relaxation resistors, which up to now we have considered to be  $\gamma_{\uparrow\downarrow} = 3 \times \gamma^c$ . Furthermore, we note that the calculated nonlocal  $1/f$  noise, using the latter consideration, is in a better agreement with the measured nonlocal  $1/f$  spin-independent background noise, given by the magnitude of the blue arrow in Fig. 8.4. An agreement with this background, present when an out-of-plane magnetic field is applied to dephase the injected spins and there is no spin accumulation present at the detector, suggests that with the present consideration we only capture the nonlocal contribution from the noise sources in the local circuit, where a current is present, but not that contribution originating from the nonlocal spin transport.

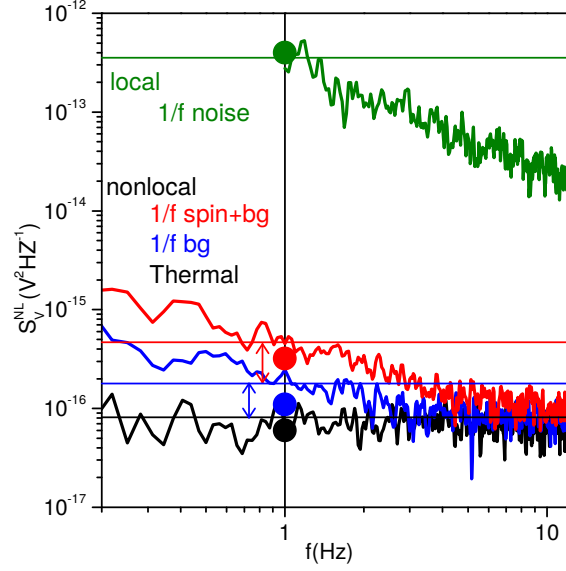


**Figure 8.4:** Charge and spin-dependent  $1/f$  noise measurements for the experimental device of Ref. [13]. The green spectrum is the charge  $1/f$  noise measured in the local four-probe geometry. The black spectrum is the nonlocal thermal noise background, in the absence of any applied current. The red spectrum is the measured total nonlocal  $1/f$  noise, which is the sum of the thermal noise, the background charge noise, and the spin-dependent noise (magnitude denoted by the red arrow) due to spin transport. The blue spectrum is the spin-independent background (thermal and charge backgrounds), measured when the spin accumulation is suppressed by a spin-dephasing applied out of plane magnetic field. The horizontal lines indicate the noise levels measured at 1 Hz, and the dots the corresponding results for the model calculations.

thermal noise ( $V^2 \text{ Hz}^{-1}$ )		$1/f$ noise ( $V^2 \text{ Hz}^{-1}$ )	
		$\gamma_{\uparrow\downarrow}=5\times 10^{-8}$	$\gamma_{\uparrow\downarrow}=5\times 10^{-4}$
$R_C^{\uparrow(\downarrow)}$	$5\times 10^{-17}$	$3.2\times 10^{-17}$	
$R_{\text{ch}}^{\uparrow(\downarrow)}$	$9\times 10^{-18}$	$1.5\times 10^{-17}$	
$R_{\uparrow\downarrow}$	$10^{-21}$	$2\times 10^{-20}$	$2\times 10^{-16}$
total	$6\times 10^{-17}$	$4.7\times 10^{-17}$	$3.1\times 10^{-16}$

**Table 8.1:** Summary of thermal noise and  $1/f$  nonlocal noise contributions from injection/detection contacts, transport spin resistors (channel), and spin-relaxation resistors (spin-flip processes), obtained from simulations with a two-channel model.



From the spin-dependent noise measurements in Ref. [13], we experimentally obtained the spin noise magnitude  $\gamma^s \sim 10^{-4} - 10^{-3}$ , by fitting the dependence of  $\Delta S_V^{\text{NL}}$  on the spin signal  $\Delta V_{\text{NL}}$  with Eq. 8.7. This value was surprisingly up to four orders of magnitude higher than  $\gamma^c$  for the charge noise. The main question is to find out to which process we can assign this  $\gamma^s$ , which would result in a simulated total  $1/f$  noise closer to the experimental value. Let us briefly consider the case where we use this experimental  $\gamma^s$  to calculate the noise from the channel and contact resistors. This exercise results in a  $1/f$  noise level  $\sim 10^{-13} \text{ V}^2 \text{ Hz}^{-1}$ , higher by three orders of magnitude than the observed noise level in the experiments. This result indicates that, according to our circuit model, the experimental  $\gamma^s$  can not be assigned to the channel nor the contact resistances. Therefore, we forgo our initial consideration of  $\gamma_{\uparrow\downarrow} = 3 \times \gamma^c$ , and recalculate the nonlocal  $1/f$  noise for the case of a spin-relaxation resistance noise magnitude given by the experimentally measured spin noise magnitude, i.e.  $\gamma_{\uparrow\downarrow} = 3 \times \gamma^s$ . The results shown in the rightmost column of Table 8.1, demonstrate a similar magnitude for the  $1/f$  nonlocal noise due to the spin-relaxation resistors,  $\sim 2 \times 10^{-16} \text{ V}^2 \text{ Hz}^{-1}$ , to the measured spin-dependent  $1/f$  noise in [13], shown by the red arrow in Fig. 8.4. Based on simulation results, we argue that  $\gamma_{\uparrow\downarrow}$  is orders of magnitude higher than that of the channel resistors. More importantly, it is in a quantitative agreement with the experimentally obtained  $\gamma^s$ .

In conclusion, we present a two-channel model to simulate  $1/f$  noise, associated with charge and spin transport. The noise contribution from different circuit elements show that the measured spin-dependent  $1/f$  noise in Ref. [13] is dominated by the noise from the spin-relaxation resistances, i.e. which corresponds with the spin relaxation processes with noise magnitude  $\gamma_{\uparrow\downarrow} \simeq 10^{3-4} \times \gamma^c$ . This insight, combining a novel experimental approach with a basic circuit model, offers a tool to explore a different signature of spin scattering mechanisms, such as impurity assisted spin-flip processes [7] which could provide a marked  $1/f$  contribution to spin-dependent noise.

### 8.3 Derivation for Spin Relaxation Resistance

The expression for the spin-relaxation resistance in the circuit can be derived easily. The current  $I_{\text{sh}}$  corresponds to the spin relaxation within the volume  $w\Delta x$ , represented by the relaxation resistance  $R_{\uparrow\downarrow}$  is given by:

$$I_{\text{sh}} = \frac{V_{\uparrow} - V_{\downarrow}}{R_{\uparrow\downarrow}} = \frac{\mu_{\uparrow} - \mu_{\downarrow}}{e(R_{\uparrow\downarrow})} \quad (8.8)$$

$$\frac{I_{\text{sh}}}{w\Delta x} = \frac{e(n_{\uparrow} - n_{\downarrow})}{\tau_s} = \frac{eN(\mu_{\uparrow} - \mu_{\downarrow})}{\tau_s} \quad (8.9)$$

Here,  $n_{\uparrow}(n_{\downarrow})$  is the number of spin up(down) electrons,  $\tau_s$  is the spin-flip time, and  $N$  is the electron density of states at Fermi energy. The expression can be simplified using the Einstein relation:

$$\frac{1}{R_{\text{sq}}} = Ne^2D \quad (8.10)$$

where  $R_{\text{sq}}$  is the sheet resistance of the channel and  $D$  is the diffusion coefficient. Replacing Eq.8.10 and  $D = \lambda_s^2/\tau_s$  into Eq.8.9, we can rewrite  $I_{\text{sh}}$  as

$$I_{\text{sh}} = \frac{\mu_{\uparrow} - \mu_{\downarrow}}{eR_{\text{sq}}\lambda_s^2} \quad (8.11)$$

By solving Eq.8.9 and Eq.8.11, we obtain the expression for  $R_{\uparrow\downarrow}$

$$R_{\uparrow\downarrow} = \frac{2R_{\text{sq}}\lambda_s^2}{w\Delta x} \quad (8.12)$$

## 8.4 Scaling of Noise Current in a Two Channel Model

In Eq. 8.6

$$\gamma^c = \frac{\gamma_H^c}{n \times W \times L} \quad (8.13)$$

and 8.7:

$$\gamma^s = \frac{\gamma_H^s}{n \times W \times \lambda_s} \quad (8.14)$$

the noise magnitudes of the charge (spin) transport channel  $\gamma^c(\gamma^s)$  need to be scaled with respect to the carrier concentration and device parameters ( $W, L$ ), in order to estimate the accurate noise current  $i_n$  of the resistor, unlike in the case of the intrinsic  $\gamma_H^c(\gamma_H^s)$ , which are constant. Note that  $L$ , here is the separation between the inner injector and detector electrodes, i.e., the transport channel.

In this section, we build a two channel model and explain the scaling of  $\gamma$ , that can be either  $\gamma^c$  or  $\gamma^s$  associated with the resistors, that converts the charge or spin current to a noise current. In Fig. 8.5(a), a charge(spun) current  $I$  is flowing in a resistance  $R$  of length  $l = L \sim \lambda_s$  and width  $W$ . This current produces a  $1/f$  noise current  $i_n = \sqrt{\gamma}I$ , which is measured as noise voltage  $v_n$  due to  $i_n$  flowing in  $R$ , i.e.,

$$v_n = i_n \times R = \sqrt{\gamma}IR \quad (8.15)$$

## 8.5 Acknowledgments

This research work was financed under EU-graphene flagship program Core-I project (190637100) and supported by the Zernike Institute for Advanced Materials, the

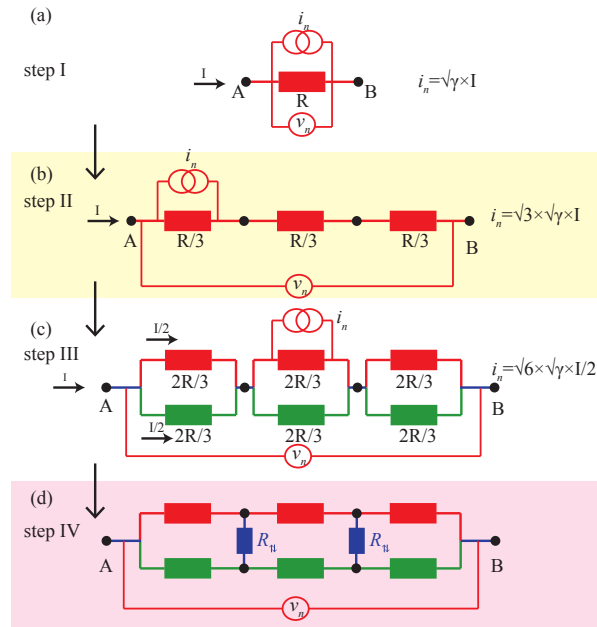


**Figure 8.5:** (a) noise representation of a resistor of resistance  $R$ . (b) in a series and (b) parallel arrangements. (d) A two channel model for spin-transport channel. The spin relaxation resistances  $R_{\uparrow\downarrow}$  are shown in blue.  $R_{\uparrow\downarrow}$  are inactive in the absence of a spin-accumulation in the transport channel due to symmetry of the circuit.

Netherlands Organization for Scientific Research (NWO) and the Future and Emerging Technologies (FET) programme within the Seventh Framework Programme for Research of the European Commission, under FET-open Grant No. 618083 (CN-TQC).

## References

- [1] E. Paladino, Y. Galperin, G. Falci, and B. Altshuler, "1/f noise: Implications for solid-state quantum information," *Rev. Mod. Phys.* **86**(2), pp. 361–418, 2014.
- [2] P. Dutta and P. M. Horn, "Low-frequency fluctuations in solids: 1/f noise," *Rev. Mod. Phys.* **53**, pp. 497–516, July 1981.
- [3] A. A. Balandin, "Low-frequency 1/f noise in graphene devices," *Nat. Nanotechnol.* **8**, pp. 549–555, Aug. 2013.
- [4] A. N. Pal, S. Ghatak, V. Kochat, E. S. Sneha, A. Sampathkumar, S. Raghavan, and A. Ghosh, "Microscopic Mechanism of 1/f Noise in Graphene: Role of Energy Band Dispersion," *ACS Nano* **5**, pp. 2075–2081, Mar. 2011.
- [5] C. Ertler, S. Konschuh, M. Gmitra, and J. Fabian, "Electron spin relaxation in graphene: The role of the substrate," *Phys. Rev. B* **80**, p. 041405, July 2009.
- [6] M. B. Lundeberg, R. Yang, J. Renard, and J. A. Folk, "Defect-mediated spin relaxation and dephasing in graphene," *Phys. Rev. Lett.* **110**, p. 156601, Apr. 2013.
- [7] D. Kochan, M. Gmitra, and J. Fabian, "Spin relaxation mechanism in graphene: Resonant scattering by magnetic impurities," *Phys. Rev. Lett.* **112**, p. 116602, Mar. 2014.
- [8] D. Soriano, D. V. Tuan, S. M.-M. Dubois, M. Gmitra, A. W. Cummings, D. Kochan, F. Ortman, J.-C. Charlier, J. Fabian, and S. Roche, "Spin transport in hydrogenated graphene," *2D Mater.* **2**, p. 022002, June 2015.
- [9] S. Omar, M. Gurram, I. J. Vera-Marun, X. Zhang, E. H. Huisman, A. Kaverzin, B. L. Feringa, and B. J. van Wees, "Spin relaxation in graphene with self-assembled cobalt porphyrin molecules," *Phys. Rev. B* **92**, p. 115442, Sept. 2015.
- [10] J. Ingla-Aynés, M. H. D. Guimarães, R. J. Meijerink, P. J. Zomer, and B. J. van Wees, "24-um spin relaxation length in boron nitride encapsulated bilayer graphene," *Phys. Rev. B* **92**, p. 201410, Nov. 2015.
- [11] L. Banszerus, M. Schmitz, S. Engels, M. Goldsche, K. Watanabe, T. Taniguchi, B. Beschoten, and C. Stampfer, "Ballistic transport exceeding 28 m in cvd grown graphene," *Nano Lett.* **16**(2), pp. 1387–1391, 2016.
- [12] N. Tombros, C. Józsa, M. Popinciuc, H. T. Jonkman, and B. J. van Wees, "Electronic spin transport and spin precession in single graphene layers at room temperature," *Nature* **448**, pp. 571–574, Aug. 2007.
- [13] S. Omar, M. H. D. Guimares, A. Kaverzin, B. J. van Wees, and I. J. Vera-Marun, "Spin relaxation 1/f noise in graphene," *Phys. Rev. B* **95**(8), p. 081403, 2017.
- [14] A. Fert and H. Jaffrès, "Conditions for efficient spin injection from a ferromagnetic metal into a semiconductor," *Phys. Rev. B* **64**, p. 184420, Oct. 2001.
- [15] T. Maassen, I. J. Vera-Marun, M. H. D. Guimarães, and B. J. van Wees, "Contact-induced spin relaxation in hantle spin precession measurements," *Phys. Rev. B* **86**, p. 235408, Dec. 2012.
- [16] M. Popinciuc, C. Józsa, P. J. Zomer, N. Tombros, A. Veligura, H. T. Jonkman, and B. J. van Wees, "Electronic spin transport in graphene field-effect transistors," *Phys. Rev. B* **80**, p. 214427, Dec. 2009. 00121.
- [17] L. Jiang, E. R. Nowak, P. E. Scott, J. Johnson, J. M. Slaughter, J. J. Sun, and R. W. Dave, "Low-frequency magnetic and resistance noise in magnetic tunnel junctions," *Phys. Rev. B* **69**, p. 054407, Feb. 2004.
- [18] S. Ingvarsson, G. Xiao, R. A. Wanner, P. Trouilloud, Y. Lu, W. J. Gallagher, A. Marley, K. P. Roche, and S. S. P. Parkin, "Electronic noise in magnetic tunnel junctions," *J. Appl. Phys.* **85**, pp. 5270–5272, Apr. 1999.
- [19] B. Razavi, *Fundamentals of Microelectronics*, John Wiley & Sons, Hoboken, NJ, 2nd edition edition ed., Dec. 2012. 00217.



## Chapter 9

# Spin Transport & Spin-relaxation in Graphene hBN Heterostructures

### Abstract

*The present generation of the state-of-the-art graphene-spintronic devices relies on isolating graphene from the external environment, such as from the underlying oxide substrate and further a complete encapsulation of the graphene flake between two insulating boron nitride crystals. This heterostructure assembly not only has shown to improve the charge and spin-transport properties of graphene, but also has provided the access to some novel phenomena such as band-gap opening, and electrically inducing Rashba spin-orbit-coupling in graphene which were missing in the pristine flake. In this chapter, I provide a brief summary of the results for the exfoliated single and bilayer hBN tunnel barriers, replacing the conventional oxide based tunnel barriers. In our experiments, we show that a long distance spin-transport is possible underneath the single hBN as a tunnel barrier, due to its pin-hole free crystalline nature. The bilayer hBN stands out due to its unique behavior. On application of a dc bias across the injector/detector electrode with a bilayer tunnel barrier, the differential spin injection/detection efficiency can be enhanced more than 100% (Details can be found in ref. [1]). We also measure the spin-transport in graphene/hBN heterostructures, using two layer CVD hBN tunnel barriers and obtain a completely different bias dependence for 2L-CVD hBN tunnel barriers, compared to that for the exfoliated 2L-hBN. In the last part, I discuss the spin-relaxation in graphene/hBN heterostructures, both with the exfoliated and the CVD tunnel barriers.*

published as:

M. Gurram, S. Omar, and B.J. van Wees  
*Nat. Comm.* **8**, 248 (2017).

&

M. Gurram, S. Omar, S. Zihlmann, P. Makk, C. Schönenberger, and B.J. van Wees  
*Phys. Rev. B* **93**, 115441 (2016).

&

M. Gurram, S. Omar, S. Zihlmann, P. Makk, C. Schönenberger, and B.J. van Wees  
*Phys. Rev. B* **97**, 045411 (2018).

&

M. Gurram, S. Omar, and B.J. van Wees  
*arXiv:1712.07828*

## 9.1 Introduction

Graphene on SiO<sub>2</sub>, has shown a very low  $\tau_s$  due to its roughness [2], charge inhomogeneities introduced by the dangling bonds on SiO<sub>2</sub> [3], impurities at the substrate-graphene interface [4] and electron-phonon coupling [5]. In order to alleviate the shortcomings of SiO<sub>2</sub>, one can use a thin hBN crystal as a potential substrate, which, due to its higher band-gap, atomically smooth and impurity free interface, promises to be an ideal choice to improve the charge and spin transport properties of graphene [6].

In order to preserve the pristine properties of graphene and to protect it from coming in contact with the external impurities during the lithography, one can encapsulate it between two hBN crystals. This geometry not only provides the encapsulation to improve the mobility of graphene, but also enables the application of top gating, which can be used to induce a Rashba SOC in graphene [7] and open a band gap in a bilayer graphene by breaking layer symmetry [8]. Even the high mobility of these samples in the encapsulated regions makes it possible for directional guiding of the spin current with a very high efficiency [9], which can be a stepping stone for realizing future spin logic circuits.

For graphene spintronics, ferromagnetic contacts with oxide tunnel barriers play a very important role and affect the spin transport. Therefore, the quality of the graphene-tunnel barrier interface is extremely crucial in terms of a homogeneous growth of an oxide tunnel barrier on graphene with a reduced pinhole density. There have been a lot of efforts to improve the quality of the tunnel barriers but it has not resulted in a reproducible and controlled growth of the tunnel barriers. The use of thin hBN flakes due to their crystalline, pinhole free nature [1, 10–13], can overcome the aforementioned shortcomings of the oxide tunnel barrier and result in a high differential spin-injection/detection efficiency of the contacts, with a reduced effect on the spin relaxation in graphene [13].

In this chapter, I will discuss novel hBN/graphene/hBN architectures where we fully encapsulate a graphene flake between two hBN flakes. The bottom hBN flake serves as a substrate and the top hBN flake which can be a mono/bi/tri layer, completely covers the graphene flake so that it never comes in contact with external impurities and this flake also is used as a tunnel barrier between the ferromagnet and graphene, replacing the conventional oxide tunnel barrier. In this heterostructure, we demonstrate the use of single and bi layer hBN as efficient tunnel barriers. The ML-hBN layer does not show a high spin injection efficiency, though a pinhole free nature of the layer can be concluded from the measurements. However, bilayer-hBN stands out. With the application of a bias voltage, we can tune the differential spin injection/detection efficiencies more than 100 % with a successful demonstration of the 2-terminal spin-valve signal [1], which clearly demonstrates the potential of bilayer-hBN for future spintronic applications.

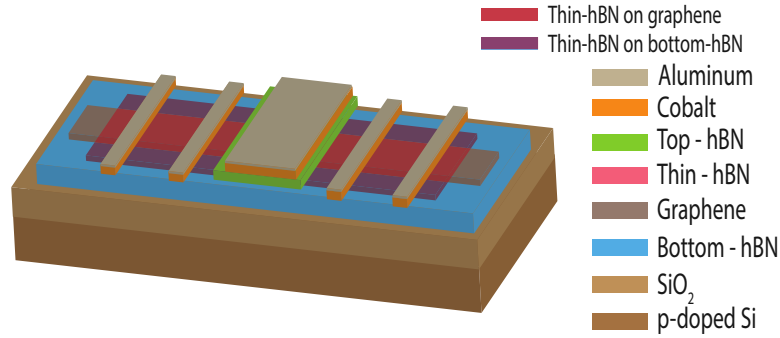


**Figure 9.1:** Schematic of the fully hBN encapsulated graphene spin valve device.

We also explore the possibility of using the chemical vapor deposition (CVD)-hBN layers as tunnel barriers. However, due to the shortcomings of the wet transfer method, the graphene quality deteriorates. Also, because of nonuniform growth of the CVD-hBN tunnel barriers along with the presence of impurities in the tunnel barriers, the results are not as good as for the exfoliated tunnel barriers.

In the last part, I discuss spin-relaxation in graphene/hBN heterostructures, both with the exfoliated and the CVD hBN tunnel barriers, where two major conclusions are obtained for these heterostructures. First, the spin-relaxation time ( $\tau_s$ ) in graphene increases with increasing the tunnel barrier thickness for the exfoliated hBN tunnel barriers. The thickness enhancement has two-fold advantages: it reduces the contact-induced spin-relaxation and also its shielding against the external impurities increases, which could improve the graphene quality. Second, for low mobility samples with the CVD-hBN tunnel barriers, the spin-relaxation processes have significant contribution from both EY and DP mechanisms.

## 9.2 Spin Transport in 1L hBN/Gr/hBN Heterostructure

The 1L hBN/Gr/hBN stack is prepared via the dry pick-up transfer method, explained in Ch. 5. The detailed analysis of the charge and spin transport measurements is described in ref.[10]. I will only mention the key features of this measurements.

Due to the full encapsulation of the graphene flake, between the bottom-hBN substrate and the top-monolayer hBN, it never comes in contact with the chemicals and the external environment which reflects in the homogeneous charge transport and spin transport across different regions of the flake underneath and outside the top gate. This was not the case with the partially encapsulated stacks in ref. [7–9] where the graphene outside the top gated region was uncovered and exposed to



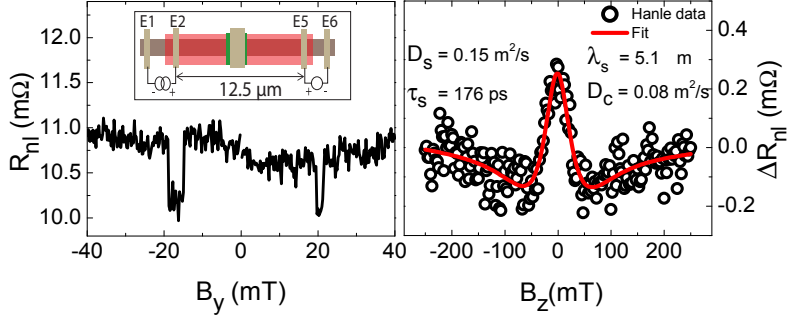


**Figure 9.2:** A spin-valve and the corresponding Hanle signal obtained across the  $12.5 \mu\text{m}$  long spin-transport channel.

the polycarbonate (PC) layer, used for the pick up-transfer method. This PC layers induces n-type doping in the non-encapsulated graphene.

A monolayer (ML) hBN flake, obtained via mechanical exfoliation is supposed to be a crystalline, pinhole free layer, which is theoretically predicted to be suitable for spin injection. However, its interface resistance with graphene is very low ( $< 1 \text{ k}\Omega - \mu\text{m}^2$ ), which is of the order of the flake resistance. This puts the hBN/graphene interface in the conductivity mismatch regime where the spins can flow back into the FM contact and relax in there. In case of oxide tunnel barriers having contact resistance in this range, the spin transport is observed only between the injector and detector electrodes with the pinhole dominated oxide tunnel barriers. Most of the spin accumulation at the detector is relaxed by the detector. However, for the monolayer hBN barriers, even in the conductivity mismatch regime, this is not case as the spin transport is observed over a long distance up to  $12.5 \mu\text{m}$ , as shown in Fig. 9.2 where the spins have to travel through the spin transport channel which has 4 contacts in the mismatch regime and they could induce a significant spin relaxation in the presence of pinholes and would hinder the observation of spin-transport over such a long distance. This indicates that in addition to the contact-induced spin relaxation, the quality of graphene underneath the contact is also crucial. Therefore, we attribute the observed long-distance spin-transport to a clean graphene-hBN interface and the pinhole free nature of the ML hBN flake.

### 9.3 Spin Transport in Bilayer hBN/Gr/hBN Heterostructure

In order to circumvent the effect of the contact-induced spin-relaxation and to improve the spin-injection efficiency of the tunneling contacts, we go for an obvious

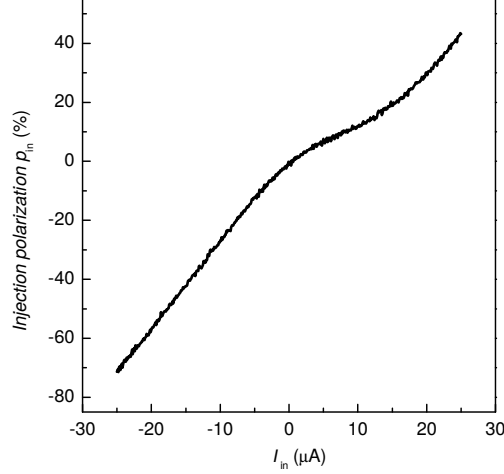


**Figure 9.3:** Bias enhanced differential spin-injection polarization of an injector contact,  $p_{in}$  as a function of  $I_{in}$ .

choice, i.e., replacing the single layer hBN with the bilayer hBN, and prepare a fully encapsulated bottom hBN substrate/graphene/bilayer-hBN heterostructure and deposit 55 nm thick cobalt on it, as described in detail in ref. [1]. The device schematic is shown in Fig. 9.1. We first characterize the charge and spin-transport properties via the low-frequency lock-in detection method and, get a very small spin-signal  $\Delta R_{NL} \sim 50\text{-}100$  m $\Omega$ . However, we obtain decent spin-transport parameters, e.g.,  $D_s \sim 0.04$  m $^2$ s $^{-1}$  and  $\tau_s \sim 0.9$  ns ( $\lambda_s = \sqrt{D_s \tau_s} \sim 6$   $\mu$ m). It initially suggests a low contact polarization.

In order to explore the effect of a static electric field on the spin-injection process, predicted in the recent theoretical proposals [13], we apply a fixed dc bias across the injector contact, and observe an enhancement in the spin-signal while increasing the magnitude of the applied bias. Note that the lock-in detection is only sensitive to the ac signal, the application of the dc bias does not affect the measured signal with respect to additional dc spin-injection. The observed enhancement in  $\Delta R_{NL}$ , therefore, can be attributed to the enhanced differential spin-injection efficiency or the modified spin-transport, following the equation:

$$\Delta R_{NL} = \frac{p_i p_d R_{sq} \lambda_s e^{-\frac{L}{\lambda_s}}}{2w} \quad (9.1)$$

Next, we perform the Hanle measurements to explore the effect of the applied dc

bias on the spin-transport and measure the Hanle curves at different  $I_{dc}$ . However, we do not see any significant change in  $D_s$  and  $\tau_s$  with respect to the applied bias and can unambiguously ascertain the enhanced  $\Delta R_{NL}$  to the enhanced contact polarization. We, not only observe an enhanced polarization with the bias magnitude but also see a sign reversal of the spin-signal as the polarity of the dc signal changes, which means the contact polarization changes its sign around zero bias. Even, for  $I_{dc} < 0$ , the polarization magnitude enhances in the opposite direction with the bias and does not seem to saturate, as shown in Fig.9.3. This behavior is not observed before and is unique to the bilayer nature of the hBN tunnel barrier. When we extract the differential injection polarization as a function of bias, it reach up to the high magnitudes of about 70%.

Now, we apply the same procedure on the detector, i.e. when the detector is biased with a dc current, the differential detection efficiency also enhances like the differential spin-injection efficiency and even reaches more than 100%. The observed behavior is quite surprising and cannot be explained within the available theoretical framework. For the exfoliated 2L-hBN/graphene/hBN heterostructures, we observe a dramatic increase in the spin-polarization of the contacts with the application of the bias. We repeat the same experiment for the monolayer and trilayer hBN and do not observe such bias dependence. We attribute this behavior specific to the bilayer nature of the hBN tunnel barrier.

In order to explore further, whether the observed behavior is a feature of the layer thickness or it also depends on the quality and the relative alignment of the two individual monolayers, we prepare 2L-CVD hBN/Graphene/bottom hBN heterostructures. First, the graphene/bottom hBN stack is prepared via the dry pick-up transfer method like before. The 2L-hBN tunnel barrier is transferred onto the graphene-hBN via the wet transfer method. The fabrication details are provided in [14]. In contrast with the exfoliated 2L-hBN, for the 2L-CVD hBN tunnel barrier where the two layers are obtained by transferring the two CVD monolayers on each other, the bias-dependent differential spin-injection polarization does not change its sign around zero bias and it only increases at negative bias (refer to Mallik thesis for details). It marks a clear distinction between the 2L-exfoliated and CVD hBN tunnel barriers with respect to the spin-injection processes. This can be attributed to the random crystallographic orientation and the individual crystal quality of the two-layer CVD hBN tunnel barriers, compared to the exfoliated 2L-hBN tunnel barriers.

## 9.4 Spin-relaxation in all Exfoliated hBN/graphene/hBN Heterostructures

We perform spin-transport measurements in fully encapsulated hBN/graphene/hBN heterostructures where the top layer has served both as an encapsulating layer and a

tunnel barrier and the bottom hBN serves as a impurity-free, smooth substrate. For this architecture, one would expect the best quality of graphene, which never comes in contact with any lithographic impurity, with a minimal effect of the contacts due to high quality tunnel barriers. Here, we would like to make a general remark that the substrate quality does not seem significantly affect the  $\tau_s$  in graphene. However, it can improve the diffusion constant  $D$ , due to improved sample quality. For example, Zomer *et al.* [6] achieve a high mobility (also high  $D$ ) for graphene on hBN. But they do not observe a high  $\tau_s$ , possibly because of using the oxide tunnel barriers. On the other hand Singh *et al.* [11] measure the  $\tau_s$  in nanoseconds even with graphene on SiO<sub>2</sub> substrate with the high quality pinhole free hBN tunnel barriers, marking the importance of the tunnel barrier quality.

For 1L-hBN encapsulation, we achieve  $\tau_s \sim 170$  ps with a mobility around 10,000 cm<sup>2</sup>V<sup>-1</sup>s<sup>-1</sup>, and for the 2L-hBN encapsulation,  $\tau_s \sim 170$  ps and a mobility < 5000 cm<sup>2</sup>V<sup>-1</sup>s<sup>-1</sup>. Based on the obtained values, we believe that we have been able to reduce the contact induced spin-relaxation, by increasing the thickness of the tunnel barriers from 1L to 2L. But, such a thin encapsulation from the top is not optimal for preventing the impurities from contaminating the graphene and affecting the spin-transport.

## 9.5 Spin-relaxation in 2L-CVD hBN/Graphene/thick hBN Heterostructures

For the 2L-CVD hBN/graphene/bottom-hBN heterostructures, we achieve graphene-mobility < 3000 cm<sup>2</sup>V<sup>-1</sup>s<sup>-1</sup> with  $\tau_s$  in the range of 90 ps-400 ps, depending on the carrier density, sample quality and contact resistance. Again, for the samples with low contact resistance, we observe a reduced  $\tau_s$ . A commonly observed low  $\tau_s$  for these samples is attributed to the poor mobility of the exfoliated graphene due to the wet transfer method. In order to study the relative contribution of the Elliot-Yafet (EY) and Dyakonov-Perel (DP) mechanism [6], we analyze the spin-relaxation ( $\tau_s$ ) and momentum relaxation ( $\tau_p$ ) dependence with following relation:

$$\frac{\varepsilon_F^2 \tau_p}{\tau_s} = \Delta_{EY}^2 + \left( \frac{4\Delta_{DP}^2}{\hbar^2} \right) \varepsilon_F^2 \tau_p^2 \quad (9.2)$$

where  $\varepsilon_F$  is the Fermi energy of graphene, which can be calculated from the carrier density  $n$ , using the relation  $\varepsilon_F = \hbar v_F \sqrt{\pi n}$ , with the Fermi velocity  $v_F = 10^6$  m/s.  $\Delta_{EY}$  and  $\Delta_{DP}$  are the spin-orbit strengths of the EY and DP mechanisms, respectively. As shown in Fig. 9.4, using Eq. 9.2, we extract  $\Delta_{EY}$  and  $\Delta_{DP}$ , and now, the respective spin-relaxation rates  $\tau_{s,EY}^{-1} = \frac{\Delta_{EY}^2}{\varepsilon_F^2 \tau_p}$  and,  $\tau_{s,DP}^{-1} = \frac{4\Delta_{DP}^2 \tau_p}{\hbar^2}$  can be calculated. We find almost equal spin relaxation rates for both the mechanisms in the order of

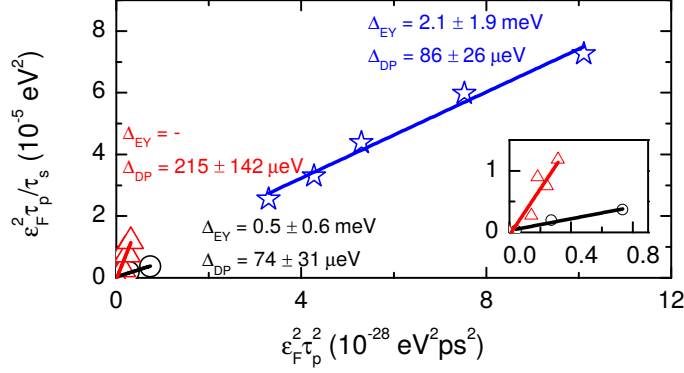


**Figure 9.4:** The linear fits (solid lines) of the data using the Eq. 9.2 give the strengths of the EY and DP spin relaxation mechanisms for three different devices. The inset shows the data and fits close to zero. For the data in red, a good fit was not obtained with Eq. 9.2, due to deviation from the linear behavior. Therefore, we cannot comment on the magnitude of the EY mechanism. Still, we could obtain the estimate of the DP mechanism from the slope.

$10^9 \text{ s}^{-1}$ , concluding that the spin-relaxation in these samples is not uniquely dominated by the either of the mechanisms.

## 9

## 9.6 Conclusions

To summarize, we measure the spin-transport in graphene/hBN heterostructures using the exfoliated mono- and bi-layer hBN tunnel barriers, and the CVD two-layer hBN tunnel barriers. For the exfoliated tunnel barriers, we observe an enhanced  $\tau_s \sim 1 \text{ ns}$ , on increasing the number of layers upto bilayer hBN. This could be due to the combined effect of a reduced contact-induced spin-relaxation and improved screening of the encapsulated graphene from the external impurities, both due to enhanced thickness and the contact resistance of the bilayer tunnel barrier. For the samples using CVD 2-layer hBN tunnel barriers, we observe a much reduced  $\tau_s \sim 80\text{-}400 \text{ ps}$ , which we attribute to the contamination of the graphene-flake during the wet transfer process, used for transferring the CVD-hBN onto the graphene/bottom-hBN heterostructures. For these samples, we find similar contribution of the EY and DP spin-relaxation mechanisms with no clear dominance of either of the mechanisms. We also find out via the bias-dependence that exfoliated bilayer hBN is different from the 2-layer CVD hBN tunnel barrier. This can be attributed to the lack of relative crystallographic orientation of two hBN mono-layers and also due to con-

taminations introduced during the wet-transfer process. In order to explore the full potential of the CVD hBN tunnel barriers, the future experiments should involve the dry pick-up transfer of the CVD tunnel barriers also. For a detailed overview of spin-transport in graphene-hBN heterostructures, readers are encouraged to explore the review article [15].

## 9.7 Acknowledgements

We acknowledge J. G. Holstein, H. M. de Roos and H. Adema for their technical assistance. This research work was financed under EU-graphene flagship program (637100) and supported by the Zernike Institute for Advanced Materials and the Netherlands Organization for Scientific Research (NWO).

## References

- [1] M. Gurram, S. Omar, and B. J. v. Wees, "Bias induced up to 100% spin-injection and detection polarizations in ferromagnet/bilayer-hBN/graphene/hBN heterostructures," *Nat. Commun.* **8**, p. 248, Aug. 2017.
- [2] I. M. Vicent, H. Ochoa, and F. Guinea, "Spin relaxation in corrugated graphene," *Phys. Rev. B* **95**(19), p. 195402, 2017.
- [3] D. V. Tuan, F. Ortman, A. W. Cummings, D. Soriano, and S. Roche, "Spin dynamics and relaxation in graphene dictated by electron-hole puddles," *Sci. Rep.* **6**, p. srep21046, 2016.
- [4] A. H. Castro Neto and F. Guinea, "Impurity-induced spin-orbit coupling in graphene," *Phys. Rev. Lett.* **103**(2), p. 026804, 2009.
- [5] C. Ertler, S. Konschuh, M. Gmitra, and J. Fabian, "Electron spin relaxation in graphene: The role of the substrate," *Phys. Rev. B* **80**(4), p. 041405, 2009.
- [6] P. J. Zomer, M. H. D. Guimarães, N. Tombros, and B. J. van Wees, "Long-distance spin transport in high-mobility graphene on hexagonal boron nitride," *Phys. Rev. B* **86**(16), p. 161416, 2012.
- [7] M. Guimarães, P. Zomer, J. Ingla-Aynés, J. Brant, N. Tombros, and B. van Wees, "Controlling spin relaxation in hexagonal BN-encapsulated graphene with a transverse electric field," *Phys. Rev. Lett.* **113**(8), p. 086602, 2014.
- [8] J. Ingla-Aynés, M. H. D. Guimarães, R. J. Meijerink, P. J. Zomer, and B. J. van Wees, "24-um spin relaxation length in boron nitride encapsulated bilayer graphene," *Phys. Rev. B* **92**(20), p. 201410, 2015.
- [9] J. Ingla-Aynés, R. J. Meijerink, and B. J. v. Wees, "Eighty-eight percent directional guiding of spin currents with 90 m relaxation length in bilayer graphene using carrier drift," *Nano Lett.* **16**(8), pp. 4825–4830, 2016.
- [10] M. Gurram, S. Omar, S. Zihlmann, P. Makk, C. Schönenberger, and B. J. van Wees, "Spin transport in fully hexagonal boron nitride encapsulated graphene," *Phys. Rev. B* **93**(11), p. 115441, 2016.
- [11] S. Singh, J. Katoch, J. Xu, C. Tan, T. Zhu, W. Amamou, J. Hone, and R. Kawakami, "Nanosecond spin relaxation times in single layer graphene spin valves with hexagonal boron nitride tunnel barriers," *Appl. Phys. Lett.* **109**, p. 122411, Sept. 2016.
- [12] M. V. Kamalakar, A. Dankert, J. Bergsten, T. Ive, and S. P. Dash, "Enhanced Tunnel Spin Injection into Graphene using Chemical Vapor Deposited Hexagonal Boron Nitride," *Sci. Rep.* **4**, p. srep06146, Aug. 2014.
- [13] Q. Wu, L. Shen, Z. Bai, M. Zeng, M. Yang, Z. Huang, and Y. P. Feng, "Efficient Spin Injection into Graphene through a Tunnel Barrier: Overcoming the Spin-Conductance Mismatch," *Phys. Rev. Appl.* **2**, p. 044008, Oct. 2014.
- [14] M. Gurram, S. Omar, S. Zihlmann, P. Makk, Q. C. Li, Y. F. Zhang, C. Schönenberger, and B. J. van Wees, "Spin transport in two-layer-CVD-hBN/graphene/hBN heterostructures," *Phys. Rev. B* **97**, p. 045411, Jan. 2018.
- [15] M. Gurram, S. Omar, and B. J. van Wees, "Electrical spin injection, transport, and detection in graphene-hexagonal boron nitride van der Waals heterostructures: progress and perspectives," *arXiv:1712.07828 [cond-mat]*, Dec. 2017. arXiv: 1712.07828.

## Chapter 10

# Graphene-WS<sub>2</sub> Heterostructures for Tunable Spin Injection and Spin Transport

### Abstract

*We report the first measurements of spin injection into graphene through a 20 nm thick tungsten disulphide (WS<sub>2</sub>) layer, along with a modified spin relaxation time ( $\tau_s$ ) in graphene in the WS<sub>2</sub> environment, via spin-valve and Hanle spin-precession measurements, respectively. First, during the spin-injection into graphene through a WS<sub>2</sub>-graphene interface, we can tune the interface resistance at different current bias and modify the spin injection efficiency, in a correlation with the conductivity-mismatch theory. Temperature assisted tunneling is identified as a dominant mechanism for the charge transport across the interface. Second, we measure the spin transport in graphene, underneath the WS<sub>2</sub> crystal and observe a significant reduction in the  $\tau_s$  down to 17 ps in graphene in the WS<sub>2</sub> covered region, compared to that in its pristine state. The reduced  $\tau_s$  indicates the WS<sub>2</sub>-proximity induced additional dephasing of the spins in graphene.*



## 10.1 Introduction

Graphene, an ideal material for spin transport due to low spin-orbit coupling and small hyperfine interactions [1, 2], has shown a significant improvement in its spin transport properties over the years [3, 4]. However, tuning of the spin injection and transport properties remains illusive for graphene, inhibiting the demonstration of graphene as a spin-transistor [5]. There is also a rapidly growing interest in other layered two-dimensional materials such as transition metal dichalcogenides (TMDs) due to their novel properties such as presence of band-gap accompanied by a significant spin orbit coupling up to few hundreds of meV, which is lacking in graphene [6–10]. In the absence of an inversion center in the lattice, these materials with an odd number of layers also provide access to the novel physical phenomena related to the valley coupled spin degree of freedom of the charge carriers [11–13], which adds extra functionality to these materials. A combination of graphene with these 2-D materials appears to be a plausible option to overcome the aforementioned shortcomings.

In recent years, there have been a lot of studies on graphene-2-D material heterostructures demonstrating novel charge transport properties across the interface [14–17]. The 2-D materials such as hexagonal boron nitride (h-BN) can be used in spintronic devices as tunnel barriers for spin injection in graphene, replacing the conventional oxide tunnel barriers [18–20]. In contrast to an insulating tunnel barrier, the use of band-gap 2-D semiconductors such as TMDs (i.e. MoS<sub>2</sub>, WS<sub>2</sub>) during spin-injection, can lead to attractive features such as tuning of the interface resistance along with the induced spin orbit coupling at the graphene-TMD interface [21–27], which in turn can modulate the spin-injection efficiency as well as the spin transport properties in graphene. Recently reported weak localization [28], Shubnikov-de Haas magnetoresistance measurements [25] and spin-Hall experiments [29] on graphene-WS<sub>2</sub> (Gr-WS<sub>2</sub>) heterostructures reveal that the spin-lifetime ( $\tau_s$ ) in graphene is greatly reduced from nanoseconds to picoseconds due to significantly induced spin-orbit coupling ( $\sim 5$ -15 meV) in graphene. Recent reports on spin-transport in Graphene-MoS<sub>2</sub> structures demonstrated via spin-valve measurements that the MoS<sub>2</sub> flake in the spin transport channel acts as a controllable spin-sink [30, 31].

Among the TMDs, WS<sub>2</sub> has higher spin-orbit coupling magnitude than in MoS<sub>2</sub> and lower SOC than in WSe<sub>2</sub>. Therefore, we expect that a sufficient SOC ( $\sim$  meV) can be induced in graphene in contact with a WS<sub>2</sub> surface, which is expected to reduce the spin-relaxation time in graphene between 1-10 ps [28]. However, WSe<sub>2</sub> can introduce much stronger SOC [25, 27], which would reduce the spin relaxation time down to 0.1 ps and hinder a measurable effect of TMD induced SOC in graphene, via nonlocal spin transport measurements. Therefore, to observe a measurable effect of the TMD -induced SOC on spin-transport in graphene, we fabricate the Gr-TMD heterostructures, using WS<sub>2</sub> as a TMD.

We report the first measurements of spin injection into graphene through a 20 nm thick WS<sub>2</sub> layer, along with a reduced spin relaxation time in graphene in the WS<sub>2</sub> environment, via Hanle spin-precession measurements. By applying a voltage bias between graphene and the semiconducting TMD layer, we tune the interface resistance and modify the spin injection efficiency. We measure a higher spin signal for a higher interface resistance at the injector. In this way spins cannot flow back and get relaxed at the interface or in the bulk WS<sub>2</sub>, suppressing the contact induced spin relaxation. We also perform temperature dependent measurements for a Gr-WS<sub>2</sub> heterostructure and find that the ideality factor, which is a measure of thermionic emission of the charge carriers across a potential energy barrier, is much greater than one. It indicates that there are other transport mechanisms such as temperature or field assisted tunneling across the interface, contributing to the spin injection process in graphene. We also measure the spin transport in graphene underneath the WS<sub>2</sub> crystal, where we inject and detect the spin accumulation in graphene using the ferromagnetic tunneling contacts. We observe a significant reduction in  $\tau_s$ , when the spins travel across the WS<sub>2</sub> encapsulated region, compared to  $\tau_s$  obtained for the non-encapsulated region. The reduced  $\tau_s$  suggests towards an induced spin-orbit coupling/ spin absorption at the Gr-WS<sub>2</sub> interface [25, 27, 28].

## 10.2 Sample Preparation

We prepare graphene-WS<sub>2</sub> heterostructures via a pick up transfer method) using a single layer graphene and a thick WS<sub>2</sub> flake, obtained via scotch tape exfoliation procedure. The graphene flake is exfoliated from a bulk HOPG (highly oriented pyrolytic graphite) ZYA grade crystal (supplier: SPI) onto a pre-cleaned Si-SiO<sub>2</sub> substrate ( $t_{\text{SiO}_2}$ =300 nm). A single layer is identified via an optical microscope. A WS<sub>2</sub> flake (supplier: HQ Graphene) is exfoliated on a viscoelastic PDMS (polydimethylsiloxane) substrate. The freshly cleaved WS<sub>2</sub> flake on the PDMS is brought in contact with the graphene flake in a transfer stage. Since the adhesion of WS<sub>2</sub> on the PDMS stamp is relatively weak compared to the GrW van der Waals interaction and the SiO<sub>2</sub>-WS<sub>2</sub> adhesion, the flake is easily stacked onto the desired graphene flake. As a result a smooth interface is formed, which is identified with an atomic force microscope (AFM). This dry transfer method enables the formation of a clean and chemical free Gr-WS<sub>2</sub> interface, which has been reported to have less impurities and superior charge transport properties [32] compared to the stacks prepared via CVD grown 2-D materials [14]. Moreover, we transfer a thick WS<sub>2</sub> flake onto graphene, in order to reduce the bubble formation during the transfer process [33]. The prepared stacks are annealed at 250°C for 5 hours in an Ar-H<sub>2</sub> environment for removing the residue polymers. However, for most of the stacks, we only observe that the uncovered graphene and WS<sub>2</sub> flake looks more clean after the annealing steps, leaving the

graphene-WS<sub>2</sub> interface more or less similar to that before the annealing (Fig. 10.1).

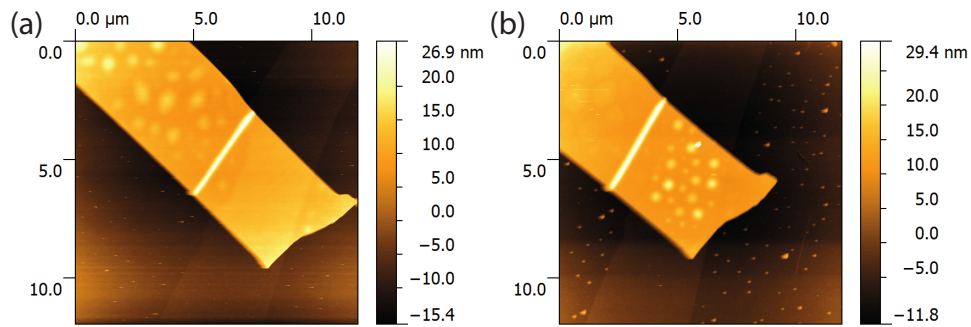


**Figure 10.1:** A graphene-WS<sub>2</sub> stack (a) before annealing and after (b) annealing. For the thin WS<sub>2</sub> flakes ( $t_{WS_2} \sim 5\text{nm}$ ), the graphene flake underneath the WS<sub>2</sub> flake can be seen through. Here, the annealing step does not seem to improve the interface quality significantly.

For the stack with a thick WS<sub>2</sub>  $\sim 20\text{ nm}$  flake, transferred onto a graphene flake, we do not see a bubble formation at the graphene-WS<sub>2</sub> interface (Fig. 10.2). Still the furnace annealing is performed to clean the polymer residues from the uncovered surfaces.

The ferromagnetic (FM) contacts are patterned both on graphene and on WS<sub>2</sub> via electron beam lithography on the PMMA (poly (methyl methacrylate)) coated Gr-WS<sub>2</sub> stack. Then, 0.6 nm of aluminum (Al) is deposited in two steps, each step of 0.3 nm of Al deposition followed by in-situ oxidation by pure O<sub>2</sub> to form an oxide

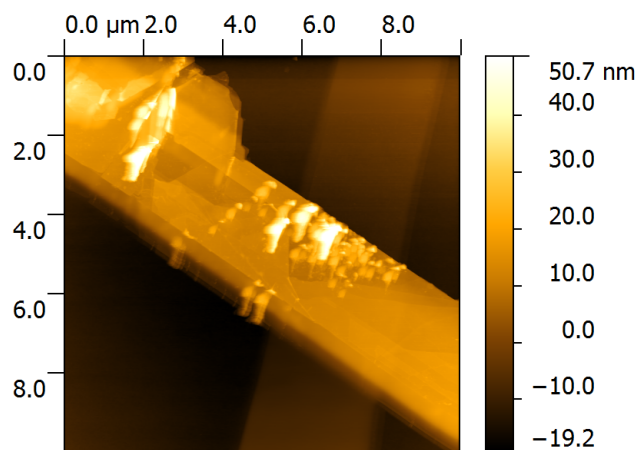


**Figure 10.2:** A graphene-WS<sub>2</sub> stack formed with thick WS<sub>2</sub> flakes ( $t_{WS_2} \sim 20\text{nm}$ )

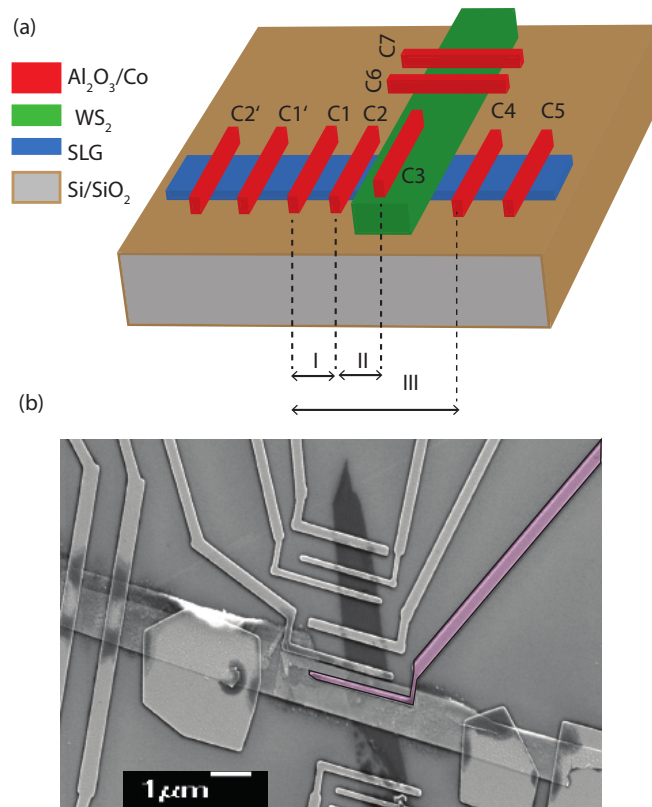


**Figure 10.3:** (a) A schematic of graphene- $WS_2$  heterostructure with ferromagnetic contacts with  $Al_2O_3$  tunnel barriers between cobalt and graphene ( $WS_2$ ). The regions labeled as I, II and III are  $2.0 \mu m$ ,  $2.5 \mu m$  and  $6.5 \mu m$  long, respectively. The  $WS_2$  covered region is  $\sim 3.0 \mu m$ . (b) A scanning electron microscope (SEM) image of the stack with the ferromagnetic contacts. The pink electrode is used as a spin injector into graphene through  $WS_2$ .

tunnel barrier to overcome the conductivity mismatch problem [34]. On top of the oxide barrier we deposit 55 nm of cobalt for the spin polarized contacts. To prevent the oxidation of the ferromagnetic electrodes, the contacts are covered with 3 nm thick aluminum layer.

### 10.3 Measurement

We characterize the charge and spin transport in graphene at three different regimes, labeled as I, II and III in Fig. 10.3(a): i) non-encapsulated region (I) as a reference; ii) through the  $WS_2$  crystal (II), where the charge/spin current is injected from a

ferromagnet C3 on top of the TMD crystal into graphene and is detected in graphene (Fig. 10.3(b))<sup>1</sup>, iii) across the encapsulated region ( $\sim 3 \mu\text{m}$ ) (III), where a charge/spin current is injected in graphene on one side of the TMD via contact C2 and is detected on the other side via contact C4.

All the measurements are performed using a cryostat in vacuum ( $\sim 1 \times 10^{-7}$  mbar) at different temperatures between 4K and 297K. The graphene resistivity was characterized via lock-in detection ( $f=27.7$  Hz) using a four probe method by applying a current between contacts C2-C2' and measuring a voltage drop between C1-C1', in order to eliminate the effect of the contacts. The graphene sheet resistance ( $R_{\text{sq}}$ ) for the non-encapsulated region (region I) is  $\sim 400 \Omega$  (charge carrier density  $\sim 10^{13} \text{cm}^{-2}$ <sup>2</sup> where ) i.e. three times lower than for region III ( $\sim 1.2 \text{k}\Omega$ ), indicating that graphene is less doped underneath the WS<sub>2</sub> crystal. The contact resistances for the FM electrodes were characterized using a three probe connection scheme, where an AC current is applied between contacts C1-C2 and a voltage drop is measured between C1-C2'. For the FM contacts on graphene, we measure a very low contact resistance ( $R_{\text{c}}^{\text{FM}} \sim 200 \Omega$ ), putting our contacts in the so called conductivity mismatched regime where the contacts influence the spin transport properties of graphene [34]. Since we also fabricate the contacts on the WS<sub>2</sub> flake outside the WS<sub>2</sub>-graphene interface (i.e. contacts C6-C7 on WS<sub>2</sub> in Fig. 10.3(a)), the channel resistance ( $R_{\text{sq}}^{\text{WS}_2} \sim 70 \text{k}\Omega$ ) and the contact resistance of the FM electrodes on the WS<sub>2</sub> flake ( $\sim 2\text{-}3 \text{k}\Omega$ ) can be characterized independently. The I-V behavior of the FM contacts, both on graphene and on WS<sub>2</sub> is characterized independently using a Keithley 2410 DC source meter. The measured I-V behavior has a linear dependence at low bias, which becomes slightly non-linear at higher bias values ( $R_{\text{c}} \leq 4\text{k}\Omega$ ), as shown in Fig. 10.4.

Next, we measure a non-linear I-V behavior across the graphene-TMD interface via FM contacts (Fig. 10.5(a)) which is clearly different from the I-V behavior at the WS<sub>2</sub>-AlO<sub>2</sub>-Co interface in Fig. 10.4, and is dominated by the Gr-WS<sub>2</sub> interface. The observed non-linearity can be easily attributed to the presence of a potential energy barrier present only at the Gr-WS<sub>2</sub> interface [26, 32, 35].

Spin transport is measured in a four probe non-local detection scheme i.e. in region I, by applying a current between contacts C1 and C2' and measuring the voltage associated with the spin-accumulation between contacts C2-C5 (Fig. 10.3(a)). This method decouples the paths of the spin and charge transport and thus minimizes the contribution of the charge signal to the measured spin signal [36]. For the spin valve measurements, we first apply an in-plane high magnetic field ( $B_{\parallel}$ ) along the

<sup>1</sup>A SEM image was recorded after the measurements. The graphene and WS<sub>2</sub> flake were damaged after the measurements during storage.

<sup>2</sup>Since we do not have a working back gate for the reported sample, we estimate the carrier density  $n$  from the relation  $n = 1/R_{\text{sq}}e\mu$ , where  $e$  is the electron charge and  $\mu$  is the field effect mobility. Here, we take  $\mu \sim 5000 \text{cm}^2\text{V}^{-1}\text{s}^{-1}$  which is usually obtained for good quality graphene samples on SiO<sub>2</sub> substrate

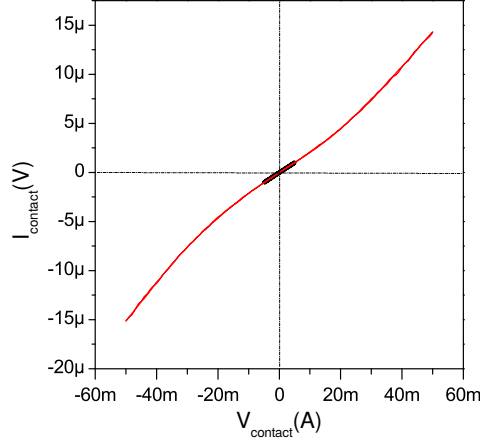


**Figure 10.4:** I-V characteristics of a Co/AlO<sub>x</sub> contact on the WS<sub>2</sub> flake.

easy axes of the ferromagnets to align their relative magnetization. Then, the magnetic field is swept in the opposite direction to reverse the magnetization of the ferromagnets selectively based on their coercivity. We measure a sharp transition in the non-local signal ( $R_{NL} = V_{NL}/I_{AC}$ ) when the individual electrodes switch their magnetization direction (Fig. 10.6(a)). For the Hanle precession measurements, an out of plane magnetic field ( $B_{\perp}$ ) is applied to precess the injected spins around the applied field for a fixed magnetization configuration of the ferromagnetic electrodes. While diffusing the spins precess around the applied magnetic field and dephase, showing a decrease in the magnitude of measured spin accumulation for higher fields.

Due to a barrier formation at the Gr-WS<sub>2</sub> interface, we can modulate the barrier resistance for difference bias currents and therefore the spin injection efficiency. The spin transport measurements are performed in the same configuration for region II. In order to modulate the interface resistance, we vary the DC injection current ( $I_{DC}$ ) between contacts C3-C5 (Fig. 10.3(a)), while keeping a fixed small alternating current ( $i_{ac} \sim 0.5 \mu A$ ) and detect the diffused spin accumulation potential via lock-in detection between C2 and the reference electrode, which only is sensitive to the excitation frequency of  $i_{AC}$ . In order to measure the spin transport across the encapsulated region, a fixed AC current is injected at contact C2 and the spin transport is measured at contact C4.

Hanle precession measurements for region I, II and III are shown in Fig. 10.6 and Fig. 10.7, respectively. With these measurements, we fit the Hanle signal  $\Delta R_{NL} = (R_P - R_{AP})/2$ , where  $R_{P(AP)}$  is the Hanle signal measured for the parallel (anti-parallel) magnetization of the the injector-detector pair. We extract the spin diffu-

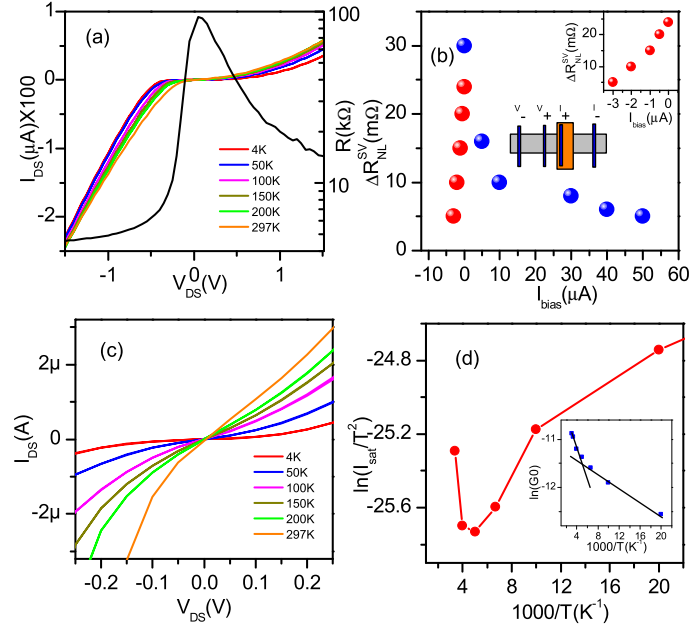


**Figure 10.5:** (a) 2-probe I-V measurements for the graphene-WS<sub>2</sub> interface at different temperatures. Here WS<sub>2</sub> is the positive electrode. On the right y-axis, the interface resistance ( $dV_{DS}/dI_{DS}$ ) is plotted as a function of  $V_{DS}$  for room temperature shows a non-linear behavior. (b) A plot of non-local spin signal ( $\Delta R_{NL}^{SV} = R_P - R_{AP}$ ) as a function of DC bias current, injected through WS<sub>2</sub>. The measurement scheme is shown in the cartoon. The current is applied between contacts C3-C5 of Fig. 10.3(a) and a voltage is measured between contacts C2-C2'. The spin signal is significantly reduced for a lower interface resistance. A zoomed in version for the negative  $I_{bias}$ -spin signal dependence is shown in the inset. (c) Zoomed in  $I_{DS} - V_{DS}$  plot around zero bias shows more symmetric behavior, suggesting the dominance of tunnel transport over thermionic emission. (d)  $\ln(I_{DS})$  versus  $1000/T$  plot shows a cross-over temperature ( $T_{cross}$ ) around 250K from negative to positive slope, which is a signature of cross over from thermionic emission to thermal assisted tunneling in a broad temperature range. In the inset, the slope of logarithmic conductance changes around the same  $T_{cross}$ , implying the same cross-over of conduction mechanisms.

sion coefficient  $D_s$  and spin relaxation time  $\tau_s$ , following the procedure described in ref. [36] and use them to calculate the contact polarization ( $P$ ). For region I, we obtain  $D_s \sim 0.09 \text{ m}^2/\text{s}$ ,  $\tau_s \sim 40 \text{ ps}$  and  $P \sim 2.3\%$ , for region II,  $D_s \sim 0.09 \text{ m}^2/\text{s}$ ,  $\tau_s \sim 17 \text{ ps}$  and  $P \sim 2.7\%$  and for region III, we observe a  $D_s \sim 0.1-0.5 \text{ m}^2/\text{s}$ ,  $\tau_s \sim 18 \text{ ps}$  and  $P \sim 0.3\%$ . For region III, the  $D_s$  value obtained via Hanle fitting, is sensitive to the selection of the spin-independent background, which cannot be uniquely deter-

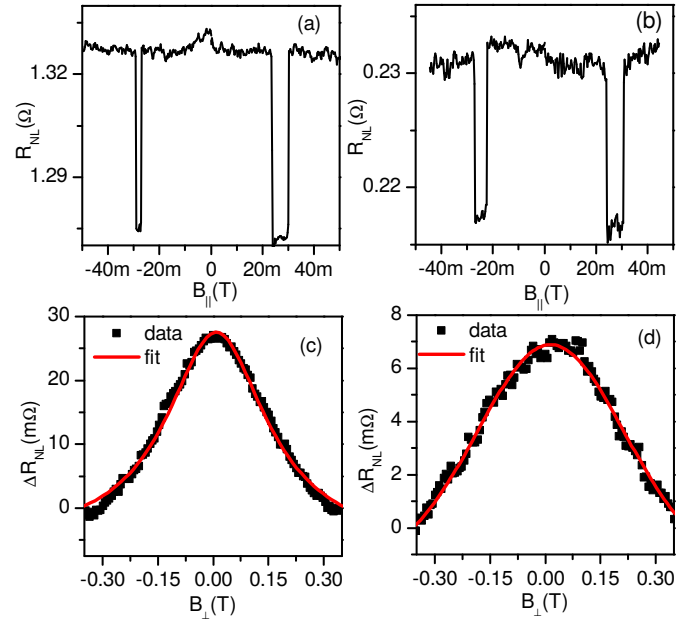


**Figure 10.6:** (a) Spin-valve and (c) Hanle precession measurements for non-encapsulated part (region I), with the FM contacts used for spin transport. (b) spin-valve and (d) Hanle measurements for region II, where  $WS_2$ , inserted between FM contacts and graphene is used as spin-injector and the FM contact on graphene is used for measuring the spin accumulation.

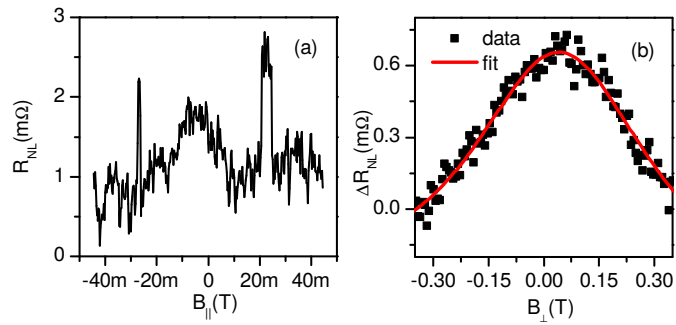


**Figure 10.7:** (a) Spin valve and (b) Hanle measurement for the encapsulated part (region III), where a spin current is injected via a FM contact C2 (Fig. 10.3(a)) on one side of the  $WS_2$  crystal and is measured via contact C4 on the other side after traveling underneath the  $WS_2$  environment.



mined here. However, we consistently obtain a reduced  $\tau_s$  for region III  $\sim 17$  ps-20 ps. In conclusion, a reduced  $\tau_s \leq 20$  ps is obtained via Hanle measurements for both region II and III where the spin-transport occurs underneath the WS<sub>2</sub> flake. Here, we would like to emphasize that a low  $\tau_s$  observed in region I is probably due to the contact induced spin relaxation. For a lower contact resistance the spins can easily flow back to the contact and get relaxed, and one would obtain a lower  $\tau_s$ . The actual value for  $\tau_s$  can be estimated by following the procedure as described by Maassen *et al.* [34]. In this method, the effect of the contact induced spin relaxation can be quantified via ' $R'$ ' parameter ( $R = R_c \lambda_s / R_s$ ), which is a ratio of the contact resistance  $R_c$  to the spin resistance ( $R_s$ ) of the transport channel i.e.  $R_s = R_{sq} \lambda_s / W$ . Here  $\lambda_s$  is the spin relaxation length in graphene, and  $W$  is the width of the graphene flake. Based on this method, the actual  $\tau_s$  will be three times higher than the fitted  $\tau_s$  for the non-encapsulated region. For region II and III, the correction factor is  $\sim 1$ , implying that the  $\tau_s$  obtained via Hanle fitting procedure represents the true spin relaxation time, confirming that the spin transport is affected significantly underneath the high spin-orbit coupled material i.e. WS<sub>2</sub> in our case.

In order to determine the nature of charge and spin transport through the Gr-WS<sub>2</sub> interface, we characterize the interface resistance as a function of applied bias and temperature (Fig. 10.5(a)). There is an increase in the zero bias interface resistance from 80 k $\Omega$  -500 k $\Omega$  from RT to 4K. A non-linear current-voltage characteristics of the Gr-WS<sub>2</sub> heterostructure indicates a potential energy barrier formation at the interface. We analyze the interface I-V characteristics with the standard Schottky-Mott model at higher bias ( $V_{DS} > 3k_B T/e$ ), which is described by the following equation:

$$I_{DS} = AA^* T^2 \exp \frac{eV_{DS}}{nk_B T} \exp \frac{-e\phi_B}{k_B T} \quad (10.1)$$

where  $I_{DS}$  is the current flowing through Gr-WS<sub>2</sub> interface,  $A$  is the area of the interface,  $V_{DS}$  is the voltage drop across the interface,  $n$  is the ideality factor ( $n=1$ , for ideal Schottky diode),  $A^*$  is the Richardson constant,  $\phi_B$  is the effective Schottky barrier height at the Gr-WS<sub>2</sub> interface,  $e$  is the electronic charge,  $k_B$  is the Boltzmann constant and  $T$  is the temperature of the device. For our device, we use Co/AIOx as a contact for source and drain, which forms an ohmic contact with graphene, possibly due to high pinhole density at the oxide-graphene interface. However, it can form a Schottky barrier at the FM contact-WS<sub>2</sub> interface. For this purpose, a DC source meter (KTH 2410) is used. For the FM contacts on WS<sub>2</sub>, we see a linear I-V behavior for WS<sub>2</sub> in a low bias regime which becomes slightly non-linear at high bias values (Fig. 10.4). Still, the observed non-linearity is not as strong as measured for Gr-WS<sub>2</sub> interface.

From the asymmetric I-V plot of the Gr-WS<sub>2</sub> interface, one can easily say that for the positive bias regime, where the electrons enter from graphene to the TMD, they face the higher energy barrier compared to the situation for the negative bias

when they enter from the oxide tunnel barrier to WS<sub>2</sub>. To estimate the voltage drop across the barrier, we extract the channel series resistance, using the analysis described in ref. [37]. We extract the ideality factor  $n$  and the saturation current  $I_0 = AA^*T^2 \exp \frac{-e\phi_B}{k_B T}$  for different temperatures from the slope and the intercept of  $\ln(I_{DS})$ - $V_{DS}$  curve of Eq. 10.1. The ideality factor  $n$  is highly temperature dependent ( $\geq 3$ ), exhibiting a strong deviation from thermionic emission theory at lower temperatures. In Fig. 10.5(d),  $\ln(I_0/T^2)$  versus  $1000/T$  plot shows a positive slope for the major temperature range and the slope is only negative for very high temperatures, indicating that the electron transport mechanism in our sample is dominated by thermally assisted tunneling or field assisted tunneling, not by the thermionic emission. We also try to fit the zero-bias conductance-temperature dependence (inset Fig. 10.5 (d)) with the tunnel transport model, described in ref.[35]. A plot of temperature-zero-bias conductivity shows the crossover of the two mechanisms around 200 K around the same temperature as reported in the ref. [15]. However, a reasonable agreement between the data and the fit is not obtained, possibly because of the moderate temperature dependence of the conductivity at the lower temperature. All the presented analyses support temperature assisted tunneling as a dominant charge transport mechanism across the Gr-WS<sub>2</sub> interface.

Novelty of the Gr-WS<sub>2</sub> interface is its bias dependent resistance, which in combination with the FM contact can be used to modify the conductivity mismatch condition for the spin injection. Since the charge transport across the interface is dominated by temperature assisted tunneling, it is possible to inject spins into graphene through TMD due to small Schottky barrier and low depletion width at the interface, in contrast to the case of Si spin-valves, where no spin transport is measured due to a higher Schottky barrier at the ferromagnet-silicon interface of the injector and the detector electrodes [38, 39]. In order to bias the interface, we use a DC current source at different currents with a fixed small AC current ( $0.5 \mu\text{A}$ ) superimposed on it. The spin accumulation is measured non-locally via the lock-in detection. The bias-dependent spin-valve signal is shown in Fig. 10.8

On changing the bias current, the interface resistance is modulated from  $15 \text{ k}\Omega$  -  $100 \text{ k}\Omega$  for the positive current bias and to  $4 \text{ k}\Omega$  for the negative bias. The change in the resistance is much sharper for the negative bias regime. The spin signal decreases slowly from  $50 \text{ m}\Omega$  to  $5 \text{ m}\Omega$  for the positive current range of  $50 \mu\text{A}$ . For the negative bias, we observe similar change in within  $5 \mu\text{A}$  current range, suggesting a strong correlation between the interface resistance and spin injection efficiency. However, for the oxide tunnel barriers with  $4 \text{ k}\Omega$  interface resistance, one can get a reasonable spin injection, as this situation is not a poor conductivity mismatch. Even for smaller interface resistance in region I, we were able to achieve spin injection. A negligible spin injection for a reasonable interface resistance, suggests towards either low spin polarization of the interface as it is not a pure tunneling or additional spin-relaxation underneath the WS<sub>2</sub> encapsulated region. Also, we were unable to detect any spin

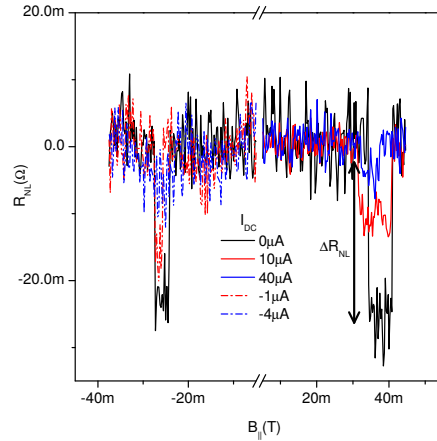


**Figure 10.8:** Spin valve measurements as a function of the DC current bias. Spin valve measurements for different positive (negative) DC bias values are plotted on the right (left) half of the plot ( $B_{||} > 0\text{T}$  ( $< 0\text{T}$ )).

accumulation on the other side of WS<sub>2</sub> (contact C4), probably due to the combined effect of poor spin injection through the TMD, accompanied by relatively long distance experienced by spins underneath WS<sub>2</sub>, before getting detected. However, from the present measurements, we cannot comment on the the source of enhanced spin relaxation process.

10

## 10.4 Conclusions

In conclusion, we demonstrate that spin transport across the WS<sub>2</sub> encapsulated region and the spin transport is reduced in the proximity of the TMD crystal. At present, we cannot comment on the source of additional spin-relaxation whether it is caused by proximity induced spin orbit coupling or due to spin absorption via the TMD. We also demonstrate the use of WS<sub>2</sub> as a bias dependent spin injector due to the non-linear charge transport properties of Gr-WS<sub>2</sub> interface. Via a temperature-dependent charge transport analysis, we find out that the dominating charge transport mechanism across the interface is thermally assisted tunneling, which helps the spins to tunnel through the Schottky barrier.

## **10.5 Acknowledgement**

We acknowledge J. G. Holstein, H. M. de Roosz and H. Adema for their technical assistance. This research work was financed under EU-graphene flagship program (637100) and supported by the Zernike Institute for Advanced Materials and the Netherlands Organization for Scientific Research (NWO).

## References

- [1] C. Ertler, S. Konschuh, M. Gmitra, and J. Fabian, "Electron spin relaxation in graphene: The role of the substrate," *Phys. Rev. B* **80**, p. 041405, July 2009.
- [2] D. Huertas-Hernando, F. Guinea, and A. Brataas, "Spin-Orbit-Mediated Spin Relaxation in Graphene," *Phys. Rev. Lett.* **103**, p. 146801, Sept. 2009.
- [3] P. J. Zomer, M. H. D. Guimarães, N. Tombros, and B. J. van Wees, "Long-distance spin transport in high-mobility graphene on hexagonal boron nitride," *Phys. Rev. B* **86**, p. 161416, Oct. 2012.
- [4] J. Ingla-Aynés, M. H. D. Guimarães, R. J. Meijerink, P. J. Zomer, and B. J. van Wees, "24-um spin relaxation length in boron nitride encapsulated bilayer graphene," *Phys. Rev. B* **92**, p. 201410, Nov. 2015.
- [5] S. Datta and B. Das, "Electronic analog of the electrooptic modulator," *Appl. Phys. Lett.* **56**, pp. 665–667, Feb. 1990.
- [6] G. R. Bhimanapati, Z. Lin, V. Meunier, Y. Jung, J. Cha, S. Das, D. Xiao, Y. Son, M. S. Strano, V. R. Cooper, L. Liang, S. G. Louie, E. Ringe, W. Zhou, S. S. Kim, R. R. Naik, B. G. Sumpter, H. Terrones, F. Xia, Y. Wang, J. Zhu, D. Akinwande, N. Alem, J. A. Schuller, R. E. Schaak, M. Terrones, and J. A. Robinson, "Recent advances in two-dimensional materials beyond graphene," *ACS Nano* **9**(12), pp. 11509–11539, 2015.
- [7] H. Jiang, "Electronic band structures of molybdenum and tungsten dichalcogenides by the gw approach," *J. Phys. Chem. C* **116**(14), pp. 7664–7671, 2012.
- [8] X. Xu, W. Yao, D. Xiao, and T. F. Heinz, "Spin and pseudospins in layered transition metal dichalcogenides," *Nat. Phys.* **10**, pp. 343–350, May 2014.
- [9] Z. Y. Zhu, Y. C. Cheng, and U. Schwingenschlögl, "Giant spin-orbit-induced spin splitting in two-dimensional transition-metal dichalcogenide semiconductors," *Phys. Rev. B* **84**, p. 153402, Oct. 2011.
- [10] D. W. Latzke, W. Zhang, A. Suslu, T.-R. Chang, H. Lin, H.-T. Jeng, S. Tongay, J. Wu, A. Bansil, and A. Lanzara, "Electronic structure, spin-orbit coupling, and interlayer interaction in bulk MoS<sub>2</sub> and WS<sub>2</sub>," *Phys. Rev. B* **91**, p. 235202, June 2015.
- [11] L. Bawden, S. P. Cooil, F. Mazzola, J. M. Riley, L. J. Collins-McIntyre, V. Sunko, K. W. B. Hunvik, M. Leandersson, C. M. Polley, T. Balasubramanian, T. K. Kim, M. Hoesch, J. W. Wells, G. Balakrishnan, M. S. Bahramy, and P. D. C. King, "Spin-valley locking in the normal state of a transition-metal dichalcogenide superconductor," *Nat. Commun.* **7**, p. 11711, May 2016.
- [12] W. Yao, D. Xiao, and Q. Niu, "Valley-dependent optoelectronics from inversion symmetry breaking," *Phys. Rev. B* **77**, p. 235406, June 2008.
- [13] Q. H. Wang, K. Kalantar-Zadeh, A. Kis, J. N. Coleman, and M. S. Strano, "Electronics and optoelectronics of two-dimensional transition metal dichalcogenides," *Nat. Nanotechnol.* **7**, pp. 699–712, Nov. 2012.
- [14] W. J. Yu, Z. Li, H. Zhou, Y. Chen, Y. Wang, Y. Huang, and X. Duan, "Vertically stacked multi-heterostructures of layered materials for logic transistors and complementary inverters," *Nat. Mater.* **12**, pp. 246–252, Mar. 2013.
- [15] T. Georgiou, R. Jalil, B. D. Belle, L. Britnell, R. V. Gorbachev, S. V. Morozov, Y.-J. Kim, A. Gholinia, S. J. Haigh, O. Makarovskiy, L. Eaves, L. A. Ponomarenko, A. K. Geim, K. S. Novoselov, and A. Mishchenko, "Vertical field-effect transistor based on graphene-WS<sub>2</sub> heterostructures for flexible and transparent electronics," *Nat. Nanotechnol.* **8**, pp. 100–103, Feb. 2013.
- [16] N. Myoung, K. Seo, S. J. Lee, and G. Ihm, "Large Current Modulation and Spin-Dependent Tunneling of Vertical Graphene/MoS<sub>2</sub> Heterostructures," *ACS Nano* **7**, pp. 7021–7027, Aug. 2013.
- [17] Y.-F. Lin, W. Li, S.-L. Li, Y. Xu, A. Aparecido-Ferreira, K. Komatsu, H. Sun, S. Nakaharai, and K. Tsukagoshi, "Barrier inhomogeneities at vertically stacked graphene-based heterostructures," *Nanoscale* **6**, pp. 795–799, Dec. 2013.
- [18] M. Gurram, S. Omar, S. Zihlmann, P. Makk, C. Schönenberger, and B. J. van Wees, "Spin transport in fully hexagonal boron nitride encapsulated graphene," *Phys. Rev. B* **93**, p. 115441, Mar. 2016.

- [19] M. V. Kamalakar, A. Dankert, J. Bergsten, T. Ive, and S. P. Dash, "Enhanced Tunnel Spin Injection into Graphene using Chemical Vapor Deposited Hexagonal Boron Nitride," *Sci. Rep.* **4**, p. 6146, Aug. 2014.
- [20] C. A. Joiner, P. M. Campbell, A. A. Tarasov, B. R. Beatty, C. J. Perini, M.-Y. Tsai, W. J. Ready, and E. M. Vogel, "Graphene-Molybdenum Disulfide-Graphene Tunneling Junctions with Large-Area Synthesized Materials," *ACS Appl. Mater. Interfaces* **8**, pp. 8702–8709, Apr. 2016.
- [21] P. Goswami, "Spin-orbit coupling and exchange field induced band inversion in graphene on a two dimensional transition metal dichalcogenide substrate," *arXiv:1606.02413 [cond-mat]*, June 2016. arXiv: 1606.02413.
- [22] A. Avsar, J. Y. Tan, T. Taychatanapat, J. Balakrishnan, G. K. W. Koon, Y. Yeo, J. Lahiri, A. Carvalho, A. S. Rodin, E. C. T. O'Farrell, G. Eda, A. H. Castro Neto, and B. Özyilmaz, "Spinorbit proximity effect in graphene," *Nat. Commun.* **5**, p. 4875, Sept. 2014.
- [23] P. Wei, S. Lee, F. Lemaitre, L. Pinel, D. Cutaia, W. Cha, F. Katmis, Y. Zhu, D. Heiman, J. Hone, J. S. Moodera, and C.-T. Chen, "Strong interfacial exchange field in the graphene/EuS heterostructure," *Nat. Mater.* **15**, pp. 711–716, Mar. 2016.
- [24] W. Yang, J. Shang, J. Wang, X. Shen, B. Cao, N. Peimyoo, C. Zou, Y. Chen, Y. Wang, C. Cong, W. Huang, and T. Yu, "Electrically Tunable Valley-Light Emitting Diode (vLED) Based on CVD-Grown Monolayer WS<sub>2</sub>," *Nano Lett.* **16**, pp. 1560–1567, Mar. 2016.
- [25] Z. Wang, D.-K. Ki, J. Y. Khoo, D. Mauro, H. Berger, L. S. Levitov, and A. F. Morpurgo, "Origin and magnitude of 'designer' spin-orbit interaction in graphene on semiconducting transition metal dichalcogenides," *Phys. Rev. X* **6**(4), p. 041020, 2016.
- [26] J. Tian, T.-F. Chung, I. Miotkowski, and Y. P. Chen, "Electrical spin injection into graphene from a topological insulator in a van der Waals heterostructure," *arXiv:1607.02651 [cond-mat]*, July 2016. arXiv: 1607.02651.
- [27] M. Gmitra, D. Kochan, P. Högl, and J. Fabian, "Trivial and inverted dirac bands and the emergence of quantum spin hall states in graphene on transition-metal dichalcogenides," *Phys. Rev. B* **93**(15), p. 155104, 2016.
- [28] Z. Wang, D.-K. Ki, H. Chen, H. Berger, A. H. MacDonald, and A. F. Morpurgo, "Strong interface-induced spin-orbit interaction in graphene on WS<sub>2</sub>," *Nat. Commun.* **6**, p. 8339, Sept. 2015.
- [29] E. C. T. O'Farrell, A. Avsar, J. Y. Tan, G. Eda, and B. Özyilmaz, "Quantum transport detected by strong proximity interaction at a graphene/WS<sub>2</sub> van der waals interface," *Nano Lett.* **15**(9), pp. 5682–5688, 2015.
- [30] W. Yan, O. Txoperena, R. Llopis, H. Dery, L. E. Hueso, and F. Casanova, "A two-dimensional spin field-effect switch," *Nat. Commun.* **7**, p. 13372, 2016.
- [31] A. Dankert and S. P. Dash, "Electrical gate control of spin current in van der Waals heterostructures at room temperature," *Nat. Commun.* **8**, p. ncomms16093, July 2017.
- [32] R. Moriya, T. Yamaguchi, Y. Inoue, S. Morikawa, Y. Sata, S. Masubuchi, and T. Machida, "Large current modulation in exfoliated-graphene/MoS<sub>2</sub>/metal vertical heterostructures," *Appl. Phys. Lett.* **105**, p. 083119, Aug. 2014.
- [33] B. Yang, M.-F. Tu, J. Kim, Y. Wu, H. Wang, J. Alicea, R. Wu, M. Bockrath, and J. Shi, "Tunable spinorbit coupling and symmetry-protected edge states in graphene/WS<sub>2</sub>," *2D Mater.* **3**(3), p. 031012, 2016.
- [34] T. Maassen, I. J. Vera-Marun, M. H. D. Guimarães, and B. J. van Wees, "Contact-induced spin relaxation in Hanle spin precession measurements," *Phys. Rev. B* **86**, p. 235408, Dec. 2012.
- [35] T. Yamaguchi, R. Moriya, Y. Inoue, S. Morikawa, S. Masubuchi, K. Watanabe, T. Taniguchi, and T. Machida, "Tunneling transport in a few monolayer-thick WS<sub>2</sub>/graphene heterojunction," *Appl. Phys. Lett.* **105**, p. 223109, Dec. 2014.
- [36] N. Tombros, C. Józsa, M. Popinciuc, H. T. Jonkman, and B. J. van Wees, "Electronic spin transport and spin precession in single graphene layers at room temperature," *Nature* **448**, pp. 571–574, Aug. 2007.
- [37] L. Yu, Y.-H. Lee, X. Ling, E. J. G. Santos, Y. C. Shin, Y. Lin, M. Dubey, E. Kaxiras, J. Kong, H. Wang,

- and T. Palacios, "Graphene/mos2 hybrid technology for large-scale two-dimensional electronics," *Nano Lett.* **14**(6), pp. 3055–3063, 2014. PMID: 24810658.
- [38] R. Jansen and B. C. Min, "Detection of a Spin Accumulation in Nondegenerate Semiconductors," *Phys. Rev. Lett.* **99**, p. 246604, Dec. 2007.
- [39] R. Jansen, B. C. Min, S. P. Dash, S. Sharma, G. Kioseoglou, A. T. Hanbicki, O. M. J. van 't Erve, P. E. Thompson, and B. T. Jonker, "Electrical spin injection into moderately doped silicon enabled by tailored interfaces," *Phys. Rev. B* **82**, p. 241305, Dec. 2010.

# Spin transport in High-mobility Graphene on WS<sub>2</sub> Substrate with Electric-field Tunable Proximity Spin-orbit Interaction

### Abstract

Graphene supported on a transition metal dichalcogenide (TMD) substrate offers a novel platform to study the spin transport in the presence of substrate induced spin-orbit coupling, while preserving its intrinsic charge transport properties. We report the first non-local spin transport measurements in graphene, completely supported on a 3.5 nm thick WS<sub>2</sub> substrate, and encapsulated from the top with a 8nm thick hBN layer. For graphene-on-WS<sub>2</sub>, we observe high electron and hole mobilities up to 16000 cm<sup>2</sup>V<sup>-1</sup>s<sup>-1</sup>. For spin-transport, we measure almost a constant spin-signal in a broad range of carrier densities both in electron and hole-doped regimes, which rules out any major role of spin-absorption by the underlying WS<sub>2</sub> substrate. Surprisingly,  $\tau_s$  for the electrons in graphene-on-WS<sub>2</sub> is drastically reduced down to  $\sim 10$  ps by approximately two orders of magnitude, compared to the  $\tau_s \sim 800$  ps for graphene on the SiO<sub>2</sub> substrate in the same chip. This strong suppression of  $\tau_s$  in the high mobility graphene-on-WS<sub>2</sub> substrate, along with a detectable weak anti-localization signature in the quantum magneto-resistance measurements, is a clear effect of the WS<sub>2</sub> induced spin-orbit coupling (SOC) in graphene. Finally, via the top-gate voltage application, we modify the carrier density and electric field in the encapsulated region, and identify the presence of a Dyakonov-Perel type mechanism in the hole transport regime, accompanied by the electric field tunable surface Rashba SOC, responsible for an enhanced spin-relaxation at the graphene-WS<sub>2</sub> interface.



## 11.1 Introduction

Graphene is an ideal material for spin transport due to its extremely low spin-orbit coupling (SOC) of about  $\sim 1\mu\text{eV}$  and small hyperfine interactions [1–3]. On the other hand, lack of a sizable SOC has also hindered the demonstration of graphene as a spin-transistor [4]. Recent exploration of various 2D-materials and their heterostructures has provided access to novel charge- [5, 6] and spin-related phenomena [7–12] which are either missing or do not have a measurable effect in intrinsic graphene. Graphene can interact with the neighboring material via weak van der Waals interactions which help to preserve its charge transport properties, but it can acquire some foreign properties from the host substrate such as a sizable band gap at the Dirac point due to a sublattice dependent crystal potential on a boron nitride (BN) substrate [5, 6], an enhanced intrinsic spin-orbit coupling in the range of 5 meV–15 meV, along with a meV order valley-Zeeman splitting, due to the inequivalent K and K' valleys in graphene [10, 13], Rashba SOC due to breaking of inversion symmetry at the graphene-transition metal dichalcogenide (TMD) interface [7, 8] and the possibility of spin-valley coupling [14, 15]. This unique ability of graphene-TMD interfaces makes them an attractive platform for studying the spin-related proximity induced effects.

In recent reports of spin-transport in graphene-TMD heterostructures [16, 17], a reduced spin-signal and spin-relaxation time was measured in graphene with a TMD on top when the TMD was conducting, which was attributed to the spin-absorption/enhanced spin-relaxation via the TMD. On the contrary, in WAL magnetotransport measurements [9, 10], a reduced and a constant spin time, independent of the carrier-type, carrier-density and the conducting state of the TMD was observed, which was attributed to the greatly enhanced spin-orbit coupling in graphene via the proximity effect of the neighboring TMD. Also, the existence of the interplay between the valley-Zeeman and Rashba SOC was theoretically and experimentally demonstrated in the anisotropy of the spin relaxation time for the out-of-plane and in-plane spin-signals [15, 18] in a single-layer TMD/graphene heterostructure.

Surrounded by distinct conclusions, which seem to depend on the device geometry and the experiment-type, it calls for revisiting the problem in a different way, i.e., a direct spin-transport measurement using the TMD as a substrate for graphene. It has multiple advantages: i) Similar to hBN, TMDs as substrate, have already shown to improve the charge transport properties of graphene significantly [19] due to their atomic flatness and screening the roughness and dangling bonds of  $SiO_2$ , which are believed to be responsible for low charge carrier mobility in graphene-on- $SiO_2$  [2, 3]. This improvement can be helpful in possibly compensating for the reduced  $\tau_s$ , due to either of the proposed mechanisms in ref. [16, 17], and improve the spin-signal magnitude, and ii) unlike the partial encapsulation of graphene with the TMD, where the encapsulated and the non-encapsulated graphene regions have different charge and

spin-transport properties and require a complex analysis for the accurate interpretation of the TMD induced spin-relaxation in graphene [17, 18], spin-transport measurements in graphene, fully supported on a TMD substrate can directly distinguish the possible effects of spin-absorption via the TMD or a proximity-induced SOC, due to a uniform carrier density and identical effect of the substrate present everywhere in graphene. Also, in contrast with the TMD-on-top geometry, where graphene partially shields the back-gate induced electric field, and one cannot clearly comment on the conducting state of the TMD on top and correlate its effect on spin-transport in graphene, the inverted geometry does not have this drawback. Lastly, it would be worth exploring, whether the recently observed spin-relaxation anisotropy for the in-plane and out-of-plane spins in graphene [15, 18], is specific to the graphene-single layer TMD heterostructure or it also depends on the TMD thickness.

We study the charge and spin-transport properties of graphene, fully supported on a tungsten di-sulfide ( $\text{WS}_2$ ) substrate and partially encapsulated via a top hBN flake, using a four-probe local and non-local geometry, respectively. We measure high values of charge mobility up to  $16,000 \text{ cm}^2\text{V}^{-1}\text{s}^{-1}$  due to the atomically flat  $\text{WS}_2$  substrate and due to the screening of impurities and dangling bonds present on the  $\text{SiO}_2$  surface. We study the spin-transport via spin-valve and Hanle spin-precession experiments [20], and measure a constant spin signal  $\Delta R_{\text{NL}}$  for a wide range of the carrier densities. The obtained signal is independent of the carrier type and carrier density, ruling out the effect of spin-absorption via the underlying  $\text{WS}_2$  flake. For the Hanle measurements, we observe very broad Hanle curves with a spin-relaxation time  $\tau_s \sim 10 \text{ ps}$  in the electron-doped regime which is almost 80 times smaller than  $\tau_s \sim 800 \text{ ps}$  of a reference graphene flake on the  $\text{SiO}_2/\text{Si}$  substrate in the same chip. Via the top-gate voltage application, we can access the hole doped regime, where  $\tau_s$  is enhanced up to 40-80 ps for various carrier densities. However, we do not observe a clear measurable signature of the recently reported strong anisotropic spin-relaxation [15, 18]. In our case, the ratio of the out-of-plane to the in-plane  $\Delta R_{\text{NL}}$  (therefore  $\tau_s$ ) is less than one, an indicative of the in-plane Rashba-type systems [15, 21]. For both regimes (stronger for the hole regime), we observe a reduced  $\tau_s$  on increasing the carrier density (or the momentum relaxation time  $\tau_p$ ), which indicates the presence of the Dyakonov-Perel (DP) type mechanism for spin-relaxation in our system, similar to that obtained in the weak anti-localization measurements [7, 8].

We also confirm the signature of  $\text{WS}_2$  induced SOC in graphene by measuring the weak anti-localization (WAL) signature in the same sample, similar to the low temperature quantum magneto-transport studies performed in ref. [7–10], while graphene on a  $\text{SiO}_2$  substrate shows a clear WL signature. Therefore, the low  $\tau_s$  in graphene-on- $\text{WS}_2$  substrate, with an electric-field tunable Rashba SOC, supported by the hall mark WAL signature, can be easily attributed to the  $\text{WS}_2$  enhanced proximity SOC at the graphene- $\text{WS}_2$  interface.

## 11.2 Sample preparation

The WS<sub>2</sub>/graphene stacks are prepared on a n<sup>++</sup>-doped SiO<sub>2</sub>/Si substrate ( $t_{\text{SiO}_2} \sim 300$  nm) via a dry pick-up transfer method [11, 22]. After the stack is prepared, it is put in a chloroform solution for 3 hours in order to remove the poly-carbonate film, used in the stack preparation. After that, the stack is annealed in Ar/H<sub>2</sub> environment for five hours to remove the remaining polymer residues.

In order to define the contacts, a poly-methyl methacrylate (PMMA) solution is spin-coated over the stack and the contacts are defined via the electron-beam lithography (EBL). The PMMA polymer exposed via electron beam gets dissolved in a MIBK:IPA solution. In the next step, 0.7 nm Al is deposited in two steps, each step of 0.35 nm followed by 12 min oxidation, to form a Al<sub>2</sub>O<sub>3</sub> tunnel barrier. On top of it, 70 nm thick cobalt (Co) is deposited to form the ferromagnetic (FM) contacts, with a 3 nm thick Al capping layer in order to prevent the oxidation of the FM electrodes, followed by the lift-off process in acetone solution at 30°C.

## 11.3 Sample Characterization

We study two samples: i) stack A: a WS<sub>2</sub>/Gr/hBN stack consisting of a single layer graphene (SLG) encapsulated between a bottom WS<sub>2</sub> ( $t_{\text{WS}_2} \sim 3.5$  nm) and a top hBN flake ( $t_{\text{hBN}} \sim 8$  nm), as shown in and Fig. 11.1(a,b,d) and ii) stack B: a WS<sub>2</sub>/Gr stack consisting of a SLG, supported on a bottom WS<sub>2</sub> flake ( $t_{\text{WS}_2} \sim 4.2$  nm), without any hBN encapsulation from the top, as shown in Fig. 11.1(c,e). On the same SiO<sub>2</sub>/Si chip, there are reference graphene flakes near stack A (Fig. 11.1(d)) and stack B. We, therefore, can directly compare the charge and spin-transport properties of the reference graphene flakes and graphene on WS<sub>2</sub> substrate, prepared via identical steps. The reference flakes on the same SiO<sub>2</sub>, shared by stack A and stack B, are labeled as 'ref A' and 'ref B' respectively. Moreover, stack A has non-encapsulated region (region-I) and encapsulated region (region-II) both, as shown in the device schematic of Fig. 11.1(a). On the other hand, stack B only consists of region I. Therefore, we will discuss the data of stack A as a representative device. We use a low-frequency lock-in detection method to measure the charge and spin transport properties of the graphene flake in vacuum. The measurements reported here are performed at room temperature and at 4K.

### 11.3.1 Charge Transport Measurements

We measure the charge transport, via a four probe local measurement scheme. For measuring the gate-dependent resistance of graphene-on-WS<sub>2</sub> in region-I (II), a fixed ac charge current  $i_{\text{ac}} \sim 100$  nA is applied between contacts C1-C4 (C1-C6) and a

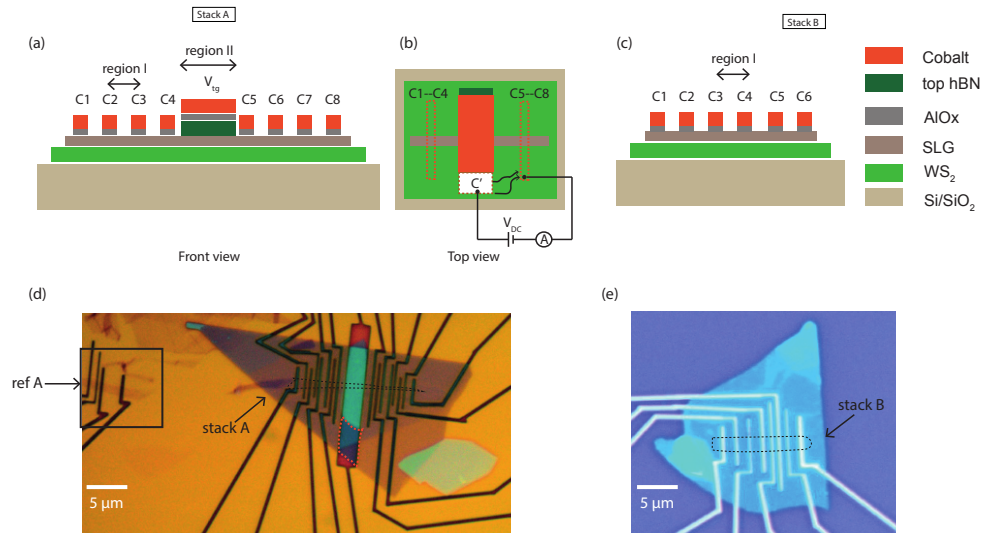


**Figure 11.1:** (a) Stack A: bottom  $\text{WS}_2$  / graphene/ top hBN stack with  $\text{AlO}_x$ -Co (FM) contacts and top gate. (b) top-view of the device. White region marked by C' represents the cobalt contacting the  $\text{WS}_2$  flake, which is not separated by hBN and the connection scheme for measuring the  $I - V$  behavior of  $\text{WS}_2$ . (c) Stack B: graphene supported on a bottom  $\text{WS}_2$  substrate. (d) an optical image of the stack A, before the contact fabrication. The graphene flake is outlined by the black dotted line and the orange dotted line denote the  $\text{WS}_2$  flake region to be contacted by the top-gate electrode after the contact deposition. On the top left corner, outlined with the black square, a graphene flake (ref A) and the developed contacts can be seen on the same  $\text{SiO}_2/\text{Si}$  substrate. (e) An optical image of stack B, i.e., graphene (dashed lines)/bottom  $\text{WS}_2$  heterostructure, after the contact deposition. It also has a reference flake 'ref B' on the same  $\text{SiO}_2$  substrate (not shown in the image).

voltage-drop is measured between contacts C2-C3 (C4-C5) and the back-gate (top-gate) voltage is swept. We also characterize the charge-transport properties of the reference graphene flake on  $\text{SiO}_2$ , via the same connection scheme. For graphene-on- $\text{WS}_2$ , it is possible to tune the Fermi energy ( $E_F$ ) in graphene, until the  $E_F$  lies within the band-gap of  $\text{WS}_2$ . After the  $E_F$  coincides with the conduction band edge of  $\text{WS}_2$ , it also starts conducting.  $V_{\text{bg}}$  corresponding to this transition, is denoted as  $V_{\text{on}}$ . At high  $V_{\text{bg}} > V_{\text{on}}$ , the  $\text{WS}_2$  flake screens the electric field from the back-gate, due to charge accumulation at the  $\text{SiO}_2$ - $\text{WS}_2$  interface [9] and the  $R_{\text{sq}}$  of graphene is not modified anymore via the back-gate application.

The Dirac curves for region-I and -II as a function of back-gate and top gate voltage are shown in Fig. 11.2(a)-(c). In order to extract the carrier mobility  $\mu$ , we fit the

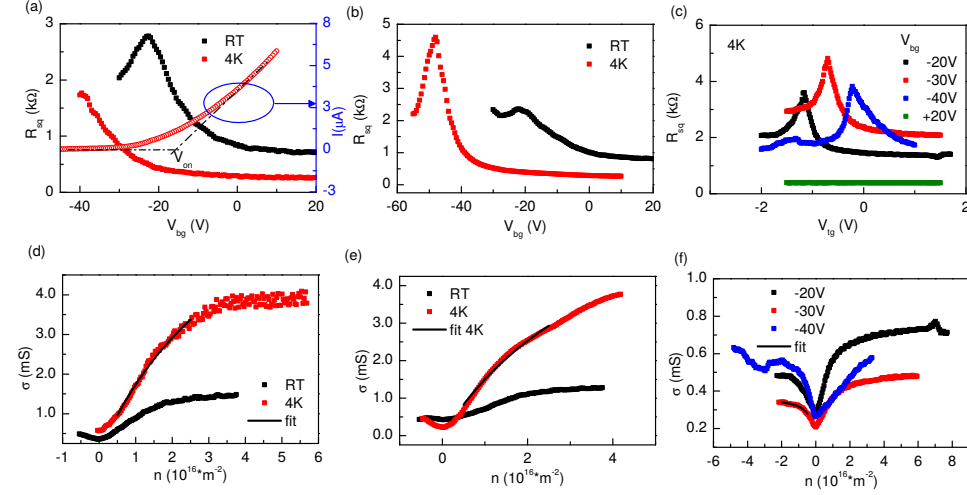


**Figure 11.2:** (a)  $R_{sq} - V_{bg}$  dependence of the non-encapsulated graphene on WS<sub>2</sub> (region I in Fig. 11.1(a)) of stack A is shown on the left axis (solid lines). The  $I_{DS} - V_{bg}$  behavior of WS<sub>2</sub> at 4K (open circle), using the connection scheme of Fig. 11.1(b). (b)  $R_{sq} - V_{bg}$  and (c)  $R_{sq} - V_{bg}$  behavior of the graphene encapsulated between WS<sub>2</sub> and hBN flakes (region II in Fig. 11.1(a)). The corresponding  $\sigma - V_{bg(tg)}$  behavior is plotted in (d), (e) and (f).

charge-conductivity  $\sigma$  versus carrier density  $n$  plot with the following equation:

$$\sigma = \frac{1}{R_{sq}} = \frac{ne\mu + \sigma_0}{1 + R_s(ne\mu + \sigma_0)} \quad (11.1)$$

Here  $R_{sq}$  is the sheet resistivity of graphene,  $\sigma_0$  is the conductivity at the CNP,  $R_s$  is the residual resistance due to short-range scattering [22–24] and  $e$  is the electronic charge. We fit the  $\sigma - n$  plot for  $n$  in the range  $5 \times 10^{11} - 2.5 \times 10^{12} \text{ cm}^{-2}$  with Eq. 11.1. For the non-encapsulated region we obtain the electron-mobility  $\mu_e \sim 9700 \text{ cm}^2\text{V}^{-1}\text{s}^{-1}$  at room temperature (RT), which is enhanced to  $13400 \text{ cm}^2\text{V}^{-1}\text{s}^{-1}$  at 4K. For the encapsulated region, we extract a relatively lower  $\mu_e \sim 7300 \text{ cm}^2\text{V}^{-1}\text{s}^{-1}$  at RT which is enhanced at 4K to  $11500 \text{ cm}^2\text{V}^{-1}\text{s}^{-1}$ . Since we can modulate the carrier density in the encapsulated region via the top gate application as well as change the position of the CNP, we can access the hole regime up to higher carrier densities. We extract the hole mobility  $\mu_h$  at different values of back-gate  $V_{bg}$  in the range  $12600 - 16000 \text{ cm}^2\text{V}^{-1}\text{s}^{-1}$  at 4K (Fig. 11.2(f)). Via this analysis, we get  $\mu_e \sim 6000 - 13000 \text{ cm}^2\text{V}^{-1}\text{s}^{-1}$  at different  $V_{bg}$  values, similar to that extracted from the back-gate sweep in Fig. 11.2(e). Charge mobility of about  $10^4 \text{ cm}^2\text{V}^{-1}\text{s}^{-1}$  in our samples, without any optimization of the fabrication procedure reflects the clean-WS<sub>2</sub> interface

quality and we believe that the graphene-WS<sub>2</sub> interface is not significantly affected by the lithographic process during the sample preparation.

In order to characterize the transfer characteristics of the WS<sub>2</sub> substrate and to know when it is switched 'on' and starts conducting, we use a specific geometry. The BN flake used as a top gate insulating layer, does not encapsulate the WS<sub>2</sub> crystal completely, as marked by the orange dashed lines in Fig. 11.1(d), therefore, the WS<sub>2</sub> crystal is contacted via the top gate electrode (white region in Fig. 11.1(b), labeled as C') and the electrodes C1–C8 shorted via graphene. Since,  $\sigma_{\text{gr}} \gg \sigma_{\text{WS}_2}$ , for the voltage applied between any two electrodes from C1–C8, the current flow will occur through graphene. However, for the voltage applied between C' and C<sub>j</sub> ( $j = 1, 8$ ), the current flow in graphene is blocked by the hBN insulating layer and instead it flows through WS<sub>2</sub>, as shown in the schematic of Fig. 11.1(b). The  $I_{\text{DS}} - V_{\text{bg}}$  transfer curve for WS<sub>2</sub>, measured using this geometry is plotted in Fig. 11.2(a) (marked by blue ellipse). It is also noteworthy that there is negligible gating action from the top gate when the WS<sub>2</sub> is conducting, shown in green curve of Fig. 11.2(c), which is measured for the  $V_{\text{bg}} = +20\text{V}$  ( $V_{\text{on}} \sim -20\text{V}$  of WS<sub>2</sub>).

In conclusion, for the samples having graphene-on-WS<sub>2</sub> substrate, we obtain high electron and hole mobilities, reaching up to  $16000 \text{ cm}^2\text{V}^{-1}\text{s}^{-1}$ . We obtain similar mobilities for both encapsulated and the non-encapsulated regions, implying that the observed high mobility is due to a clean WS<sub>2</sub>-graphene interface in our devices.

### 11.3.2 Spin Transport Measurements

We measure the spin-signal in our devices, using the four probe nonlocal connection scheme. In order to measure the spin signal  $\Delta R_{\text{nl}}$  in the non-encapsulated (encapsulated) region,  $i_{\text{ac}}$  is applied between contacts C2-C1 (C4-C1) and the nonlocal voltage  $v_{\text{nl}}$  is measured between C3-C4 (C5-C8), in Fig. 11.1(a) [20].

For spin-valve measurements, we first apply a magnetic field  $B_{\parallel} \sim 0.2 \text{ T}$  along the easy axes of the FM contacts so that they have their magnetization in the same direction. We design our contacts with different widths, therefore they have different coercivities. Now, we sweep  $B_{\parallel}$  in the opposite direction and depending on their coercivity, the FM contacts reverse their magnetization direction along the applied field one by one. This magnetization reversal appears as a sharp transition in  $v_{\text{nl}}$  or in the nonlocal resistance  $R_{\text{nl}} = v_{\text{nl}}/i_{\text{ac}}$ . Since we choose our outer injector and detector contacts far enough from the inner FM contacts, they do not influence the spin transport and we only observe two switches corresponding to the inner FM contacts, as shown in Fig. 11.3(a) and Fig. 11.6(a). The spin-signal is  $\Delta R_{\text{nl}} = \frac{R_{\text{nl}}^{\text{P}} - R_{\text{nl}}^{\text{AP}}}{2}$ , where  $R_{\text{nl}}^{\text{P(AP)}}$  represent the high (low)  $R_{\text{nl}}$  values of the two level spin-valve signal.

For the Hanle precession measurements, first the FM electrodes are magnetized in a parallel (P) or anti-parallel (AP) configuration. Next, for a fixed P (AP) configuration, an out of plane magnetic field ( $B_{\perp}$ ) is applied and the injected spin-

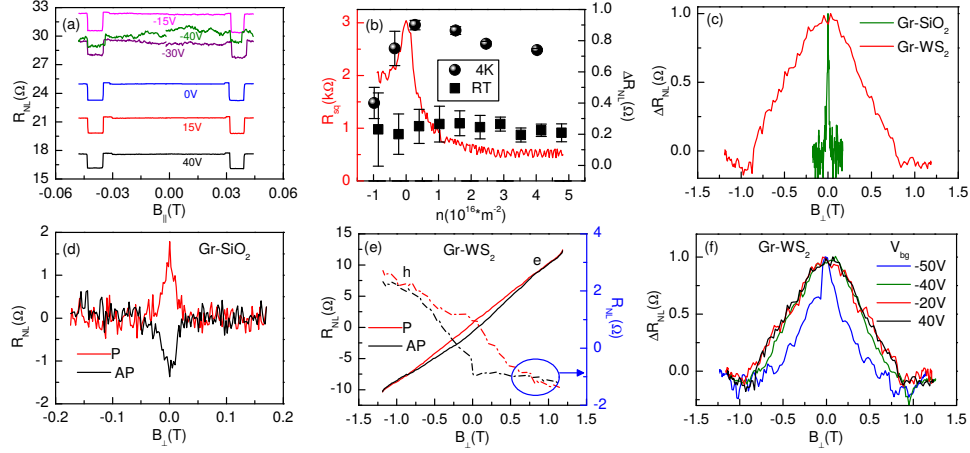


**Figure 11.3:** (a) Spin-valve measurements of stack A (region-I) for the injector-detector separation  $L=800$  nm at different  $V_{bg}$  and (b)  $\Delta R_{NL}$  as a function of carrier density in graphene at RT and 4K, for stack A.  $\Delta R_{NL}$  does not change much at RT and in the electron-doped regime at 4K. Though it shows a decrease in the hole-doped regime. (c) Normalized Hanle curves for graphene on SiO<sub>2</sub> (green) and WS<sub>2</sub> (red) at 4K. (d) parallel (P) and anti-parallel (AP) Hanle curves for graphene on SiO<sub>2</sub>. (e) A huge linear background is observed in the Hanle curves for graphene on WS<sub>2</sub>. It can be seen both in P and AP configuration and in electron and hole doped regime. Sign of the slope changes with the change in the sign of the carrier density. (f) Hanle curves for Gr-WS<sub>2</sub> stack (stack A) at different  $V_{bg}$  at 4K

accumulation precesses around the applied field with the Larmor frequency  $\vec{\omega}_L = \frac{g\mu_B}{\hbar} \vec{B}$ , while diffusing towards the detector, and get dephased. Here  $g$  is the gyromagnetic ratio=2 for an electron,  $\mu_B$  is the Bohr magneton and  $\hbar$  is the reduced Planck constant. The measured Hanle curves are fitted with the steady state solution to the Bloch equation:

$$D_s \nabla^2 \vec{\mu}_s - \frac{\vec{\mu}_s}{\tau_s} + \vec{\omega}_L \times \vec{\mu}_s = 0 \quad (11.2)$$

with spin diffusion constant  $D_s$ , spin relaxation time  $\tau_s$  and the spin-accumulation  $\vec{\mu}_s$  in the transport channel. The spin diffusion length  $\lambda_s$  is  $= \sqrt{D_s \tau_s}$ . Hanle measurements for a reference graphene flake on SiO<sub>2</sub>/Si are shown in Fig. 11.3(e).

## 11.4 Results and Discussion

We report the spin-valve and Hanle measurements for stack A at different carrier densities at 4K. First, we start characterizing the reference graphene sample ref A, on the same substrate. The Hanle measurements are shown in Fig. 11.3(d). Since

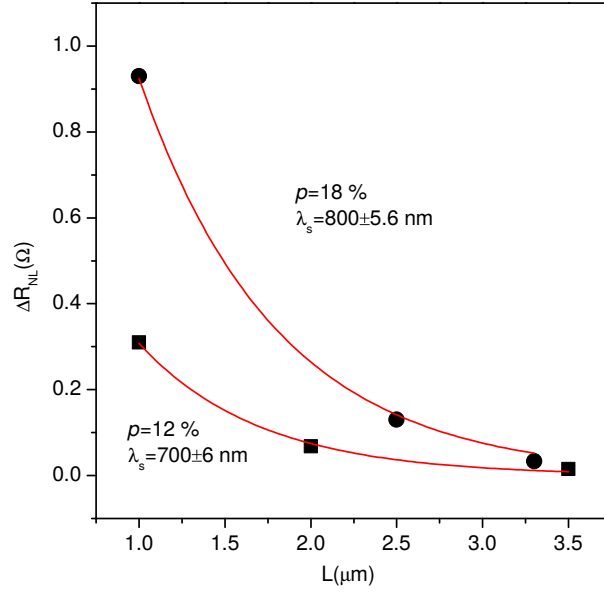


**Figure 11.4:** Exponentially decaying spin signal  $\Delta R_{\text{NL}}$  in stack A (region-I), for an increasing injector-detector separation  $L$ . Here, we assume same contact polarization for all the electrodes. This is fitted using Eq. 11.3.

we could not observe the CNP due to n-doping of the flake, we measure the spin-transport in electron-doped regime and obtain  $D_s \sim 0.02 \text{ m}^2\text{s}^{-1}$  and  $\tau_s$  in the 730 ps-870 ps range, i.e.,  $\lambda_s = \sqrt{D_s \tau_s} \sim 3.6 \mu\text{m}-3.8 \mu\text{m}$ , with no 'proximity-effect'.

After obtaining the spin-transport parameters for ref A, we measure the spin-transport in graphene on  $\text{WS}_2$  substrate (stack A) on the same chip. For a varying range of carrier density, from electron to hole regime with the application of  $V_{\text{bg}}$ , we observe an almost constant spin signal at RT, plotted in Fig. 11.3(b)(black solid squares). At 4K the spin signal shows a modest increase around the charge neutrality point (CNP), i.e., the resistance maximum, and then it decreases. For  $V_{\text{bg}} < -30\text{V}$ , there is a negligible in-plane charge conduction in  $\text{WS}_2$  and if spin-absorption via  $\text{WS}_2$  was the dominant spin-relaxation mechanism, the signal should enhance in this regime. We, on the other hand, observe almost a constant  $\Delta R_{\text{NL}}$  in the regime where  $\text{WS}_2$  conducts at RT, with a slight decrease in the signal at 4K when the  $\text{WS}_2$  flake is switched 'off'. Either of the observations cannot be explained by considering spin-absorption as a dominant source of spin-relaxation at the graphene- $\text{WS}_2$  interface within the applied back-gate voltage range. Next, we perform spin-valve measure-



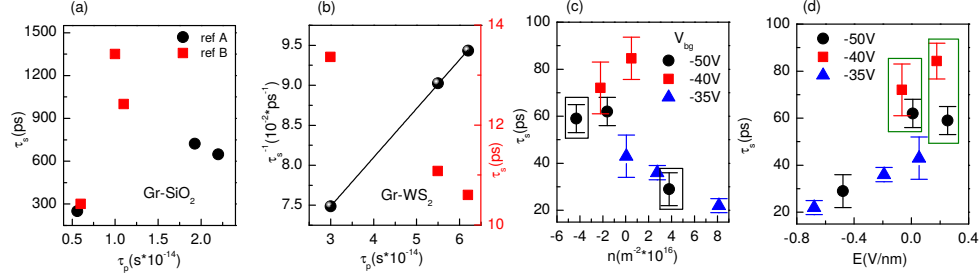


**Figure 11.5:** (a) Spin-relaxation time as a function of momentum scattering time ( $\tau_p$ ) for the reference graphene on SiO<sub>2</sub> substrate, ref A and ref B in the electron doped-regime shows an enhanced  $\tau_s$  with the increase in  $\tau_p$ , suggesting EY-type spin-relaxation. Due to high n-type doping of the flakes, the hole transport regime could not be accessed within the applied  $V_{bg}$ . (b)  $\tau_s$  versus  $\tau_p$  (red data points) for graphene on WS<sub>2</sub> substrate (region I-stack A), shows an enhanced  $\tau_s$  for a reduced  $\tau_p$ , suggesting the DP-type spin relaxation in presence of the substrate induced SOC. Black line represents a linear fit of  $1/\tau_s - \tau_p$  data (black sphere). (c)  $\tau_s$  as a function of carrier density  $n$  and (d) Electric field  $E$  at different values of  $V_{bg}$  for the electron and hole transport regime in region-II of stack A.  $E$  and  $n$  in the encapsulated-region are calculated by following the procedure in Ref. [21].

ments for the encapsulated region, where we vary the carrier density in graphene via the top-gate (Fig. 11.6(a)). For a wide range of carrier density in graphene which is equivalent to applying a back-gate voltage in the range of  $\pm 60$  V, we do not see any significant change in the spin-signal, similar to the back-gate dependent spin-valve measurements and conclude that  $\Delta R_{NL}$  is independent of the carrier density, carrier type in graphene and the conducting state of the TMD. Note that this configuration is similar to the TMD on graphene with a back gate application, except graphene is uniformly covered with the WS<sub>2</sub> flake in our sample. We also measure  $\Delta R_{NL}$  at different injector-detector separation  $L$  and assuming same polarization  $P$  for all the contacts, we can estimate  $\lambda_s$  using eq.:

$$\Delta R_{NL} = \frac{P^2 R_{sq} \lambda_s e^{-\frac{L}{\lambda_s}}}{2w} \quad (11.3)$$

where  $w$  is the width of the spin-transport channel. We estimate the spin-relaxation-length  $\lambda_s$  around 700-800 nm, which is almost five times lower than  $\lambda_s$  of the reference sample. We obtain  $D_c \sim 0.05$  m<sup>2</sup>s<sup>-1</sup> of graphene on WS<sub>2</sub> substrate from the Dirac measurements, using the Einstein relation:  $\sigma = e^2 D_c \nu(E)$ , where  $\nu(E)$  is the density of states in graphene. Assuming  $D_s = D_c$ , we estimate  $\tau_s \sim 10$  ps, using  $\lambda_s$  obtained from the spin-valve measurements. Note that this value may be uncertain due to possible different polarization values of the individual contacts, still it gives an estimate of  $\lambda_s$  [25].

Based on the spin-valve measurements on stack A, one would expect a broad Hanle curve due to a significantly reduced  $\tau_s$ . Indeed, we measure broad Hanle curves with their full-width half maximum in the range of  $\sim 1$ T. A direct comparison between the Hanle curve of the reference sample and for graphene-on- $\text{WS}_2$  substrate, plotted together in Fig. 11.3(c), clearly demonstrates the effect of the  $\text{WS}_2$  substrate in the broadening of the Hanle curve. Along with the broad Hanle spin-signal  $\Delta R_{\text{NL}}$ , we also observe a large linear background ( $\sim 10$ - $20 \Omega$ ) for the individual Hanle curves measured in the  $P$  and  $AP$  configurations (Fig. 11.3(e)). We also observe a sign change in the slope of this background with respect to change in the sign of carriers from electrons to holes, similar to a Hall like signal. However, such a large Hall background is not possible because we design the FM electrodes across the flake and it should eliminate the Hall like behavior. The source of such background is non-trivial and at the moment is not clear to us. We also perform Hanle measurements at different carrier densities. The line shape of  $\Delta R_{\text{NL}}$  remains similar in the electron-doped regime from the CNP to the carrier densities up to  $6 \times 10^{16} \text{ m}^{-2}$ . Note that  $\text{WS}_2$  is in the conducting state in this regime and just gets switched off around the CNP of graphene. By fitting these curves with the steady state solution to the Bloch equation, we obtain  $\tau_s \sim 10$ - $13$  ps and  $D_s$  about  $0.03$ - $0.04 \text{ m}^2\text{s}^{-1}$  which matches with the  $D_c$  within a factor of two obtained from the charge transport measurements. With the obtained  $D_s$  and  $\tau_s$  via Hanle measurements, we achieve  $\lambda_s \sim 600$ - $700$  nm, using  $\lambda_s = \sqrt{D_s \tau_s}$ , in a good-agreement with the  $\lambda_s$  obtained from the spin-valve measurements. It should be noted that at such high out-of-plane magnetic fields, the magnetization direction of the ferromagnets does not fully lie in the sample-plane and makes an angle with the sample plane [21]. When we analyze the measured data, while correcting for the angular dependence of the magnetization (not shown here) using the procedure in ref.[26], the 'corrected' Hanle curves become even broader. From these Hanle curves, we would obtain even lower  $\tau_s$ . Therefore, the  $\tau_s$  values, reported here, represent the upper bound. We estimate the contact polarization  $P \sim 15$ - $20$  % using Eq. 11.3 for this device which, along with a reasonably good  $D_s \sim 0.04 \text{ m}^2\text{s}^{-1}$ , enables us to measure the large  $\Delta R_{\text{NL}}$  of the order of Ohms, even with such a short  $\tau_s$ . For the Hanle measurements in hole transport regime, we could only measure one data set at  $V_{\text{bg}} = -50$ V ( $D_s \sim 0.35 \text{ m}^2\text{s}^{-1}$ ,  $\tau_s \sim 35$  ps) with  $D_s$  and  $D_c$  ( $\sim 0.03 \text{ m}^2\text{s}^{-1}$ ) differing by an order of magnitude. Therefore, we cannot comment on the spin-transport parameters in the hole transport regime in region-I. For stack B, we have a small  $P \sim 1 - 3\%$  and therefore a small  $\Delta R_{\text{NL}} \sim 7 \text{ m}\Omega$ , making it difficult to measure a clear Hanle curve at high magnetic fields in presence of a huge linear background.

In graphene, there are two dominant spin-relaxation mechanisms [27–29] : 1)- Elliot-Yafet (EY) mechanism where a electron-spin is scattered during the interaction with the impurities and therefore the spin-relaxation time is proportional to the momentum relaxation time  $\tau_p$ , i.e.,  $\tau_s \propto \tau_p$ , 2)-Dyakonov-Perel (DP) mechanism, where

the electron-spin precesses in a spin-orbit field between two momentum scattering events, following the relation  $\tau_s \propto \frac{1}{\tau_p}$ . In order to check the relative contribution of the EY and DP mechanisms, we plot the  $\tau_s$  versus  $\tau_p$  behavior, shown in Fig. 11.5 for ref A and ref B samples on SiO<sub>2</sub> and for region-I of stack A. Here,  $\tau_p$  can be calculated from the diffusion coefficient, using the relation  $D_s \sim v_F^2 \tau_p$ . In Fig. 11.5(a), for the reference samples, we see that  $\tau_s$  increases with  $\tau_p$  for the electron doped regime, suggesting the dominance of EY-type spin relaxation in SLG on SiO<sub>2</sub> substrate, similar to previous observations [25, 28, 29] on this system. We could not quantify the spin-orbit strength due to unknown carrier density and the corresponding Fermi energy [30]. For stack A, processed in identical condition, we observe an opposite trend between  $\tau_s$  and  $\tau_p$  in Fig. 11.5(b) in the electron-doped regime, which resembles the DP type mechanism. We fit the data with the relation  $\frac{1}{\tau_s} = \frac{4\lambda_R^2}{\hbar^2} \tau_p$  and extract  $\lambda_R \sim 250 \mu\text{ eV}$ , which is 4-to-6 times higher than the spin orbit coupling strength in a similar mobility sample on hBN substrate in ref. [30] and distinguishes the effect of the WS<sub>2</sub> substrate in enhancing the SOC in graphene, compared to a hBN or SiO<sub>2</sub> substrate. The obtained magnitude of  $\lambda_R$  is of similar order as reported in ref. [8, 10, 13, 15]. However, for such a small variation of spin-relaxation rates from  $75 \text{ ns}^{-1}$  to  $95 \text{ ns}^{-1}$ , a slight variation in  $\tau_s$  can change the  $\tau_s - \tau_p$  dependence and consequently changing  $\lambda_R$  drastically, which restricts us from claiming the dominance of the DP spin-relaxation via this method.

We do not observe any measurable effect of the anisotropic spin-relaxation, i.e., different  $\tau_s$  for the spins in the the graphene plane and perpendicular to the graphene plane, at high magnetic fields, as reported by Ghiasi *et al.* [18]. This might be due to a large linear magneto-resistance background, we constantly observe during the Hanle measurements, which makes it difficult to distinguish the saturation of the relatively small spin-signal when the ferromagnetic electrodes are aligned perpendicular to the graphene plane at high  $B_{\perp}$  and only out-of-plane spins are injected. The multilayer nature of the TMD in our sample could also be responsible for modifying the magnitude of this effect. Even after removing the linear background, we do not observe an enhanced out-of-plane spin signal at high magnetic fields, compared to the in-plane signal. For our measurements, the out-of-plane to in-plane spin signal ratio is always less than one. It could also be due to the presence of in-plane Rashba SOC [21] in our system. According to Cummings *et al.* [15], the anisotropy in the in-plane and out-of plane spin-relaxation can not be always observed. It depends on the intervalley scattering rate and the relative strengths of the in-plane Rashba SOC  $\lambda_R$  (in meV) induced at the graphene-WS<sub>2</sub> interface due to broken inversion symmetry [7, 8, 15] and the out-of-plane valley-Zeeman SOC  $\lambda_V$  (in meV) induced in graphene due to the intrinsic SOC in WS<sub>2</sub> [8, 9, 15]. In case of a strong intervalley scattering both in-plane and out-of-plane spins experience the motion narrowing and they get dephased. However, due to  $\lambda_V > \lambda_R$ , the in-plane spins relax faster

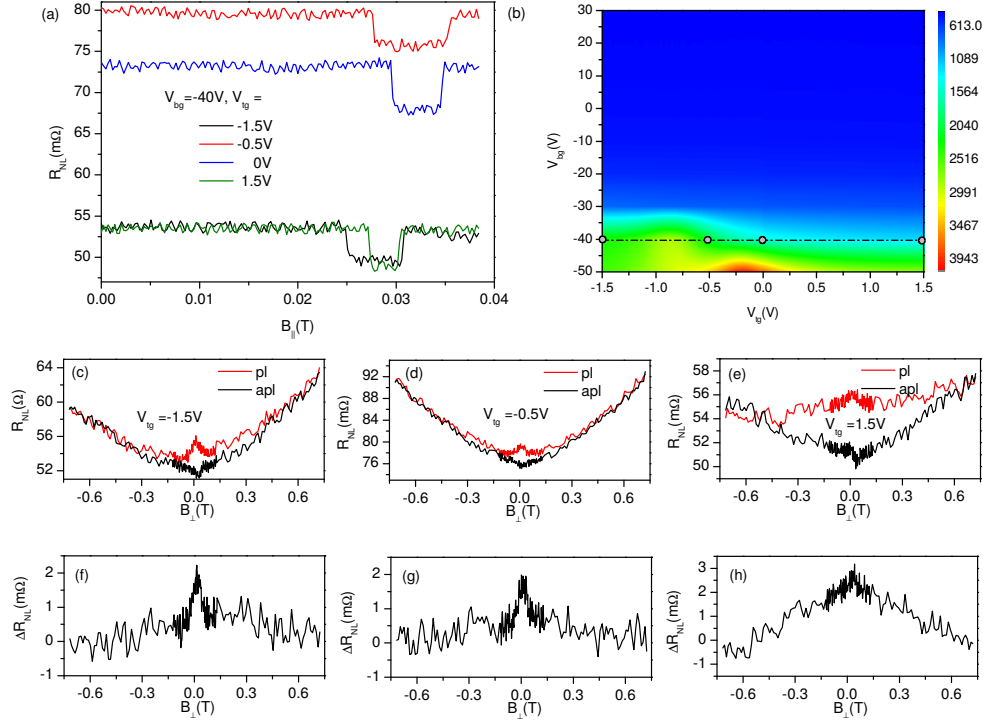


**Figure 11.6:** (a) SV measurements across the encapsulated region (region-II) of stack A at different top-gate voltages, which change the doping of the encapsulated region from hole to electron doped regime. The spin-signal  $\Delta R_{NL}$  remains unaffected. (b)  $R_{sq}$  for the encapsulated region as a function of  $V_{bg}$  and  $V_{sg}$ . The gray circles on the dotted horizontal at  $V_{bg} = -40$  V, denote the  $V_{sg}$  values at which the spin valve and the Hanle measurements have been taken. Hanle measurements for the encapsulated region for the hole doped regime, at the CNP and electron-doped regime are shown in (c), (d) and (e), respectively.

than the out-of plane spins, which get dephased by the Rashba SOC, thus giving rise to the anisotropy. In our case, it could be possible that there is a weak-intervalley scattering with the dominant Rashba SOC which gives rise to faster relaxation of the out-of-plane spins, expected for a typical Rashba system and hinders us from observing a strong anisotropic effect [15]. However, a direct conclusion regarding intervalley scattering rate cannot be drawn from the spin-transport measurements alone.

Now we perform the Hanle spin-precession measurements in the encapsulated region of stack A ( $L \sim 6.7 \mu\text{m}$ ). Due to the partial encapsulation of  $\text{WS}_2$  via hBN, we can study the effect of the top-gate when the bottom  $\text{WS}_2$  does not conduct. We can access both electron and hole regime via top gating, for a fixed  $V_{bg} < -30$  V. For

the Hanle measurements shown in Fig. 11.6(c)-(f) at  $V_{bg}=-40$  V, corresponding to the CNP of the back-gated graphene and perform the Hanle measurements, while varying  $V_{ig}$  from the hole regime at  $V_{ig}=-1.5$ V to the electron-doped regime at  $V_{ig}=+1.5$ V. With the top gate application, we can control two parameters: first, we can tune the carrier densities from electron to hole regime and vice versa. Second, we also apply an out of plane electric field which again breaks the  $z \leftrightarrow -z$  symmetry and modifies the surface Rashba SOC [1, 21, 31]. For the hole regime, i.e.,  $V_{ig}=-1.5$  V, -0.5 V, we measure a narrow Hanle shape, an indicative of higher  $\tau_s$  for the hole spins, plotted in Fig. 11.6(f)-(g). Now, at  $V_{ig}=+1.5$  V, when the encapsulated region is again electron-doped, the sharp Hanle feature disappears and a broad Hanle corresponding to lower  $\tau_s$  of electrons is visible again. We fit the Hanle data for  $|B_{\perp}| < 200$  mT, while assuming  $D_s = D_c$ , where  $D_c$  is obtained from the  $\sigma - V_{ig}$  dependence, and obtain  $\tau_s \sim 40$  ps-80 ps, as shown in Fig. 11.5(c). We repeat the measurements for  $V_{bg}=-50$ V, -35V and see a similar behavior, confirming that the hole and electron spins have different  $\tau_s$  values with  $\tau_s^h > \tau_s^e$ . The higher  $\tau_s^h$  could be possibly due to the combined effect of a intrinsically reduced spin-orbit coupling in the hole regime [15, 32] and the modification of the electric-field induced Rashba SOC [7, 8, 21]. There are two features evident from Fig. 11.5(c) and (d). First, for similar carrier densities in the electron and hole regimes, a reduced  $\tau_s$  is observed for  $E$  pointing towards WS<sub>2</sub>, i.e.  $E < 0$  (black box in Fig. 11.5(c)). Second, for the same electric field an enhanced  $\tau_s$  is observed at lower carrier densities, denoted by the green box in Fig. 11.5(d), similar to that obtained from the WAL experiments in [7, 10]. These observations support the presence of an electric field controllable SOC at the graphene-WS<sub>2</sub> interface and the DP type mechanism for the hole transport.

Our results also provide an alternative explanation to the observation of ref.[16, 17] where the spin-signal enhancement is observed when the TMD does not conduct. At this point,  $E_F$  in graphene is shifted to the hole doped regime. The net spin-relaxation rate is dominated by the relaxation at the graphene-TMD interface and is reflected in the reduced  $\Delta R_{NL}$ , while switching on the TMD, coinciding with the electron-doped regime in graphene. Based on our results, we argue that it is the modulation of the spin-orbit coupling strength than the spin-absorption which changes the spin-relaxation time, leading to the same results.

## 11.5 Low Temperature Quantum Magnetotransport Measurements

Alternatively, in order to confirm the presence of the substrate induced SOC in graphene, we perform quantum magneto-resistance (MR) measurements in graphene in the electron-doped regime at 4K, using the local four probe geometry. Here we measure the flake resistance as a function of an out-of plane magnetic field with several

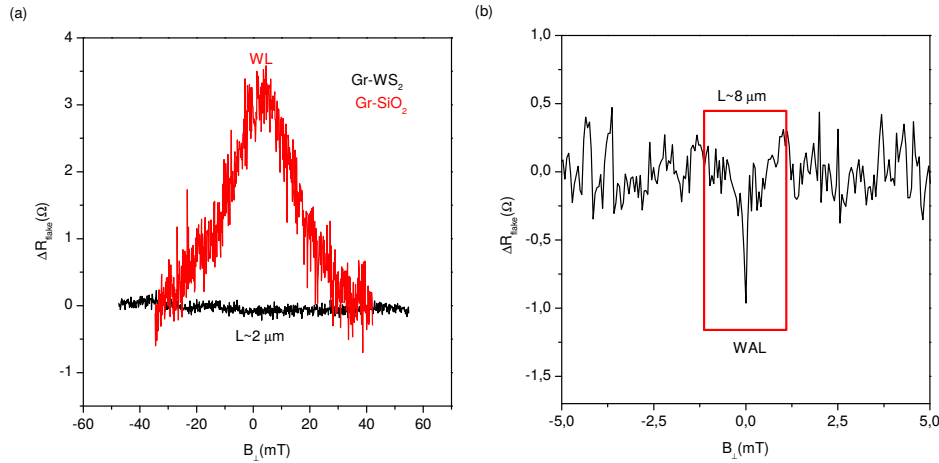


**Figure 11.7:** (a) Weak localization signal on ref B flake on a  $\text{SiO}_2$  substrate (red) and no WL/WAL signature was detected in graphene-on- $\text{WS}_2$  (region-I of stack A) (b) a narrow WAL signature in the encapsulated region was detected, probably due to possibility of more spatial averaging at long region ( $L \sim 8 \mu\text{m}$ ) and high mobility in the encapsulated region (region-II of stack A). All the data shown here is taken at 4K.

averaging operations, in order to suppress the universal conductance fluctuations in the sample resistance at low temperatures [33]. First, we measure the MR of reference graphene-flake on  $\text{SiO}_2$  substrate at 4K. Here we see a broad weak-localization (WL) signature (Fig. 11.7(a)), probably due to the low mobility of the sample [8, 10, 33]. However, for the graphene on  $\text{WS}_2$  (region-I), under the same measurement conditions, we do not observe any signature of the weak localization which is typical hall mark for single layer graphene, and appears at low magnetic field due to suppressed back-scattering of the electrons [33]. Even for graphene-on  $\text{WS}_2$  we have three times higher mobility, which should help in observing a peak at the low scan of the magnetic field. The absence of the WL signal in graphene-on  $\text{WS}_2$  stack indicates towards the emergence of a competing effect such as weak anti-localization (WAL) effect. In fact, when we measure the magneto-resistance for a longer flake region up to  $\sim 7\text{-}10 \mu\text{m}$ , including the encapsulated region as well, we observe a clear WAL signature (Fig. 11.7(b)), which could be due to the more spatial averaging of the signal in the longer channel. The observation of the WAL signature in  $\text{WS}_2$  supported single layer graphene confirms the existence of the enhanced spin-orbit coupling in graphene.

## 11.6 Conclusions

In conclusion, by demonstrating the signature of proximity induced SOC via WAL measurements in the electron doped regime, with no signs of spin-absorption via top and back-gate applications in a broad carrier density range, resulting in a constant  $\Delta R_{NL}$ , we unambiguously show that the spin-relaxation process in graphene on WS<sub>2</sub> substrate is affected by the WS<sub>2</sub> induced SOC. The proximity effect reflects in broad Hanle curves with a  $\tau_s \sim 10$  ps. Via top-gate voltage application, we access the hole transport regime and show that the hole spins have a longer  $\tau_s \sim 40$  ps- 80 ps, implying a reduced  $\lambda_R$  in this regime. Via carrier-density dependence of  $\tau_s$  in both electron- and hole- regime, where WS<sub>2</sub> is in off-and -on state, we observe DP -type mechanism, i.e., a reduced  $\tau_s$  with increasing the carrier density, a typical hall mark of surface induced Rashba SOC. The effect is more (less) pronounced for the hole (electron) regime due to a higher (lower)  $\tau_s$ . The lack of out-of-plane anisotropy suggests towards the presence of an in-plane Rashba field. We also demonstrate the modification of  $\tau_s$  as a function of perpendicular electric field in the hBN-encapsulated region, which suggests the control of in-plane Rashba SOC via electrical gating.

Summarizing our results, via pure spin-transport measurements, we, for the first time, unambiguously demonstrate the effect of the proximity-induced-SOC in graphene on a high SOC semiconducting WS<sub>2</sub> substrate, opening a new avenue for high mobility spintronic devices with enhanced spin-orbit strength materials. A gate controllable spin-orbit coupling and thus the modulation of spin-relaxation time almost by an order in our graphene/WS<sub>2</sub> heterostructure, paves a way for realizing the future spin-transistors.

## 11.7 Acknowledgements

We acknowledge J. G. Holstein, H. M. de Roos, T. Schouten and H. Adema for their technical assistance. We are thankful to M. Gurram for the scientific discussion and his help during the sample preparation and measurements. This research work was financed under EU-graphene flagship program (637100) and supported by the Zernike Institute for Advanced Materials and the Netherlands Organization for Scientific Research (NWO).



## References

- [1] H. Min, J. E. Hill, N. A. Sinitsyn, B. R. Sahu, L. Kleinman, and A. H. MacDonald, "Intrinsic and Rashba spin-orbit interactions in graphene sheets," *Phys. Rev. B* **74**, p. 165310, Oct. 2006.
- [2] C. Ertler, S. Konschuh, M. Gmitra, and J. Fabian, "Electron spin relaxation in graphene: The role of the substrate," *Phys. Rev. B* **80**, p. 041405, July 2009.
- [3] D. Huertas-Hernando, F. Guinea, and A. Brataas, "Spin-Orbit-Mediated Spin Relaxation in Graphene," *Phys. Rev. Lett.* **103**, p. 146801, Sept. 2009.
- [4] S. Datta and B. Das, "Electronic analog of the electrooptic modulator," *Appl. Phys. Lett.* **56**, pp. 665–667, Feb. 1990.
- [5] G. Giovannetti, P. A. Khomyakov, G. Brocks, P. J. Kelly, and J. van den Brink, "Substrate-induced band gap in graphene on hexagonal boron nitride: Ab initio density functional calculations," *Phys. Rev. B* **76**, p. 073103, Aug. 2007.
- [6] C. R. Woods, L. Britnell, A. Eckmann, R. S. Ma, J. C. Lu, H. M. Guo, X. Lin, G. L. Yu, Y. Cao, R. V. Gorbachev, A. V. Kretinin, J. Park, L. A. Ponomarenko, M. I. Katsnelson, Y. N. Gornostyrev, K. Watanabe, T. Taniguchi, C. Casiraghi, H.-J. Gao, A. K. Geim, and K. S. Novoselov, "Commensurate-incommensurate transition in graphene on hexagonal boron nitride," *Nat. Phys.* **10**, pp. 451–456, June 2014.
- [7] B. Yang, M. Lohmann, D. Barroso, I. Liao, Z. Lin, Y. Liu, L. Bartels, K. Watanabe, T. Taniguchi, and J. Shi, "Strong electron-hole symmetric Rashba spin-orbit coupling in graphene/monolayer transition metal dichalcogenide heterostructures," *Phys. Rev. B* **96**, p. 041409, July 2017.
- [8] B. Yang, M.-F. Tu, J. Kim, Y. Wu, H. Wang, J. Alicea, R. Wu, M. Bockrath, and J. Shi, "Tunable spinorbit coupling and symmetry-protected edge states in graphene/WS<sub>2</sub>," *2D Mater.* **3**(3), p. 031012, 2016.
- [9] Z. Wang, D.-K. Ki, H. Chen, H. Berger, A. H. MacDonald, and A. F. Morpurgo, "Strong interface-induced spinorbit interaction in graphene on WS<sub>2</sub>," *Nat. Commun.* **6**, p. ncomms9339, Sept. 2015.
- [10] Z. Wang, D.-K. Ki, J. Y. Khoo, D. Mauro, H. Berger, L. S. Levitov, and A. F. Morpurgo, "Origin and Magnitude of 'Designer' Spin-Orbit Interaction in Graphene on Semiconducting Transition Metal Dichalcogenides," *Phys. Rev. X* **6**, p. 041020, Oct. 2016.
- [11] S. Omar and B. J. van Wees, "Graphene-ws2 heterostructures for tunable spin injection and spin transport," *Phys. Rev. B* **95**, p. 081404, Feb. 2017.
- [12] A. Avsar, J. Y. Tan, T. Taychatanapat, J. Balakrishnan, G. K. W. Koon, Y. Yeo, J. Lahiri, A. Carvalho, A. S. Rodin, E. C. T. O'Farrell, G. Eda, A. H. Castro Neto, and B. Özyilmaz, "Spinorbit proximity effect in graphene," *Nat. Commun.* **5**, p. 4875, Sept. 2014.
- [13] M. Gmitra and J. Fabian, "Graphene on transition-metal dichalcogenides: A platform for proximity spin-orbit physics and optospintronics," *Phys. Rev. B* **92**, p. 155403, Oct. 2015.
- [14] D. Xiao, W. Yao, and Q. Niu, "Valley-Contrasting Physics in Graphene: Magnetic Moment and Topological Transport," *Phys. Rev. Lett.* **99**, p. 236809, Dec. 2007.
- [15] A. W. Cummings, J. H. García, J. Fabian, and S. Roche, "Giant Spin Lifetime Anisotropy in Graphene Induced by Proximity Effects," *arXiv:1705.10972 [cond-mat]*, May 2017. arXiv: 1705.10972.
- [16] A. Dankert and S. P. Dash, "Electrical gate control of spin current in van der Waals heterostructures at room temperature," *Nat. Commun.* **8**, p. ncomms16093, July 2017.
- [17] W. Yan, O. Txoperena, R. Llopis, H. Dery, L. E. Hueso, and F. Casanova, "A two-dimensional spin field-effect switch," *Nat. Commun.* **7**, p. ncomms13372, Nov. 2016.
- [18] T. S. Ghiasi, J. Ingla-Aynés, A. A. Kaverzin, and B. J. van Wees, "Large Proximity-Induced Spin Lifetime Anisotropy in Transition Metal Dichalcogenide/Graphene Heterostructures," *arXiv:1708.04067 [cond-mat]*, Aug. 2017. arXiv: 1708.04067.
- [19] A. V. Kretinin, Y. Cao, J. S. Tu, G. L. Yu, R. Jalil, K. S. Novoselov, S. J. Haigh, A. Gholinia, A. Mishchenko, M. Lozada, T. Georgiou, C. R. Woods, F. Withers, P. Blake, G. Eda, A. Wirsig, C. Hucho, K. Watanabe, T. Taniguchi, A. K. Geim, and R. V. Gorbachev, "Electronic Properties of Graphene



- Encapsulated with Different Two-Dimensional Atomic Crystals," *Nano Lett.* **14**, pp. 3270–3276, June 2014.
- [20] N. Tombros, C. Jozsa, M. Popinciuc, H. T. Jonkman, and B. J. van Wees, "Electronic spin transport and spin precession in single graphene layers at room temperature," *Nature* **448**, pp. 571–574, Aug. 2007.
- [21] M. Guimarães, P. Zomer, J. Ingla-Aynés, J. Brant, N. Tombros, and B. van Wees, "Controlling Spin Relaxation in Hexagonal BN-Encapsulated Graphene with a Transverse Electric Field," *Phys. Rev. Lett.* **113**, p. 086602, Aug. 2014.
- [22] P. J. Zomer, M. H. D. Guimarães, J. C. Brant, N. Tombros, and B. J. v. Wees, "Fast pick up technique for high quality heterostructures of bilayer graphene and hexagonal boron nitride," *Appl. Phys. Lett.* **105**, p. 013101, July 2014.
- [23] S. V. Morozov, K. S. Novoselov, M. I. Katsnelson, F. Schedin, D. C. Elias, J. A. Jaszczak, and A. K. Geim, "Giant Intrinsic Carrier Mobilities in Graphene and Its Bilayer," *Phys. Rev. Lett.* **100**, p. 016602, Jan. 2008.
- [24] M. Gurram, S. Omar, S. Zihlmann, P. Makk, C. Schönenberger, and B. J. van Wees, "Spin transport in fully hexagonal boron nitride encapsulated graphene," *Phys. Rev. B* **93**, p. 115441, Mar. 2016.
- [25] M. Popinciuc, C. Józsa, P. J. Zomer, N. Tombros, A. Veligura, H. T. Jonkman, and B. J. van Wees, "Electronic spin transport in graphene field-effect transistors," *Phys. Rev. B* **80**, p. 214427, Dec. 2009.
- [26] M. Isasa, M. C. Martínez-Velarte, E. Villamor, C. Magn, L. Morelln, J. M. De Teresa, M. R. Ibarra, G. Vignale, E. V. Chulkov, E. E. Krasovskii, L. E. Hueso, and F. Casanova, "Origin of inverse Rashba-Edelstein effect detected at the Cu/Bi interface using lateral spin valves," *Phys. Rev. B* **93**, p. 014420, Jan. 2016.
- [27] W. Han, R. K. Kawakami, M. Gmitra, and J. Fabian, "Graphene spintronics," *Nat. Nanotech.* **9**, pp. 794–807, Oct. 2014.
- [28] W. Han and R. K. Kawakami, "Spin Relaxation in Single-Layer and Bilayer Graphene," *Phys. Rev. Lett.* **107**, p. 047207, July 2011.
- [29] C. Józsa, T. Maassen, M. Popinciuc, P. J. Zomer, A. Veligura, H. T. Jonkman, and B. J. van Wees, "Linear scaling between momentum and spin scattering in graphene," *Phys. Rev. B* **80**, p. 241403, Dec. 2009.
- [30] P. J. Zomer, M. H. D. Guimarães, N. Tombros, and B. J. van Wees, "Long-distance spin transport in high-mobility graphene on hexagonal boron nitride," *Phys. Rev. B* **86**, p. 161416, Oct. 2012.
- [31] M. Gmitra, S. Konschuh, C. Ertler, C. Ambrosch-Draxl, and J. Fabian, "Band-structure topologies of graphene: Spin-orbit coupling effects from first principles," *Phys. Rev. B* **80**, p. 235431, Dec. 2009.
- [32] M. Gmitra, D. Kochan, P. Högl, and J. Fabian, "Trivial and inverted Dirac bands and the emergence of quantum spin Hall states in graphene on transition-metal dichalcogenides," *Phys. Rev. B* **93**, p. 155104, Apr. 2016.
- [33] M. B. Lundeberg, R. Yang, J. Renard, and J. A. Folk, "Defect-Mediated Spin Relaxation and Dephasing in Graphene," *Phys. Rev. Lett.* **110**, p. 156601, Apr. 2013.



---

## Summary

Transporting the spin of an electron over long distances, without the loss of its initial properties, is viable for future spin-based devices. Graphene, a honeycomb lattice of carbon atoms, has the potential to carry spins up to millimeter length scales. Therefore, since last decade it has been the work-horse in the field of spintronics research. Still, the research community is unable to transport them at such long distances and even with the best possible devices, researchers have been able to realize spin-relaxation length only up to  $30 \mu\text{m}$  which is almost lower by two orders of magnitude than the expected values. This is a big puzzle being faced by the graphene community, and there is a lot of theoretical work along with some experiments, which suggests that the impurities, specifically magnetic impurities present at the graphene surface, greatly suppress its spin transport properties. However, no direct spin-transport experiments have been performed in this direction. Another aspect, on which the spintronic community is putting a lot of efforts on, is controlling the spin-current in graphene. This requires an electrical control of the parameters influencing the spin current in graphene, such as inducing and controlling the spin-orbit coupling in graphene.

In this thesis titled "Spin transport and relaxation in graphene, functionalized-graphene and graphene-TMD heterostructures", I experimentally study the spin-transport in graphene in two major directions. First, I study the effect of impurities on spin transport. Second, I explore the possibility of inducing spin-orbit coupling and controlling it via an external electric field in graphene, by putting it in the proximity of a transition metal dichalcogenide crystal.

I also explore the effect of magnetic impurities in two different ways. In the first, we directly put magnetic cobalt-porphyrin molecules on graphene via a non-destructive self-assembly method, and observe that the spin-relaxation time is significantly reduced in presence of magnetic-impurities. This behavior is attributed to an enhanced spin-flip scattering in presence of magnetic scattering centers. In the second method, we study the effect of impurities via an indirect method, i.e., by

measuring the noise of the spin-signal in graphene. In this experiment, we measure a spin-dependent  $1/f$  noise present in the spin-accumulation in graphene, and note that the noise is enhanced at a higher spin-relaxation rate. This implies that the noise is produced due to spin-relaxation processes in graphene. This noise is believed to originate from the interaction of the spin-current with the impurities, giving rise to the  $1/f$  nature of the measured noise. Also, the spin-dependent noise is orders of magnitudes higher than the  $1/f$  noise in the charge transport. The higher noise magnitude quantifies the higher scattering strength of impurities for the spin degree of freedom of electron than for the charge degree of freedom. Here, we again obtain the same conclusion from a completely different experiment that impurities are detrimental to the spin transport in graphene.

The interesting aspect of electronics does not lie only in high-quality charge transport but in the virtue how efficiently we can control the charge transport via the gating action. Spin-transport follows similar rules. Even one can achieve a millimeter long spin-transport, a practical spin-transistor cannot be realized until and unless we know how to control the spin-current.

Recently, there has been a lot of buzz about layered semiconductors such as transition metal dichalcogenides, which can be exfoliated down to monolayers like graphene and have a handle to control the spins, i.e. via, spin-orbit coupling. When graphene is put in contact with a transition metal dichalcogenide, a significant spin-orbit coupling (SOC) in the order of milielectron volts can be induced in graphene that is about 100 times higher than the SOC in intrinsic graphene.

In this thesis, I study spin-transport in two types of graphene- $WS_2$  heterostructures. In first architecture, graphene is partially encapsulated via a  $WS_2$  flake from the top. Here, I study the possibility of enhancing SOC in graphene, in contact with  $WS_2$ , via nonlocal spin-transport measurements, and also injecting spins in graphene through the same  $WS_2$  intermediate layer. Since the resistance of the graphene- $WS_2$  interface can be modified as a function of bias, its spin-injection efficiency can be tuned as well. As expected, I measure an enhanced spin-relaxation in graphene underneath the  $WS_2$  flake. We can also successfully control the spin-injection efficiency with the bias at the graphene- $WS_2$  interface. Next, I study the proximity effect of  $WS_2$  on graphene in a different device architecture where I reverse the stacking order of graphene and  $WS_2$ , and use  $WS_2$  as a substrate for spin transport in graphene. Here, I clearly see the effect of proximity induced SOC on the spin-transport properties of graphene. First, due to a smooth and impurity free  $WS_2$  surface, the mobility of graphene is increased which helps to observe small spin signals in spite of much-reduced spin relaxation time due to a proximity induced SOC. With the application of an electric-field in the spin-transport channel, we can even tune the spin-orbit coupling strength in graphene and therefore, the spin-relaxation time almost by an order of magnitude, which is a significant step towards realizing the practical graphene-based spin-transistors.

I also briefly touch upon the graphene/hBN heterostructures where we fully encapsulate graphene between two hBN flakes and use the first hBN flake as a bottom substrate to improve the charge transport properties of graphene and the second hBN flake as a tunnel barrier for efficient spin-injection into graphene. With the exfoliated bilayer hBN tunnel barriers, we can achieve even up to 100% spin polarization which is certainly a good news for the spintronic community. These results will push forward towards realizing practical graphene-based spintronic devices with improved figure of merit. For a scalable production of spintronic devices, one needs to realize the same performance with the CVD counterparts. We also perform experiments with CVD hBN tunnel barriers. However, due to inhomogeneous CVD hBN tunnel barriers and the wet transfer process of the CVD barriers onto graphene which involves its immersion in water, the performance is not as good as in the case of exfoliated tunnel barriers. We still need to optimize the device fabrication process using the CVD hBN, in order to enhance the prospects for the use of CVD hBN/graphene for the industrial scale production of graphene-based spintronic devices.

This thesis provides a very first set of spin-transport measurements in graphene with respect to control over spin injection/detection and transport properties in graphene, which has been realized up to a certain degree. The presented study will play an important role in laying the foundation for future spintronic devices. Certainly, graphene spintronic research is very close to realizing a practical graphene-based spin-transistor, which will provide the scientific community an opportunity to pursue the long-sought dream of spin-logic circuits.



---

## Samenvatting

Het transporteren van elektronenspins over een grote afstand, zonder verlies van initiële informatie, is haalbaar voor toekomstige, op spin gebaseerde apparaten. Gelukkig heeft grafeen de potentie om de spins tot op millimeter lengteschalen te vervoeren en daarom is het al bijna een decennium het werkpaard voor het spintronicaonderzoek. Toch is de onderzoeksgemeenschap niet in staat om de spins over zulke lange afstanden te vervoeren en zelfs met de best mogelijke apparaten konden mensen slechts tot 30  $\mu\text{m}$  meten, wat bijna twee orde van grootte kleiner is dan de verwachte waarden. Deze sterke onderdrukking van de spintransporteigenschappen is een grote uitdaging voor de grafeengemeenschap. Inmiddels zijn er veel publicaties, zowel theoretische als enkele experimentele, die suggereren dat hoofdzakelijk magnetische onzuiverheden aan het grafeenoppervlak hiervoor verantwoordelijk zijn. Er zijn echter geen directe spin-transportexperimenten uitgevoerd in deze richting. Een ander aspect, waar de spintronic-gemeenschap veel inspanningen aan levert, is het controleren van de spinstroom in grafeen. Dit vereist het elektrisch reguleren van de parameters die de spinstroom in grafeen beïnvloeden, zoals het induceren en manipuleren van de spin-orbitaalkoppeling in grafeen.

In dit proefschrift onderzoek ik het spintransport met behulp van experimenten in twee hoofdrichtingen. Ten eerste onderzoek ik het effect van onzuiverheden op spintransport. Ten tweede onderzoek ik de mogelijkheid om de spin-orbitaalkoppeling te induceren en deze te regelen via een extern elektrisch veld in grafeen door het in de nabijheid van een kristallen overgangsmetaal dichalcogenide te plaatsen.

Ik onderzoek het effect van magnetische onzuiverheden op twee manieren. Ten eerste plaatsen we de magnetische kobalt-porfyrimoleculen rechtstreeks op grafeen via niet-destructieve zelfassemblage en zien we dat de spin-relaxatietijd aanzienlijk wordt verminderd in de aanwezigheid van de magnetische onzuiverheden. Dit gedrag wordt toegeschreven aan een versterkte spin-flip-verstrooiing in aanwezigheid van de magnetische verstrooiingscentra. Ten tweede bestuderen we het effect van de onzuiverheden via een indirecte methode, namelijk door het meten van de  $1/f$ -

ruis van het spin-sigitaal in grafeen. In dit experiment meten we een spinafhankelijke  $1/f$ -ruis die aanwezig is in de spin-accumulatie in grafeen en zien we dat de ruis wordt versterkt bij hogere spin-relaxatiesnelheid. Dit impliceert dat de geproduceerde ruis het gevolg is van spin-relaxatieprocessen in grafeen. De ruis is order van grootte hoger dan de  $1/f$  ruis veroorzaakt door het ladingstransport, hetgeen kan worden genterpreteerd dat de  $1/f$  aard van de gemeten ruis wordt veroorzaakt door de interactie van de spinstroom met de onzuiverheden. De hogere ruismagnitude kwantificeert de hogere verstrooiingssterkte van de onzuiverheden voor de vrijheidsgraden van de elektronspin in vergelijking met de vrijheidsgraden van de electronlading. Dit compleet verschillende onderzoek brengt ons tot dezelfde conclusie: onzuiverheden zijn nadelig voor spintransport in grafeen.

Het interessante aspect van elektronica ligt niet zodanig in hoogwaardig ladingstransport, maar kenmerkt zich in de efficiënte manier waarop de ladingstransport beïnvloed wordt door een spanning over de basis aan te leggen. Spin-transport moet soortgelijke regels volgen. Zelfs als spin transport over millimeters kan bereikt worden, kan een praktische spin-transistor niet worden gerealiseerd tenzij we weten hoe je spins kunt controleren.

Er is veel te doen geweest over de gelaagde halfgeleiders zoals de overgangsmetal-dichalcogenidenfamilie. Deze kunnen worden geëfolieerd tot monolagen zoals grafeen en hebben de mogelijkheid om de spins te regelen door middel van spin-orbitaal koppeling. Wanneer grafeen in de nabijheid van een overgangsmetaaldichalcogenide wordt geplaatst, kan een significante spin-orbitaalkoppeling (SOK) in de orde van milli-elektronvolt worden geïnduceerd welke 100 keer groter is dan de SOK in intrinsiek grafeen. In dit proefschrift bestudeer ik spin-transport in twee soorten grafeen- $WS_2$  heterostructuren. De eerste constructie is een grafeen spintransportkanaal gedeeltelijk ingekapseld met een  $WS_2$ -laag vanaf de bovenkant. Hier bestudeer ik de mogelijkheid van een door de nabijheid van  $WS_2$  geïnduceerde SOK in grafeen via niet-lokale spin-transport metingen en injecteer ook spins in grafeen via dezelfde  $WS_2$ -tussenlaag. Omdat de weerstand van het grafeen- $WS_2$ -grensvlak kan worden gewijzigd als een functie van het voltage over de basis, kan de spin-injectie-efficiëntie ook worden afgestemd. Ik laat zien dat er een verbeterde spin-relaxatie is in grafeen onder  $WS_2$  en we kunnen met succes de spin-injectie efficiëntie regelen met het voltage over de basis. Vervolgens bestudeer ik het nabijheidseffect van  $WS_2$  op grafeen in een andere apparaatconstructie, waarbij ik de volgorde van grafeen en  $WS_2$  omkeert en  $WS_2$  dus als substraat voor spintransport in grafeen functioneert. Hier zie ik duidelijk het effect van de door de nabijheid geïnduceerde SOK op de spintransporteigenschappen van grafeen. Ten eerste is de beweeglijkheid van grafeenelectronen groter dankzij een glad en vrij van onzuiverheden  $WS_2$ -oppervlak. Dit vereenvoudigt het waarnemen van kleine spinsignalen ondanks een veel lagere spin-relaxatietijd als gevolg van een geïnduceerde spin-orbitaal koppeling. Met de toepassing van een elektrisch veld in het spintransportkanaal

kunnen we zelfs de sterkte van de spin-orbitaalkoppeling in grafeen afstemmen en de spin-relaxatietijd bijna in een orde van grootte moduleren, wat een belangrijke stap is naar het realiseren van het praktische grafeen gebaseerde spin-transistors.

Ik bespreek ook kort de grafeen/hBN heterostructuren waar we het grafeen volledig inkapselen en hBN gebruiken zowel als bodemsubstraat als een tunnelbarrière voor efficiënte spin-injectie. Met de gefolieerde dubbellaagse hBN-tunnelbarrières kunnen we zelfs tot 100% spinpolarisatie bereiken, wat zeker goed nieuws is voor de spintronica-gemeenschap en met deze resultaten kunnen verdere stappen zetten in de realisatie van praktische, op grafeen gebaseerde, spintronische apparaten met een verbeterd prestatievermogen. Voor schaalbare productie van de spintronische apparaten, moet men hetzelfde realiseren met chemische damp afzetting (CDA) tegenhangers. We voeren ook experimenten uit met CDA-hBN-tunnelbarrières.

Omdat het overdrachtsproces van de CDA-tunnelbarrières op grafeen onderdompeling in water vereist, en vanwege de inhomogeniteit van de tunnelbarrières zijn de prestaties echter niet zo goed als in het geval van gefolieerde tunnelbarrières. Voor het verbeteren van de vooruitzichten voor het gebruik van CDA hBN/grafeen voor praktische spintronische toepassingen moeten deze aspecten worden geoptimaliseerd.

Dit proefschrift probeert te voorzien in een eerste reeks spin-transport metingen in grafeen met betrekking tot een controle over spininjectie en -detectie en transportprocessen in grafeen die tot op zekere hoogte is gerealiseerd. De gepresenteerde studie zal een belangrijke rol spelen bij het leggen van de basis voor toekomstige spintronische apparaten. Zeker is dat het spintronische onderzoek van grafeen heel dichtbij is om een praktische, op grafeen gebaseerde, spin-transistor te realiseren die de wetenschappelijke gemeenschap een kans zal bieden om de lang gezochte droom van een spin-logica netwerk na te streven.





## शोध-सारांश

इलेक्ट्रान के स्पिन पर आधारित सूक्ष्म-यंत्रों का निर्माण मुख्यतः इस तथ्य पर निर्भर करता है कि इलेक्ट्रान का स्पिन अपनी प्रारंभिक अवस्था को अपरिवर्तित रखते हुए कितनी दूरी तय कर सकता है। ग्राफीन एक मधुमक्खी के छत्ते के बनावट में सजे कार्बन (C) परमाणुओं पर आधारित द्विविमिय संरचना वाला पदार्थ है जो इलेक्ट्रान के स्पिन को दूर तक ले जाने में सक्षम है। यही कारण है कि स्पिनट्रॉनिक्स-अनुसंधान के क्षेत्र में ग्राफीन पिछले एक दशक से वैज्ञानिकों के बीच एक चर्चा का मुख्य विषय रहा है। अनेक अनुसंधानों के बावजूद भी वैज्ञानिक, ग्राफीन आधारित सूक्ष्म-यंत्रों से अपेक्षित परिणाम पाने में अभी तक पूर्ण रूप से सफल नहीं हो पाये हैं। इसका एक सटीक उदाहरण है कि अभी तक के सर्वश्रेष्ठ ग्राफीन यंत्र से मात्र 30 माइक्रोमीटर की दूरी तक ही इलेक्ट्रान का स्पिन परिवहन संभव हो पाया है, जबकि अपेक्षित आंकड़ों पर विश्वास किया जाय तो ग्राफीन द्वारा मिलीमीटर की दूरी तक स्पिन परिवहन संभव है। इस यक्ष-प्रश्न का सही उत्तर ढूँढने के लिए अनेकों प्रयास किये गये हैं। हाल-फिलहाल में यदि इस दिशा में किये गये प्रयोगों की परिणामों की बात करें तो ग्राफीन में उपस्थित अशुद्ध परमाणु, विशेष रूप से ग्राफीन की सतह पर उपस्थित चुम्बकीय परमाणुओं के कारण स्पिन परिवहन में व्यवधान उत्पन्न होता है। यद्यपि इस परिणाम को किसी प्रामाणिक प्रयोग द्वारा सिद्ध नहीं किया जा सका है। स्पिनट्रॉनिक्स पर अनुसंधान करने वाले कुछ वैज्ञानिक अन्य पहलुओं पर भी कार्य कर रहे हैं। तथा उनका ये अभिमत है कि एक सफल स्पिनट्रॉनिक्स यंत्र का निर्माण इस बात पर ज्यादा निर्भर करता है कि उसमें प्रवाहित स्पिन धारा को विद्युत क्षेत्र द्वारा स्पिन के वृत्त कक्षीय परिक्रमण क्रिया-विधि से नियंत्रित किया जा सकता है या नहीं? इस सिद्धांत के परीक्षण पर भी अनुसंधान कार्य तीव्र गति से आगे बढ़ रहा है।

अपने इस अनुसंधान कार्य में जिसका विषय है “ग्राफीन, क्रियाशील ग्राफीन तथा ग्राफीन-संक्रमण धातु काल्कोजन हेटरो संरचना में स्पिन परिवहन और विश्राम” में मैंने मुख्य रूप से इलेक्ट्रान के स्पिन परिवहन पर दो अलग-अलग दिशाओं में प्रयोग किया है। प्रथम में मैंने स्पिन परिवहन पर अशुद्धियों के प्रभाव का अध्ययन किया है तथा दूसरे में कृत्रिम विधियों द्वारा, जैसे ग्राफीन को टंगस्टन डाई सल्फाइड ( $WS_2$ ) नामक पदार्थ में रखकर ग्राफीन में उत्पन्न इलेक्ट्रान के स्पिन कक्षीय परिक्रमण युग्मन की संभावना और उससे उत्पन्न विद्युत क्षेत्र के नियंत्रण को प्रयोगों के माध्यम से अध्ययन किया है। दूसरी विधि की उल्लेखनीय बात यह है कि इसमें  $WS_2$  को एक उत्प्रेरक(//)स्नेहक की तरह प्रयोग किया जाता है, क्योंकि इससे स्पिन कक्षीय परिक्रमण युग्मन का प्रभाव उपयुक्त मात्रा में उपस्थित होता है।

इलेक्ट्रान के स्पिन परिवहन पर चुम्बकीय अशुद्धियों के प्रभाव को भी मैंने दो विधियों से अध्ययन किया है। प्रथम विधि में हम ग्राफीन को कोबाल्ट-पारफिरीन नामक रासायन से

## शोध-सारांश

प्रतिक्रिया कराते हैं, जिसमें कोबाल्ट एक चुम्बकीय अशुद्ध परमाणु है। इसका परिणाम यह होता है कि यह रासायन ग्राफीन की सतह पर स्वतः व्यवस्थित हो जाता है। हालांकि इस प्रक्रिया में ग्राफीन को किसी प्रकार की भौतिक या रासायनिक गुणों में हानि नहीं होती। इस प्रयोग से यह निष्कर्ष निकला जा सकता है कि चुम्बकीय अशुद्धियों की उपस्थिति में ग्राफीन में स्पिन का जीवन-अवधि बहुत कम हो जाता है। इसका मूल कारण यह है कि चुम्बकीय अशुद्धि के प्रभाव में इलेक्ट्रान के स्पिन का दिशा परिवर्तन आकस्मिक हो सकता है। द्वितीय विधि में हम स्पिन परिवहन पर अशुद्धियों के प्रभाव का अध्ययन अप्रत्यक्ष रूप से करते हैं। इस विधि में हम ग्राफीन के स्पिन सिग्नल में उपस्थित यादृच्छिक ध्वनि की मात्रा मापते हैं। यह मात्रा ध्वनि की आवृत्ति (अंतराल) पर भी निर्भर करता है और यह आवृत्ति (f) निर्भरता  $1/f$  प्रकृति की है। इस प्रयोग में  $1/f$  ध्वनि स्पिन सिग्नल पर निर्भर करती है व स्पिन आकस्मिक दिशा परिवर्तन की आवृत्ति के साथ बढ़ती है। इसका अर्थ यह भी हो सकता है कि स्पिन का जीवन-काल कम होने से  $1/f$  ध्वनि बढ़ती जाती है व इलेक्ट्रान स्पिन द्वारा उत्पन्न यादृच्छिक ध्वनि की मात्रा इलेक्ट्रान आवेश द्वारा उत्पन्न यादृच्छिक ध्वनि से अधिक हो जाती है, माप के अनुसार। इससे यह भी निष्कर्ष निकलता है कि ध्वनि जो कि स्पिन या आवेश धारा की अशुद्धि के साथ संपर्क में आने से उत्पन्न होती है, अधिक शक्तिशाली होने की वजह से परिमाण में ज्यादा है। सरल शब्दों में अशुद्धि स्पिन को आवेश की तुलना में अधिक प्रभावित करती है। अतः इस प्रयोग से यही निष्कर्ष निकलता है कि अशुद्धियाँ स्पिन परिवहन के लिये हानिकारक हैं। उत्तम आवेश परिवहन इलेक्ट्रॉनिक्स का उतना रोचक पहलु नहीं है जितना कि नियंत्रण वाल्व द्वारा आवेश नियंत्रण। स्पिन नियम पर भी समान रूप से यही नियम लागू होते हैं। भविष्य में यदि हम मिलीमीटर दूरी तक इलेक्ट्रान के स्पिन परिवहन को प्राप्त भी कर लें, पर बिना एक क्रियात्मक स्पिन ट्रांजिस्टर (जो कि एक स्पिनट्रॉनिक्स यंत्र है) के निर्माण के, स्पिन धारा को नियंत्रित नहीं कर सकते।

दर-परत-दर सतह वाले अर्ध-चालक हमेशा वैज्ञानिकों के बीच चर्चा का विषय रहे हैं। ये अर्ध-चालक संक्रमण धातुओं से बने यौगिक हैं और ग्राफीन की भांति "स्काँच टेप" की तरह एक-एक सतह के रूप में पृथक किये जा सकते हैं। इन यौगिकों की रोचक बात यह है कि इनके पास स्पिन नियंत्रण की क्रिया-विधि पहले से ही उपस्थित है व परिमाण में ग्राफीन से एक हजार गुना ज्यादा है। इस शोध में मैंने ग्राफीन- $WS_2$  पर आधारित दो ज्यामितियों का अध्ययन किया है। पहली ज्यामिति में ग्राफीन का स्पिन परिवहन पथ  $WS_2$  से आंशिक रूप से आच्छादित रहता है। इस ज्यामिति में मैंने  $WS_2$  की संपर्क में आयी ग्राफीन में स्पिन नियंत्रण क्रियाविधि के उत्पन्न होने की संभावना का विदेशीय (non-local) स्पिन संग्रह तरीके से अध्ययन किया है तथा  $WS_2$  को स्पिन धारा प्रवाहित करने वाली सतह की तरह भी उपयोग किया है। चूँकि विद्युत विभव के कारण ग्राफीन- $WS_2$  निकाय का प्रतिरोध बदला जा सकता है, यह इस निकाय की स्पिन-धारा प्रवाहित करने की दक्षता को भी नियंत्रित करता है। इस प्रयोग में मुझे दो प्रभाव देखने को मिले। पहला यह था कि  $WS_2$  के संपर्क से ग्राफीन

## शोध-सारांश

में स्पिन का जीवन काल बहुत कम हो जाता है | दूसरा कि  $WS_2$ -Gr निकाय में विभव के प्रभाव में स्पिन धारा परिवहन दक्षता को नियंत्रित किया जा सकता है | प्रयोग के अगले चरण में मैंने ग्राफीन को  $WS_2$  की सतह पर रखा है ताकि  $WS_2$  का प्रभाव समान रूप से ग्राफीन में उत्पन्न हो | इस प्रयोग से मुझे स्पष्ट रूप से ज्ञात होता है कि  $WS_2$  संपर्क का प्रभाव ग्राफीन पर दिखाई देता है |  $WS_2$  की सतह चिकनी होने की वजह से व उसमें अशुद्धियों की कम मात्रा होने से ग्राफीन में इलेक्ट्रॉनों की गतिशीलता बढ़ जाती है जो कि संपर्क प्रभाव के कारण छोटे स्पिन सिग्नल को मापने में सहायक हैं | विद्युत क्षेत्र के प्रभाव में हम स्पिन जीवन काल को और स्पिन नियंत्रण क्षमता को भी नियंत्रित कर सकते हैं | इस विधि से हम स्पिन जीवन-काल में 10गुणा परिवर्तन कर सकते हैं | यह ग्राफीन आधारित स्पिन-ट्रांजिस्टर यंत्रों के अनुसंधान में एक महत्वपूर्ण कदम है |

इस शोध में मैंने ग्राफीन-बोरोन नाईट्राईड ( Gr/BN ) निकाय पर आधारित प्रयोग को भी संक्षिप्त रूप में समावेशित किया है | यहाँ हम ग्राफीन को एक पतली और मोटी BN सतह के बीच संपुटित करते हैं | पतली BN सतह एक टनल अवरोध की तरह कार्य करती है | इसमें उल्लेखनीय बात यह है कि BN एक कुचालक है | BN की दो परमाणु जितनी मोटी सतह का उपयोग करके हमने आश्चर्यजनक रूप से शत-प्रतिशत(100%) तक स्पिन धारा प्रवहन क्षमता प्राप्त की है |

स्पिनट्रॉनिक्स समाज के प्रौद्योगिक-विकास की दिशा में एक उल्लेखनीय कदम है तथा इससे स्पिनट्रॉनिक्स-यंत्रों को औद्योगिक स्तर पर उत्पादन करने में मदद मिलेगी | औद्योगिकरण के लिये हमें बड़े पैमाने पर बने सतह चाहिये जो कि रासायनिक वाष्पीकरण से बनते हैं | हमने रासायनिक वाष्पीकृत-बोरोन-नाईट्राईड का भी अपने प्रयोग में उपयोग किया है | हालांकि ट्रांजिस्टर बनाने की प्रक्रिया में द्रव का उपयोग होने से अशुद्धियाँ ज्यादा मात्रा में आती हैं जो कि ग्राफीन ट्रांजिस्टर के सर्वोत्तम गुणवत्ता को नष्ट कर देती हैं, अतः अन्य वैकल्पिक विधियों के अनुसंधान की जरूरत है |

यह शोध नियंत्रण/ धारा क्षमता को प्रदर्शित करने की दिशा में किये गये प्रयोगों में प्रथम प्रयास है जिसमें हम साकारात्मक दिशा में आगे बढ़ रहे हैं | मुझे पूरा विश्वास है कि यह शोध आने वाले प्रयोगों के लिये एवं भविष्य में स्पिनट्रॉनिक्स यंत्रों के निर्माण में एक महत्वपूर्ण आधार प्रस्तुत कर मील का पत्थर साबित होगा |निश्चित रूप से ग्राफीन स्पिनट्रॉनिक्स शोध प्रथम स्पिन ट्रांजिस्टर के निर्माण के काफी समीप व सक्षम है और यह खोज वैज्ञानिक समुदाय को स्पिन लॉजिक आधारित यंत्र बनाने में एक अहम् कदम साबित होगा |

शोधकर्ता - सिद्धार्थ ओमर

\*\*\*\*\*



---

## Acknowledgements

Though I had no plans of pursuing a PhD, I was carried away by my interesting master project and had to rethink my future plans. After some initial struggle, I managed to get a PhD position in the group of Prof. Bart van Wees. However, the struggle did not end here as successful device fabrication became a nightmare during the initial phase and it took me almost a year to overcome it, and then started my happy PhD life! In this happy PhD life, I met a lot of important people, some could endure with me and now, I would like to acknowledge them.

I would first like to thank my daily supervisor Prof. Bart van Wees. I first heard about you when I was about to make a decision about the admission to the top master nanoscience program in Groningen. A friend of mine mentioned about your research work on transistors but those transistors are not the conventional ones. Having special interest in device physics and in circuit design, it was enough to motivate me. I was clear from the day one in Groningen that I would join your group for my one-year master project. Things worked according, and following my bachelor degree training, that choose the hardest and the most interesting project, and go for it, I had no hesitation in choosing spin-noise measurements in graphene under the daily supervision of Marcos Guimarães and Ivan Vera-Marun. The project was so exotic that we did not have a very clear idea what to measure and how to measure. I, Marcos, and Ivan worked hard on the conceptual, instrumental and experimental aspects of it. Though it was not a success at that time, later during my PhD, I could finally understand and measure the very phenomenon of spin-relaxation noise. Through this beautiful project which still gives me the immense satisfaction, I was able to acknowledge and admire your intellectual acumen, and insight for experiments in physics. Besides this, you were always careful to warn me about what not to do. This certainly saved me a lot of time and gave me an opportunity to try several other important things in parallel. I do appreciate the level of freedom you bestowed upon me. I must mention that I learned a lot from you during our daily discussion sessions for Mallik's pioneering work on bilayer hBN tunnel barriers.

Ivan, I still remember our first encounter in the FND, you explained me the basics of spintronics when I came to Bart, inquiring for a master project. You had almost convinced me to join the group. In these five years, in person and through our skype sessions, I really learned a lot from you and tried to transform myself from a slow,

and complicated person to a more simplified, and hardworking researcher. To some extent, I succeeded. I must acknowledge that our first and last work was published solely because of your efforts and academic acumen. It has already been fruitful to walk the lines drawn by you.

Marcos, I did enjoy working with you right from the day one. I have always admired your experimental and conceptual clarity, and tried to learn as much as I could during our interactions. Still whenever I require your help, you are always available. I always appreciate it and expect to continue in future as well.

Tamalika, first I should thank you for maintaining the trust throughout, you had set initially. Sometimes, even I felt you were happier than me for whatever big or small success I had achieved. A big thank you for that. I know you were expecting more delightful performance. I was about to reach it and the time was up! But you can be happy about my culinary skills. During my FND days, I enjoyed several academic, non-academic conversations and sponsored dinners outside. I am thankful to you for all these lovely gestures.

I would also like to acknowledge the professors from my reading committee, Prof. Aandras Kis, Prof. Gerrit Bauer and Prof. Justin Ye, for taking time to read my thesis.

Caspar, I still have memories of the interview for the top masters nanoscience program. It was among the most enjoyable interviews, I ever had in my life. Good luck with your new responsibilities as the director of the Zernike Institute!

Mallik, you were the first person, I met in Groningen. We gelled extremely well. Because of you, my academic life went extremely smooth. Outside the office, I had a great friend. Thanks for the countless academic and nonacademic discussions, which I will always cherish along with our several cooking attempts, including the legendary Masala Dosa attempt!

Arijit, everyone enjoys your company so do I, in spite of having very different approaches towards life! I will miss the yellow buildings beti ki shadi gatherings which eventually gave sunlight to my social life in Groningen. All credit to you for that! You have worked hard for last two years, and now its time to hit the ground. I wish you all the best.

Kumar, we had a lot of good times together, and shared a lot of secrets and gossips. Let's keep them safe. I am happy to see you working really hard. Good luck with your future.

Madhu, it took me some time to gel with you because of your level of enthusiasm. I am completely opposite. After some encounters, I was able to acknowledge that you are a gem of a person. I like your clarity. My best wishes for your future (wink).

I would like to acknowledge the happy FND faces: Jing, Crystal, Ping, and Tom (Bosma). I learned from you guys that smile on your face matters and can make the other person's day better. Jing, it was very nice of you to take a pause on the way and talk. To me it's unconventional. Also big thanks for the delicious dinner we

cooked at my place. Crystal, it was always a pleasure talking to you. I wish all you guys success and happiness.

I would also like to thank Arjan, Martijn, and Gerjan for the lively discussions during lunch break in the coffee room. I always enjoyed it.

Alexey, thank you for your generous help on several occasions. I appreciate it.

Pep, we had some nice discussions. I wish we should have done it quite often. Its on the unfortunate side that we could not work together. All the best with the final phase of your phd.

Juliana, special thanks for all the help and patience in the sample preparation and ebl during my learning period. Jasper, you were always nice, relaxed and responsible for the happy environment in the graphene-team. Thanks for your nice gestures during my transition from a master-student to a PhD-researcher in the group. Thomas, you were leaving the group when I joined at FND, and we met for a very brief period. However, I must admit, I learned most of the spintronics basics from your thesis. It is my favorite thesis so far. Even, you were very kind to share your very nice thesis template with me. Very much appreciated!

I would also like to acknowledge my office mates who, without any option had to bear with me. And no one complained! Juan, we shared the office almost for five years amicably. Well done! Your endurance is well appreciated. Saurabh (Roy), I have always relished the walks and the discussions we had during your academic life in Groningen. Your kind help was always available to me. Jakko, you are a very balanced person. I have always admired you. Thanks for the small gesture like asking for a cup of coffee during office hours. It mattered to me. Big thanks for sharing the thesis template with me. Very much appreciated! Geert, you joined the crew late but I expect you are not hating it. Thanks for your help during Tesla measurements and for the Dutch translation of the thesis summary. It is very nice of you. Wish you all the best for your future career.

Lei, we had not had many interactions, I admire your scientific acumen. I wish you success in your scientific career. Ludo, though we had only a short interaction during your final days, I have always admired your disciplined work-style and clarity. Keep it up!

Mithilesh and Maikel, you both put excellent efforts on your research projects. I was lucky to have supervised both of you. The fundamental physics, we were trying to probe, has not yet been realized due to the 'glamorized' world of 2D-materials. In my opinion, it requires the right amount of fundamental clarity and sincere efforts, you guys possessed. I should have been more available during that period in order to achieve what we were aiming for.

To all my FND colleagues, Talieh, Christian, Xu, Carmem, Julian, Tian, Jorge, Freddie, Frits, Xiangyang, Frank, Anouk, and all the rest, thank you for the scientific input and help I received during all these years at the group.

A very special thank you to the FND technical and administrative staff. Anna,



thanks for your help on many occasions. Also, when I made mistakes you were always able to find a way out. Johan, my first impression of you was that you are very strict. However, it turned out to be the opposite. You were always available for help and support. Thank you for several encouragements, you did time to time, especially during my toughest time, when I was under a deep personal trouble in India while writing my thesis. You were trying to help me in any possible way you could. I am touched! Herman and Martijn, thanks for your help in designing the test circuits for me. Martijn, thank you very much for a lot of things: for wire-bonding my samples, helping with helium filling, and a lot of small and big glitches we encountered during my research. Tom (Schouten), thank you for your kind offerings at the coffee room, and for your help during the repair of magnetic power supply and the transfer-stage heater.

I also made some friends outside the FND community, who helped me a lot during these years. Raj, you have always been very kind and helpful. Thank you for several planned and (mostly) unplanned lavish dinners which we had your place. My best wishes for your married life. Dhwani, I was on the same plane to Amsterdam from Dubai when you were coming to Groningen with your parents for the first time. We got to know each other later in Groningen, and started our reveling with gossips, food and old Hindi-songs. I would like to congratulate both of us for our successful attempts on 'larger than life' yummy pani-poories :), which can make any food-loving Indian envy of us. We should continue this practice in future. I will always be thankful to Groningen for I could discover you! Shubham, you are a different beast, who loves to decorate and keep things arranged. I exploited you to arrange my house and you were happy to take over the task with your emotional Ikea recommendations! Akash (Sharma), I met you at Raj's place, and we continued the same culture even after he left. I loved your place, hospitality and the food, of course! I hope you are able to enjoy in London now. Ketan (Mohini) you are a lovely person. Thanks for your help on many occasions. Pulkesh, I will fulfill my promise of making paneer (cottage cheese) for you before I leave. Hemant, I will always miss the running sessions. Special thanks for several chai (tea) sessions. Anil, our squash training is still on and will continue till one of us leaves. Thanks for several delicious dinners from Bhabhi and you. Anurag, I appreciate how far you go to help out any random person. I am happy that we are still in touch. Akanksha, you have been responsible for dragging the yellow building Indian association to come to the gossip sessions with tea. You really spoiled us. No one dared to say no to you. After you left, the beautiful environment you had created, was also gone. Subir (Thakur), you are a gentleman. All the best with ASML. Dipayan, I have always appreciated your enthusiasm and almost perfect way of working. I wish you a happy life in Groningen. Subir (Parui) aka pagla, I met you for the first time in a Zernike colloquium, and after discovering the IIT connection, we immediately became friends. You have been always helpful to me. I am happy that we are still in contact. Nilesh, I will

always cherish the study sessions we held at Black n Bloom. Your commitment to the appointments is deeply appreciated which is usually missing in the Indian community. We have to catch up again. Sumedh, we have started interacting recently, I enjoy your company. Also, I would like to thank Tenzin, Yamo, Musti, Ankur, Tarun, RP, Milon, Saurabh (Soni), Gurudas, Avishek Chris and Onni.

To my top master nanoscience cohort, I have always cherished the company of you guys. Jin, special thanks for your kind help on several occasions. I still cherish the long gossip sessions we had over these years. You will be missed. Eric, you are a very nice person. I really appreciate your selfless help on several occasions. Daniel and Jorge, good luck with your upcoming defenses and the life ahead. Edmond, all the best with your scientific career.

I also have some IIT friends in Europe, with whom I did my bachelor study in India. Akash (Sardar), you kept motivating me in my hard time in India and convinced to leave my job and pursue a master degree here. You have always welcomed me during your stay in Delft. I have always admired your scientific acumen and am looking forward to working together at some point. Mohit, you know my lazy habits very well, and also know how to treat a person like me. Thanks for the several travel-plans with Anupam Ashish (Aunto). You guys (literally) forced me to come. Thanks for taking those initiatives. Abhishek (Baba), though you were in India, we managed to meet during holidays. I have always enjoyed your company and 'Gyan'. Thank you for designing the thesis cover on one day notice! Naveen and Deepak (DK), thank you for staying in touch. Pranav (PG), I am happy that we could manage to meet at Mainz. It was a good memory-visit of our old IIT days, and you and Akash were kind enough not to rag me this time. At some point, I hope to meet you all together.

I would like to express my gratitude to Mr. Shatrusudan Srivastava and Geert for their time and efforts in the Hindi and the Dutch translation of my thesis, respectively.

Finally, the most special people for me. Maa, you are always behind every big decision, I took. May it be coming to Groningen right after papa's death, leaving my relaxed-government job, or taking a decision in my favor for IIT, you were always rock-solid and stood by me. That's the freedom I got and could perform. I have to appreciate, how you compose yourself and reach the right decision. Even, working with some well-educated and so-called 'powerful' people in different phases of my life, I have seen them shaken from inside and running away at the moment they have to take a decision. They should really learn from you. Sudhanshu, I am happy to see you growing as a mature, truthful and hardworking person. I am impressed with the way you managed so many things at this young age. It was a bad luck with the Indian Statistical Institute, you could make it to the waiting list but keep it up. You will get what you want. Sneha, since school days you always stood for me. Together with mom, you both create magic. It is remarkable to see how you

both handle situations, when everyone gives away. Jitendra, you joined us later (with laddoo junior and senior :D), I am sure you are enjoying it. I wish both of you a very happy and healthy married life ahead. Papa, you get the last mention in this acknowledgement list. However, you were not in a big favor of me coming to Groningen, I am sure you would be the happiest person to see me graduating as a PhD. I would like to dedicate this thesis to you.

I hope, I have not missed anyone who I wanted to acknowledge. I would like to express my gratitude towards all those who came in contact with me during my stay in Groningen and helped me with their kind intentions.

---

## List of publications

### Publications described in this thesis

1. "Spin relaxation in graphene with self-assembled cobalt porphyrin molecules",  
S. Omar, M. Gurram, I.J. Vera-Marun, X. Zhang, E.H. Huisman, A. Kaverzin,  
B.L. Feringa, and B.J. van Wees  
*Phys. Rev. B*, **92**, 115442 (2015).
2. "Spin transport in fully hexagonal boron nitride encapsulated graphene",  
M.Gurram, S. Omar, S. Zihlmann, P. Makk, C. Schönenberger, and B.J. van  
Wees  
*Phys. Rev. B* **93**, 115441 (2016).
3. "Spin relaxation 1/f noise in graphene",  
S. Omar, M. H. D. Guimarães, A. Kaverzin, B. J. van Wees, and I. J. Vera-Marun  
*Phys. Rev. B* **95**, 081403(R) (2017).
4. "Graphene-WS<sub>2</sub> heterostructures for tunable spin-injection and spin transport",  
S. Omar, and B. J. van Wees  
*Phys. Rev. B* **95**, 081404(R) (2017).
5. "Bias induced up to 100% spin-injection and detection polarizations in  
ferromagnet/bilayer-hBN/graphene/hBN heterostructure",  
M.Gurram, S. Omar, and B. J. van Wees  
*Nat. Commun.* **08**, 248 (2017).
6. "Two-channel model for spin-relaxation noise",  
S. Omar, B. J. van Wees, and I. J. Vera-Marun  
*Phys. Rev. B* **96**, 235439 (2017).
7. "Spin transport in high mobility graphene on WS<sub>2</sub> substrate with an electric-  
field tunable spin-orbit coupling",  
S. Omar, and B. J. van Wees  
*Phys. Rev. B* **97**, 045414 (2018).

8. "Spin-transport in two-layer-CVD-hBN/graphene/hBN heterostructures",  
M.Gurram, S. Omar, S.Zihlmann, P. Makk, Q.LI, Y.Zhang, C. Schönenberger, and  
B.J. van Wees  
*Phys. Rev. B* **97**, 045411 (2018).
9. "Electrical spin injection, transport, and detection in graphene-hexagonal boron  
nitride van der Waals heterostructures: progress and perspectives",  
M.Gurram, S. Omar, and B. J. van Wees  
<http://arxiv.org/abs/1712.07828>.  
(under review in 2D Materials).

### **Publication(s) resulting from my B.Tech at IIT, Kanpur - India**

10. "Organic Inverter: Theoretical Analysis using Load Matching Technique",  
S. Omar, S. Mandal, A. Ashok, A.R. Harish, and M. Katiyar  
*Microelectronics Reliability* **51**, 12 pp. 2173-2178 (2011).

---

## Curriculum Vitae

Siddhartha Omar

01<sup>st</sup> June 1987      Born in Hamirpur, India.

### Education

- 09/2013–08/2017      The European Graphene Flagship Program  
190637100  
PhD research in the group “Physics of Nanodevices”  
Supervisor: Prof. B. J. van Wees  
Performed at the Zernike Institute for Advanced Materials,  
University of Groningen, The Netherlands
- 09/2012–07/2013      University of Groningen, The Netherlands  
Master of Science, Top Masters in Nanodevices  
Thesis: Towards Spin-dependent noise measurements in  
Graphene  
Supervisors: Prof. Bart J. van Wees and Marcos H.D.  
Guimarães
- 08/2005–06/2009      Indian Institute of Technology, Kanpur (IITK), India  
Bachelor of Technology (B. Tech.),  
Electrical Engineering (EE)

**Work Experience**

- 05/2008–07/2008     Research intern  
Advanced Display Research Center,  
Kyung-Hee University  
Seoul, South Korea  
circuit simulation and performance optimization:  
Pentacene based OTFTs  
Supervisor: Prof. Jin Jang
- 09/2009–08/2011     Steel Authority of India Limited,  
Rourkela, India  
Designation: Junior Manager, Tech.  
High voltage power distribution